Image de-noising techniques to improve the observability of oceanic fine-scale dynamics by the SWOT mission

Laura Gómez Navarro

Universitat de les
Illes Balears

Doctoral Thesis

2020

IMAGE DE-NOISING TECHNIQUES TO IMPROVE THE OBSERVABILITY OF OCEANIC FINE-SCALE DYNAMICS BY THE SWOT MISSION.

Laura Gómez Navarro

Université Grenoble Alpes

Universitat de les Illes Balears

THÈSE

Pour obtenir le grade de

DOCTEUR DE L'UNIVERSITE GRENOBLE ALPES

préparée dans le cadre d'une cotutelle entre la Communauté Université Grenoble Alpes et la *Universitat de les Illes Balears*

Spécialité : Océan, Atmosphère, Hydrologie (CEOAH)

Arrêté ministériel : 25 mai 2016

Présentée par

Laura GÓMEZ NAVARRO

Thèse dirigée par **Emmanuel Cosme**
codirigée par **Ananda Pascual et Julien Le Sommer**

préparée au sein de **l'Institut des Geosciences de l'Environnement (IGE)** et de ***l'Institut Mediterrani d'Estudis Avançats* (IMEDEA)**

dans les Écoles Doctorales de **Terre-Univers-Environnement de l'UGA** et ***Física* de l'UIB**

Techniques de débruitage d'image pour améliorer l'observabilité de la fine échelle océanique par SWOT

Thèse soutenue publiquement le **29 Septembre 2020**,
devant le jury composé de :

M. Eric BLAYO
Professeur UGA (LJK, France), Président
Mme. Rosemary MORROW
Directrice de Recherche CNRS (LEGOS, France), Rapporteur
M. Joaquim BALLABRERA POY
Chargé de Recherche CSIC (ICM, Espagne), Rapporteur
M. Francesco D'OVIDIO
Chargé de Recherche CNRS (LOCEAN, France), Examinateur
M. Emmanuel COSME
Maître de Conférence UGA (IGE, France), Directeur de thèse
Mme. Ananda PASCUAL
Directrice de Recherche CSIC (IMEDEA, Espagne), Co-Directrice de thèse
M. Julien LE SOMMER
Chargé de Recherche CNRS (IGE, France), Co-Encadrant de thèse (invité)

Universitat de les Illes Balears

Doctoral Thesis

2020

Doctoral programme of Physics **Image de-noising techniques to improve the observability of oceanic fine-scale dynamics by the SWOT mission.**

Laura Gómez Navarro

Thesis Supervisor: Emmanuel Cosme

Thesis Supervisor: Ananda Pascual

Thesis Supervisor: Julien Le Sommer

Thesis Tutor: Damià Gomis Bosch

Doctor by the *Université Grenoble Alpes* and the *Universitat de les Illes Balears*

Universitat de les Illes Balears

This thesis has been written by Laura Gómez Navarro under the supervision of Dr. Emmanuel Cosme, Dr. Ananda Pascual and Dr. Julien Le Sommer.

Grenoble, July 17, 2020

Supervisors:

Emmanuel Cosme

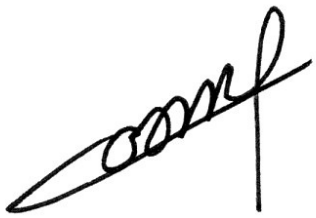

Ananda Pascual

Julien Le Sommer

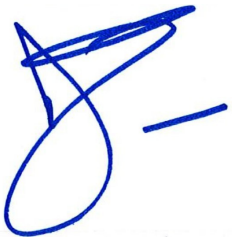

PhD student:

Laura Gómez Navarro

A totes les “topitas” i al Mar
À toutes les “topitas” et à la Mer.
To all “topitas” and to the Sea.
A todas las “topitas” y al Mar.

Abstract

Sea Surface Height (SSH) observations describing scales in the range 10 - 100 km are crucial to better understand energy transfers across scales in the open ocean and to quantify vertical exchanges of heat and biogeochemical tracers. The Surface Water Ocean Topography (SWOT) mission is a new wide-swath altimetric satellite which is planned to be launched in 2022. SWOT will provide information on SSH at a kilometric resolution, but uncertainties due to various sources of errors will challenge our capacity to extract the physical signal of structures below a few tens of kilometers. Filtering SWOT noise and errors is a key step towards an optimal interpretation of the data.

The aim of this study is to explore image de-noising techniques to assess the capabilities of the future SWOT data to resolve the oceanic fine scales. Pseudo-SWOT data are generated with the SWOT simulator for Ocean Science, which uses as input the SSH outputs from high-resolution Ocean General Circulation Models (OGCMs). Several de-noising techniques are tested, to find the one that renders the most accurate SSH and its derivatives fields while preserving the magnitude and shape of the oceanic features present. The techniques are evaluated based on the root mean square error, spectra and other diagnostics.

In Chapter 3, the pseudo-SWOT data for the Science phase is analyzed to assess the capabilities of SWOT to resolve the meso- and submesoscale in the western Mediterranean. A Laplacian diffusion de-noising technique is implemented allowing to recover SSH, geostrophic velocity and relative vorticity down to 40 - 60 km. This first step allowed to adequately observe the mesoscale, but space is left for improvement at the submesoscale, specially in better preserving the intensity of the SSH signal.

In Chapter 4, another de-noising technique is explored and implemented in the same region for the satellite's fast-sampling phase. This technique is motivated by recent advances in data assimilation techniques to remove spatially correlated errors based on SSH and its derivatives. It aims at retrieving accurate SSH derivatives, by recovering their structure and preserving their magnitude. A variational method is implemented which can penalize the SSH derivatives of first, second, third order or a combination of them. We find that the best parameterization is based on a second order penalization, and find the optimal parameters of this setup. Thanks to this technique the wavelengths resolved by SWOT in this region are reduced by a factor of 2, whilst preserving the magnitude of the SSH fields and its derivatives.

In Chapter 5, we investigate the finest spatial scale that SWOT could resolve after de-noising in several regions, seasons and using different OGCMs. Although a method is found to mitigate the impact of SWOT instrumental noise and errors, large uncertainties remain due to the incomplete understanding of the impact of fast unbalanced motions (e.g. internal gravity waves) on SSH signals, and therefore the impact on the performance of the de-noising algorithm. Our study focuses on different regions and seasons in order to document the variety of regimes that SWOT will sample. The de-noising algorithm performs well even in the presence of intense unbalanced motions, and it systematically reduces the smallest resolvable wavelength. Advanced de-noising algorithms also allow to reliably reconstruct SSH gradients (related to geostrophic velocities) and second order derivatives (related to geostrophic vorticity). Our results also show that a significant uncertainty remains about SWOT's finest resolved scale in a given region and season because of the large spread in the level of variance predicted among our high-resolution ocean model simulations.

The de-noising technique developed, implemented and tested in this doctoral thesis allows to recover, in some cases, SWOT spatial scales as low as 15 km. This method is a very useful contribution to achieving the objectives of the SWOT mission. The results found will help better understand the ocean's dynamics and oceanic features and their role in the climate system.

Keywords: wide-swath altimetry, image de-noising, ocean circulation, fine-scale dynamics, SWOT satellite

Résumé

Les observations de la hauteur de la surface de la mer (SSH) décrivant des échelles entre 10 et 100 km sont cruciales pour mieux comprendre les transferts d'énergie à travers les différentes échelles en plein océan et pour quantifier les échanges verticaux de chaleur et de traceurs biogéochimiques. La mission *Surface Water Ocean Topography* (SWOT) est un nouveau satellite altimétrique à large fauchée dont le lancement est prévu en 2022. SWOT fournira des informations sur la SSH à une résolution kilométrique, mais des incertitudes dues à diverses sources d'erreurs mettront à l'épreuve notre capacité à extraire le signal physique des structures inférieures à quelques dizaines de kilomètres. Le filtrage du bruit et des erreurs SWOT est une étape clé vers une interprétation optimale des données.

L'objectif de cette étude est d'explorer des techniques de débruitage d'image afin d'évaluer les capacités des futures données SWOT à résoudre les fines échelles océaniques. Les données pseudo-SWOT sont générées avec le simulateur SWOT pour l'océanographie, qui utilise comme données d'entrée les sorties SSH des modèles de circulation générale océanique (OGCMs) à haute résolution. Plusieurs techniques de débruitage sont testées, afin de trouver celle qui rend le plus précisément les champs de SSH et de ses dérivées tout en préservant l'amplitude et la forme des structures océaniques présentes. Les techniques sont évaluées sur la base de la racine carrée de l'erreur quadratique moyenne, des spectres et d'autres diagnostiques.

Au Chapitre 3, les données pseudo-SWOT pour la phase scientifique sont analysées pour évaluer les capacités de résolution de la méso et la sousmésoéchelle en Méditerranée occidentale. Une technique de débruitage par diffusion laplacienne est mise en œuvre permettant de récupérer la SSH, la vitesse géostrophique et la vorticité relative jusqu'à 40 - 60 km. Cette première étape a permis d'observer correctement la mésoéchelle, mais il reste de la place pour des améliorations à la sousmesoéchelle, notamment pour mieux préserver l'intensité du signal SSH.

Au Chapitre 4, une autre technique de débruitage est explorée et mise en œuvre dans la même région pour la phase d'échantillonnage rapide du satellite. Cette technique est motivée par les progrès récents des techniques d'assimilation de données pour supprimer les erreurs spatialement corrélées basées sur la SSH et ses dérivées. Elle vise à retrouver adéquatement des dérivées de SSH, en récupérant leur structure et en préservant leur ampleur. Une méthode variationnelle est mise en œuvre qui peut pénaliser les dérivées de la SSH de premier, deuxième, troisième ordre ou une combinaison de ceux-ci. Nous constatons que le meilleur paramétrage est basé sur une pénalisation de second ordre, et nous avons trouvé les paramètres optimaux de cette configuration. Grâce à cette technique, les longueurs d'onde résolues par SWOT dans cette région sont réduites d'un facteur 2, tout en préservant l'ampleur des champs de SSH et de ses dérivées.

Au Chapitre 5, nous étudions l'échelle spatiale la plus fine que SWOT pourrait résoudre après avoir débruité dans plusieurs régions, saisons et en utilisant différents OGCMs. Bien qu'une méthode est trouvée pour atténuer l'impact du bruit et des erreurs instrumentales SWOT, de grandes incertitudes subsistent en raison de la compréhension incomplète de l'impact des mouvements rapides non équilibrés (par exemple, les ondes internes gravitationnelles) sur les signaux SSH, et donc l'impact sur la performance de l'algorithme de débruitage. Notre étude se concentre sur différentes régions et afin de documenter la variété des régimes que SWOT échantillonnera. L'algorithme de débruitage fonctionne bien même en présence de mouvements rapides non équilibrés intenses, et permet de réduire systématiquement la plus petite longueur d'onde résolue. Algorithmes de débruitage avancés permettent également de reconstruire de manière fiable les gradients SSH (liés aux vitesses géostrophiques) et les dérivées de second ordre (liées à la vorticité géostrophique). Nos résultats montrent également qu'une incertitude importante subsiste quant à l'échelle la plus fine résolue par SWOT dans une région et saison données en raison de la grande dispersion du niveau de variance estimé par nos simulations des modèles océaniques à haute résolution.

La technique de débruitage développée, mise en œuvre et testée dans cette thèse doctorale permet de récupérer, dans certains cas, des échelles spatiales SWOT jusqu'à 15 km. Cette méthode est une contribution très utile pour atteindre les objectifs de la mission SWOT. Les résultats trouvé aideront à mieux comprendre la dynamique et les structures océaniques et leur rôle dans le système climatique.

Mots clés: altimétrie large-fauchée, débruitage d'image, circulation océanique, dynamique fine-échelle, satellite SWOT

Resum

Les observacions d'altura de superfície del mar (SSH) que descriuen escales espacials de 10 - 100 km són crucials per millor entendre la transferència d'energia a través les diferents escales en l'oceà obert i per quantificar intercanvis verticals de calor i traçadors biogeoquímics. La missió *Surface Water Oceen Topography* (SWOT) és un nou satèl·lit altimètric de feix ample que és previst de ser llançat en 2022. SWOT proporcionarà informació de la SSH a una resolució quilomètrica, però incerteses a causa de diverses fonts d'errors desafiaran la nostra capacitat d'extreure el senyal físic d'estructures de menys d'unes quantes desenes de quilòmetres. El filtratge del soroll i els errors SWOT és un pas clau cap a una interpretació òptima de les dades.

L'objectiu d'aquest estudi és explorar tècniques de reducció de soroll d'imatge per avaluar les capacitats de les futures dades SWOT per resoldre la petita escala oceànica. Les dades pseudo-SWOT són generades amb el simulador SWOT per a les ciències oceàniques, el qual utilitza com entrada les sortides SSH de models oceànics de circulació general (OGCMs) d'alta resolució. Diverses tècniques de reducció de soroll són provades per a trobar la que més fidelment representa els camps de SSH i les seves derivades, preservant al mateix temps la magnitud i la forma de les estructures oceàniques presents. Les tècniques són avaluades amb l'error de l'arrel quadrada de la mitjana, espectres i altres diagnòstics.

En el Capítol 3, les dades pseudo-SWOT per a la fase científica són analitzades per avaluar les capacitats de SWOT per resoldre la meso i submesoescala al Mediterrani Occidental. Una tècnica de reducció de soroll per difusió laplaciana és implementada la qual permet recuperar la SSH, velocitat geostròfica i vorticitat relativa fins a 40 - 60 km. Aquest primer pas va permetre observar adequadament la mesoescala, però encara queda marge de millora en la submesoescala, especialment per a preservar millor la intensitat del senyal SSH.

En el Capítol 4, una altra tècnica de reducció de soroll és explorada i implementada en la mateixa regió per la fase de mostreig-ràpid del satèl·lit. Aquesta tècnica és motivada per avanços recents en tècniques d'assimilació de dades, per reduir els errors correlacionats espacialment, basades en la SSH i les seves derivades. Aquesta tècnica té com a objectiu l'obtenció precisa de les derivades de SSH, en recuperant la seva estructura i preservant la seva magnitud. Un mètode variacional és implementat el qual pot penalitzar les derivades de SSH de primer, segon, tercer ordre o una combinació d'elles. Trobem que la millor parametrització es basa en una penalització de segon ordre, i trobem també els paràmetres òptims d'aquesta configuració. Gràcies a aquesta tècnica les longituds d'ona resoltes per SWOT en aquesta regió són reduïdes per un factor de 2, en preservant la magnitud dels camps de SSH i de les seves derivades.

En el Capítol 5, investiguem l'escala espacial més petita que SWOT podria resoldre després de la reducció del soroll en diverses regions, estacions i utilitzant diferents OGCMs. Encara que s'hagi trobat un mètode per a mitigar l'impacte del soroll i els errors instrumentals de SWOT, continuen existint grans incerteses a causa de la comprensió incompleta de l'impacte dels processos d'alta freqüència no geostròfics (per exemple, les ones internes de gravetat) en el senyal de SSH i, per tant, l'impacte en el rendiment de l'algoritme de reducció de soroll. El nostre estudi se centra en diferents regions i estacions per documentar la varietat de règims que SWOT mostrejarà. L'algoritme de reducció de soroll funciona fins i tot en presència de processos d'alta freqüència no geostròfics intensos i redueix sistemàticament la més petita longitud d'ona resoluble. Els algoritmes avançats de reducció de soroll també permeten reconstruir de manera fiable els gradients de SSH (relacionats amb les velocitats geostròfiques) i les derivades de segon ordre (relacionades amb la vorticitat geostròfica). Els nostres resultats també mostren que continua existint una incertesa significativa sobre l'escala més petita resolta per SWOT en una regió i estació donades, a causa de la gran dispersió en el nivell de variància predit entre les simulacions de models oceànics d'alta resolució.

La tècnica de reducció de soroll desenvolupada, implementada i provada en aquesta tesi doctoral permet recuperar, en alguns casos, les escales espacials de SWOT fins a 15 km. Aquest mètode és una contribució molt útil per a aconseguir els objectius de la missió SWOT. Els resultats obtinguts ajudaran a comprendre millor la dinàmica i les estructures oceàniques i la seva funció en el sistema climàtic.

Paraules clau: altimetria de feix ample, reducció de soroll d'imatge, circulació oceànica, dinàmica de petita-escala, satèl.lit SWOT

Resumen

Las observaciones de la altura de la superficie del mar (SSH) que describen las escalas entre 10 y 100 km son cruciales para comprender mejor las transferencias de energía a través las diferentes escalas en el océano abierto y para cuantificar los intercambios verticales de calor y de trazadores biogeoquímicos. La misión *Surface Water Ocean Topography* (SWOT) es un nuevo satélite altimétrico de banda ancha cuyo lanzamiento está previsto para 2022. SWOT proporcionará información sobre la SSH a una resolución kilométrica, pero las incertidumbres debidas a las diversas fuentes de error pondrán a prueba nuestra capacidad de extraer la señal física de estructuras de menos de unas pocas decenas de kilómetros. Filtrar el ruido y los errores de SWOT es un paso clave para una interpretación óptima de los datos.

El objetivo de este estudio es explorar técnicas de reducción de ruido de imagen para evaluar las capacidades de los futuros datos SWOT para resolver las escalas finas oceánicas. Los datos pseudo-SWOT son generados con el simulador SWOT para las ciencias oceánicas, que utiliza como entrada las salidas de SSH de modelos de circulación general oceánica (OGCMs) de alta resolución. Varias técnicas de reducción de ruido son probadas para encontrar la que más fielmente representa los campos de SSH y sus derivadas, preservando al mismo tiempo la magnitud y la forma de las estructuras oceánicas presentes. Las técnicas son evaluadas en base a la raíz del error cuadrático medio, espectros y otros diagnósticos.

En el Capítulo 3, se analizan los datos pseudo-SWOT de la fase científica para evaluar las capacidades de SWOT para resolver la meso y submesoescala en el Mediterráneo occidental. Se implementa una técnica de difusión laplaciana que permite recuperar la SSH, la velocidad geostrófica y la vorticidad geostrófica relativa hasta 40 - 60 km. Este primer paso permitió observar adecuadamente la mesoescala, pero aún queda margen de mejora en la submesoescala, especialmente para preservar mejor la intensidad de la señal de SSH.

En el Capítulo 4, se explora e implementa otra técnica de reducción de ruido en la misma región para la fase de muestreo rápido del satélite. Esta técnica está motivada por los avances recientes en las técnicas de asimilación de datos para eliminar los errores de correlación espacial basándose en SSH y sus campos derivados. El objetivo es recuperar de manera precisa las derivadas de SSH, recuperando su estructura y preservando su magnitud. Se implementa un método variacional que puede penalizar las derivadas de SSH de primer, segundo, tercer orden o una combinación de estas. Encontramos que la mejor parametrización se basa en una penalización de segundo orden, y encontramos los parámetros óptimos de esta configuración. Gracias a esta técnica las longitudes de onda resueltas por SWOT en esta región se reducen por un factor 2, preservando a su vez la magnitud de los campos de SSH y sus derivadas.

En el Capítulo 5, investigamos la escala espacial más fina que SWOT podría resolver después de la reducción del ruido en varias regiones, estaciones y usando diferentes OGCMs. Aunque se haya encontrado un método para mitigar el impacto del ruido y los errores instrumentales de SWOT, siguen existiendo grandes incertidumbres debido a la comprensión incompleta del impacto de los procesos de alta frecuencia no geostróficos (por ejemplo, las ondas de gravedad internas) en las señales de SSH y, por lo tanto, el impacto en el rendimiento del algoritmo de reducción de ruido. Nuestro estudio se centra en diferentes regiones y estaciones para documentar la variedad de regímenes que SWOT muestreará. El algoritmo de reducción de ruido funciona incluso en presencia de procesos de alta frecuencia no geostróficos intensos, y reduce sistemáticamente la más pequeña longitud de onda resoluble. Los algoritmos avanzados de eliminación de ruidos también permiten reconstruir de manera fiable los gradientes de SSH (relacionados con las velocidades geostróficas) y las derivadas de segundo orden (relacionadas con la vorticidad geostrófica). Nuestros resultados también muestran que sigue existiendo una incertidumbre significativa sobre la escala más pequeña resuelta por SWOT en una región y estación dadas, debido a la gran dispersión en el nivel de varianza predicho entre las simulaciones de modelos oceánicos de alta resolución.

La técnica de reducción de ruido desarrollada, implementada i probada en esta tesis doctoral permite recuperar, en algunos casos, las escalas espaciales de SWOT hasta 15 km. Este método es una contribución muy útil para lograr los objetivos de la misión SWOT. Los resultados obtenidos ayudarán a comprender mejor la dinámica y las estructuras oceánicas y su función en el sistema climático.

Palabras clave: altimetría de banda ancha, reducción de ruido de imagen, circulación oceánica, dinámica de pequeña-escala, satélite SWOT

Acknowledgements

Going from here to there during my PhD years, the acknowledgements might get long and in diverse languages, sorry in advance for the mash-up.

First of all I would like to thank my supervisors Emmanuel Cosme, Ananda Pascual and Julien Le Sommer for having made possible for me to carry out this PhD, something I thought at some point that I might not have the opportunity to do. Thanks, for having given me the opprotunity to participate in this adventure and to attend several courses, summer schools, conferences, a field campaign, ...; and for not only making me do a study I had to do, but one that I liked to do, by adapting with me to new projects that appeared during this journey. Thanks again to Ananda and Emmanuel, for helping me handle the cotutelle and its administrative procedures, and the double bureacracy we have had to handle. Thanks also to Emmanuel and Julien for their patience with my troubles expressing myself in French, or sometimes in any language at all.

Merci Emmanuel par la patience que t'as eue avec moi, et avec ça, merci par avoir réussi à que (i) j'apprends beaucoup de nouvelles choses et (ii) que j'apprends à m'exprimer mieux (j'espère) à l'orale et à l'écrit, en mieux rangeant mes pensées divergents et chaotiques. Merci aussi de m'avoir donné l'opportunité de découvrir le monde de l'enseignement à l'université en pouvant donner des cours d'océanographie et en pouvant aider a encadré des étudiants en stage à l'équipe. Aussi, même si finalement je n'ai pas mis trop la tête dedans, merci de m'avoir fait mieux comprendre le monde de l'assimilation des données, et pouvoir maintenant comprendre "la langue", les enjeux et les avantages de ce champ de recherche.

Merci Julien aussi pour la patience que t'as eue avec moi, en particulier mon chaos vers ton ordre. J'appris à mieux ranger et organiser mes codes et mes notes (même si c'est toujours du *work in progress*), et comment faire pour que ça puisse être partagé, d'une manière claire, compréhensible et surtout, ouverte. Merci aussi pour me donner de l'espoir pour une science plus ouverte et partagé, en voyant tes efforts pas seulement dans l'équipe mais aussi en réunions des projets ou conférences, comme le SWOT meeting.

Muchas gracias Ananda, por estar siempre ahí y haberme ayudado tanto a conseguir una beca de doctorado. Por todo lo que he aprendido contigo ya desde el máster, de ciencia, pero también de su gestión. Gracias por la manera en que siempre me has tenido en cuenta en los proyectos y me has dejado participar, gracias a lo cual no solo he podido aprender mucho pero también me ha ayudado a tener más confianza en mí como científica. Gracias también por la oportunidad de haberme dejado descubrir el mundo de la divulgación, y haber tenido la confianza en mi para organizar talleres. Finalmente, gracias por ser una inspiración para las mujeres en ciencia, y más aún para las que trabajamos en el campo de la Física.

I would like to acknowledge CNES and FP7 funding, which made possible this PhD. Also, I would like to acknowledge other sources of funding that allowed me to carry out different activities during my PhD: the Pre-SWOT project and COST Action ES140.

During this PhD I had the chance to do a short research stay at the University of Michigan. Thank you very much Brian, for having given me the opportunity to collaborate not only with a great expert in our field, but also a great person. I have learned a lot with you about internal waves and more. Thank you for trying to help us, earlier career scientists, in having a good career in Science. More importantly, your implication with African students, being an example for making Science and a scientific career more inclusive and accessible to all. Thank you also to Paige and Molly for hosting me during my stay, and showing me around the campus, and making me enjoy more my research stay. Lastly, thanks to Stacy Wilkin and Mike Messina, for helping me with administrative and IT logistics, not only during my stay, but during this whole collaboration.

Merci aux membres de mon comité thèse: Thierry Penduff et Aurelien Ponte. Merci pour vos avis scientifiques sur mon travail, en me donnant autre perspective fraîche.
Merci à Nicolas Papadakis pour son aide mathématique, et pour faire possible l'implémentation de la méthode de débruitage développé pendant cette thèse.
Thank you also to many other researchers with whom I have had the chance to interact and have had very intersting discussions, many from the SWOT-ST: Michel Tchilibou, Guillaume Serazin, Lucile Gaultier and Jinbo Wang.

Encore merci à tous et toutes les membres de mon jury de thèse: Rosemary Morrow, Joaquim Ballabrera Poy, Francesco d'Ovidio et Eric Blayo. Thanks for having accepted to take part in my thesis' jury during these complicated COVID19 times, and for the interesting discussion at the PhD defense. Special thanks to Rosemary and Quim for being the "rapporteurs" and their input to improve this PhD manuscript.
Thanks also to the other people who virtually attended the PhD defense, without the option of afterwards joining for the "pot de these". I hope to be able to celebrate with you in a COVID19-friendly future!

J'aimerais dire merci à toutes les personnes qui ont fait que mon temps à Grenoble c'est très bien passé.
À l'équipe MEOM, toujours quelqu'un.e a était là pour m'aider avec une problème scientifique, informatique, administrative, avec la communication en français, pour avoir une café ou une bière, ... Merci par le bon accueil en arrivant, surtout à Marina, Pedro, Nacho, Florent, Mondher, Jean-Michel, Jean-Marc, Gildas et Aurelie pour toute votre aide avec plein des choses différentes au début de ma thèse.
Thank you AJ and Ixetl for these PhD years together, I have enjoyed a lot being in this adventure with you guys, and have learned and laughed a lot with you!
Merci à Sally qui a eu la patience d'être ma co-bureau pendant la plupart de mon temps au MEOM, et tout le fois qu'on a rigoler ensemble, merci pour tout!
Thanks to Ghina, for sharing the office with me during these tough last PhD months, and making your good mood contagious.
Merci à Josiane pour nous faire la vie plus facile, merci de te préoccuper pour que le MEOM soit bien, confortable, facile, pour le bien-être de tous et toutes. Gros merci aussi a Stéphanie pour faire possible qu'on a toujours du café, je n'aurais pas survécu!
Et c'est sûr que j'oublie de mentioner quelque chose, mais merci à toute le MEOM qui reste: Bernard, Sammy, Yeray, Imane, Redouane, AnnSo', Victor, Simon, Takaya, Quentin, Florian, Olivier, Cyril, Jacques, Pierre, (et j'espere oublier personne...)
Aussi à nos voisins du LEGI, en éspecial à Cruz y Miguel. Gracias por estar ahí chicos!
Au group de doctorants.es de l'IGE, surtout à ces doctorantes qui se sont impliqué pour améliorer la vie des doctorant.es et qui ont organisé des activités, en espécial à Maria et Albane! Au groupe de basket de doctorants.es de l'IGE (Hans, Jai, Marco, Anil, Diego, Jonathan, Nathan et autres!), pour les bons moments ensemble surtout pendant cette dernière année de thèse.
À Defne, la meilleure coloc que j'ai eu par hasard! Pour son aide en arrivant à Grenoble et bon pour tout, et à sa famille pour m'avoir accueilli en arrivant. Merci Defne et Floriane pour m'accueillir au sud quand j'avais un peu besoin de vitamin Sea (et de vous voir bien sûr).
Gracias a Jai y Gabi por haberme acogido con vosotrxs en la casa mas linda! Merci à Julien Beaumet aussi pour ces dernieres mois à la CMP et ta patience avec des doctorant.es en fin de thèse! And also our other CMP colocs Jinhwa, Romain, Aurelie and Anil, thanks for making the end of this experience much better! Muchas gracias Jai et Julien pour tout tout (surtout le piment dans la sauce), les mieux colocs que j'ai pu avoir en fin de thèse!

Muchas gracias a toda la gente de Mallorca, que ha estado ahí en algún momento durante todas estas idas y venidas.
Gracias al equipo TMOOS : Ananda, Simón, Evan y Antonio. Muchas gracias por todo, he aprendido muchísimo con vosotr@s, y disfrutado mucho trabajando con vosotr@s. Thanks a lot Evan for having me introduced to the python and latex worlds prior to this PhD, you prepared me well for the PhD adventure! Also, thanks for being there when I needed to discuss not only science and coding, but also the ethics behind Science. Gracias también a Ismael, Angel, Marta Marcos y Jano por la ayuda y/o discusiones sobre física cuando he necesitado ayuda. Gracias Ismael por todas las discusiones de ciencia y no ciencia, por explícarme los FSLE y trabajar junt@s con los pájaros. Gracis Ángel per totes les discussions científiques i per ensenyar-nos a fer sobressada!
Unas gracias especiales a Álex Axica y a Vero Córdoba. Gracias Álex por crear un ambiente más acogedor en IMEDEA con tu simpatía y buen rollo, y por habernos ayudado tanto a tod@s l@s que hemos defendido la tesis después de ti con toda la burocracia final. Gracias Vero también por hacer que el ambiente en IMEDEA sea mejor con tu energía, pero sobretodo por tus abrazos en los pasillos. Muchas gracias chicas, que os voy a decir sino!
Otras gracias especiales a Julia (la punky), por haber estado ahí desde que empezó esta aventura, por todo! Gracias a VillaTopitas (Lara, Vero Galega, Vero canaria)! Por las risas, las fiestas y los ratos en el sofá viendo la TV o hablando de ciencia. Por ayudarme con mis mudanzas (y mi diogenes), por todo! Y a l@s que luego continuaron en VillaTopitas Andrea SOCIB y Quique, y Javi Canario.
Gracias a tod@s l@s Imedeic@s por la ciencia junt@s, las risas, los cafés, los ratos en el ágora después de

comer, las verbenas, las nits de l'art: Carlota, Miguel, Xisca, Albert, Ana, Edu, Noemi, Julia Garriga, Andrea (peces), Esther, Gemma, Fran, Noe, Juanma, Adri, Eva chilena, Eva galega, Jaime, Julia Madrid, Gal.la, Julia Vic, Marina, Bàrbara, Marc, Manu, Javi, Manuel, ... (y seguro me olvido a alguien).
Gracias también a l@s del IEO (grupo sensato) : Safo, Albert P., Javi F., Mariel, Ale, Merlu, por todas las risas!!!

During this PhD, I have become aware of how lucky I have been to have encountered the people I have before starting this PhD during my bachelor and master's studies, which have made me normalize a spirit in Science of sharing and helping each other, instead of being competitive; to value more a group work spirit instead of working without collaborating and helping each other out:

Muchas gracias a la penyi de la primera promoción de Grado de CC del Mar. Por seguir riéndonos junt@S y haber mantenido el contacto todos estos años. Por no solo ser grandes compañerxs, pero amigxs con lxs que contar para hacer un asadero, bucear (nocturna incluida), estudiar, ir a urgencias, bailar, viajar, irse a otra isla de carnavales, irse de pateo, organizar limpiezas de playas, hacer zooms durante pandemias pero sobretodo por trabajar juntxs y no unxs contra lxs otrxs. También a toda la gente de la Facultad, esutdiantes de promociones de arriba y abajo, técnicxs, doctorandxs y profesorxs. Por enseñarme que la ciencia puede ser una gran familia y no un mar de tiburones.

À mes bebitos du master à Brest : Mat, Nico, Pauline, Defne, Flo et Max. Merci pour tout, pour rigoler ensemble, mais aussi s'aider avec les choses qu'on ne comprends pas. Pour etudier ensemble la GFD et chanter les abeilles. Pour essayer de comprendre mon français et me montrer et decrouvir ensemble la Bretagne. Pour travailler ensemble en G016 jusqu'à (trop) tard et danser la physique (des vortex, Kelvin waves, et Ekman) et mambo n5. Encore une fois, j'ai eu la chance de retrouver pendant mes études des gens qui preferent travailler ensemble et pas l'un.e contre l'autre.
Also thanks to the great people we met during the MSc of the Univeristy of Southampton, specially Vero Galega, Anda and Sofi. Thanks girls for having been there during these years to share our ups and lows, but most importantly, laugh together.

To my family and hometown friends.
Muchas gracias Laura, Meli y Sean, por haber estado ahí en estos años, con esta locura de no saber donde estaba, o cuando venía a casa y me iba. También me gustaría dar las gracias al resto de caraculxs del cole, que me han aguantado con mis freakadas marinas y por su canción de Cousteau, y que habéis estado ahí de alguna manera u otra: Marina, Lucía, Bea, Leire, Mónica, Anja, Pelayo y Charly.
Moltes gràcies a la Amparo, Jesus, Toni i Conxita, per ajudar-me a descobrir el mar, i fer-me adonar-me que volia seguir descobrint i explorant-ho. Unas gracias especiales a Jesús por el apoyo en tierra yendo y viniendo en ferry entre Mallorca y Barcelona.
A la meva familia, a la que hi és i a la que ja no. Gràcies per fer-me descobrir el mar, passar els estius passejant amunt i avall la platja de Castelldefels, a Calella i Lloret, les vacances a la Costa Brava o Menorca. Gràcies per aguantar-me amb les freakadas del mar, com deixar-me veure si el llagostí era mascle o femella abans de menjarvos-lo. Per encara que va costar una miqueta, acompanyar-me i donar-me suport en aquesta aventura d'estudiar el mar. A les 4 mosqueters, al Francesc, a les Pos Sara i Eva, al Padri, al Papa. A la Iaia i el Tete, per tot. A la mami, gràcies per tot, sense el teu support i carinyo no ho hagués pogut fer. Tros. Us estimo molt.

Contents

Chapter 1

Introduction

Contents

The ocean is a key component of the Earth's climate system. About 70% of the Earth's surface is covered by it and acts as its primary reservoir of heat and carbon. Sustained ocean observations are vital to establish the ocean state and variability, to understand the ocean's role in climate variability. This is necessary for climate prediction and scenario development and to test and improve climate models. Fine-scale dynamics play a critical role in the exchanges of heat, fresh water and biogeochemical tracers of the ocean surface with the atmosphere and the ocean interior. Integrating our understanding of these processes to a climate scale, is one of the key challenges that faces Earth observation, limited by the high resolution of ocean data required.

With the increased preocupation on global change, oceanic climatic studies have gained relevance. Following *Pörtner et al.* (2019), in recent years the ocean has: absorbed the heat in excess in the climate system, absorbed more CO_2 (and thus a surface ocean acidification), suffered more and more intense marine heatwaves and lost oxygen in the surface waters. Although most of these impacts remain quite restrained to surface waters, changes have also been observed in the deeper ocean. For example *Arbic and Brechner Owens* (2001) found a warming in Atlantic intermediate waters, and a stronger effect has been found in the Southern Ocean intermediate waters (*Banks et al.*, 2000). Since the 90s a warming of deep waters has also been observed in the western Mediterranean (*Bethoux et al.*, 1990; *Rixen et al.*, 2005), and has been further confirmed by recent studies (*Schroeder et al.*, 2017; *Barceló-Llull et al.*, 2019).

The study of the oceanic circulation has many applications. Maritime transport is one of these, as not only the ocean and weather forecast are of their interest, but also accurate information on marine currents. Sea rescue operations can sometimes highly rely on the latter, where accurate information on currents can imply a successful rescue or not. Environmental hazards such as oil spills, need this information to know where to put the effort into reducing the impact and cleaning. Oceanographic research efforts have been established posterior to big oil spill events e.g. *Smith et al.* (2014); *Ruiz-Villarreal et al.* (2006).

Understanding specific oceanic features that have an impact on nutrients is of great interest for the different fields of biology and ecology. The horizontal and vertical ocean dynamics establish the distribution of nutrients in the global ocean. The availability of these nutrients at a certain depth, for example, can be a limiting factor for the proliferation of a particular species. Horizontally, eddies and filaments redistribute different nutrients via lateral advection. The effect of the presence of eddies on chlorophyll has been thoroughly studied, for example in the Southern Ocean (*Frenger et al.*, 2018). The vertical velocities associated to eddies and fronts mix nutrients vertically. *Ruiz et al.* (2019) show how the vertical velocities associated to oceanic fronts help explain the vertical chlorophyll distribution.

The impact of ocean dynamics on biogeochemistry is consequently important for fisheries. As explained above, the ocean dynamics have an impact on nutrients which then influence fish populations. Mainly, it is the upwelling systems which have a high impact in the fishing industry. At a smaller scale, the mesoscale, can affect the spawning ecology of some species, like bluefin tuna (*Alvarez-Berastegui et al.*, 2016). At even smaller spatial scales, turbulent mixing exposure can be determining for spawning (*Lima and Castello*, 1995).

The study of the ocean is also necessary due to its environmental, climatic, economical and society impact. All of these are related to one another, but the first two impacts could be simplified to that about 2/3 of the Earth's planet is covered by water. An important fact impacting society and the economy is that a great percentage of the Earth's population lives at the coast, and in addition to its dependence on sea level change, many economical and social activities related to the oceans and Seas, affect most of the population. Some of these are for example activities concerning the fisheries industries, touristic sectors and a range of leisure activities and sports occurring there.

1.1 Oceanic scales and dynamics

The ocean is a complex system characterized by a large range of temporal and spatial scales that has to be studied integrating observations and modeling. At each scale there can be one or several features present, as shown in fig. 1.1. This usually implies a use of a particular or modified theory (e.g., geostrophy or quasi-geostrophy) and measuring tool (e.g. satellite or mooring). Then, we also study the interaction of these different scales by for example trying to understand the energy cascade.

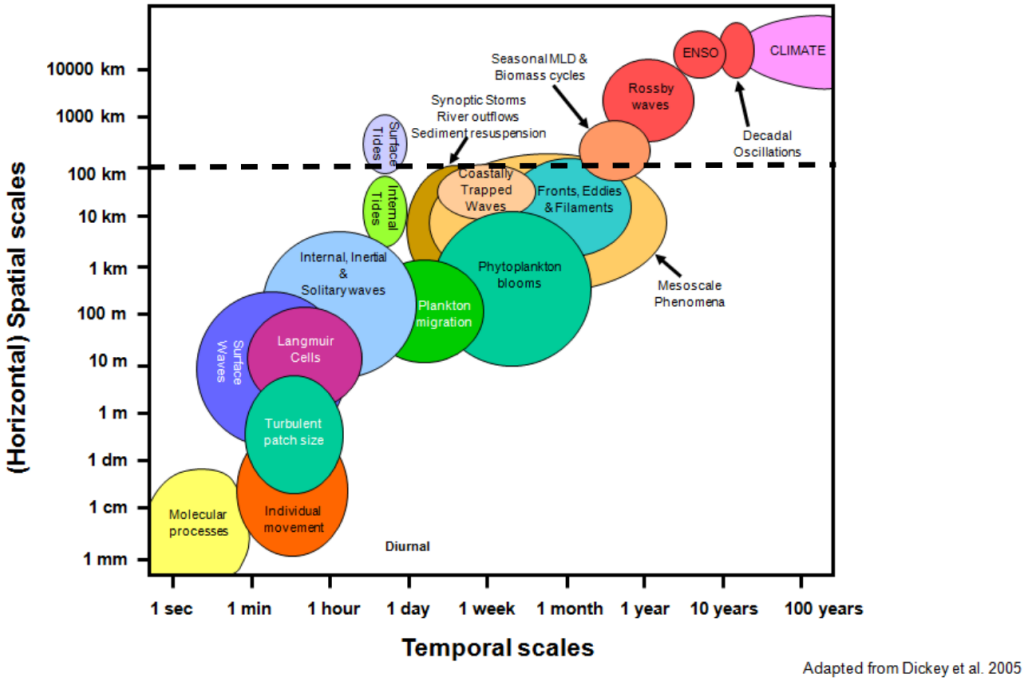

Figure 1.1: Schematic diagram with temporal and spatial scales of oceanic processes. (From M. Ramirez; 2017). Horizontal dashed black line represents the large / fine scales separation at 100 km.

All these different scales can be grouped into large and fine scales. These are defined in different ways. The fine scales are defined here following *d'Ovidio et al.* (2019) as oceanic features with a spatial scale between 1 and 100 km. The large-scales then describe the oceanic features with scales above 100 km. It is important to separate these oceanic phenomena in terms of scale because, as we will see below, the theories they follow and the instruments and tools necessary for their observation differ. For example, fig. 1.1 shows that the large-scales have different temporal scales associated than fine scales, and this can imply a different sampling strategy when taking measurements. The synopticity necessary to measure a large or fine-scale feature will not be the same. Also, important differences exist when modeling these features. For large-scales' modeling, like climate models, coarser horizontal resolutions are needed than fine-scale resolving models because the simulation runs need time spans from decades to centuries. (*Stewart et al.*, 2008)

The large-scale provides the broad picture of the ocean. This includes phenomena such as climate change, basin-scale variability, El Niño / La Niña Southern Oscillation, Rossby waves, seasonal cycles (such as that of the MLD), barotropic variability, surface tides, decadal oscillations and large-scale eddies and fronts. This is also sometimes referred to as planetary scales, which describe too the mean oceanic circulation (*McWilliams*, 2016; *Zhang and Qiu*, 2018). These large-scale features allow us to have knowledge on the heat transport in the ocean, like knowing the main locations of heat sources and sinks. The same happens with other variables such as carbon dioxide. This has a huge impact on the climate system.

An ocean dynamics description restricted to the large scales will have some limitations, like not accurately quantifying some processes with global impact such as air-sea energy fluxes or vertical exchanges of nutrients. The pathways described by the large scales are not enough to have a full 4D (x, y, z, t) description. In

particular, the description of vertical pathways remains quite limited. Their completion can be achieved by a better understanding of the fine scales, as some of these features have strong vertical velocities associated. Submesoscale features such as fronts, have been found to account for the vertical exchanges missing from just the eddy pumping fluxes, to complete the nutrient fluxes required in subtropical gyres' observed productivity (*Mahadevan and Tandon*, 2006). Moreover, *Ruiz et al.* (2019) found that to explain the observed vertical chlorophyll features with widths between 1 to 10 km, mesoscale ageostrophic vertical velocities were not enough without taking into account submesoscale features. A complete understanding of these vertical motions is important, specially in the surface ocean layers, where phytoplankton can greatly benefit from a nutrient supply from deeper layers. It is also important for the salt, heat, momentum and gas fluxes with the atmosphere and deeper layers. (*Mahadevan and Tandon*, 2006)

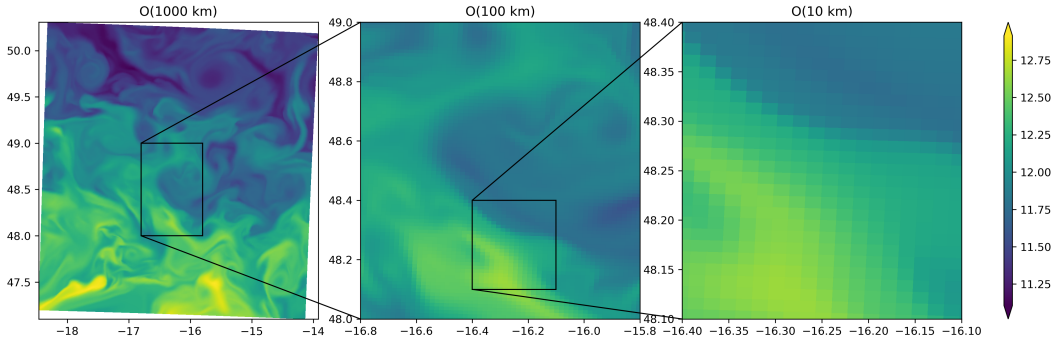

Figure 1.2: Spatial scales illustrated in NATL60 model SST ($°C$) snapshot.

The fine scales can provide us the missing details which makes our "broad picture" complete. As can be observed in fig. 1.1, these scales include fine-scale eddies and fronts, filaments, coastal upwellings, coastly trapped waves, synoptic storms, river outflows and sediment resuspension, internal tides, internal waves and motions, bio-physical interactions, phytoplankton blooms, plankton migration, surface gravity waves, vertical turbulent mixing, Langmuir cells and capillary waves. Of all of these features, we are mainly interested in those with a spatial scale above 1 km and we will pay special attention to features with a closer connection to the SWOT mission. These are eddies, fronts, filaments and internal tides and waves. These oceanographic features are also of great importance due to their impact on climate and biodiversity. In a lesser extent, I will also discuss the effect of surface gravity waves on SWOT, but will focus on the other features in what follows.

Here we englobe the fine scales as the meso- and submesoscale, as the spatial scales that define them slightly vary in the literature. For example *Thomas et al.* (2008) define the submesoscale as having horizontal spatial scales of order ∼1 km, and *Molemaker et al.* (2015) as ∼10 km. Another way to differentiate them is via a-dimensional numbers such as the Rossby (Ro) and Richardson (Ri) numbers. For mesoscale eddies Ro $<<$ 1 and Ri $>>$1, whilst for the submesoscale both are of order 1. (*Thomas et al.*, 2008) Specially when we approach the meso/submesoscale limit, seasonality can imply a change of size of some features like eddies and fronts that can make them be in the mesoscale instead of the submesoscale (Winter versus Summer) or vice-versa. The meso- and submesoscale have different aspect ratios and thus impacts on oceanic motions. The mesoscale has a greater aspect ratio than the submesoscale, i.e., the horizontal scale of the mesoscale is greater than its vertical, and so has a big impact on horizontal transports, such as stirring of tracers. The submesoscale in contrast, entrains important vertical motions. Another big difference between the two is the understanding of their generation. Mesoscale eddies have been much more widely observed than submesoscale, due to the observational limitations of the latter's small spatial and temporal scales. Consequently, the understanding of submesoscale eddies generation is not as understood. Several studies have been recently done to try and understand this better like *Gula et al.* (2016), and also their associated energy pathways (*Capó et al.*, 2019).

Eddies, perhaps one of the most important oceanic structures, can be defined as flows which are spinning or turbulent at scales from a few to hundred of kilometres. They have a temporal scale of weeks (*McWilliams*, 2016) and a relatively large range of spatial scales. Thus, both meso- and submesoscale eddies exist. Eddies can be either anticyclonic (AEs) or cyclonic (CEs). We can know their rotation direction by applying

Margules' method, which in the northern hemisphere would be: AEs spin clockwise and CEs anti-clockwise. In the southern hemisphere it is the opposite. (*Stewart et al.*, 2008) This implies that AEs (CEs) have a negative (positive) vorticity and an associated downward (upward) vertical velocity. As a consequence, AEs (CEs) are usually warm (cold)-cored due to the lowering (rise) of isopycnals.

They can also be defined regarding their formation process, as perturbations of the mean flow (*Colling and Oceanography Course Team Open University*, 2001). This happens for example in western boundary currents like the Gulf Stream, where when it becomes unstable, it sheds warm-cored eddies northward, and cold-cored southward. They can also be formed when the mean flow interacts with topography, either bottom topography or islands. Smaller scale eddies can be formed in the Winter season, when deep mixed layers generate and energetic instabilities occur (*Morrow et al.*, 2018). This formation dependence on dynamic phenomena with a high seasonality, makes the oceanic eddy field be very seasonal too.

An important role of eddies is their associated horizontal and vertical transport. Large-scale eddies are key for ocean stirring due to their lateral advection, whilst smaller scale eddies have a greater role in vertical motions. There are also vertical motions associated to the mesoscale eddies' border (*Capet et al.*, 2008b; *Beron-vera et al.*, 2019), where the eddy boundary presents wiggles and is not straight convex. The direction propagation tendency and warm (cold)-core characteristic of AEs (CEs) are of great importance for the ocean's heat distribution, helping to move the greater heat received at low-latitudes, towards high-latitudes (*Morrow et al.*, 2004). Consequently, they have a crucial role not only in the transfer of energy in the ocean (*Colling and Oceanography Course Team Open University*, 2001) through their impact on the global heat budget, but also on salt and tracer budgets (*Morrow et al.*, 2004). Lastly, energetic-wise, eddies (specifically mesoscale) have an in important role as the main oceanic Kinetic Energy (KE) reservoir (*McWilliams*, 2016).

Oceanic fronts can be defined as strong temperature and/or salinity variations at a particular location. Its location varies around a mean at temporal scales from weeks to months (seasonally or longer). They can also define the boundary of different water masses. When these variations occur, meandering can take place at the front, which can end up shedding eddies. (*Talley*, 2011) Fronts are often found too in upwelling regions. They have important implications for marine ecosystems. For example, they determine the spawning of certain species, like for example bluefin tuna in the western Mediterranean Sea or the albacore tuna distribution in their feeding migratory stages. (*Alvarez-Berastegui et al.*, 2014)

Filaments present strong horizontal gradients like fronts, but the latter have an uni-directional density gradient across their axis, whilst filaments have a central density extreme. (*McWilliams and Fox-Kemper*, 2013) Different kinds of filaments exist depending on their formation process. Vortex filaments can occur due to the interaction of eddies. These elongated filaments are considered submesoscale structures and a very common in between eddies. (*Lapeyre and Klein*, 2006) Upwelling filaments appear when the upwelled waters interact for example with the coastline or islands (*Batteen*, 1997; *Castelao et al.*, 2006). In addition to their biogeochemical impact, the study of these structures is of relevance as in areas where filaments and fronts are dominant, some theoretical hypotheses can longer be assumed, and alternatives to the commonly used geostrophic theory like surface quasi-geostrophy or frontogenesis theory should be implemented.

Submesoscale motions can be divided into balanced (BMs) and unbalanced motions (UMs). BMs are defined as such because their main balance is obtained through the Coriolis and pressure force balance, i.e., geostrophy. Consequently, they have frequencies smaller or equal to the Coriolis frequency. (*Torres et al.*, 2019) The scales of the submesoscale (balanced) overlap with that of IGWs (unbalanced), and following *McWilliams* (2016) they can be separated by their evolutionary behaviours, specially due to the oscillation and propagation of IGWs. It is important to distinguish them to better understand the KE budgets in the ocean, as for example illustrated in fig. 1.3, but also because BMs and UMs strongly interact and this has an impact on KE budgets (*Torres et al.*, 2019).

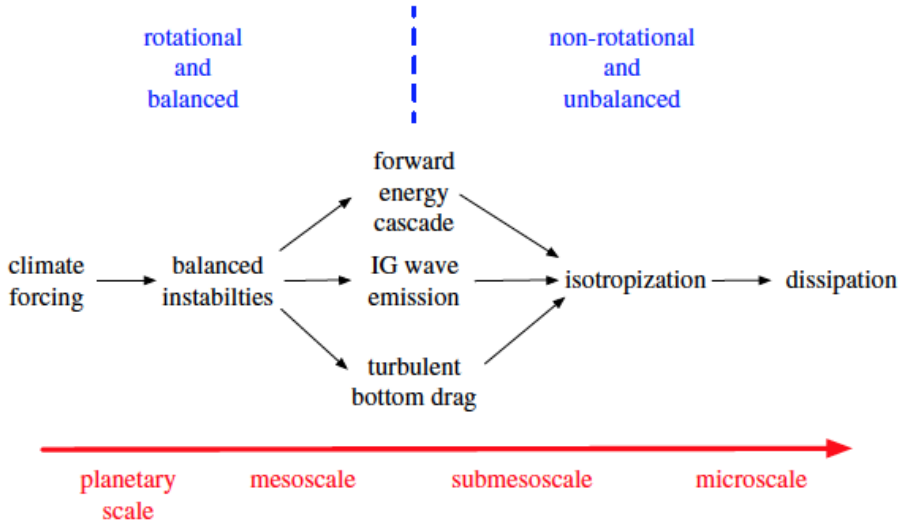

Figure 1.3: The flow of energy and information in the oceanic general circulation. Stages in the oceanic general circulation from planetary-scale forcing to micro-scale dissipation and mixing. The dynamical parameters Ro and Fr pass through order 1 values within the submesoscale regime. (*McWilliams*, 2016)

The transition scale (Lt) is defined as the spatial scale at which there is a change from a geostrophic BMs dominated regime to a wave UMs one (*Qiu et al.*, 2018). Lt can also be defined as the transition from "geostrophic motions to inertia-gravity waves" (*Qiu et al.*, 2017), or from rotational to divergent and unbalanced flows (see fig. 1.3 (*McWilliams*, 2016)). This again can help us know which theoretical framework we should follow. Lt can be estimated in several ways. One of these is by using spatial spectra, by looking at where there is a change of slope. As we move to large wavenumbers (small wavelengths), if IGWs (UMs) are present, they will flatten the spectral slope. Alternatively, we can separate our signal in low (BMs) and high (UMs) frequency motions, by for example applying a 3-day high/low-pass filter, and then estimate at which wavelength the low and high-pass filtered data's spatial spectra intersect. Other approaches are Helmholtz and wave-vortex decompositions (*Qiu et al.*, 2017). Lt varies strongly geographically ranging from values below 40 km (at the Antarctic Circumpolar Current and western boundary current regions) to 200 km (tropical oceans), and also seasonally (*Qiu et al.*, 2018).

Internal gravity waves are unbalanced motions as they do not follow the geostrophic balance.We can find them at the interphase between oceanic layers, and their restoring force is gravity. (*Arbic et al.*, 2018) From the depth at which their occur, their signal decreases towards the surface. Nevertheless, they can still be detected at the ocean surface, e.g. *Apel et al.* (1975); *Fu and Holt* (1984); *Da Silva et al.* (1998); *Ramos et al.* (2009). Another important characteristic of IGWs is that they are not geostrophic, but super-inertial. Their frequency is between the buoyancy and the inertial/Coriolis frequency (as can be seen in fig. 1.1, between O(1 min.) and O(1 day)). Within IGWs we find near-inertial waves and internal tides. They are "driven by rapidly changing winds" and with frequencies near f, and driven by barotropic tides flowing over topography and tidal frequencies, respectively. Other than from changes in sea level/pressure, these waves can be detected by changes in sea temperature (*Luecke et al.*, 2020). These waves are important because they drive the internal (below MLD) mixing of the ocean. They also have an impact on oceanic energy dissipation, specially from tidal waves over topography (*Egbert and Ray*, 2000).

The interaction of BMs and UMs, as well as their separation, is currently an important scientific discussion. The interaction of IGWs with mesoscale eddies is nowadays well understood, for example the interaction of the mesoscale with topography is one of the generation mechanisms of IGWs (*Nikurashin and Ferrari*, 2010). On the other hand the interaction with the submesoscale still remains quite unknown, probably due to their often hybrid BMs/UMs behaviour. (*McWilliams*, 2016)

1.2 Fine-scale modeling and observation

Fine-scale ocean observations and models resolving them are key to understanding the fine-scale dynamics and their interactions with the large scales. This has been limited by the high resolution required, but has improved during this last decade. High quality observations are also needed for operational oceanographic systems to be useful (*Davidson et al.*, 2019). This has lead to the development and use of new instruments (e.g. saildrones), more deployments of existing instruments (e.g. Argo array), launching of new satellite missions and the continuation of existing ones (e.g the Sentinel altimeters), and the development of new OGCM configurations.

Modeling and observational tools need each other. On the one hand, oceanic models need observations for validation and for data assimilation in forecasts and re-analysis. On the other, observations need oceanic models to for example fill their spatial and/or temporal gaps, and to help decide when and where it is best to deploy different instruments. Consequently, Observing System Simulation Experiments (OSSEs) have gained importance in recent years to plan different projects, for example *Wang et al.* (2018) in the context of the SWOT mission. Another concept that has therefore grown is that of a multi-platform approach. Not only between *in situ* instruments, but also with satellite and model data. For example, several multi-platform experiments have been carried in the western Mediterranean Sea, allowing to study fine-scale features (*Juza et al.*, 2016; *Pascual et al.*, 2017; *Ruiz et al.*, 2019; *Tintoré et al.*, 2019).

With recent technological advances, a large range of instruments exist nowadays measuring a wide range of ocean variables at different spatial and temporal resolution. Nevertheless, a lack of observations still exists to correctly monitor fine-scale features. Below some of the most relevant tools and observations for the present and future fine scales' observation are described.

1.2.1 OGCMs

The ocean is simulated using numerical models to reproduce its physical mechanisms defining its properties (such as temperature, salinity and, horizontal and vertical velocities) and their temporal and spatial evolution. To do this models solve an approximation of the Navier-Stokes equations. (*Le Sommer et al.*, 2018) More idealistic, theoretical ocean models exist that study specific processes like for example vortex merging (e.g. *Carton et al.*, 2017) or eddy life-cycles (e.g. *Morvan et al.*, 2019). Oceanic General Circulation Models (OGCMs) are more realistic in the sense that different configurations exist in which different approaches are used to try to replicate the ocean circulation. Within other, examples of these are: Nucleus for European Modeling of the Ocean (NEMO), HYbrid COordinate Model (HYCOM), Massachusetts Institute of Technology general circulation model (MITgcm). More details on these OGCMs will be given in the following Chapter. These are global or basin-scale ocean models, but there are regional oceanic models like for example Regional Oceanic Modeling System (ROMS). Regional configurations exist too from NEMO, HYCOM and MITgcm.

Recent OGCMs have better spatial resolutions, allowing to better understand the fine scales. This is of importance because depending on the region, different horizontal resolution are needed to resolve the first baroclinic deformation radius (*Hallberg*, 2013). This is shown in fig. 1.4. In general, the resolution required is constant at the same latitude, but variations exist of oceans versus seas, or in the presence of strong currents like the Gulf Stream or close to the Antarctic Circumpolar Current.

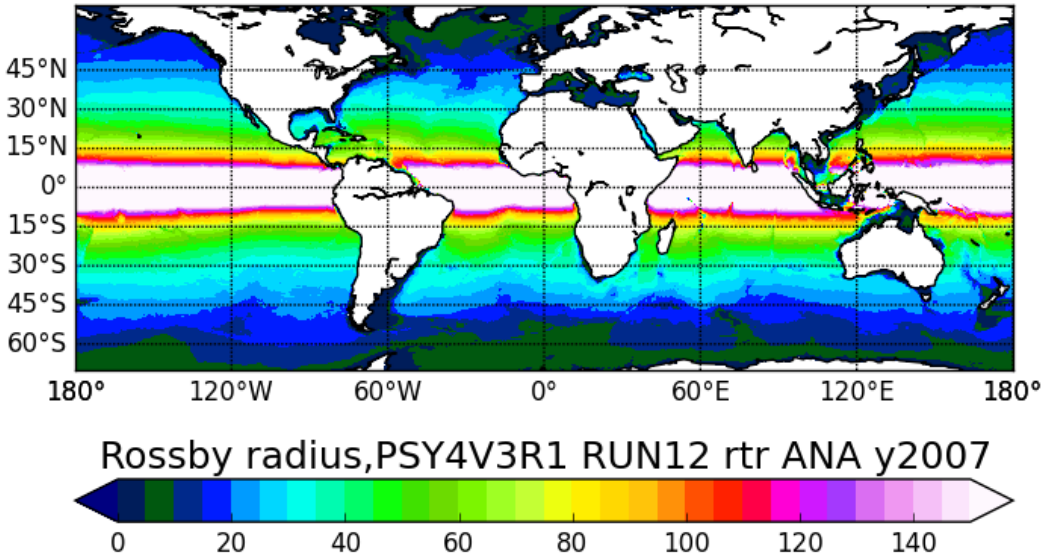

Figure 1.4: First baroclinic deformation radius (km) from a numerical simulation (Copernicus Marine Service). (Courtesy of Angélique Melet (Mercator-Ocean))

Another major improvement of recent OGCMs is the incorporation of tidal forcing. This allows not only for the representation of tidal currents, but also for example a higher and more realistic presence of IGWs. This is of importance because as said above, OGCMs have now higher spatial and temporal resolutions. Therefore, they reach scales at which in certain regions and periods of time, IGWs can be dominant at the fine scales. Nevertheless, the adequate representation of these features is strongly affected by the model's bathymetry and internal wave drag set.

OGCMs are of great importance specially when preparing for the future observation networks. For example, for the SWOT mission, as we do not have any other dataset (to day) similar to the future SWOT data. The advances in oceanic modeling described above, provide the temporal and spatial resolution necessary to be able to simulate pseudo-SWOT data. Moreover, they can help to know how new datasets will help improve present ocean forecasting and analyses products (*Bonaduce et al.*, 2018). This allows to better plan and prepare for new ocean observing systems.

The effective resolution of an OGCM, i.e. the length-scale of the structures the model actually resolves, differs from its spatial resolution. For example, *Soufflet et al.* (2016) defined effective resolution as approximately equal to 10 time the grid size. The shoaling of the spatial spectra of kinetic energy can help also estimate this scale (*Ajayi et al.*, 2020). The effective resolution of a model strongly depends on scale-selective dissipation, which at the submesoscale is numerically, not physically solved. For example, the way that vertical diffusion is parametrized in the model, can have big effects on the submesoscale representation. (*Soufflet et al.*, 2016) This is thus, an important characteristic of OGCMs modeling the fine-scales.

1.2.2 *In situ*

The technology regarding *in situ* measurements has also greatly improved over these last decades. A great range of instruments exist, Eulerian and Lagrangian, autonomous and steered. This allows to obtain data series of different natures, with high resolution in space and/or time, making possible the observation of the different oceanic structures and phenomena. Ship-based measurements have been present since the first oceanographic expeditions that were aimed to study large scale ocean variability. More recently, dedicated field experiments have been carried out to sample fine-scale structures and improve our understanding of the underlying processes (e.g. *Pascual et al.* (2017); *Barceló-Llull et al.* (2018)). Their drawback is that the spatial and temporal coverage is low. Oceanographic cruises also serve as a platform to deploy, calibrate and maintain instruments like Argo floats, drifters, gliders and moorings.

Argo floats are profiling floats which typically measure pressure, temperature and salinity from a certain depth (usually 2000 m) to the surface. They provide high spatial resolution vertically, but not in the horizontal (given they provide vertical profiles every 10 days approximately). Their spatial coverage is global (relatively, as some limitations exist), and random, as they are left to drift with the currents. (*Testor et al.*, 2010) This is a big limitation for the study of the fine-scales as the global spatial resolution of the Argo array is aimed at 300 km on average at ice-free oceans deeper than 2000 m (*Gould et al.*, 2013; *Thomson and Emery*, 2014). This spatial resolution is not even mesoscale resolving. Drifters are freely drifting, Lagrangian buoys which are remotely tracked by satellite (*Richardson*, 1983). They provide information on surface currents without wind-drift effects (drogued) or on the total surface current (undrogued), with a high temporal resolution. Like Argo floats, their main limitation for observation of the fine-scale is their spatial coverage (not many scientific campaigns allow for a large number of drifters). Moorings consist of a support cable where different sensors are attached, for example CTDs (Conductivity-Temperature-Depth) and current-meters, providing Eulerian measurements at different depths. They provide high temporal resolution and coverage data, rendering long time series of data to study the fine-scales at certain locations. Mooring arrays can sample a small region at a high frequency, for example the OSMOSIS (Ocean Surface Mixing, Ocean Submesoscale Interaction Study) array which allowed to sample submesoscale structures (*Buckingham et al.*, 2016; *Thompson et al.*, 2016; *Yu et al.*, 2019). This dataset's main drawback for fine-scale measurements is that it is very localized in space. Gliders are underwater remotely steered instruments. They measure different ocean variables continuously at high temporal and spatial resolutions by performing a transect by making a "saw-tooth" movement from the surface to a certain depth. (*Testor et al.*, 2010) The disadvantage of gliders is that they provide 1D information in the horizontal, and several gliders are needed at the same time to correctly sample the fine-scales.

In addition to technological improvements to the above-mentioned in situ instruments, other technologies are being now applied to oceanographic measurements and new ones developed. High-frequency (HF) radar network is growing worldwide (*Rubio et al.*, 2017), and this dataset is important for the study of the fine scales (e.g. bio-physical interactions (*Hernández-Carrasco et al.*, 2018)) as it provides valuable information on the total surface currents at high temporal and spatial resolution. Its observations of the fine-scales are quite limited to coastal waters, but they can still be very useful in improving their representation when assimilated into other datasets like oceanic models (for e.g. *Paduan and Shulman* (2004)). Animal bourne telemetry data is now more and more exploited in physical oceanography (*Harcourt et al.*, 2019) and observes valuable information on the fine-scales too. It provides high-resolution data profiles in space and time, and in some regions, can fill the data gaps that for example Argo floats do not provide (*March et al.*, 2019). Depending on the animal species, just with the individual's position information, one can obtain interesting information on the small-scale ocean surface dynamics like for example shown by *Miyazawa et al.* (2015); *Sánchez-Román et al.* (2019). The main limit of this dataset is that it is very localized (very low spatial and temporal coverage). Lastly, saildrones is an emerging observation platform, that from the upper-ocean and surface fluxes data it provides (*Todd et al.*, 2019), can sample fine-scale structures, like sharp fronts (*Voosen*, 2018). This is thanks to its high resolution data both in space ($<$ 1 km) and time (1 min.) (*Vazquez-Cuervo et al.*, 2019). They can be at sea for long periods (up to 12 months) and travel long distances (*Mordy et al.*, 2017; *Vazquez-Cuervo et al.*, 2019), but in general they have a low temporal and spatial coverage (specially in comparison to satellite data).

Although great advances have been made with *in situ* instruments, and their observational array is growing (e.g. Argo), they remain quite local observations. Their cost and environmental impact (specially in the case of non-recoverable instruments) are still some of the main issues preventing them from becoming more global arrays. Nevertheless, Ocean Observing Systems (OOS) are joining different instrument types and country efforts. Future observing systems will manage to have better and more complete data of the upper ocean by combining observations from different platforms (*Foltz et al.*, 2019). This is also described as a multi-platform approach, put in practice in several experiments like *Brannigan et al.* (2017); *Pascual et al.* (2017); *Pietri and Karstensen* (2018); *Aguiar et al.* (2019); *Ruiz et al.* (2019); *Mahadevan et al.* (2020). Consequently, for now, *in situ* alone are not enough to study the fine-scales completely in space and time. Satellite observations are therefore key to have complete observations of the fine-scales. Moreover, it is important to combine them both, as *in situ* data are important too for satellite data as they provide complementary information like on stratification and ageostrophic velocities. For example, the T/S profiles provided by *in situ* observations, like Argo, are necessary to estimate the steric SSH (e.g. *Roemmich and Owens* (2000)) and the 3D ocean circulation (e.g. *Ponte and Klein* (2013); *Qiu et al.* (2016)).

1.2.3 Satellite images

In comparison to the above *in situ* measurements, satellite images provide a higher spatial coverage horizontally at the surface, (and sometimes temporal) but not in the vertical. Their resolution has been increasing for the last years, thanks to technological advances both in the satellite instruments used and in the image processing methods. To obtain them, different technologies are being used, and some of the most relevant allowing the observation of fine-scale features are described below:

- Sea Surface Temperature (SST): These are infrared images which provide high-spatial resolution fields. These products can even reach a 1 km resolution, allowing for the observation of the submesoscale. Unfortunately, this data is limited by the presence of clouds which masks the signal. (*Drushka et al.*, 2019) Imaging microwave radiometers can also provide SST fields, and are limited to by geophysical phenomena such as precipitation, wind speed, and sea ice (*Minnett et al.*, 2019).

- Sea Surface Salinity (SSS): Salinity measurements can be obtained from satellite-based microwave radiometers. This data is much more recent than for example SST images. Although these measurements have been very relevant for the oceanographic community (*Font et al.*, 2009; *Reul et al.*, 2014), their present spatial resolution is not high enough for submesoscale observation. Spatial resolution varies from satellite to satellite, being for example 80 - 100 km for Aquarius and $\sim$45 km for SMOS (Soil Moisture and Ocean Salinity). (*Drushka et al.*, 2019)

- Ocean colour: It monitors chlorophyll globally, via measurements in the visible frequency. (*Le Traon*, 2018) It is not measured directly, but estimated via the Remote Sensing Reflectance ratio (Dutkiewicz et al, 2019). Like SST, high resolution spatial products exist, down to 1 km. These images provide useful information on open ocean mesoscale processes such as Rossby waves and eddies (*McClain, Charles R*, 2009), and also on the submesoscale (e.g. *Lévy et al.* (2012a); *Delandmeter et al.* (2017)).

Satellite images render complementary information on surface currents, and also on surface buoyancy. The latter is an important parameter when wanting to process SSH data to, for example, apply the surface quasigeostrophic theory to estimate a part of the deep circulation. Combining this data with altimetry helps to obtain better observations at the fine-scales, and this will be further explained in the following section.

These satellite images need to be processed (with for example advanced de-noising techniques) to be able to exploit the information they render on the surface ocean. Each satellite image requires specific processing algorithms. For example, in the case of SMOS, de-noising the salinity data was important not only to reduce the spectral noise floor, but to retrieve an improved spectral slope. Correctly, de-noising allows to better retrieve the image's gradients, in this case the SSS gradients. Moreover, one of the processing steps to reduce the noise used for the SMOS salinity products exploits the information within another type of satellite image (SST) (*Olmedo et al.*, 2016).

1.2.4 Altimetry

1.2.4.1 Concepts

Altimetry is the measurement of sea surface height variability via satellite (*Talley*, 2011). This surface height variability is sometimes referred to as ocean topography. The observed ocean topography measured by a radar altimeter is a combination of (i) the geoid and (ii) ocean dynamics. The geoid is related to the internal mass of the Earth and is the height the ocean would have if at rest, and so it is a constant geopotential surface (i.e., varies due to differences of gravity). The geoid has been estimated thanks to the GRACE (Gravity Recovery and Climate Experiment) satellite mission launched in 2002 providing data with a horizontal resolution of approximately 500 km, and the GOCE (Gravity Field and steady-state Ocean Circulation Explorer) mission launched in 2009 providing data with a horizontal resolution of approximately 100 km (*Escudier*, 2014). Then, due to dynamical processes such as currents, tides and atmospheric pressure effects, a topography generates. Its typical amplitude at the sea surface is of +/- 1 m (*Stewart et al.*, 2008).

Several steps are necessary to retrieve the information on the ocean dynamics from the SSH measurement. Firstly, the satellite position (and hence the SSH measurement) can be obtained with respect to a theoretical ellipsoid of reference (see fig. 1.5) given that the satellite altimeter flies at a constant orbit, repeating the same ground tracks every several days (depends on each satellite). The distance between the satellite and the ocean surface, known as the range, can be calculated thanks to the radar impulses sent by the altimeter onboard the satellite straight down to the surface (*Benveniste*, 2011). From the time it takes the impulses to echoe back to the satellite, and the known speed of the electromagnetic wave sent, the distance (range) can be calculated. Then, SSH is measured as the difference between the altitude and the range.

Secondly, to be able to retrieve information on the ocean dynamics, the mean of previous sea surface measurements (MSSH) is subtracted from the SSH, obtaining the Sea Level Anomaly (SLA). This is necessary due to that the geoid is still not known with high precision, and it does not resolve well scales below 100 km (fine-scales). The geoid needs to be very precisely estimated as its order magnitude is greater than that of the ADT (*Carret*, 2019), and so its errors can have a large effect on the ocean dynamics inferred. By subtracting the MSSH from the SSH, the geoid and its errors are removed (as well as the average errors of the SSH measurement and of its corrections e.g. sea state bias). This is done given that the same ground tracks are repeated and that the temporal variations of the geoid are slow compared to the relatively fast oceanic variations. (*Tchilibou*, 2018). Before, a 10-year MSSH was removed (*Marshall and Plumb*, 2008; *Stewart et al.*, 2008), and now a 20-year mean reference period is used (*Pujol et al.*, 2016). MSS gridded products exist, which resolve spatial scales reaching 100 km, and even lower with the improvements obtained with altimetric data (*Schaeffer et al.*, 2012). At these smaller spatial scales, for example one of the products, MSS CNES-CLS15, has a mean estimated global MSS error of 0.35 cm along SARAL/AltiKa tracks for wavelengths ranging from 30 to 100 km (*Pujol et al.*, 2018).

Lastly, once the SLA is known, to have information on the currents, and thus the ocean circulation, the Absolute Dynamic Topography is calculated (ADT) by adding the Mean Dynamic Topography (MDT) to the SLA. This step is necessary as in removing the MSSH to reduce the errors, the average oceanic circulation is also removed. This process is illustrated in fig. 1.5, where it shows that SLA can be defined as shown in eq. 1.1. The MDT represents the permanent circulation (e.g. major currents like the Algerian current in the Mediterranean Sea). The MDT products are obtained as the difference between the MSSH and a geoid model at the spatial scales where the geoid is accurately known (100 - 150 km). At these scales the ocean MDT is at present resolved with centimetre accuracy (*Le Traon*, 2018). So that the ocean MDT resolves scales below 100 - 150 km, this gravimetry data is combined with altimetry and *in situ* data (e.g. from Argo floats). A final MDT product is then obtained, like for example the CNES-CLS13 MDT by *Rio et al.* (2014a), with a 1/4° global resolution. Other regional MDT products exist, like the SMDT-MED-2014 (Synthetic Mean Dynamic Topography of the MEDiterranean sea) (*Rio et al.*, 2014b). These regional products are necessary as enclosed or semi-enclosed seas are usually characterized by basins with complex geometries (e.g. many islands and narrow straits), and the Mediterranean has a relatively low Rossby radius of deformation of the order of 10 km. Consequently, a higher geoid resolution is needed here and so its improvement below scales of 100 - 150 km is even more crucial than for the global ocean MDT products. It is important to note that

ADT is sometimes referred to as SSH (for example in ocean modeling), but with respect to the geoid instead of the reference ellipsoid as shown in fig. 1.5.

$$SLA = SSH - MSSH = SSH - geoid - MDT = ADT - MDT \tag{1.1}$$

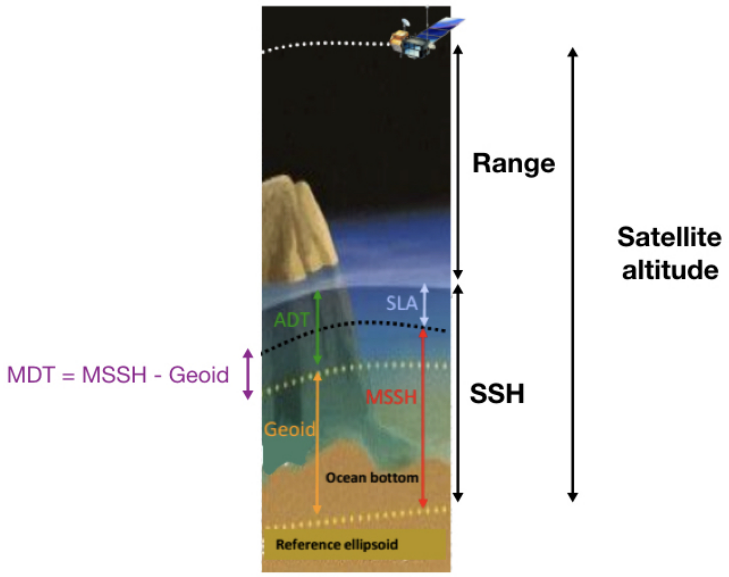

Figure 1.5: Altimetry principle (adapted from *Rio and the CLS altimetry team.* (2013)).

SSH can be separated into steric and non-steric, dominated by low-frequency mesoscale eddies and high-frequency internal tides, and barotropic tides, respectively (*Arbic et al.*, 2010). The steric effect describes the changes in sea level due to the volumetric expansion or contraction induced by variations in temperature and salinity in seawater (*Criado-Aldeanueva et al.*, 2008). An approach to remove this steric effect is by subtracting the spatial mean to a SSH snapshot. Note however that this also removes non-steric signals larger than the snapshot distance. More complex methods involve using information on the water column's sea temperature and salinity to calculate the steric SSH, e.g. *Savage et al.* (2017b).

In a further technical sense, different altimetric technologies can be used to measure SSH (*Morrow et al.*, 2018; *Rogé*, 2018):

- Nadir: This one is the most commonly used until now. Nadir refers to the local vertical direction pointing in the direction of the force of gravity at that location. For an orbiting satellite it is simply the downward view. The conventional nadir altimetry is referred to as Low Resolution Mode (LRM). The radar pulses are continuously sent at intervals long enough to avoid the correlation with return echoes .
- SAR nadir: Synthetic Aperture Radar (SAR) nadir differentiates from the above in that its footprint is reduced. This is thanks to that the emission of pulses is done in successive wave packets by Doppler effect, and this allows to have more observations at each point. It implies a gain in the along-track spatial resolution compared to LRM.
- SAR Interferometry (SARIn): This one instead of using only one radar signal combines the signal of two. The combination of two SAR images of the same place (taken at two successive overflights by the same radar or at the same time by the same satellite with two antennae) allows fine-resolution mapping.

The data measured from altimeters is presented in different formats/levels, thus rendering different products.[1]

- L0 is the raw radar data.
- L1 has some instrumental errors corrected, but mainly has the radar waveform parameters.
- L2 has the geophysical quantities calculated (SSH, SWH, sigma-0) and the full list of geophysical corrections to be applied, and the data is posted at their original position.
- L3 has the corrected SSH values, interpolated onto a nominal fixed along-track grid.
- L4 is interpolated onto a regular 2D grid.

The most common L4 altimetric products are generated via Optimal Interpolation (OI). OI (also referred to as objective analysis) combines different altimeter 1D SSH data producing daily, regular gridded maps by parameterizing the spatial and temporal oceanic correlation length scales. The spatial resolution of the products varies depending on the product, for example the global one has a resolution of $1/4°$ and the mediterranean one $1/8°$ (*Amores et al.*, 2019). DUACS (Data Unification and Altimeter Combination System) produces L4 altimetric products (as well as L3) since 1997, by using the altimetric data from the available satellites. It mainly focuses on the reconstruction of the mesoscale. The parameterization of OI used for the mapping of this L4 product depends both on the physical field's properties and the available altimeter constellation data's sampling capability. (*Pujol et al.*, 2016) These products have greatly advanced our understanding of the mesoscale, but some limitations exist due to the dependence of the method on the altimeters' sampling. *Amores et al.* (2019) find that the OI parameterization can affect the eddy properties in the generated L4 product, specially in regions with a small Rossby deformation radius. This implies a misrepresentation of the mesoscale and below in these regions (e.g. the Mediterranean Sea) (*Fablet et al.*, 2018). The location of oceanic currents is also affected by the number of altimeters present in the constellation used to derive the L4 maps, and the distance between these altimeter tracks (*González-Haro and Isern-Fontanet*, 2014). Nevertheless, the DUACS products are being constantly improved. The most recent product, DUACS DT2018, uses 25 years of altimetric data, and within other, improved the geophysical corrections and the OI parameterization. It specially managed to reduce the error in coastal regions, which are quite problematic with the present altimeters. (*Pujol and Larnicol*, 2005; *Pascual et al.*, 2007; *Ballarotta et al.*, 2019; *Taburet et al.*, 2019)

Gridded maps can also be obtained by combining the L3 products with other data sources i.e., oceanic tracers. *Fablet et al.* (2018) use multi-tracer convolutional processing by using high-resolution SST data to obtain L4 altimetric products. Other tracers can be Finite Size Lyapunov Exponents (FSLEs) (*Gaultier et al.*, 2013) or singularity exponents (*Sudre et al.*, 2015). New studies like *Ciani et al.* (2019) also use tracers (high-resolution SST in this case too) with altimetric data to obtain daily gridded maps. In this study they actually obtain gridded maps of sea surface currents by using altimetry-derived geostrophic velocities.

To obtain altimetric L4 products, data assimilation techniques are also used. These may take advantage of other datasets like SST and hydrographic profiles. For example, the Global Ocean ReanalYsis and Simulation (GLORYS) assimilates SST, temperature and salinity profiles, and altimetric data via a Kalman filter (*Ferry et al.*, 2012). To take advantage of future wide-swath satellite data, data assimilation techniques will be even more necessary to deal with the even bigger temporal gaps compared to nowadays altimetric constellation. This will be further discussed in Section 2.2. Data assimilation techniques are also important in order to assimilate altimetric data in models for operational oceanography (*Ubelmann et al.*, 2009; *Verron et al.*, 2018). No matter the technique used, whether OI or data assimilation, in regions where the gap between altimeter tracks is bigger than the Rossby radius of deformation, the eddy field representation will be compromised (*Amores et al.*, 2019).

[1] https://sentinel.esa.int/web/sentinel/user-guides/sentinel-3-altimetry/processing-levels; https://sentinel.esa.int/web/sentinel/technical-guides/sentinel-3-altimetry/products-algorithms

1.2.4.2 History

The first altimetric satellite missions started in the 1980s with GEOS-3, followed by Geosat in 1985 which had very good mesoscale resolving capabilities. Geosat and the ERS satellites aimed to observe the currents' weekly variability (*Stewart et al.*, 2008). Later, the Topex-Poseidon mission meant a major altimetric breakthrough in precision (and a high altitude orbit), which allowed an accurate measure of the large-scale signals that evolved over scales greater than 20 days. Mesoscale sampling capabilities were improved by careful calibration of a minimum of 2 satellite missions flying together, starting from the early 1990s (e.g. Topex-Poseidon and ERS, Jason and Envisat, and others). The latter satellite of this past missions' group, Jason-1, managed to resolve wavelengths down to 100 km as shown in fig. 1.7. Below the list of all past altimetric missions and their main characteristics summarized in table 1.1 (*Durán-Moro*, 2017):

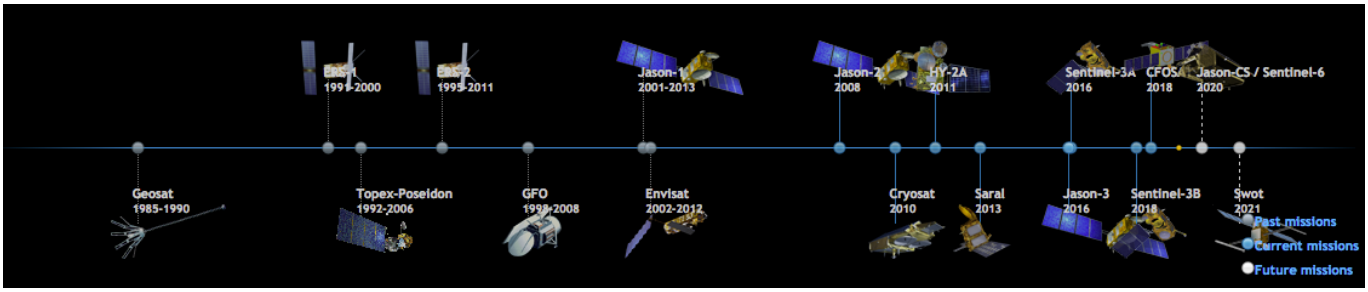

Figure 1.6: Past, current and future altimetry-related satellite missions. (`https://www.aviso.altimetry.fr/en/missions.html`)

- GEOS-3
- Geosat
- ERS-1
- Topex-Poseidon
- GFO
- ERS-2
- Envisat
- Jason-1

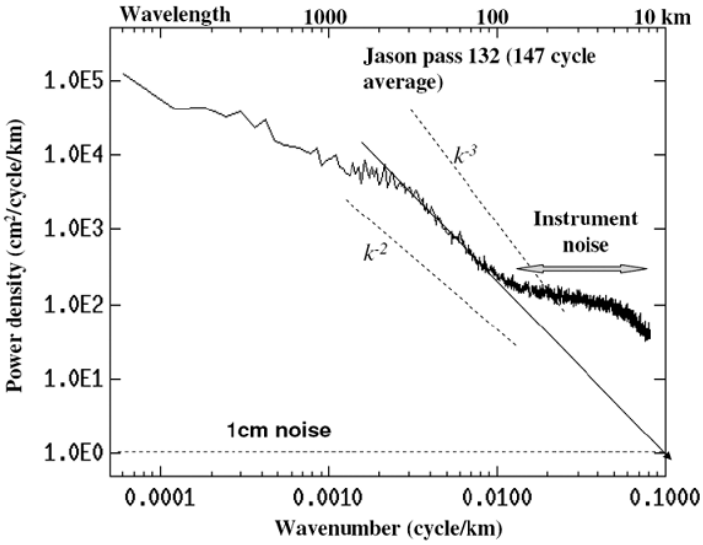

Figure 1.7: Spectrum of sea surface height anomaly from Jason altimeter data (curve). The two slanted dashed lines represent two spectral power laws with k as wavenumber. The horizontal dashed line represents the threshold of measurement noise at a 1-kilometer sampling rate. The slanted solid straight line represents a linear fit of the spectrum between 0.002 and 0.01 cycles per kilometer. (*Fu and Ferrari*, 2008)

The present altimetric satellite missions (i.e., still ongoing) are the following, and their main characteristics summarized in table 1.1 (*Durán-Moro*, 2017):

- Jason-2, -3
- SARAL/Altika
- Cryosat-2
- HY-2A
- Sentinel-3A, 3B

Satellite mission	Period	Radar mode	Band	Repeat cycle (days)	Accuracy (cm)
Seasat	1978	LRM	Ku	17	10
Geosat	1985-1990	LRM	Ku	17	5
ERS-1	1991-2000	LRM	Ku	35	3
Topex/Poseidon	1992-2006	LRM	Ku and C	10	2
ERS-2	1995-2011	LRM	Ku	35	3
GFO	1998-2008	LRM	Ku	17	5
Jason-1	2001-2013	LRM	Ku and C	10	2
ENVISAT	2002-2012	LRM	Ku and S	35	2-3
Jason-2	2008-2016	LRM	Ku and C	10	2
Cryosat-2	2010-	SARIn	Ku	369	1
HY-2A	2011-	LRM	Ku and C	14 and 168*	2-3
SARAL/Altika	2013-	LRM	Ka	35	2
Jason-3	2016-	LRM	Ku and C	10	2
Sentinel-3A	2016-	LRM and SAR	Ku and C	27	2-3

Table 1.1: Summary of the main characteristics of past and present oceanographic altimetry missions. From left to right the columns show the altimetric satellite mission name, mission period, radar altimeter mode (see section 1.2.4.1 for details), its frequency band, the orbit's repeat cycle (in days) and the accuracy of the SSH measurement (in cm). Table is adapted from *Durán-Moro* (2017). * has two phases.

These altimetric observations have been found to very useful in the observation of mesoscale eddies (*Fu and Zlotnicki*, 1989; *Morrow and Le Traon*, 2012; *d'Addezio et al.*, 2019). On the other hand, in regions where there is a high mesoscale eddy signal, there is aliasing in the along track altimetric data. (*Shriver et al.*, 2012) A major improvement of altimetric observations was made partly due to that since the launch of Jason-2, there has always been at least two orbiting altimeters at the same time with their merged observations, rendering 2D gridded maps of SSH that can resolve wavelengths down to 150 km (*d'Addezio et al.*, 2019). *Pascual et al.* (2006) found a 25% improvement when estimating sea level with four altimeters, compared to the results obtained with only two. This contributed to the improvement of the mesoscale observation, but it is important to note that in the gridding process of nowadays altimetric products, part of the mesoscale signal is lost (*Wang et al.*, 2019b).The recent altimeters Sentinel-3 and SARAL/Altika provide data with a better precision, better performance at the coast and less noise. The latter allows to resolve smaller scales. (*Heslop et al.*, 2017; *Verron et al.*, 2020)

Unfortunately, the submesoscale cannot be observed by current altimeters (*d'Addezio et al.*, 2019). The along-track altimeters, resolve wavelengths of 70 -100 km (in the case of Jason-2), and for SAR mode altimeters (like Saral and Sentinel-3), it can go down to 30 - 50 km (*Morrow et al.*, 2018). One could argue whether the latter falls within the submesoscale or not, but the resolved wavelength becomes greater for the SSH gridded products, which resolve wavelengths of approximately 150 km (*Ducet et al.*, 2000). Another limitation of nowadays altimetric data is that the radar echoe is polluted by ice and land surfaces, thus reducing the accuracy of the data in coastal and polar areas. (*Rio and the CLS altimetry team.*, 2013)

Future altimetric satellite missions aim to improve these current altimetric limitations. The upcoming missions, confirmed or not (specified with (?)) are:

- Jason-CS
- SWOT
- SKIM (?)
- SEASTAR (?)
- WaCM (?)

It is important to note, that with these new missions, new challenges will arise, specially as we move to smaller spatial scales. On of these is the presence of IGWs, and thus separating balanced and unbalanced motions (including IGWs, but also maybe unbalanced submesoscale motions). Moreover, better data assimilation techniques for gridded products of SSH will be necessary as OI will probably not be enough anymore. The presence of non-stationary semi-diurnal tides will be difficult to remove, for example from the future SWOT observations. The removal of coherent/stationary internal tides will be a new challenge too, but simpler. (*Arbic et al.*, 2018)

1.3 The SWOT mission

The Surface Water and Ocean Topography (SWOT) satellite mission is a joint mission of the National Aeronautics and Space Administration (NASA) and the *Centre National d'Études Spatiales* (CNES) with contributions of the UK and Canadian Space Agencies (*Wang et al.*, 2019a). Presently, the satellite's launch is planned for 2022. The life time of the mission is of at least 3 years (*Morrow et al.*, 2019), and it is expected to provide water elevation maps for oceanographic and hydrological purposes (*Fu and Ubelmann*, 2014). The novelty of this satellite is that it will provide 2D SSH fields on a wide-swath, 120 km wide in total. The horizontal resolution and the global coverage that SWOT will provide, will help to open the way for new studies (*Fu and Ferrari*, 2008; *Morrow et al.*, 2018).

The SWOT satellite will provide information of the Sea Surface Height (SSH) (*Ubelmann et al.*, 2015), with measurements reaching wavelengths of 15 km in most of the ocean (which implies the observation of structures with a diameter of 7.5 km). This will be thanks to that it is a wide-swath altimeter, in particular a Ka-band Radar Interferometer (KaRIn), which measures at a frequency of 200 MHz. In addition to 2 interferometer antennae at each side, it has a nadir altimeter at the center (fig. 1.8).

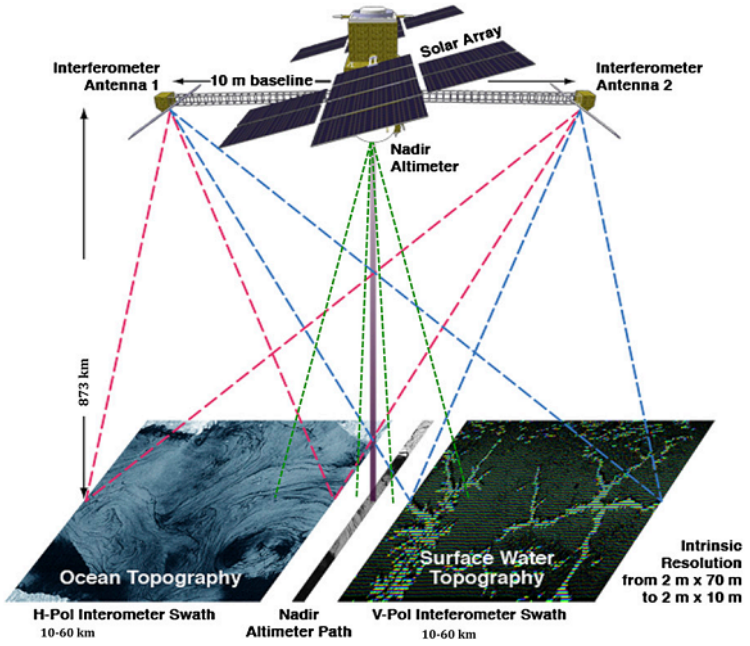

Figure 1.8: SWOT satellite configuration. The pink (blue) dashed lines show the main interferometer left (right) swath. The green dashed lines show the nadir interferometer channel (*Fu and Ubelmann*, 2014).

The satellite will have 2 orbits. Firstly, after the instrument's check out phase during approximately the first 3 months after the satellite's launch, there will be a fast-sampling orbit, lasting $\sim$ 3 months too. It is also called the Calibration/Validation (Cal/Val) phase, as it will allow to assess the instruments' performance and to validate the SWOT observations with other oceanic data (*Morrow et al.*, 2019). This will be done thanks to frequent revisits (given its 1-day repeat cycle) at the calibration sites (see *d'Ovidio et al.* (2019)). This will also allow, within other, to investigate high-frequency geophysical processes during this phase (*d'Ovidio et al.*, 2019). Then it will be the nominal orbit or Science phase, with a high spatial coverage of about 90% between 78^{o}S and 78^{o}N (*Morrow et al.*, 2019). On the other hand, its temporal resolution will not be very good. The temporal resolution of satellite data is the time between satellite revisits, which in the case of the nominal phase, will be approximately 10 days, given its 21-day repeat cycle . The 10-day revisit time is actually a good approximation for higher latitudes whilst for lower latitudes it is about 2 days (*Mouffe et al.*, 2011). Therefore, its overall capability will be limited by its low temporal resolution. This difference in time resolution with latitude can be seen in fig. 1.9 (right). This figure shows the maximum gap (in days) with latitude, between two observations. Near the Equator there is a maximum gap between 16 and 20 days which implies one or two observations in one repeat cycle as observed in the left panel. This gap reduces as latitude increases, implying a greater number of observations per repeat cycle. This also implies a spatial coverage variation with latitude.

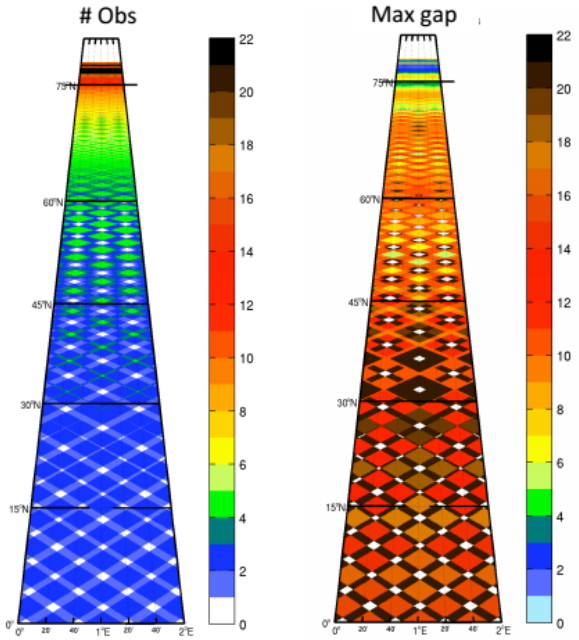

Figure 1.9: Sampling pattern of the 21-day orbit for the Science Phase (*Fu and Morrow*, 2016).

As described in Section 1.2.4.2, conventional altimetry measures Sea Surface Height (SSH) along-track in 1D, and SWOT will be the first wide-swath altimeter to measure the ocean SSH field in 2D over two 50 km wide swaths. The same SSH signal calculation of equation 1.1 and the atmospheric, geophysical and instrument corrections that are applied to along-track altimetry, will also be applied to SWOT, but extra corrections and errors associated with the interferometric calculation will be necessary. Moreover, as SWOT will provide a higher spatial resolution, it is expected that not only will it be possible to follow mesoscale eddies (about 100 km in diameter) like currently (e.g. *Escudier et al.* (2016b)), but also submesoscale eddies (about 10 km in diameter). Nevertheless, this spatial and temporal resolution mismatch (fig. 1.9), might complicate the creation of SSH maps, specially if the intention is to use them to observe submesoscale structures. This is because of their short timescales and consequently, it might actually not be possible to follow very easily the evolution of submesoscale eddies. Some data treatment techniques like for example, dynamic interpolation, have been started to be investigated to help solve this problem as discussed by *Ubelmann et al.* (2015).

The measurement noise will vary in each oceanic region. Globally, SWOT is required to have a noise level at 2.74 cm RMS on a 1x1 km grid, and 1.37 cm RMS for the 2x2 km standard products. (*Esteban-Fernandez*, 2017; *Chelton*, 2019) This varies regionally as it changes with sea-state conditions (surface waves), and it has been estimated by *Wang et al.* (2019a). The main issues are random errors and geophysical phenomena, for example internal waves. Internal gravity waves and internal tides are a SSH dynamical signal, not measurement error. However, depending on the use of the SWOT data within the ocean community, it could be necessary to separate the balanced motions from the unbalanced internal waves, to for example calculate geostrophic velocities. This separation may be particularly difficult in regions like the Gulf Stream where, at wavelengths shorter than 50 km (what SWOT intends to reach), internal tides and wave energy levels are comparable to that of low-frequency motions (*Callies et al.*, 2015). Therefore, the resolution of the balanced motions resolved by SWOT data, will also vary from region to region depending on the internal waves signal. Even if this is the case, it is important to remember that internal waves are not measurement noise.

Moreover, the effect of the noise may differ depending on the region. Not only will the presence of internal waves vary geographically, but also the size of the structures present (like eddies). For example if we look at fig. 1.4, structures with smaller spatial scales are present in the Mediterranean Sea than in other parts of the ocean at the same latitude. The first baroclinic Rossby radius of deformation values are lower in the western Mediterranean Sea, approximately between 2 and 16 km (*Escudier et al.*, 2016b; *Barceló-Llull et al.*, 2019), in comparison to the 20 - 30 km values found at mid-latitudes of the Atlantic Ocean (*Chelton et al.*, 1998). The values found by *Escudier et al.* (2016b); *Barceló-Llull et al.* (2019) are actually closer to the values found in the Arctic Ocean (*Nurser and Bacon*, 2013). Therefore, even the regions are at the same latitude, the

noise will have a different effect, given different structure sizes and energetics. The processing of the SWOT data has to been done accordingly, with respect to the latitudinal ocean dynamics variation, but also regional variation.

Several studies have been carried out to deal with SWOT noise and errors and the creation of gridded maps. One of these studies that tackles these two challenges at a time is *Qiu et al.* (2016). They use objective interpolation to combine the passes and reduce the SWOT noise and errors. The resulting gridded maps represent the structures present in the field, but their amplitude is reduced; and fine-scale structures over-smoothed. *Gaultier et al.* (2016) use optimal interpolation to reduce the SWOT swath noise, and so recover the observation of structures when velocity is derived from the SWOT SSH. We can observe their results in fig. 1.10. Although the big structure are recovered, we can observe the limitations of the method in observing smaller velocity magnitudes in the right versus the left subplots of fig. 1.10. *Chelton et al.* (2019) study the reduction of the noise variance by smoothing the SWOT data, and they look at pseudo-WaCM (Winds and Currents Mission) data too. A 2D Parzen smoother is applied to data simulated in the California Current System, and they find 30 km and 55 km resolved wavelengths for velocity and vorticity, respectively, calculated on the SWOT swath. They find that in this region, due to the sampling characteristics of SWOT in space and time, and due to its narrow swath (compared to WaCM), velocity and vorticity geostrophically constructed maps have too high sampling errors. It is important to note that these studies used ocean models with no internal tides signal, so its a simpler estimate than what it would be in reality.

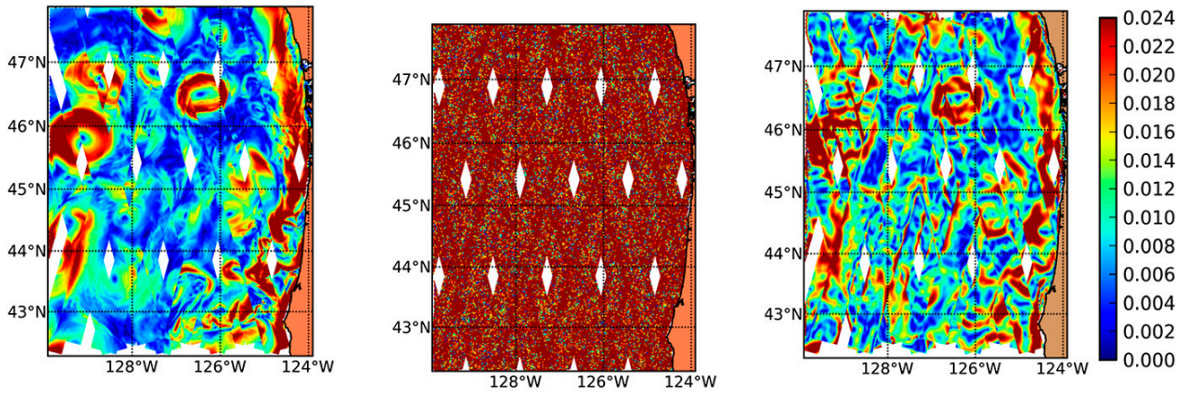

(**a**) From SWOT-like observations without noise

(**b**) From SWOT-like observations

(**c**) From SWOT-like filtered observations

Figure 1.10: Absolute geostrophic velocity (L2 norm, ms^{-1}) derived from (a) the true SSH, (b) the SWOT-like SSH and (c) the SWOT-like SSH filtered using optimal interpolation. (*Gaultier et al.*, 2016)

Ruggiero et al. (2016) studied the assimilation of SWOT data by taking into account the presence of SWOT correlated errors. The covariance matrix used in their method includes the information on SSH, but also its first and second order derivatives. They removed the uncorrelated KaRIn error by averaging the SWOT grid to 9 km pixels. One of their main conclusions is the need to use advanced image restoration techniques to filter the KaRIn error, so that they can exploit the information on the SSH derivatives which is usually masked by this error. This would allow for the technique to be applied at the expected 2 km grid resolution without having to coarsen it to 9 km.

Other studies focused on the removal of the swath's correlated errors (*Dibarboure and Ubelmann*, 2014; *Metref et al.*, 2019). *Dibarboure and Ubelmann* (2014) focus on one of the main correlated errors: the roll error. They study different methods to minimize it, using just the swath itself or the overlap of different passes, trying to minimize as much as possible any oceanic variability leakages. They find that their method is especially effective at mid and high latitudes, and at wavelengths greater than 100 km. Consequently, some roll error might be left at scales smaller than this, not directly helping to better observe the fine scales via SWOT, although its impact at larger scales will reflect in the fine scales observed. The approach of *Metref et al.* (2019) to reduce the SWOT correlated errors is to firstly obtain a detrended SSH, and then use an ensemble data assimilation analysis (ensemble Kalman filter). A reduction of the large scale SWOT errors is achieved, together with reducing small scale errors. In terms of spatial power spectra, they recover the signal down to scales of 25 km.

Several studies have also been done related to the obtention of SWOT SSH gridded maps. Most of these studies use noise-free pseudo-SWOT data. Standard interpolation techniques used in altimetry until now to produce gridded maps, like optimal interpolation, will not be appropriate for SWOT data given its spatial and temporal gaps. One of the proposed new techniques is dynamic interpolation by *Ubelmann et al.* (2015). This technique uses the conservation of potential vorticity to account for the temporal gaps between the SWOT passes. In their study they show they can recover small mesoscale eddies when the time gaps are maximum of 20 days. Although the results are promising some limitations exist. It is an idealized case where the specific sampling characteristics are not taken into account, no instrumental noise is considered and no unbalanced motions are present in the SSH signal.

Adequately de-noising the SWOT data and posteriorly mapping it, will have important operational applications. *Bonaduce et al.* (2018) found that the error of ocean analyses and forecasts could be reduced by more than 50% if instead of a three nadir constellation, a two wide-swath altimeter constellation was used for SSH observations. They point out though, that this improvement is only possible if the wide-swath data has a small instrumental error. This study also finds that this improvement in the surface ocean is propagated at depth, and thus improves the oceanic vertical structure representation. Having a good approximation of SWOT SSH derivatives on the swath, specially second order, will allow to apply data assimilation techniques that can efficiently constrain a quasi-geostrophic model to derive 2D SSH products from SWOT. Other studies that investigate the mapping of SWOT SSH fields are *Fablet et al.* (2018); *Ma and Han* (2019); *Le Guillou et al.* (2020); *Metref et al.* (2020).

1.4 Motivations, challenges and objectives

The general motivation of this study is to improve the observation of the fine scales (oceanic turbulence). This will allow to better understand the oceanic motions both in the horizontal and the vertical. SWOT will improve the upper ocean's observations spatial resolution and coverage. The latter, is of great importance as horizontal data gaps exist in present altimeter data, which in some cases cause an inadequate eddy tracking and quantification (e.g. *Amores et al.* (2018)). Vertical motions are very small, and thus difficult to measure. They need very high resolution data (*Pascual et al.*, 2017), like the one provided by SWOT's 2D swath. This information can then be used for biogeochemistry by better understanding the pathways of nutrients such as oxygen, CO_2, nitrates and chlorophyll, and thus phytoplankton. This can be applied concurrently to upper and upper across the food chain.

The challenges involved in the fine scales' observation are several, but in summary it is limited by the nowadays capacity of the OGCMs, satellite and *in situ* data. *McWilliams* (2016) describes how for example submesoscale currents are difficult to observe due their spatial and temporal scales, which limit the different observational tools (e.g. too small for nowadays satellites' footprints). Consequently, in this thesis we focus on their observation by SWOT. Specific SWOT challenges then arise, specially given it's specific sampling and new altimetric 2D data. Concerning the orbit, actually the challenge doubles as there will be the Cal/Val and Science orbits, with different spatial and temporal samplings. There is a need to understand how these might affect the fine scales' observation. Then, regarding the 2D swath, new algorithms to process the SSH data are necessary to process the data on swath as a first step, and then combine the passes to obtain 2D gridded maps of SSH and its derivatives. The goal is to find the most adequate methods that will accurately conserve the small scale signals as much as possible. The swath is not continuously 120 km, but has a 20 km gap. Taking advantage of the nadir data at the centre, the whole swath can be reconstructed across-track. As pseudo-SWOT data needs to be simulated, a more specific challenge is to use the best data sources (OGCMs) to do so. In addition, to using an OGCM that accurately represents the fine scales, the ocean dynamics that could account for important SSH variances is important too. This makes reference to for example tides, and the internal waves they generate, which become important at small spatial scales. Accounting for the sea state is also important as it will affect the SWOT SSH signal too. This together with a varying temporal and spatial sampling geographically, implies that these different challenges might be present or not depending on the region, and if present, be of different complexities. To this we have to add the general geographical variability of the ocean's dynamics.

One of the first challenges that has to be approached is obtaining SWOT SSH gradients (and thus current velocities), and its appropriate small-scale gradients. This is difficult due to SWOT SSH data being affected

by geophysical and instrumental errors. When SSH spatial derivatives are calculated by finite differences, SWOT noise and errors are amplified (*Chelton et al.*, 2019). A first approach to remove this errors was carried out by *Ruggiero et al.* (2016), who managed to remove the large-scale, correlated errors, but found an inconvenient: The small-scale, uncorrelated KaRIn error removal is necessary in order for their approach to be efficient. This provided a major motivation for this study, as it was found that it was necessary to appropriately remove this KaRIn error, before applying other error removal techniques.

Following the above mentioned, these two main questions are meant to be answered in this thesis:

1. What is the best method to remove this small-scale noise, whilst conserving the SSH signal and structures?
2. What will be the spatial resolution of the de-noised SWOT swath data in different dynamic regimes?

A preliminary objective is the analysis of OGCM outputs (used to generate pseudo-SWOT data) to evaluate their representation of the fine scales. With this evaluated the objective of adequately simulating pseudo-SWOT data can be approached. Then, due to the novelty of this data, another preliminary objective is to explore the SWOT SSH data's spatial and temporal coverage, and noise level at different oceanic regions. Knowing this allows to be able to start developing algorithms and protocols to treat the future SWOT data. The objective here is to find the best de-noising method that removes the small scale noise present in the SWOT swath, whilst conserving the SSH signal intensity and structures present. The following objective is to obtain a on swath SWOT observed wavelength, for different seasons. Lastly, extrapolate this to different oceanic regions and OGCM SSH data sources to account for the existing uncertainty on the fine-scale variability. Also, to provide an improved SWOT swath to which other larger scale error removing techniques can be applied, and then apply other techniques to combine the swaths to obtain improved 2D SSH gridded maps.

This thesis tries to attain these objectives by first focusing on a particular region: the western Mediterranean, and then expanding the study to other regions. Chapter 2 describes the main data and tools used in this study. Chapter 3 presents a first analysis of SWOT data in the western Mediterranean during the Science phase. The spatial scales resolved in this scenario are explored and a filtering algorithm is implemented to better them. To further improve the resolved scales and SWOT retrieved fields, a new de-noising method is developed and implemented. The western Mediterranean region is kept, but the fast-sampling phase is used instead in preparation for the Cal/Val experiments. The results are shown in Chapter 4. Chapter 5 is the last results Chapter which investigates the SWOT resolved scales in different dynamical regimes, after applying the de-noising method presented in the previous Chapter. Finally, the general conclusions and perspectives of this thesis are presented in Chapter 6.

Chapter 2

Data sources and methods

Contents

2.1 Ocean general circulation models

In preparation for the SWOT satellite launch different datasets and tools are developed. Firstly, high-resolution OGCMs are necessary to generate pseudo-SWOT data. The ones used in this study to obtain pseudo-SWOT data via the SWOT simulator (explained in Section 2.2) are described below:

- WMOP

The Western Mediterranean OPerational forecasting system (WMOP) is a hindcast obtained for the 2009 - 2015 period, with a spatial coverage from the Strait of Gibraltar to the Sardinia Channel. It is a regional configuration of the Regional Oceanic Model System (ROMS) nested in the Mediterranean Ocean Forecasting System (MFS) (*Lopez-Radcenco et al.*, 2019). It has a spatial resolution of approximately 2 km (varies from 1.8 to 2.2 km), and thus satisfies the horizontal resolution suggested in fig. 1.4 and described by *Hallberg* (2013). It is forced with a high resolution weather forecast forcing with a temporal resolution of 3 hours and a spatial resolution of 5 km. This introduces more energy to the system and allows to resolve the mesoscale and permits the submesoscale. This can be observed in the relative vorticity (normalized by f) snapshot below (fig. 2.1). (*Juza et al.*, 2016)

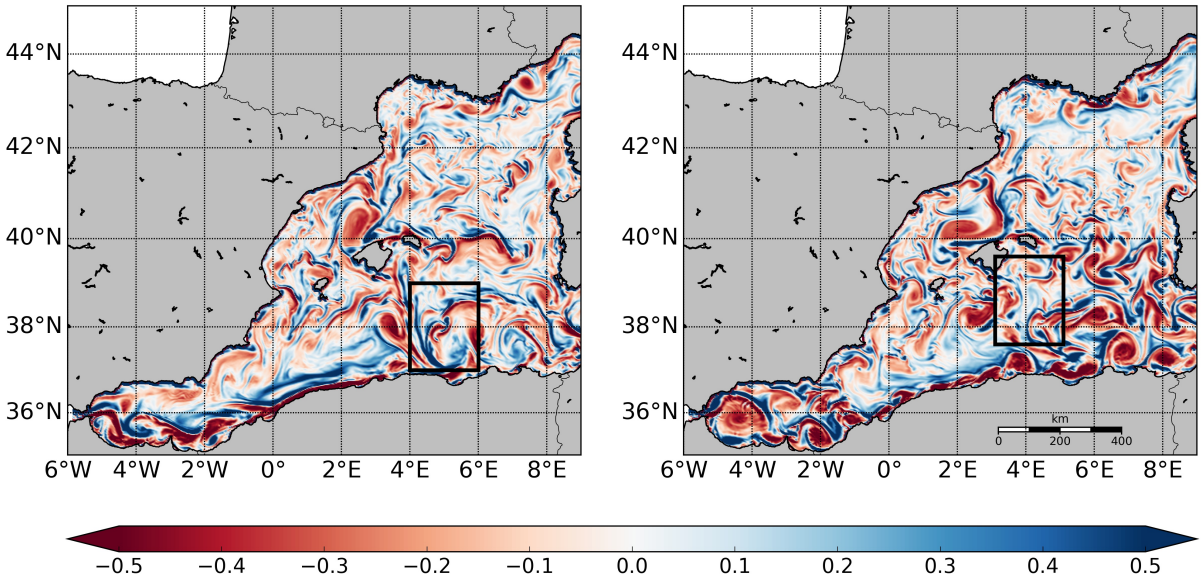

Figure 2.1: WMOP relative vorticity normalized by f on 23/01/2009 (left) and 03/02/2009 (right). (*Gómez-Navarro et al.*, 2018)

This WMOP hindcast simulation has been validated in several studies, given its importance for the forecasting system in this region. *Juza et al.* (2016) found that the WMOP forecasts based on this hindcast present a general accuracy with respect to ocean variability, large-scale circulation and water masses. *Aguiar et al.* (2019) found that the WMOP hindcast, in comparison to the CMEMS Med Rea (MEDSEA_REANALYSIS_PHYS_006_004 (*Simoncelli et al.*, 2014)) and altimetry, produces more small-scale eddies and approximately the same number of larger eddies. In terms of variability, they found that data assimilation is necessary for WMOP to correctly reproduce the mesoscale structures' phases and thus the variability of the surface currents that affected them.

- (e)NATL60

The North Atlantic at $\frac{1}{60}^\circ$ (from hereinafter referred to as NATL60) simulation run is based on the NEMO3.6 ocean model, coupled to LIM2 ice model and forced by the Drakkar Forcing Set (DFS5.2) atmospheric inputs.

The spatial domain covers the North Atlantic basin : from 26.5°N to 66°N and from 80°W to 9.5°E (fig. 2.2). The simulation time-span is from mid-June 2012 to October 2013 (simulation years, no data assimilation included). The period covered by this run encompasses the OSMOSIS observational campaign: from June 2012 to October 2013. Regarding the atmospheric forcing, the initial and open boundary conditions are built from the GLORYS2-V3 reanalysis provided by Mercator Ocean (re-analysis at $\frac{1}{25}^\circ$ and with 75 levels, so had to be adapted to $\frac{1}{60}^\circ$ and to 300 levels, as well as adapting it to the bathymetry). Boundary conditions at the ocean-atmosphere interface use DFS5.2, based on ERA-interim reanalysis. For the sub-grid closures of momentum and tracers in the horizontal and vertical, the closure scheme used is TKE (Turbulent Kinetic Energy) and the advection and dynamical scheme is UBS (Upstream-Biased Scheme).

This simulation run has been used in previous studies. *Fresnay et al.* (2018) use the NATL60 data in the Gulf Stream region, and found the simulation represents well the oceanic variability and stratification in this region. *Amores et al.* (2018) study the NATL60's eddy field to study the oceanic eddies characterization capacity by present-day gridded altimetric products. They find that the eddies captured in nowadays altimetric products is very low in both the North Atlantic Ocean and Mediterranean Sea. *Ajayi et al.* (2019) use this simulation to study ocean energetics, and compare it to HYCOM50 outputs. More precisely, they use the simulations' outputs to diagnose cross-scale kinetic energy exchanges. Overall, they found that this simulation reproduces well the North Atlantic oceanic dynamics. Thanks to its ∼1 km resolution, it allows to resolve fine-scale structures as low as 10 km. The western Mediterranean is an important study region here, which has not been previously studied with this simulation. To assess and validate this simulation in this region, an analysis and data comparison of the simulation's outputs was done and is shown in Section 2.3.

An extended version of the NATL60 run exists (eNATL60) in which a larger spatial domain is covered and with two runs: a twin experiment with and without tidal forcing. The new spatial domain includes the whole Mediterranean Sea and Black Sea and the domains goes farther south, down to 6°N, including too the Gulf of Mexico (fig. 2.2). It has the same spatial resolution as NATL60, so it is a submesoscale permitting simulation (*Verron et al.*, 2020). The simulation time-span is also the same as for NATL60. The simulation outputs were generated very recently (available since 2019), and so few published studies exist for now. *Verron et al.* (2020) compare the simulation outputs to the altimeter SARAL/Altika, focusing on a spectral comparison with the simulation's surface data. They find that the SSH spatial spectra of the model is very close to that of SARAL/Altika down to 80 km. The high frequency motions of the eNATL60 have been compared to altimetry by *Ansong et al.* (*in prep.*; *Ansong et al.* (2020)), showing a slight overestimation of SSH variance due to no explicit wave drag in the run.

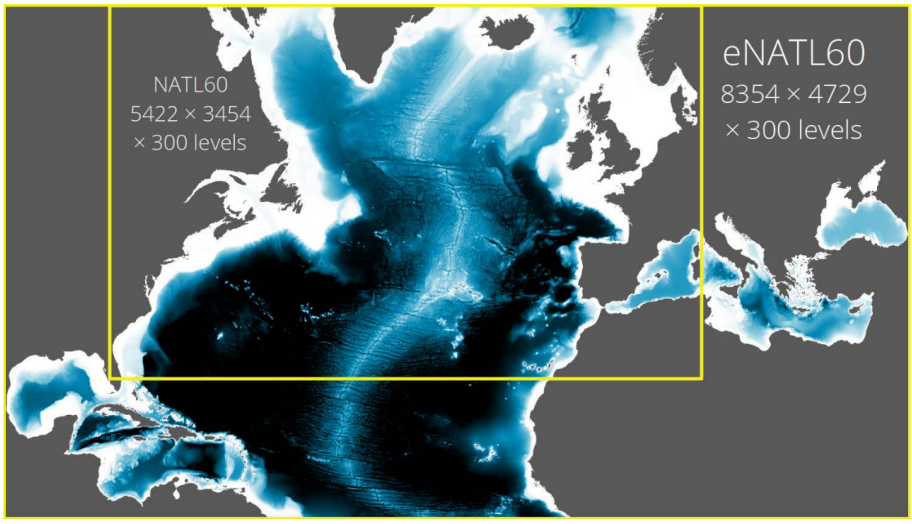

Figure 2.2: Spatial domain of NATL60 (yellow box) and eNATL60 (L. Brodeau)

- HYCOM

The HYbrid COordinate Model (HYCOM) (*Chassignet et al.*, 2009) is a global oceanic model. In this study we use a global simulation at $\frac{1}{25}^\circ$ (HYCOM25) with tidal forcing (see fig. 2.3). This corresponds to a horizontal grid spacing of ∼4 km. Hybrid coordinate makes reference to its vertical layers as it combines:

1. z-layer coordinates: depth-defined and used in the upper ocean,
2. isopycnal coordinates: density-defined and used in the open interior ocean,
3. sigma coordinates: bottom topography-defined and used coastal and deep ocean.

In total it has 41 hybrid vertical levels and it is a one year-long simulation, from January to December 2014. The tidal forcing used consists of 5 tidal constituents (K_1, O_1, M_2, S_2 and N_2), accounting for approximately 97% of the global variance of the main tidal constituents (*Savage*, 2017). To reduce the barotropic tidal errors a wave drag field is introduced (*Buijsman et al.*, 2015), which is important both for the barotropic and baroclinic tides representation (*Ansong et al.*, 2015; *Buijsman et al.*, 2016). It is forced too with atmospheric fields, allowing to represent SSH variance globally for temporal periods of hours to years, and both at the open ocean and the coast. (*Savage et al.*, 2017b)

Müller et al. (2015) use this simulation and another HYCOM simulation at $\frac{1}{12}^\circ$ to study the internal gravity wave spectra. Internal tide peaks are found in wavenumber-frequency spectra in agreement with linear internal wave theory. In this study the HYCOM25 simulation is validated with moored current meter observations. *Savage et al.* (2017b) compared the simulation outputs with tide gauges and McLane profilers (*in situ* depth-profiling observations), and found that "the model captures well-known phenomena such as mesoscale eddies and western boundary currents (steric sub-tidal), the barotropic tides (non-steric diurnal and semidiurnal), internal tides (steric diurnal and semidiurnal), and both low- and high-frequency barotropic motions driven by atmospheric pressure loading and winds (non-steric sub-tidal and super-tidal)" (*Savage et al.*, 2017b). The simulation's outputs were validated with moorings globally, focusing mainly on the semi-diurnal tide signal, by *Ansong et al.* (2017).

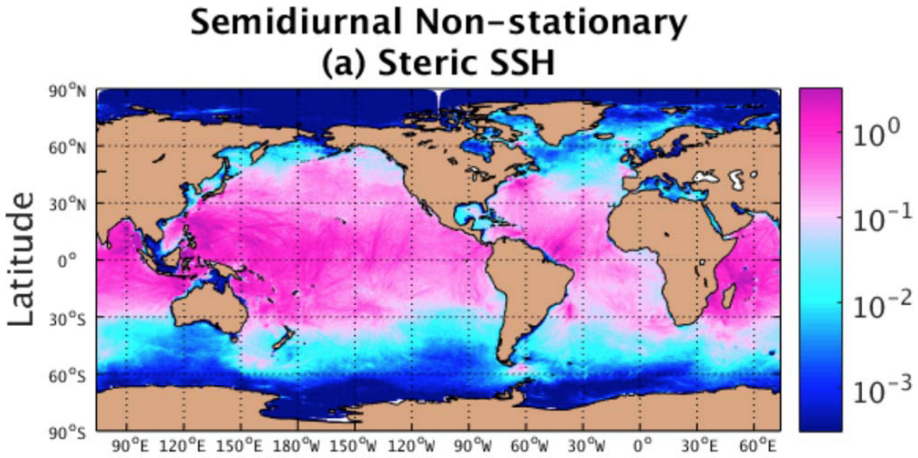

Figure 2.3: Global SSH variance (cm^2) from HYCOM25 in the semidiurnal band (frequencies 1.86–2.05 cpd) after stationary tides have been removed via harmonic analysis. The 95% confidence intervals range from 92% to 109% of shown value.(*Savage et al.*, 2017b)

- MITgcm

The Massachusetts Institute of Technology general circulation model (MITgcm) is a primitive equation global ocean model (*Marshall et al.*, 1997). In this study we use the LLC4320 simulation. LLC refers to Latitude–Longitude–polar Cap and 4320 is the number points across the common face dimension (*Forget et al.*, 2015). It is an approximately one-year long simulation, from September 2011 to 30 November 2012 (*Flexas et al.*, 2019). It has a horizontal spatial resolution of $\frac{1}{48}^\circ$, which means ∼2 km at mid-latitudes. It has 90 vertical levels that go from a 1 m at the surface to 300 m at depth grid spacing. This allows the simulation to represent physically meaningful signals down to 10 km. (*Wang et al.*, 2019a) This means this numerical run can resolve important oceanic processes down to approximately 5 km in diameter, such as mesoscale eddies, internal tides and other hydrostatic processes (*Ubelmann et al.*, 2018).

This simulation has been used and validated in many studies. On the one hand, *Rocha et al.* (2016); *Savage et al.* (2017a); *Viglione et al.* (2018) found that the low-frequency dynamics to be accurate. On the other hand in *Savage et al.* (2017a) they found the run to be slightly over-energetic at the high frequencies, which was later confirmed by a mis-parameterization (Arbic, personal communication). The model has also been validated with respect to balanced motions by *Rocha et al.* (2016); *Wang et al.* (2018) with ADCP (Acoustic Doppler Current Profiler) data. (*Torres et al.*, 2018) *Flexas et al.* (2019) looked at the model's kinetic energy (see fig. 2.4), specially focusing on the wind's energy transfer to the Ocean. These kind of studies were previously limited by the spatial and temporal resolution, but thanks to this high resolution simulation (as well as the others mentioned above) have made them possible. The tidal forcing introduced in these simulations has also been very important information on the role of internal gravity waves in the ocean dynamics studied until now. For example, *Flexas et al.* (2019) find that in general the kinetic energy fluxes due to IGWs is stronger in summer.

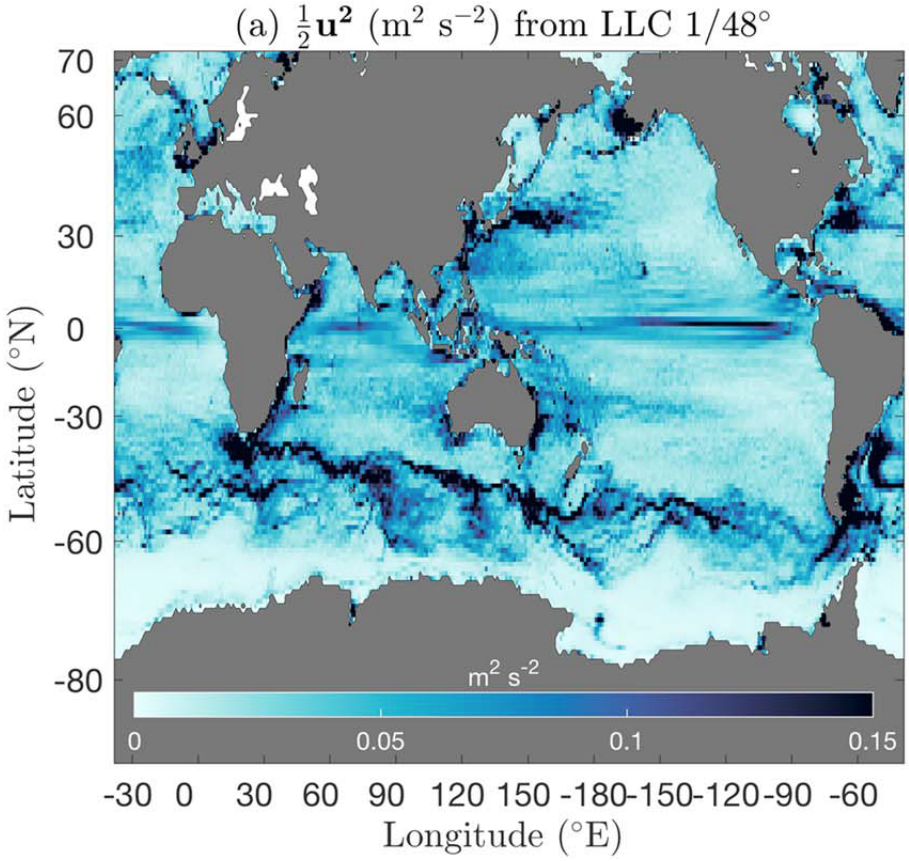

Figure 2.4: Annual-average map of surface kinetic energy from LLC 1/48°. (*Flexas et al.*, 2019)

These range of model simulations provide us a range of scenarios. The first two, WMOP and NATL60, were used for the first more regional studies in the western Mediterranean. For the posterior studies the last three OGCMs with tidal forcing have been chosen because they represent a range of oceanic dynamics. These 3 models have hourly data outputs available allowing the study of high-frequency motions. (e)NATL60 although it is not global, it has the highest spatial resolution. HYCOM25 and MITgcm48 both are global and include tidal forcing, but one does better at lower frequencies (HYCOM25) and the other at higher frequencies (MITgcm48). MITgcm48 has a better super-tidal signal than HYCOM25, but has too much energy at low frequencies (*Savage et al.*, 2017a). Lastly, none of the OGCMs include data assimilation. Table 2.1 summarizes and compares the OGCMs' main characteristics. The OGCMs comparison will be further discussed in Chapter V.

Model	WMOP	NATL60	eNATL60	HYCOM25	MITgcm48
Domain	W. Mediterranean	N. Atlantic (26.5N - 65N)	extended N. Atlantic	Global	Global
Time-span	January 2009 to December 2015	mid-June 2012 to October 2013		January to December 2014	September 2011 to November 2012
Numerical code	ROMS	NEMO v.3.6	NEMO v.3.6 + xios-2.0	HYCOM	MITgcm
Horizontal grid	$\frac{1}{50}^\circ$: ∼2 km	$\frac{1}{60}^\circ$: ∼1 km		$\frac{1}{25}^\circ$: ∼4 km	$\frac{1}{48}^\circ$: ∼2 km
Vertical grid	32 levels	300 levels		41 levels	90 levels
Vertical coord.	Stretched sigma	Z partial cells		Hybrid (Z, isopycnal and sigma)	Z-levels
Tidal forcing	No	No	Yes	Yes	Yes
BCs	CMEMS Mediterranean model	GLORYS2v3	GLORYS12 v1	GDEM	ERA-Interim
Atm. forcing	HIRLAM model	DFS5.2	DFS5.2 ERA-Interim (ECMWF)	ERA-40	ERA-Interim atmospheric reanalysis

Table 2.1: OGCMs description

2.2 SWOT simulator and simulated SWOT errors

Prior to the satellite's launch, the SWOT simulator for Ocean Science has been developed by *Gaultier et al.* (2015, 2016). It allows to generate pseudo-SWOT data in preparation for the SWOT mission. Firstly, it generates grid files following the time domain and orbit specified and region. Then, it interpolates (by a linear or nearest interpolation at choice) the model data onto the regular SWOT grid in time and space (the grid size can be set as parameter). The variable generated is SSH_model. It then generates a random realization of SWOT errors and noise on the same grid, and adds them to SSH_model. This generates the SSH_obs variable. We can see this simulation process in figure 2.5.

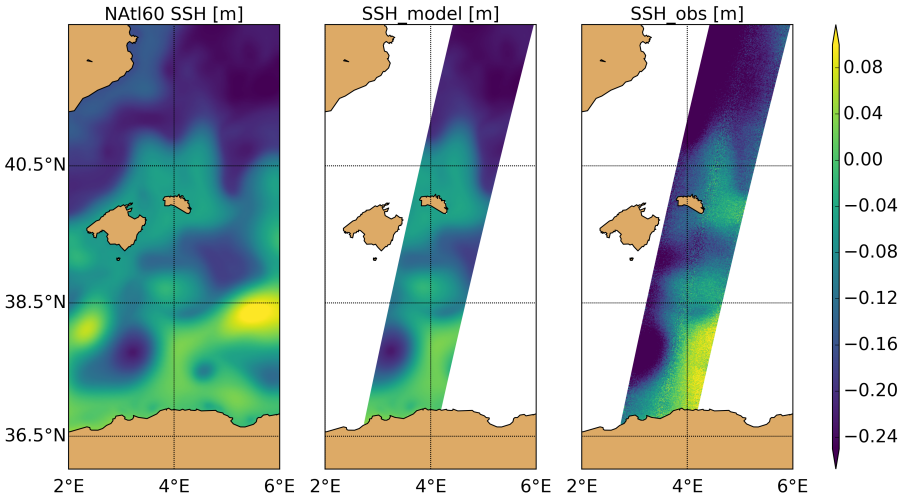

Figure 2.5: From left to right NATL60 SSH, SSH_model and SSH_obs [m] for pass 9 of the fast-sampling phase, corresponding to simulation date 01/07/2012.

There are two main groups of SWOT noises and errors: instrumental and geophysical. The first ones are due to the satellite's characteristics, and the latter because of the environment. It is important to note that the SWOT simulator error is generated randomly from spectral estimates (*Esteban-Fernandez*, 2017), and so it does not vary realistically in space and time (*Gaultier et al.*, 2016).

The instrumental errors include:

- KaRIn: Ka-band Radar Interferometer (KaRIn) noise is defined by independent Gaussian realizations of zero mean and with a standard deviation inversely proportional to the square root of the cell surface (*Gaultier et al.*, 2016; *Ubelmann et al.*, 2018). This noise is random from cell to cell (or pixel within the SWOT swath). It has a strong random component due to the height measurement's variance and the interferometer's intrinsic noise (*Esteban-Fernandez*, 2017).
- The KaRIn noise level varies in function of the across-track distance to the nadir (*Gaultier et al.*, 2016) as shown in figure 2.6 (*Wang et al.*, 2018). As further described below, the KaRIn noise level also varies with the wave steepness.
- Roll: The roll error signal has 2 components, one due to the KaRIn mechanical system which causes roll control errors and the gyro error caused by mistakes in the spacecraft roll angle. (*Gaultier et al.*, 2016)
- Phase: This error is caused by each of the satellite's antennae independently. (*Gaultier et al.*, 2016)
- Timing: It is a common group delay error of the system. It is the only error constant across track. (*Gaultier et al.*, 2016)
- Baseline dilation: This error is caused by distortions of the baseline mast (*Gaultier et al.*, 2016), changing its length and thus creating a height error (*Morrow et al.*, 2018).

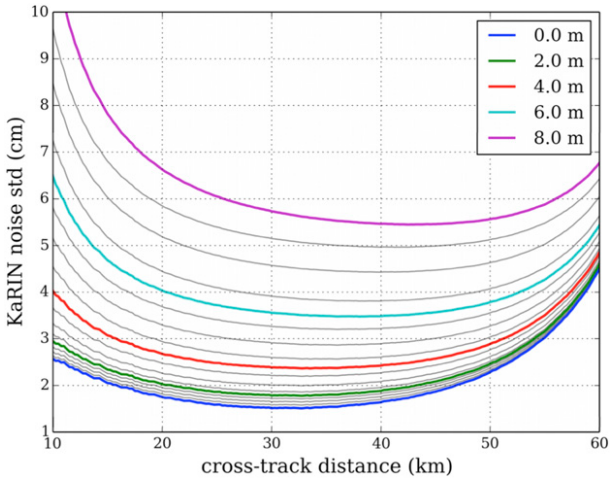

Figure 2.6: KaRIn random error, instrument plus wave effects (surfboard effects), as a function of cross-track ground range for various significant wave height values ranging from 0 to 8m plotted with a 0.5 m increment. (*Wang et al.*, 2018)

The geophysical errors intended to be represented by the SWOT simulator are after total geophysical error corrections have been applied. These residual geophysical errors include:

- Wet troposphere: This is an error due to the wet troposphere, and it is due to the signal alternation by atmospheric humidity. This translates into a 2-beam path delay error. It is a major source of geophysical error and the only geophysical one included for now in the SWOT simulator. As mentioned above, the errors simulated are after total geophysical corrections, in this case the simulator represents the residual error due to the wet troposphere after applying the on-board radiometer correction. (*Gaultier et al.*, 2016) This error is locally correlated in space.

- Sea state bias: This error is also known as electromagnetic bias, and is yet not implemented in current versions of the SWOT simulator. Height biases are introduced due to the spatial variability of the wave and wind fields. (*Esteban-Fernandez*, 2017) This variability can cause changes in the satellite's signal return waveform shape, affecting the height estimation (*Rodriguez et al.*, 2017). This error is expected to mainly have an impact on the large scales (*Gaultier et al.*, 2016).
- Dry troposphere and ionosphere: These errors, like the one due to the wet troposphere, translate into a path delay error (*Rodriguez et al.*, 2017). They are not included in the SWOT simulator, as at the Ka-band of SWOT, their impact at the meso-scale and below is very small (*Gaultier et al.*, 2015; *Esteban-Fernandez*, 2017).

An important discrimination of the errors is in their correlation in space. The KaRIn error is uncorrelated both along and across-track, and the rest have at least one direction which is correlated in space. This has important consequences on the fields of SSH derivatives, and the consequent processing of the SWOT swath (*Ruggiero et al.*, 2016). It completely masks in most regions of the Ocean the SSH derivatives' signal. It is the biggest source of SWOT error, specially at wavelengths lower than 100 cycles/km (*Morrow et al.*, 2018), and it is the one responsible for its spectral noise floor. Compared to a conventional nadir altimeter, its white noise spectral floor is lower, being approximately $100cm^2(cpkm)^{-1}$ for the latter and $2cm^2(cpkm)^{-1}$ for a 2m SWH KaRIn instrument noise (*Wang et al.*, 2019a). Moreover, the KaRIn instrument noise actually is not constant in time nor space given that it is affected by the wave steepness.

The KaRIn noise level will depend on the Sea Wave Height (SWH). The higher the SWH, the higher the noise level due to the increase in the wave steepness. As SWH varies in space and time, so will the KaRIn noise level. This has been estimated by *Wang et al.* (2019a). The wave period will also affect the wave steepness, but this is globally expected to vary less than SWH.

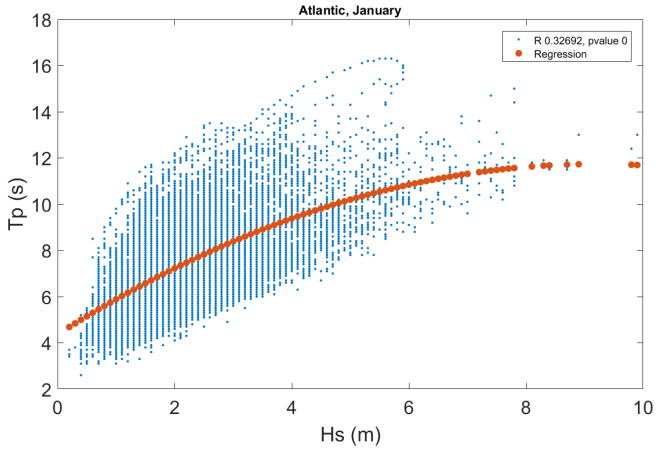

(**a**) Atlantic

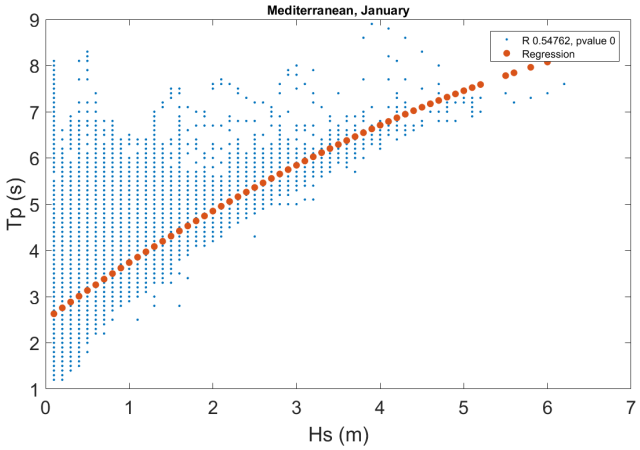

(**b**) Mediterranean

Figure 2.7: Dispersion relation of wave period (Tp (s)) and significant wave height (Hs (m), referred to also as SWH) in the Atlantic (a) and Mediterranean (b). Figures courtesy of Alejandra Rodríguez.

Nevertheless, in regions like the western Mediterranean, where the SWH is lower, the wave period variations may gain importance. This was briefly explored in collaboration with Alejandra Rodríguez and Marta Marcos. The data used consists on a 58-year wave reanalysis generated with the WAM model (WAMDI GROUP, 1988) that provides 3-hourly wave data up to 2014 and hourly data since then. The model data has already been evaluated against observations. The wave period (Tp) distribution of one point near the Balearic Islands is compared with another point in the North Atlantic (offshore the north western Spanish coast). Each point is assumed to be representative of its area. The plots are obtained from monthly data of all the years available (1958-2000). They show that, in contrast to the Atlantic results, in the Mediterranean the highest Tp dispersion is found at smaller Hs (SWH) values. This can be observed in the example figure for the month of January (fig. 2.7). This could make us think that the effect of Tp could be more relevant in the Mediterranean than Hs regarding its effect on the KaRIn noise level. On the other hand, both in the Atlantic and in the Mediterranean the maximum dispersion of Tp is approximately 8s. This adds another level of complexity to the processing of the SWOT data.

2.3 Validation in the western Mediterranean

To obtain pseudo-SWOT data, OGCM outputs are necessary. Although there are a few studies where the NATL60 outputs are analyzed, at the moment of the study, the NATL60 outputs in the western Mediterranean had not yet been studied. Even though model validation is not the objective of this thesis, a minimum validation was done to explore the simulation's outputs in this region before simulating SWOT data.

2.3.1 Analysis

Firstly, NATL60 outputs were analyzed to check if the model represented the dynamics of the western Mediterranean region accurately for our purpose. In fig 2.8, which is a SSH snapshot, we can observe some of the main features of the circulation in this area: Algerian Current, the mesoscale eddies shedded by this current, the Northern and Balearic currents, and the low SSH signal in the Gulf of Lions due to deep water formation.

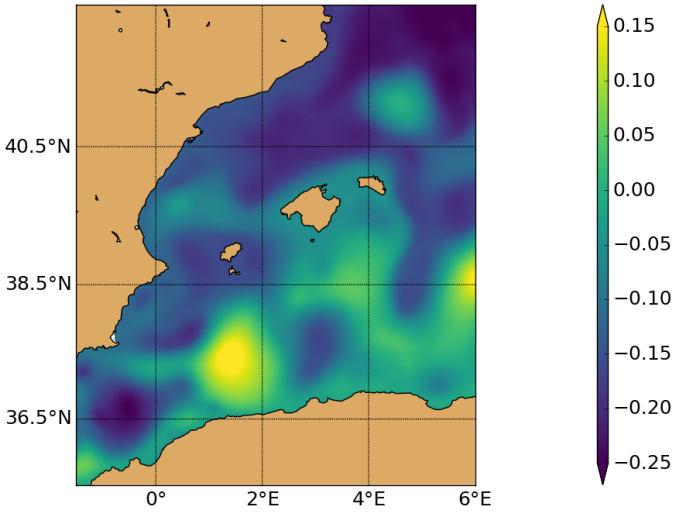

Figure 2.8: NATL60 SSH (m) snapshot on the 09/01/2012.

Then, some physical variables of the OGCM were calculated. Particularly, the focus is on SSH derived variables, due to the interest on surface velocities and vorticity. One of the main objectives of this study is to reconstruct SSH derivatives, and special attention will paid on the gradient and Laplacian in Chapters 3, 4 and 5. The following variables are calculated:

- **Absolute geostrophic velocity:**

It was calculated as follows:

$$u_g = -\frac{g}{f}\frac{\partial SSH}{\partial y} \tag{2.1}$$

$$v_g = \frac{g}{f}\frac{\partial SSH}{\partial x} \tag{2.2}$$

; where u_g is the zonal geostrophic velocity, v_g is the meridional geostrophic velocity, g is the gravitational acceleration and f is the Coriolis parameter. In fig. 2.9, the resultant absolute geostrophic velocity, U_g:

$$\mathbf{U_g} = \sqrt{u_g^2 + v_g^2} \tag{2.3}$$

, is illustrated.

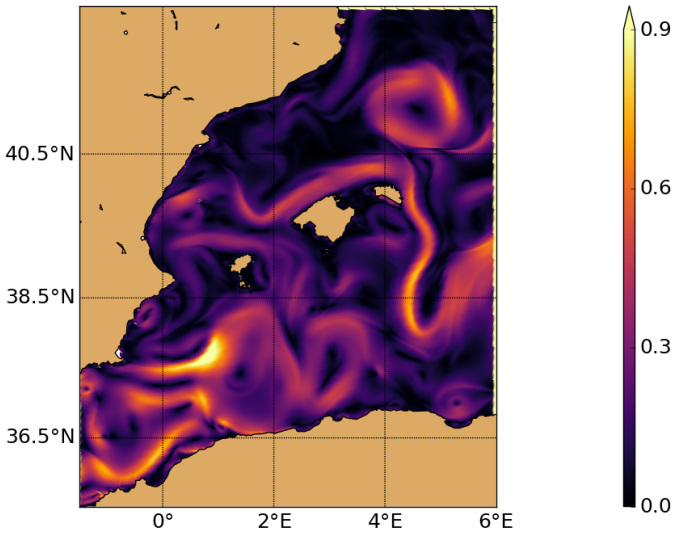

Figure 2.9: NATL60 absolute geostrophic velocity (m/s) snapshot on the 01/09/12.

- **Kinetic energy:** If u and v are respectively the zonal and meridional geostrophic velocity components, and are defined as:

$$u = u' + \overline{u} \tag{2.4}$$

$$v = v' + \overline{v} \tag{2.5}$$

; where:

$\overline{u}$, $\overline{v}$; the bar represents the mean in time rendering $\overline{u}(y,x)$, $\overline{v}(y,x)$

u', v'; the ' represents the velocity anomaly in time rendering $u'(t,y,x)$, $v'(t,y,x)$

Then we can define:

- Total Kinetic Energy, TKE:

$$TKE(t,y,x) = \frac{1}{2}(u_g^2 + v_g^2) \tag{2.6}$$

  - Mean Kinetic Energy, MKE:

$$MKE(y,x) = \frac{1}{2}(\overline{u}^2 + \overline{v}^2) \tag{2.7}$$

  - Eddy Kinetic Energy, EKE:

$$EKE(t,y,x) = \frac{1}{2}(u'^2 + v'^2) \tag{2.8}$$

If we take the time average of the above, we can also define one in function of the other:

$$\overline{TKE} = MKE + \overline{EKE} \tag{2.9}$$

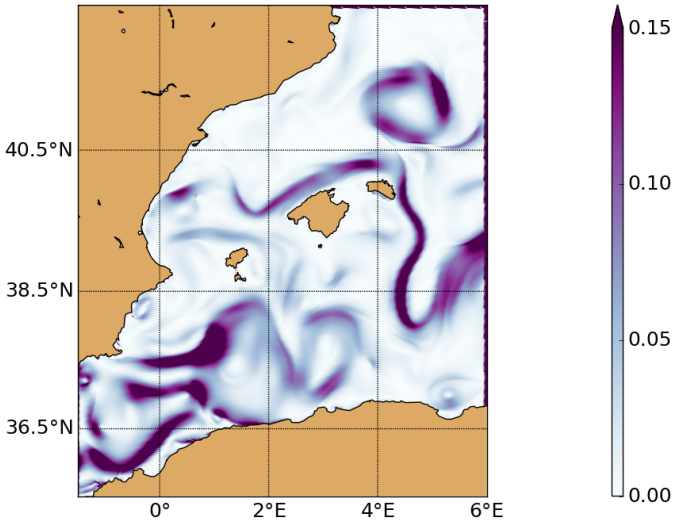

Figure 2.10: TKE (m^2/s^2) snapshot on the 01/09/12.

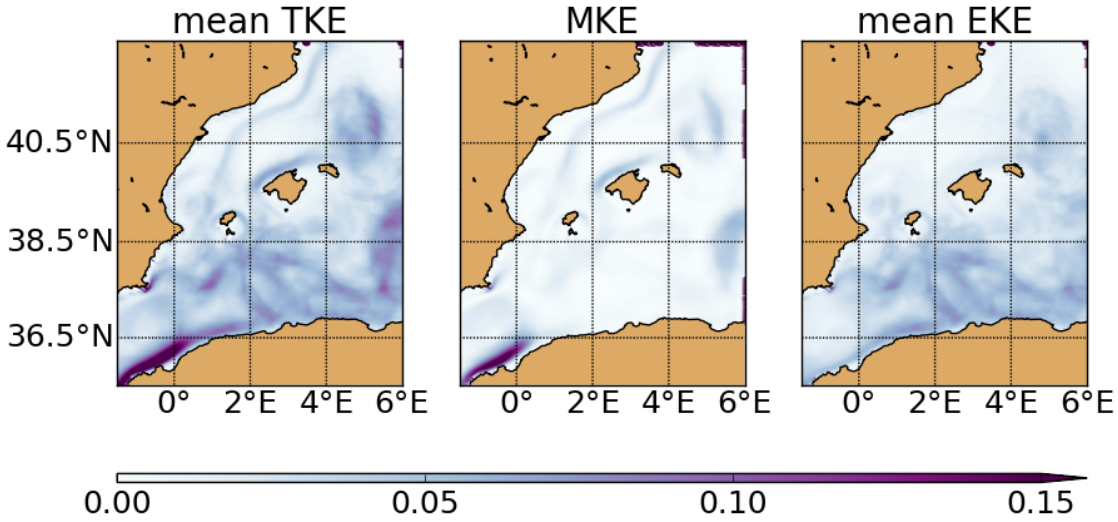

Figure 2.11: Yearly mean (starting from the day of fig. 2.10) TKE, MKE and EKE (m^2/s^2).

In these geostrophic velocity and kinetic energy figures we can also observe the signal of the main oceanographic features of the region.

- **Relative vorticity**, ζ_z:

$$\zeta_z = \frac{\partial v_g}{\partial x} - \frac{\partial u_g}{\partial y} = \frac{g}{f}\nabla^2 SSH - \frac{g\beta}{f^2}\frac{\partial SSH}{\partial y} \tag{2.10}$$

; where $\beta = \frac{\partial f}{\partial y}$

- **Rossby number**, Ro:

$$Ro = \frac{U}{fL} = \frac{\zeta z}{f} \tag{2.11}$$

As described in Chapter 1, we can define the ocean dynamics in function of the Rossby number (*Thomas et al.*, 2008):

- Ro O(1) => submesoscale dynamics (1 - 10 km)
- Ro << 1 => mesoscale dynamics (10 - 100 km)

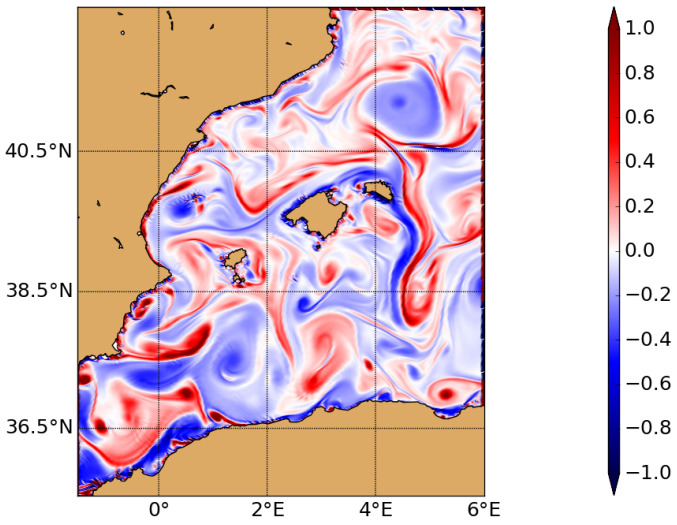

Figure 2.12: Rossby number on the 09/01/2012.

In the above figure one can observe the presence of fine-scale structures, of interest for our simulation of pseudo-SWOT data. Rossby numbers close to absolute values of 1 can be observed too indicating the presence of submesoscale dynamics.

Then, if we look at the time evolution of some spatial statistical parameters (of the box region shown in the above figures) of the other output surface variables (fig. 2.13):

- Sea Surface Temperature (SST)
- Sea Surface Salinity (SSS)
- Mixed Layer Depth (MLD)

, we can see that all three variables follow the seasonal cycle. The maximum-minimum refer to percentiles 99 and 1, and the robust maximum-minimum to percentiles 90 and 10, respectively. By looking at these values, there does not seem to be a region which has an anomalous value in the surface layer.

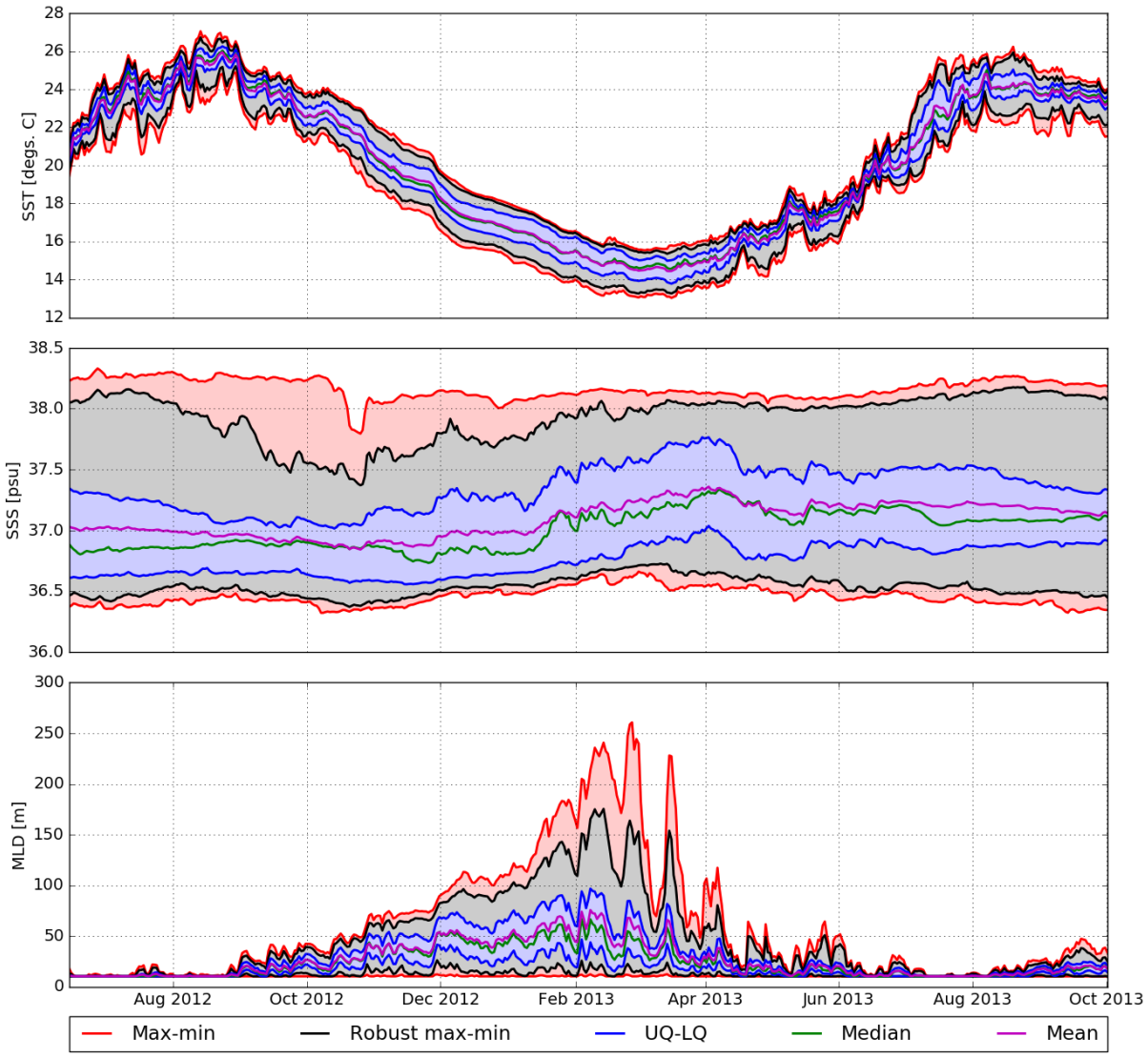

Figure 2.13: Time evolution of spatial statistical parameters of SST, SSS and MLD (from top to bottom) during the whole simulation time period.

2.3.2 Comparison to satellite data

Above, only a SSH snapshot was shown, and now we compare different yearly diagnostics to the same period for different years of the CMEMS altimetric dataset. Firstly, the mean SSH in time was calculated (by first removing the spatial mean to each snapshot to remove the steric effect). The comparison to different years CMEMS data is shown in fig 2.14. To improve the comparison of the NATL60 data to the CMEMS AVISO product, we used a NATL60 dataset, optimally interpolated in the same way as to obtain the AVISO gridded product (dataset courtesy of Angel Amores) which is shown in fig. 2.14. The NATL60 shows higher mean SSH values than the CMEMS AVISO product, but when the NATL60 SSH data is optimally interpolated, the mean SSH values are very similar to CMEMS AVISO's, specially for the 2009 - 2010, 2011 - 2012 and the 2013 - 2014 subplots.

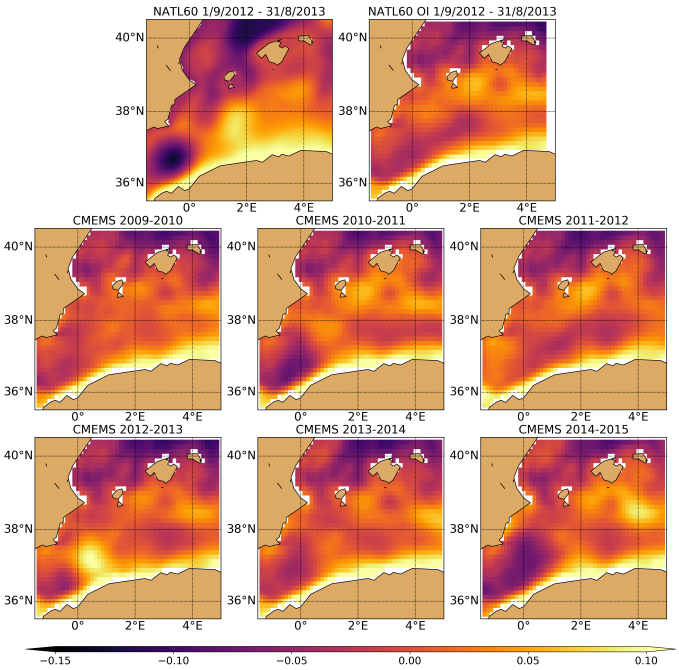

Figure 2.14: Annual mean SSH (m) of NATL60 (top left) and of optimally interpolated (OI) NATL60 (top right, courtesy of A. Amores) compared to the annual mean SSH CMEMS fields.

The same procedure was applied to calculate the Root Mean Square (RMS) and the results are shown in fig. 2.15. The RMS of NATL60 SSH is higher than for most of the CMEMS AVISO's subplots. Moreover, the location of the highest values is not the same, and this could be due to the altimeters used for the CMEMS AVISO product not capturing correctly the dynamics in that region, due to the gaps between altimeter tracks.

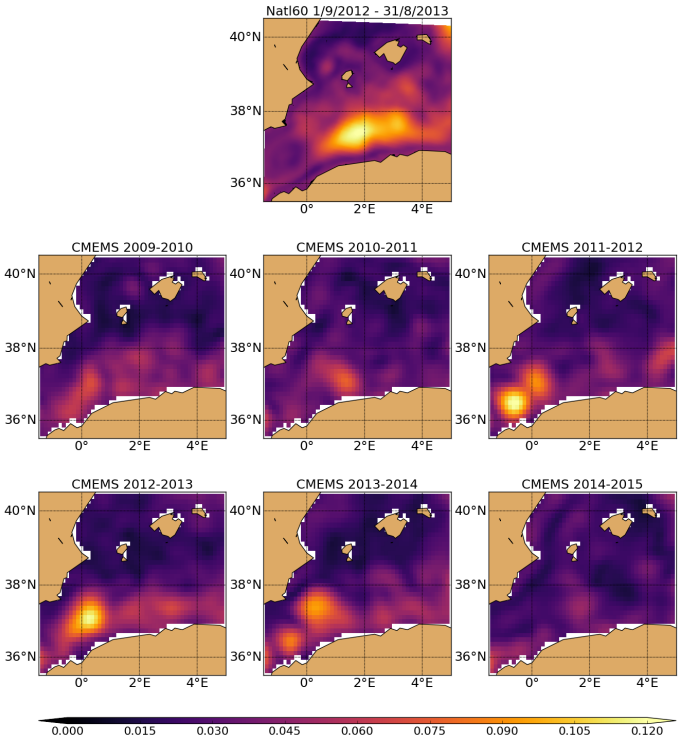

Figure 2.15: RMS of SSH of NATL60 compared to CMEMS.

The same parameters as in fig. 2.13 are calculated for the SSH of these 2 data sources and shown in fig. 2.16.

They are obtained from 01/09/12 to 30/09/13 for the same box region.

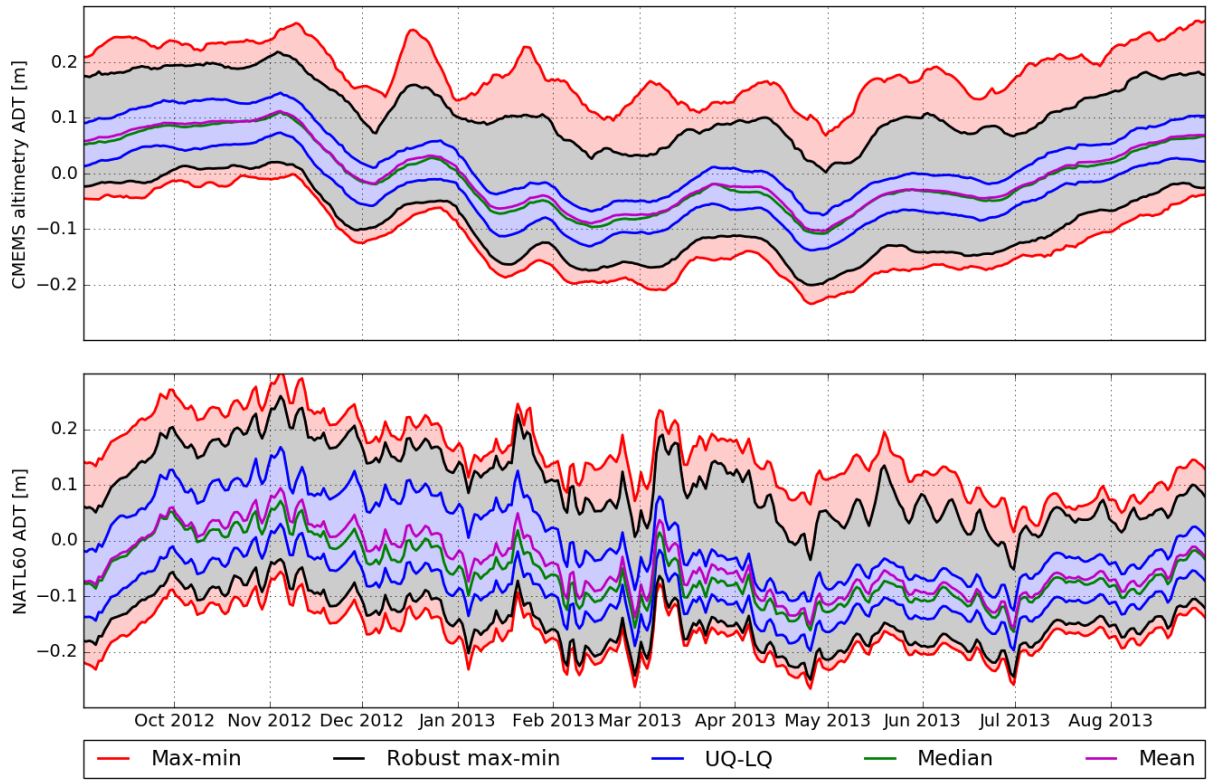

Figure 2.16: Time evolution of spatial statistical parameters of SSH of NATL60 compared to CMEMS.

In fig. 2.16 one can observe that NATL60 follows the same pattern as the CMEMS SSH with the exception of the period of time before October 2012. The intensity of the tendencies, for e.g., the value of a peak in SSH values, are not always the same, but it seems to be in accordance wit the inter-annual variability observed in figures 2.14 and 2.15.

2.3.3 Comparison to *in situ* data

Lastly, a comparison with *in situ* measurements was done to validate the vertical structure of the simulation. This part is relevant in relation for the reconstruction vertical velocities from SWOT data.

The EN4 observation dataset of the Met Office Hadley centre for the years 2012 and 2013 was used, which provides subsurface, quality controlled vertical profiles of temperature and salinity (*Good et al.*, 2013). In fig. 2.17, we can observe an example observation (EN4 *in situ* measurement) of potential temperature and salinity on the 17/03/2013 compared to the profile obtained by NATL60. For NATL60, the corresponding value in space is found as well as the corresponding day +/- 15 days. This way we have a 30 day window, to take into account that in one dataset an eddy could be present, and not in another, and so create important differences in the vertical profile. The red envelope of fig. 2.17 represents the percentile 10 and 90 of this 30 day window. In this example, both datasets follow the same trend with depth, although slight differences are present in the potential temperature example .

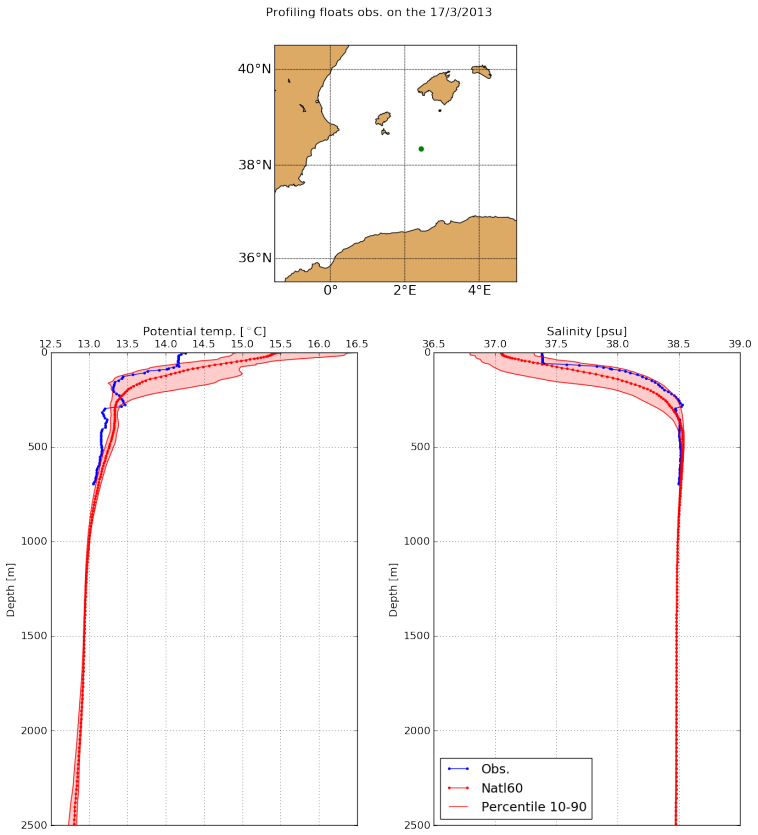

Figure 2.17: TS vertical profile. Top panel: Green dot shows the location of the observed (*in situ*) measurement. Bottom panel: Vertical profile of potential temperature (left) and salinity (right), for the observation (blue) and the model data, NATL60 (red).

If we now do this comparison for every season in the same region, we obtain the results shown in figures 2.18 and 2.19. All available Argo profiles in the region and season are selected (figs. 2.18). The corresponding NATL60 data is then obtained which is at the position of the Argo profile and an area around, and on the date of the profile +/- a 15 days window. The mean, percentile 10 and 90 of this is then calculated. All available profiles are regridded vertically to the same vertical levels to have a unique profile of the region per season. Finally, in fig. 2.19 the bias of the NATL60 with respected to the observed Argo profiles is plotted.

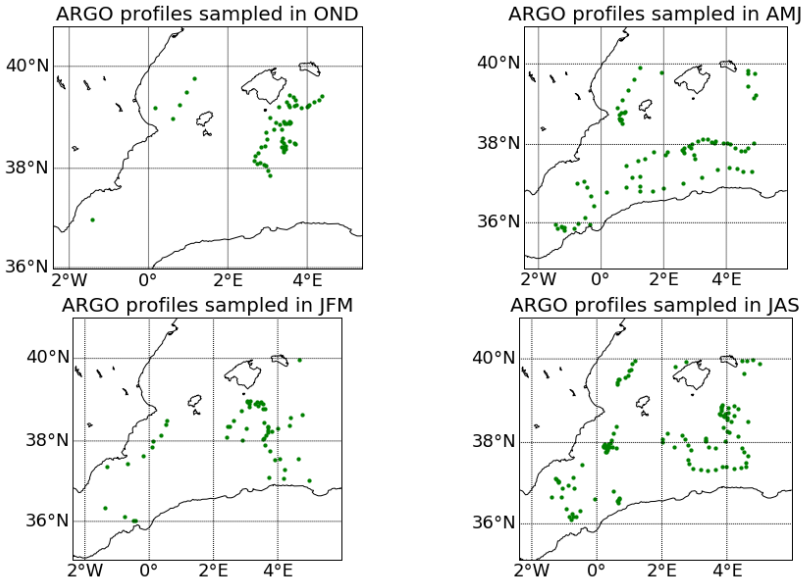

Figure 2.18: Green dot shows the location of the observed (*in situ*) measurement used for the comparison to model data.

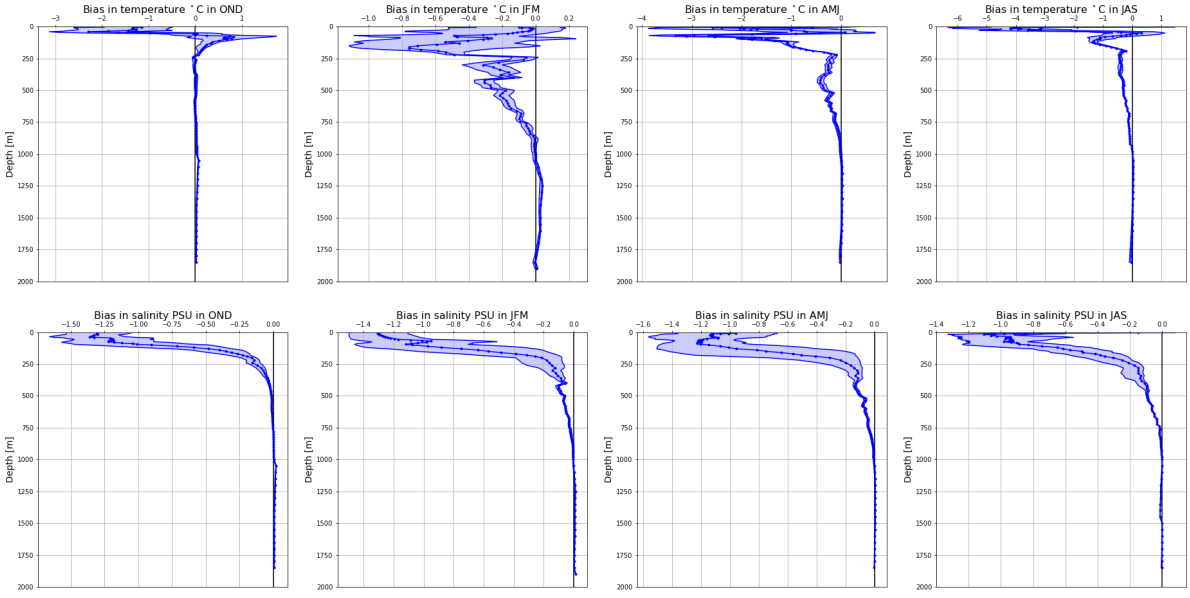

Figure 2.19: Model bias with respect to Argo profiles for each season (columns), for temperature (top panel) and salinity (bottom panel) (figure courtesy of Aurelie Albert).

A negative bias is observed in the surface waters both in temperature and salinity. This could be explained by an excess Atlantic water, given that this water mass is found at the surface. It could also be explained due to vertical diffusivity parametrization or atmospheric coupling.

The NATL60 simulation outputs were explored in the western Mediterranean Sea to assess if the sea surface fields were adequate to simulate SWOT fields. The main structures and circulation of this region are well represented, for example the predominance of the eddies shed by the Algerian Current can be observed.

The energetics and variability are comparable to those obtained from present altimetric products (CMEMS DUACS here). The seasonal variability of SST, SSS and MLD of NATL60 and the SSH time series compare well with CMEMS SSH. Although a bias in T-S profiles is found, the other surface fields and their derivatives are appropriate for the generation of pseudo-SWOT data in this region. Nevertheless, this bias could be important for the reconstruction of 3D circulation in the region, but is out of the scope of this thesis' objectives. These analyses provided important information for the preparation of the first experiments presented in the results chapters, specially Chapter 3.

Chapter 3

SWOT Spatial Scales in the Western Mediterranean Sea Derived from Pseudo-Observations and an Ad Hoc Filtering.

This chapter has been published as: Gómez-Navarro, L., Fablet, R., Mason, E., Pascual, A., Mourre, B., Cosme, E., & Le Sommer, J. (2018). SWOT spatial scales in the western Mediterranean sea derived from pseudo-observations and an Ad Hoc filtering. Remote Sensing, 10(4), 599.

Contents

3.1 Introduction

The Surface Water and Ocean Topography (SWOT) satellite mission is a joint mission by the National Aeronautics and Space Administration (NASA) and the *Centre National d'Études Spatiales* (CNES), with contributions from the UK and Canadian Space Agencies (*Alsdorf et al.*, 2011). Presently, the satellite's launch is planned for 2021 (*Fu and Morrow*, 2016). It will provide water elevation maps for oceanographic and hydrological purposes (*Lee et al.*, 2010; *Rodriguez*, 2010). The novelty of this satellite is that it carries a wide-swath altimeter with unprecedented horizontal resolution and global coverage. On the other hand, the associated irregular temporal sampling will constitute a challenge for the exploitation of the data. SWOT will have a 21-day repeat cycle and the revisit time will vary from approximately 10 days at the equator to two days at the poles (*Pujol et al.*, 2012; *Rodríguez*, 2016). This implies temporal variability in spatial coverage as the number of observations per repeat cycle will increase with latitude. Moreover, there will also be a temporal variability within a cycle. During each cycle, there are periods of time with a higher temporal sampling. This is due to a longer revisit time so that SWOT also fulfills its hydrological objectives by providing coverage of the bulk of the global land surface (*Rogé et al.*, 2017). In satellite measurements, there is always a compromise between spatial and temporal resolution. As SWOT aims for global coverage, i.e., high spatial resolution, we lose in temporal resolution (SWOT's repeat cycle will be longer than, for example, the 10-day repeat cycle of the Jason altimeter satellites (*Cipollini et al.*, 2017)).

One of the primary oceanographic objectives of the SWOT mission is to characterize the ocean meso- and submesoscale circulation (*Fu and Ferrari*, 2008) determined from ocean surface topography at spatial resolutions of 15 km (spatial resolution is defined to be perturbation wavelength in the oceanographic context). The resolution capacity of current along-track one-dimensional altimeter data, depending on the altimeter, has been found to be between 40 and 50 km at western boundary currents and between 70 and 110 km at the eastern basins (*Dufau et al.*, 2016). Two-dimensional gridded products based on the altimetric constellation allow for mapping wavelengths down to 200 km (*Chelton et al.*, 2007). The SWOT mission is expected to allow to capture wavelengths down to 15 km on its two-dimensional swaths (*Fu and Ubelmann*, 2014), therefore increasing substantially the resolution capacity of present-day altimeter data. The possibility of characterizing the submesoscale is a major breakthrough. While the mesoscale has historically received a lot of attention (*Mémery and Olivier*, 2003), the submesoscale has previously been out of reach. Theoretical calculations and advanced modeling suggest that submesoscale processes are key to understanding ocean fluxes (*Lévy et al.*, 2001; *Lapeyre and Klein*, 2006; *Omand et al.*, 2015). A pertinent example is the occurrence of mid-ocean plankton blooms (*McGillicuddy et al.*, 2007).

In the Mediterranean Sea, intense mesoscale and submesoscale variability interact across sub-basin and basin scales (*Allen et al.*, 2001; *Ruiz et al.*, 2009; *Pascual et al.*, 2017). This variability has an indirect impact on the Atlantic Ocean circulation due to exchange through the Strait of Gibraltar and, subsequently, influence on the great ocean conveyor belt (*Bethoux et al.*, 1999; *Malanotte-Rizzoli et al.*, 2014; *Robinson et al.*, 2001). Three scales of motion are therefore overlaid, making an amalgam of intricate processes that require high resolution and can help assess the potential impact that SWOT will have on the study of processes occurring at different scales.

Understanding small scale variability in the Mediterranean Sea is important as it is a region with intrinsically smaller spatial scales than those found in other parts of the world ocean at similar latitudes. *Hallberg* (2013) showed that the grid resolution necessary to resolve the first baroclinic deformation radius in the Mediterranean is around $1/16^{\text{o}}$, whilst in the Atlantic Ocean at the same latitude it is only $1/6^{\text{o}}$. This implies that smaller structures need to be resolved in the Mediterranean Sea compared to the mid-latitudes of the Atlantic Ocean. This is further demonstrated by *Escudier et al.* (2016b) who show that lower values of the first baroclinic Rossby radius of deformation are present in the western Mediterranean Sea. These values are approximately between 2 and 16 km, in comparison with a 20–30 km range found at mid-latitudes of the Atlantic Ocean (*Chelton et al.*, 1998). The Mediterranean values are actually closer to the values found in the Arctic Ocean (*Nurser and Bacon*, 2013).

The western Mediterranean Sea is one of the areas of the global ocean that will be sampled during the SWOT fast-sampling phase (*Wang et al.*, 2018). This phase covers the first 60–90 days after launch, during which the satellite will provide daily high resolution Sea Surface Height (SSH) measurements over a limited repeated orbit for purposes of calibration/validation of the SWOT sensor/instrument.

The goal of this study is to assess the capacity of SWOT to resolve the fine scales in the western Mediterranean. Our first objective is to generate pseudo-SWOT data from numerical model outputs in this region in order to understand its temporal and spatial sampling pattern in this area. We then apply a noise-reduction processing technique to pseudo-SWOT data to find out the spatial scales that SWOT may ultimately be able to resolve. Given SWOT's irregular time sampling and consequent variable spatial coverage, in this paper, we focus on the spatial scales resolved within a swath.

3.2 Data and Methods

3.2.1 The SWOT Simulator

With a view to characterizing the potential of SWOT-derived SSH data, we consider a simulation-based framework using the SWOT Simulator for Ocean Science (version 1). This simulator accounts for both SWOT space-time sampling patterns and noise processes. Using as input the SSH fields from an Oceanic General Circulation Model (OGCM), the SWOT simulator generates SWOT-like outputs along a ground swath and the nadir following the orbit ground tracks (*Gaultier et al.*, 2015). Hereinafter, we refer to these outputs as SSH outputs. Note that these simulated fields correspond to Absolute Dynamic Topography (ADT) values in altimetric terminology.

A flowchart of the simulator workflow is provided in Figure 3.1. Two features should be pointed out. Grid files, generated in the first step of the flowchart, account for the planned orbit of the satellite and the specified domain. Instrument noise and geophysical errors are added during the last step of the flowchart, following recent technical characteristics established by the SWOT project team (*Gaultier et al.*, 2015). Instrument noise is composed of Ka-band Radar Interferometer (KaRIN) noise, roll, phase, baseline dilation and timing errors (see *Gaultier et al.* (2016)). In this version of the simulator, the only geophysical error is associated with the wet troposphere. Therefore, it is important to keep in mind that additional noise patterns, such as sea state bias (*Gaultier et al.*, 2015) or the effects of internal waves (*Fu and Morrow*, 2016) are not accounted for in the generated pseudo-SWOT data.

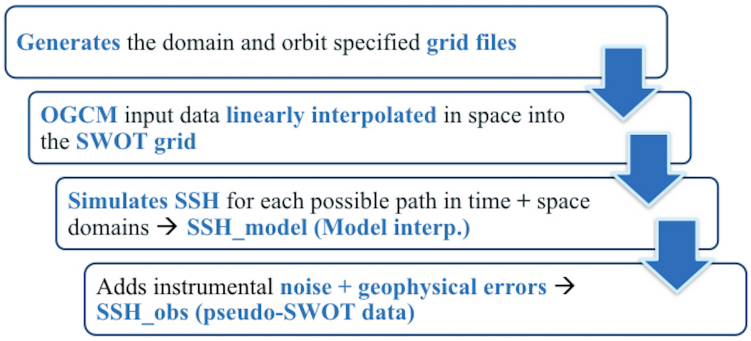

Figure 3.1: Flowchart of the SWOT simulator procedure.

For more details on the instrument noise and geophysical errors added by the SWOT simulator, see Appendix 3.B.

3.2.2 Input Data: The Western Mediterranean OPerational (WMOP) Model

A high resolution OGCM of the western Mediterranean region provides input data for the SWOT simulator. We used the WMOP model (*Juza et al.*, 2016) developed at SOCIB (Balearic Islands Coastal Observing and Forecasting System). More specifically, we consider a 7-year free run simulation of the model spanning the period 2009 – 2015, with spatial coverage from the Strait of Gibraltar to the Sardinia Channel (Figure 3.2).

WMOP is a regional configuration of the Regional Oceanic Model System (ROMS) model (*Shchepetkin and McWilliams*, 2005) with a spatial resolution of approximately 2 km. WMOP is forced with high resolution atmospheric forcing (HIRLAM model from the Spanish Meteorological Agency AEMET), with temporal resolution of 3 h and spatial resolution of 5 km. These features make WMOP a suitable choice to evaluate the potential of SWOT-derived SSH data to resolve mesoscale processes in the western Mediterranean Sea. The presence of fine-scale features of a few kilometers is illustrated in Figure 3.2. In Figure 3.2, we show snapshots of model relative vorticity (normalized by f) for days corresponding to pass 15 (Figure 3.2, left) and pass 168 (Figure 3.2, right) of cycle 2 of the SWOT orbit (see Figure 3.3).

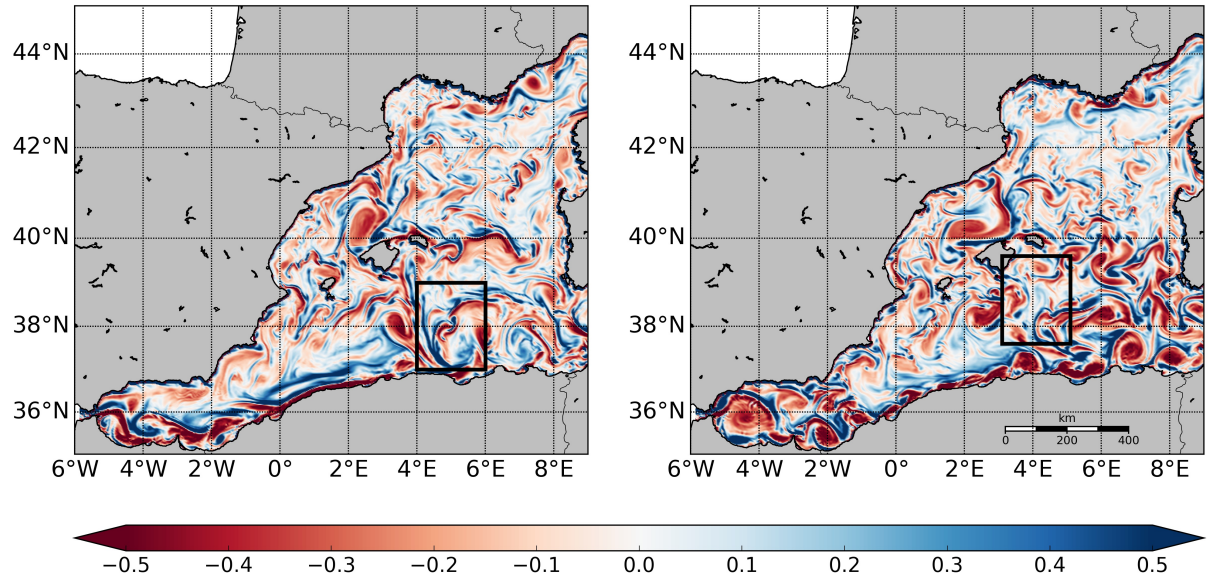

Figure 3.2: WMOP relative vorticity normalized by f on 23 January 2009 (**left**) and 3 February 2009 (**right**). Black boxes indicate the two regions studied in Section 3.3: box 1, pass 15 (**left**) and box 2, pass 168 (**right**).

3.2.3 Analysis and Processing of SWOT-Derived SSH Data

3.2.3.1 Geostrophic Velocity and Vorticity

Zonal (u_g) and meridional (v_g) (with respect to the SWOT grid) surface geostrophic velocity components are calculated as:

$$u_g = -\frac{g}{f}\frac{\partial \eta}{\partial y}, \tag{3.1}$$

$$v_g = \frac{g}{f}\frac{\partial \eta}{\partial x}, \tag{3.2}$$

where g is the gravitational acceleration, f the Coriolis parameter and η the sea level elevation.
The absolute geostrophic velocity (V_g) is obtained with:

$$V_g = \sqrt{u_g + {v_g}^2}. \tag{3.3}$$

Geostrophic relative vorticity, ζ, is calculated from the zonal and meridional velocities:

$$\zeta = \frac{\partial v_g}{\partial x} - \frac{\partial u_g}{\partial y}. \tag{3.4}$$

3.2.3.2 Noise Filtering

As illustrated in Section 3.3, noise greatly affects the computation of the velocities derived from the pseudo-SWOT data. We therefore investigate filtering procedures for noise removal. The geometry of the SWOT data prevents us from using classical Fourier and convolution-based low-pass filters (*Sonka et al.*, 2014). Fourier-based filters impose circularity constraints, which cannot be fulfilled; the masks associated with convolution-based filters should be significantly smaller than the width of the SWOT swath, which greatly limits low-pass filtering capabilities. We then considered a Partial Derivative Equation (PDE)-based formulation, such that the low-pass filtering results from an iterated Laplacian diffusion:

$$\partial_t a\,(t,y,x) - \triangle a\,(t,y,x) = 0 \iff \frac{\partial a}{\partial t} = \frac{\partial^2 a}{\partial y^2} + \frac{\partial^2 a}{\partial x^2}. \tag{3.5}$$

As the Green's function for the heat equation is a Gaussian kernel, the implementation of this PDE-based diffusion is equivalent to a Gaussian convolution and results in an isotropic filtering, that is to say that the filtering acts equally in all directions (*Aubert and Kornprobst*, 2006). Using a four-neighbourhood discretization of the Laplacian operator, we can deal with missing data (e.g., nadir) or land (e.g., island) pixels. The Laplacian operator comes to compute a local mean over the four neighbours of a given pixel. Withdrawing land pixels and missing data from the computation of this local mean, we can iterate the Laplacian diffusion to reach the expected filtering level for all pixels. Each iteration of the Laplacian diffusion can be regarded as a low-pass filtering with a high cut-off frequency. The selection of the number of iterations of the Laplacian diffusion then allows us to reach lower cut-off frequencies. By contrast, the direct application of two-dimensional low-pass filters for cut-off frequencies in the range [30 km, 60 km] would result in filter supports in the range [60 km, 120 km], meaning that no filtering output could be computed for any pixel closer than 30 km (rest. 60 km) from the swath boundaries or a missing data or land pixel. Overall, the filtering level is set by the number of iterations of the Laplacian diffusion and the parameter lambda. This is shown in the following equation, which shows the implementation that we use:

$$a^{k+1} = a^k - \lambda \triangle a^k. \tag{3.6}$$

With this being an iterative method, in contrast to a traditional Gaussian filter, we can apply cut-off wavelengths greater than the width of a half-swath. In Appendix 3.A, we apply the filter to white noise to show how different combinations of the filter's parameters (lambda and number of iterations) are associated with different cut-off wavelengths ($\lambda_c s$).

3.2.3.3 Filter Evaluation

To evaluate the performance of the filter and its different parameterizations, the following variables are calculated:

- The radial power spectral density: This variable was calculated to obtain the SWOT spatial spectra. The radially averaged power spectral density (power spectrum) of an image (in our case, the SWOT swath data) is computed.
- The Root Mean Squared Error (RMSE): The RMSE was calculated for the SSH, velocity and vorticity variables as follows:

$$RMSE = \sqrt{\frac{\sum (data - estimate)^2}{N}}, \tag{3.7}$$

where N is the number of points. Data is taken to be SSH_{model} (or its derived variables, i.e., velocity and vorticity) without filtering. An estimate is taken to be the simulated noisy SSH_{obs} fields (or its derived variables) without filtering, and filtered with different $\lambda_c s$. RMSE values are therefore calculated for different estimates.

3.3 Results

3.3.1 Spatial and Temporal Sampling

Pseudo-SWOT data were generated for the full WMOP time period (1 January 2009 to 11 September 2015). This was done for the Science orbit and corresponds to a total of 123 cycles. In a complete cycle, 292 passes are available over the globe, 12 of them crossing our study region (Figure 3.3). Data were ingested and processed by the SWOT simulator at an across and along track resolution of 2 km. As mentioned in Section 4.1, one of the specificities of future SWOT data will be their irregular temporal sampling. To better illustrate this, the passes of cycle 2 are plotted in Figure 3.3. During each cycle, there are periods of time with a higher temporal sampling. This is due to a longer revisit time so that SWOT also fulfills its hydrological objectives as described in Section 4.1. For instance, the temporal sampling during cycle 2 is as follows: from day 21.3 to 23.9 during which five passes are made; and from day 31.3 to 33.8 during which six passes are made. Then, from day 23.9 to 31.3 and from day 33.8 to 41.2, there are no measurements. Consequently, during each day within a cycle in this study region, there can be two, one or no passes at all. Even with this irregular sampling and without any processing of the data, the final SSH_{obs} map (subplot of day 41.2) allows us to observe some features such as, for example, the signal of the Algerian Current following the north African coastline and several cyclonic and anticyclonic mesoscale eddies.

3.3.2 Pre-Filtering Analysis of Simulator Outputs

In this study, we focus on the analysis of spatial scales of individual passes. Due to the irregular time sampling of the SWOT data, future studies will be devoted to temporal interpolation of passes. Moreover, prior swath filtering is necessary to determine the quality of the dynamical variables that can be derived from SWOT data, and how it can be improved before combining different swaths for temporal interpolation. As an illustration, we focus on the treatment of two $2^o \times 2^o$ boxes. Box 1 is within pass 15 and was chosen close to the north African coast as it is a region where anticyclonic eddies are shed from the Algerian Current (*Escudier et al.*, 2016b,a). For example, in the snapshot shown in Figure 3.4, part of an anticyclonic eddy is present on the eastern part of the domain. Box 2 is within pass 168, and this subdomain south of the Balearic island of Menorca was chosen because it contains smaller structures than in box 1 (see Figure 3.2). In Figure 3.5, filament-like structures and smaller eddies can be observed, especially at the northern part of the domain.

The effect of the filter is assessed for SSH and its derived dynamical variables: absolute geostrophic velocity and relative vorticity. These were calculated as explained in Section 3.2.3.1.

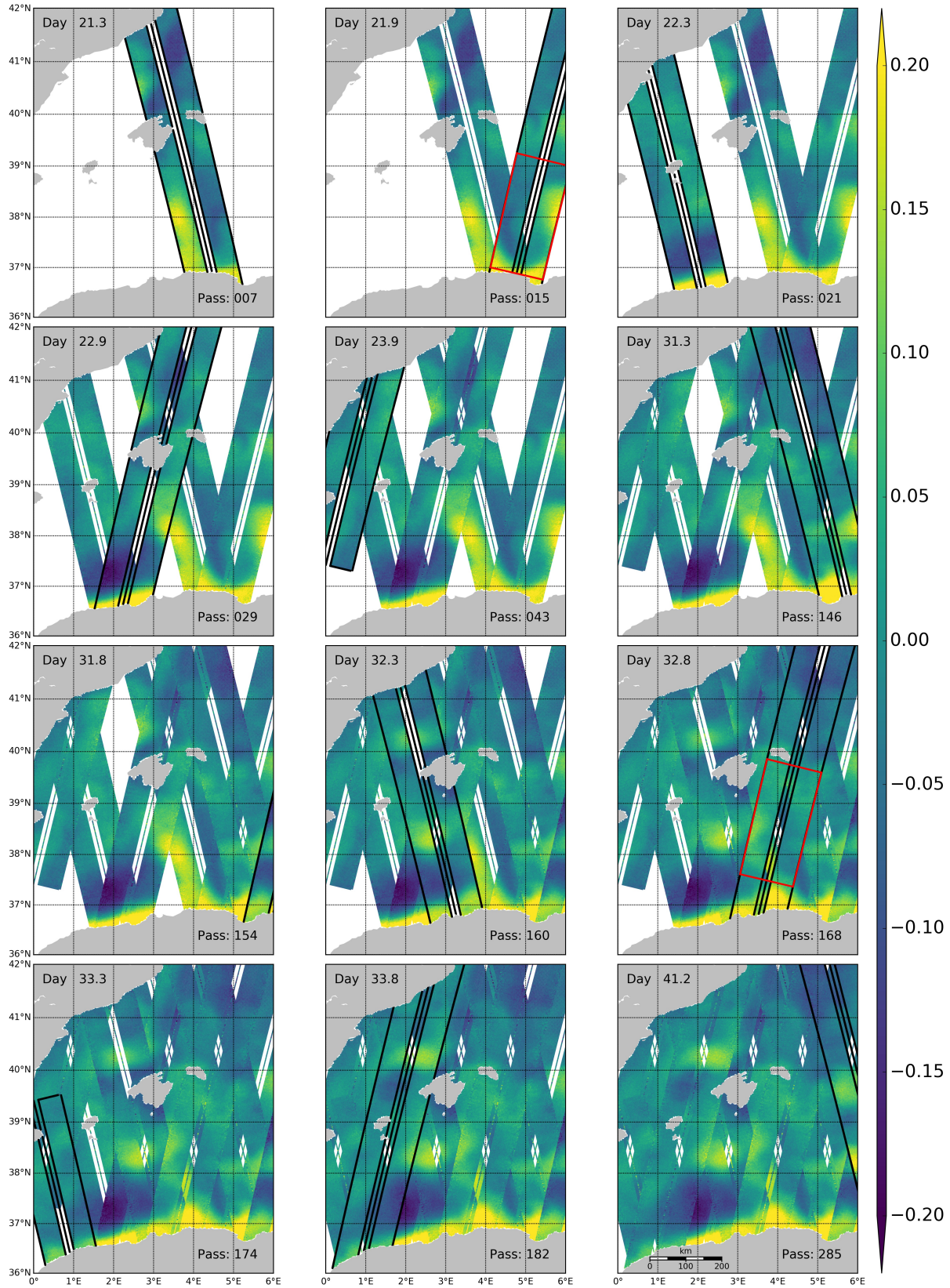

Figure 3.3: SSH_{obs} (m) obtained for cycle 2. Time increasing from left to right, top to bottom. Days from the beginning of the simulation are shown at the top left corner and the corresponding pass number at the bottom right corner. Outline of the active pass is shown in black. The red boxes show box 1 (pass 15) and box 2 (pass 168).

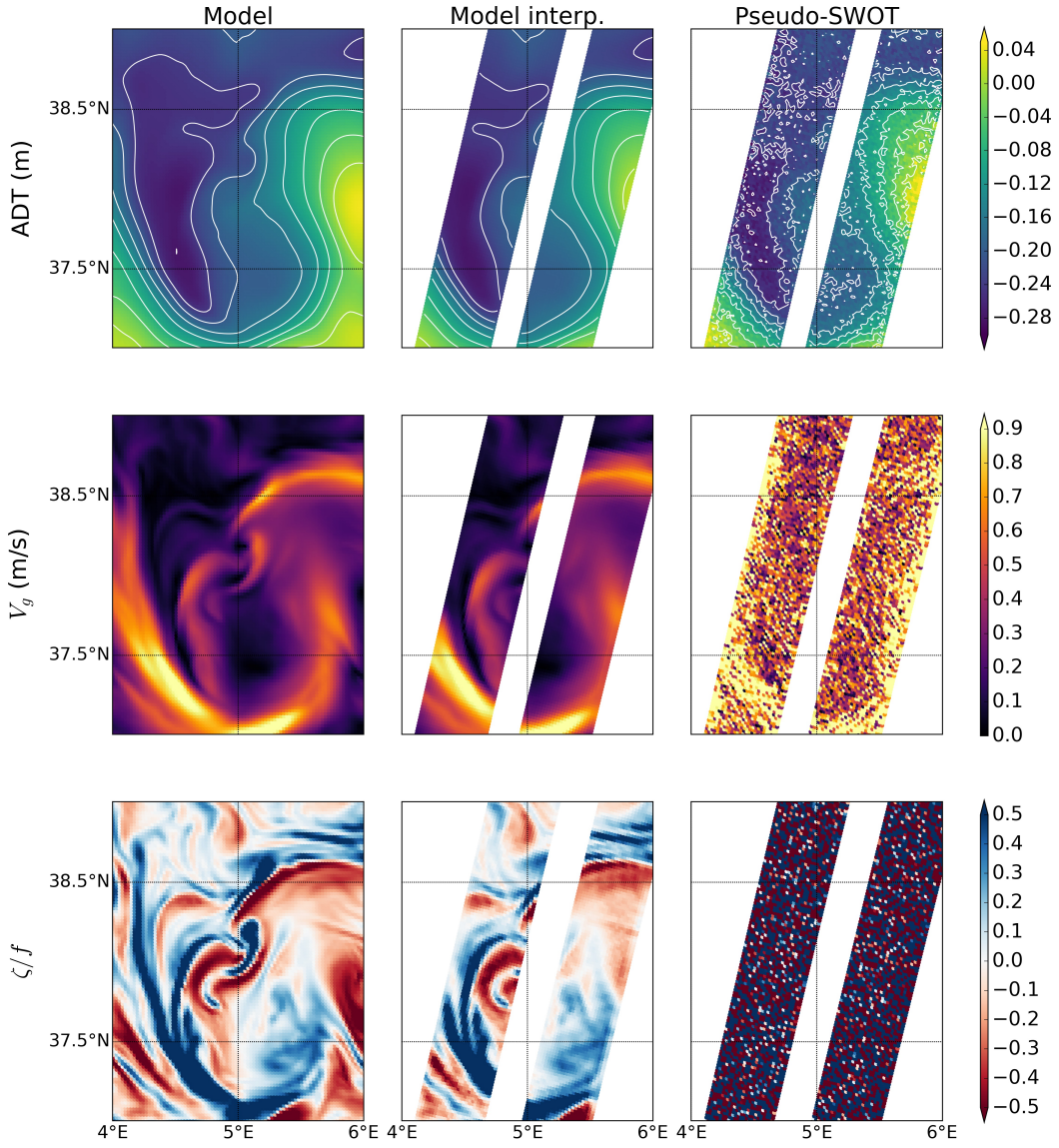

Figure 3.4: From top to bottom: SSH (m), geostrophic velocity (m/s) and relative vorticity (ζ) normalized by f, on 23 January 2009 corresponding to pass 15 of cycle 2 (box 1). The first, middle and last columns show the data obtained directly from the model (WMOP), from the model interpolated onto the SWOT grid (SSH_{model}), and with added noise (SSH_{obs}), respectively.

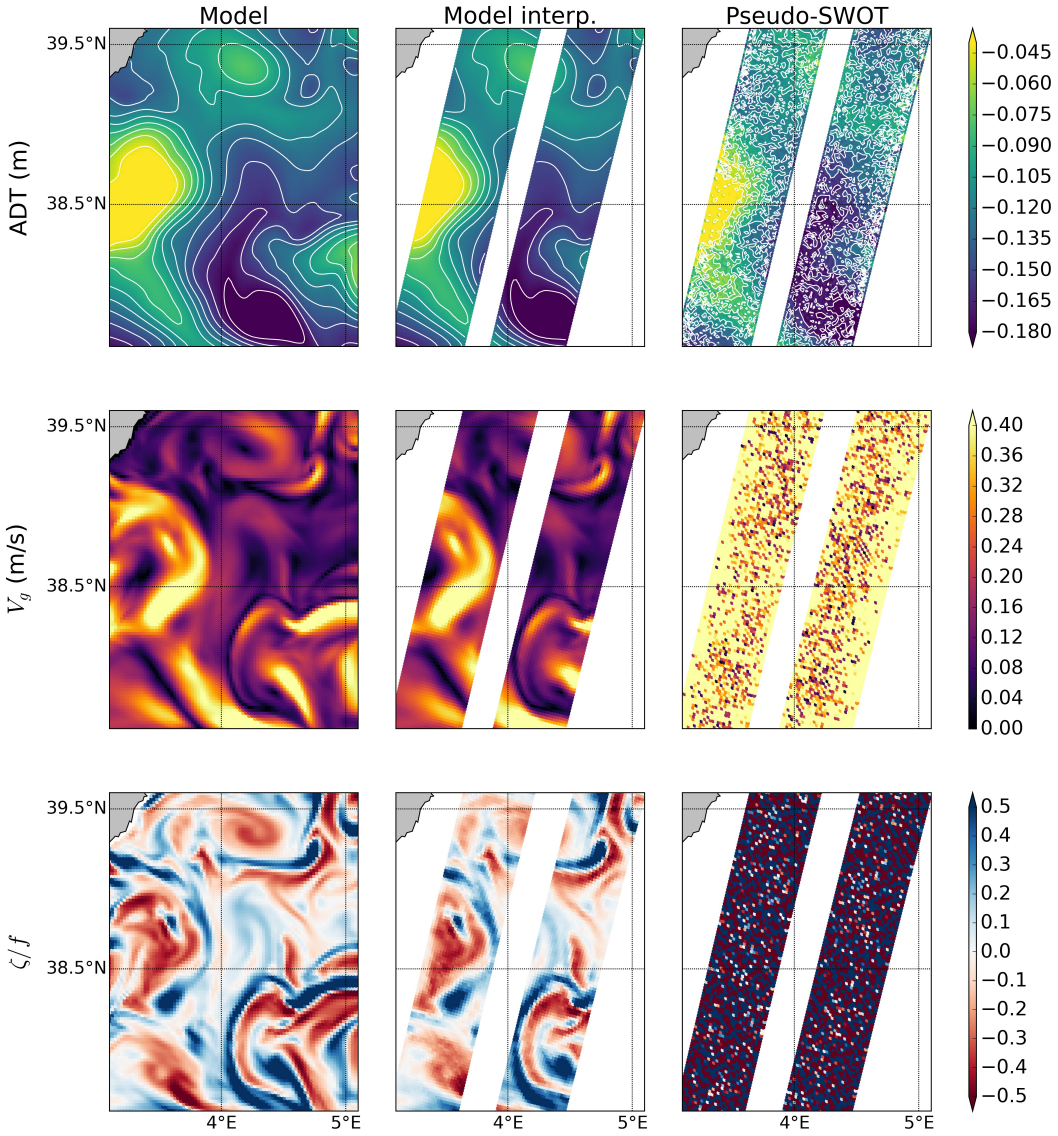

Figure 3.5: From top to bottom: SSH (m), geostrophic velocity (m/s) and relative vorticity (ζ) normalized by f, on 3 February 2009 corresponding to pass 168 of cycle 2 (box 2). The first, middle and last columns show the data obtained directly from the model (WMOP), from the model interpolated onto the SWOT grid (SSH_{model}), and with added noise (SSH_{obs}), respectively.

As observed in the first and middle columns (model and model interpolated onto SWOT grid data, respectively) of Figures 3.4 and 3.5, SSH and its derived variables reveal fine-scale features, but the noise level masks the signal of these features when derived variables are obtained from pseudo-SWOT SSH. We can also see how the effect of the noise is lower in regions with high SSH gradients. If we compare the velocity derived from pseudo-SWOT data of box 1 and 2, for box 1, the region with high values can still be appreciated as they reach 0.9 m/s, but not for box 2 as they only reach 0.4 m/s.

To have information on the spatial scales resolved and the effect of the noise, spatial Fourier power spectra for each filter were calculated as described in Section 3.2.3.2. The spectra were calculated for each individual cycle, and then averaged over the 122 cycles in which both passes 15 and 168 are available (cycle 123 stops at pass 132). Figure 3.6 compares the spectra of model data interpolated onto the SWOT grid and the pseudo-SWOT data. The SWOT noise starts to dominate at wavelengths lower than 60 km. In the top panel of Figure 3.6, the red and blue curves separate at around 60 km for both boxes. If we look at the zoom inset, we see that for pass 15 the lines separate at slightly higher wavelengths than for pass 168.

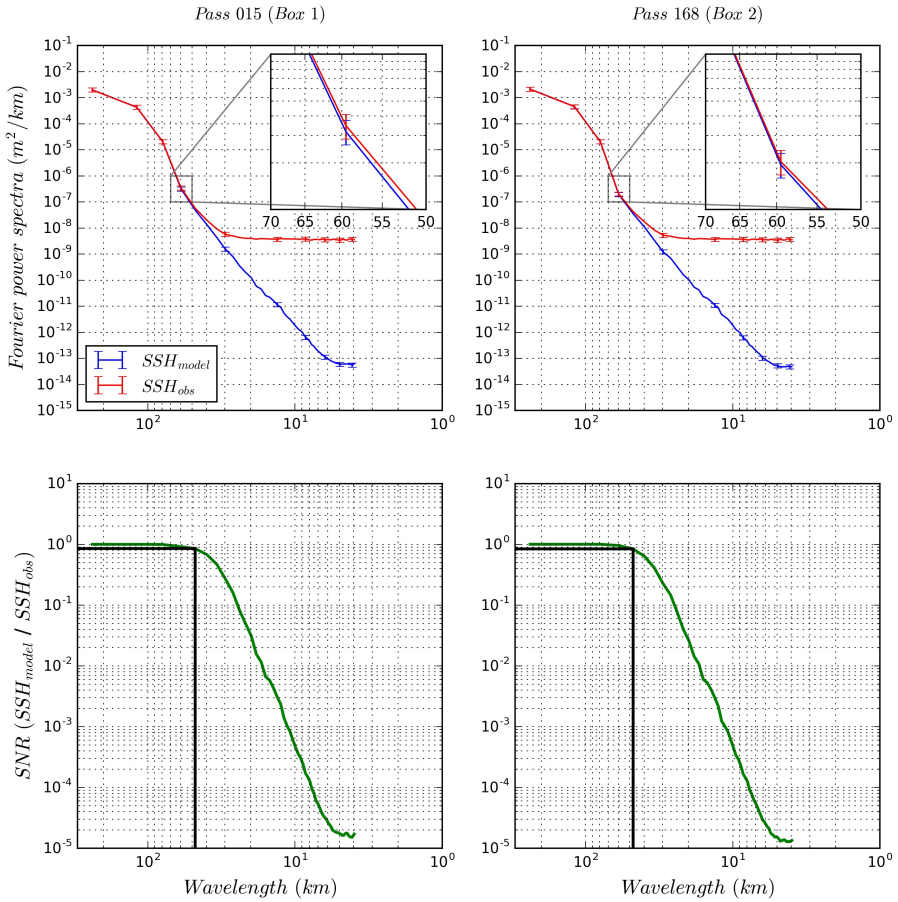

Figure 3.6: **Top:** Spectra of the data before filtering, from cycle 1 to 122, corresponding to box 1 (pass 15), **left**, and to box 2 (pass 168), **right**. Error bars denote 95% confidence intervals. **Bottom:** Corresponding Signal to Noise Ratio (SNR), with a horizontal black line indicating where the noise is more than 15% of the signal, and the vertical line the corresponding wavelength.

Nevertheless, there does not seem to be a significant difference between the mean spectra of both passes. Note also how the power spectral energy level of SSH_{obs} at wavelengths lower than 20 km stabilizes around 3.7×10^{-9} for both passes, whilst the energy level of SSH_{model} reduces until it reaches the grid scale. If we look at the signal to noise ratio (SNR), we find that below 50 km wavelength the energy of the noise is significant with respect to that of the signal (SNR values below 15 dB at wavelengths smaller than 47.6 km, i.e., the energy of the noise accounts for more than 15% of the energy of the signal for these scales). Such low SNR values make particularly challenging the denoising issue for scales below 50 km *Gunturk and Li* (2012). Consequently, we expect that the best filter parametrization will be one corresponding to λ_c between 47.6 and 60 km.

3.3.3 SWOT Data Filtering

The Laplacian diffusion filter was applied to remove the noise and, thus, reduce the difference between the spectrum obtained from SWOT estimates with and without noise (Figure 3.6). Given the results obtained from the non-filtered data spectra, λ_c is first chosen to be 60 km. We then choose smaller $\lambda_c s$ (50, 40, 30 and 15 km) to see how much lower we can go with this filter. We go down to 15 km, which is the expected wavelength at which SWOT will measure SSH. For comparison, we also choose λ_c = 200 km, which is the wavelength resolved by present-day altimeter constellation fields *Chelton et al.* (2007). We lastly choose λ_c = 100 km as an intermediate value between 60 and 200 km.

In Figures 3.7 and 3.8, we show the effect of the filter on SSH at different values of $\lambda_c s$. For Figure 3.7, the effect of the filter is mainly seen in the pseudo-SWOT data, especially in the northern part where smaller

structures are present. In Figure 3.8, as there are more, smaller structures, we can see more differences between the filtered outputs with respect to the model interpolated and pseudo-SWOT data. These differences are not only in the shape of the structures that are present, but also in their intensity. On the top row of Figures 3.7 and 3.8, the original model is also included to show that differences do also arise from the interpolation onto the SWOT grid. In Figure 3.7, especially for the 200 km λ_c, we can observe that the original structure present is significantly altered. This emphasizes the importance for development of interpolation techniques to fill the gap between the two swaths with the help of the nadir altimeter data. In Figures 3.7 and 3.8, the SSH images for the different filters look very similar, but the differences are amplified when the first derivatives (Figures 3.9 and 3.10) and second derivatives (Figures 3.11 and 3.12) are calculated.

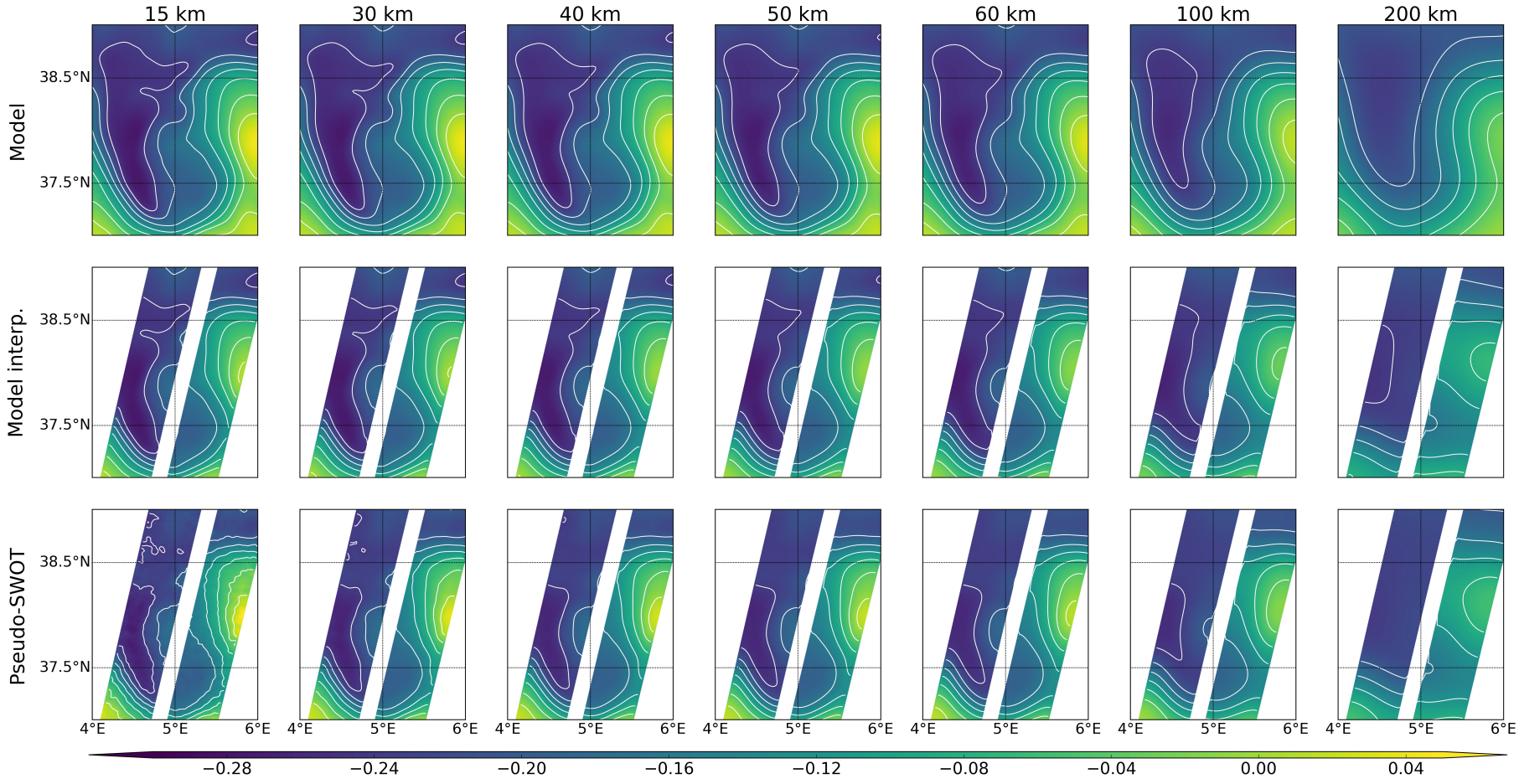

Figure 3.7: SSH (m) on 23 January 2009 corresponding to pass 15 of cycle 2.

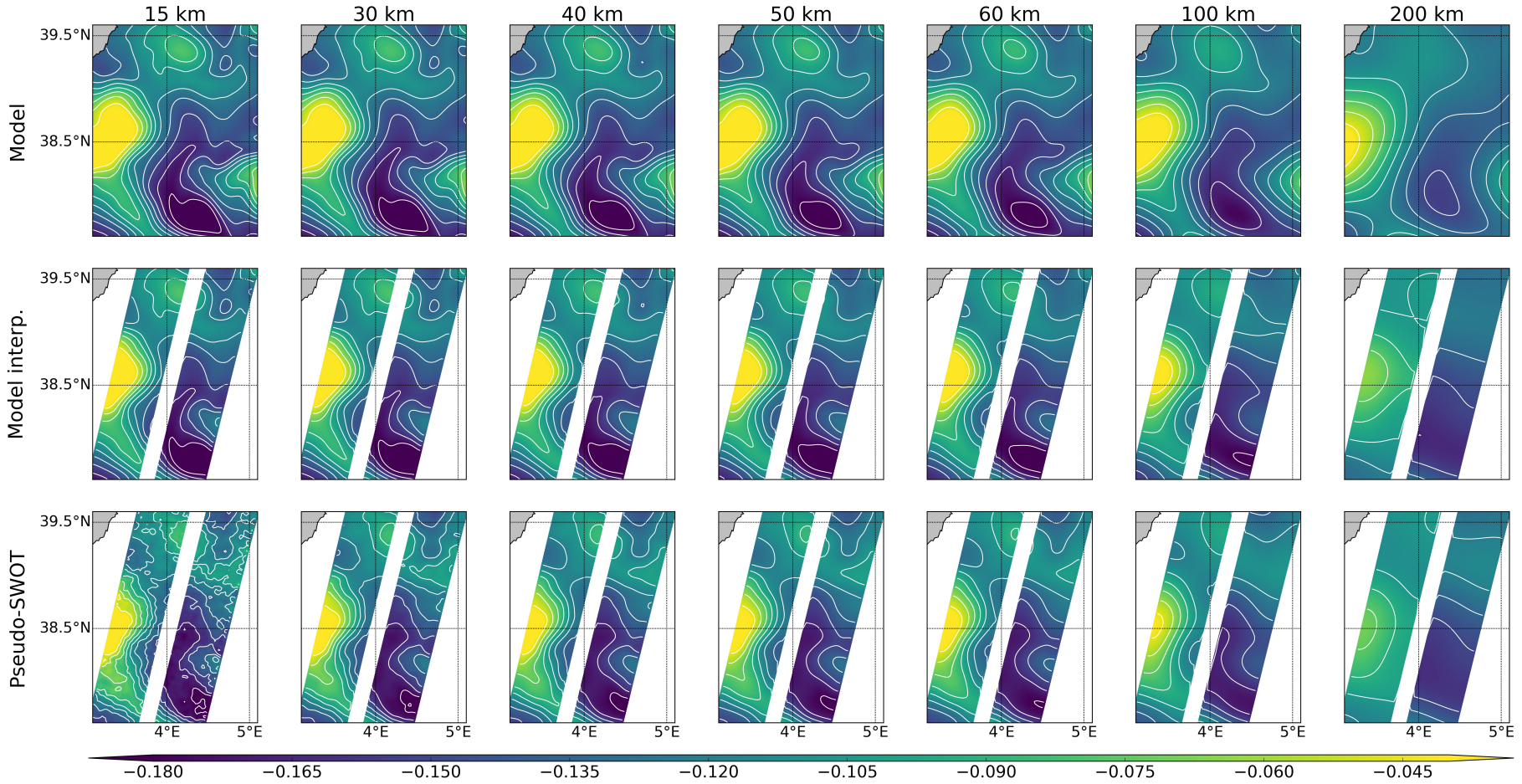

Figure 3.8: SSH (m) on 3 February 2009 corresponding to pass 168 of cycle 2.

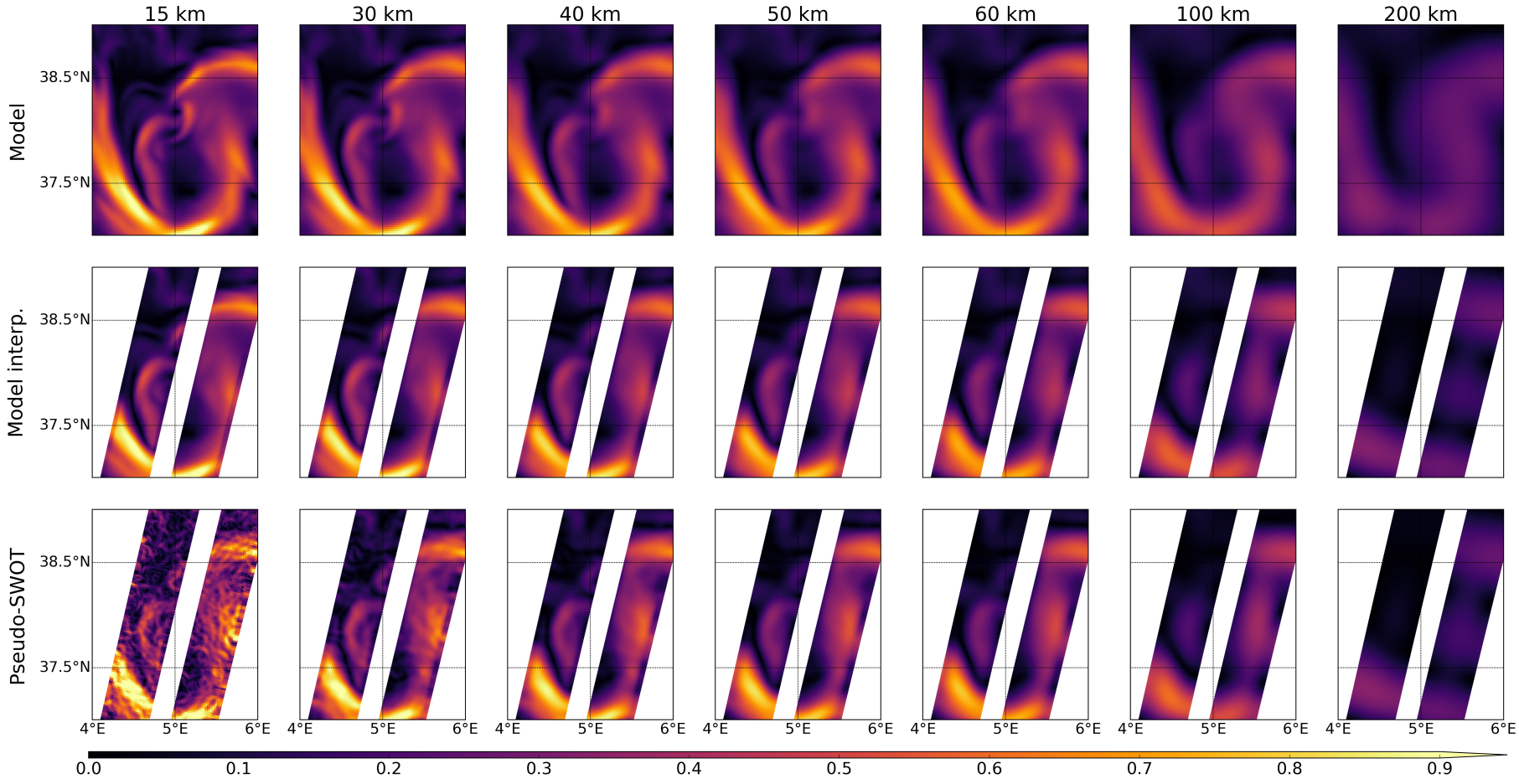

Figure 3.9: Absolute geostrophic velocity (m/s) on 23 January 2009 corresponding to pass 15 of cycle 2.

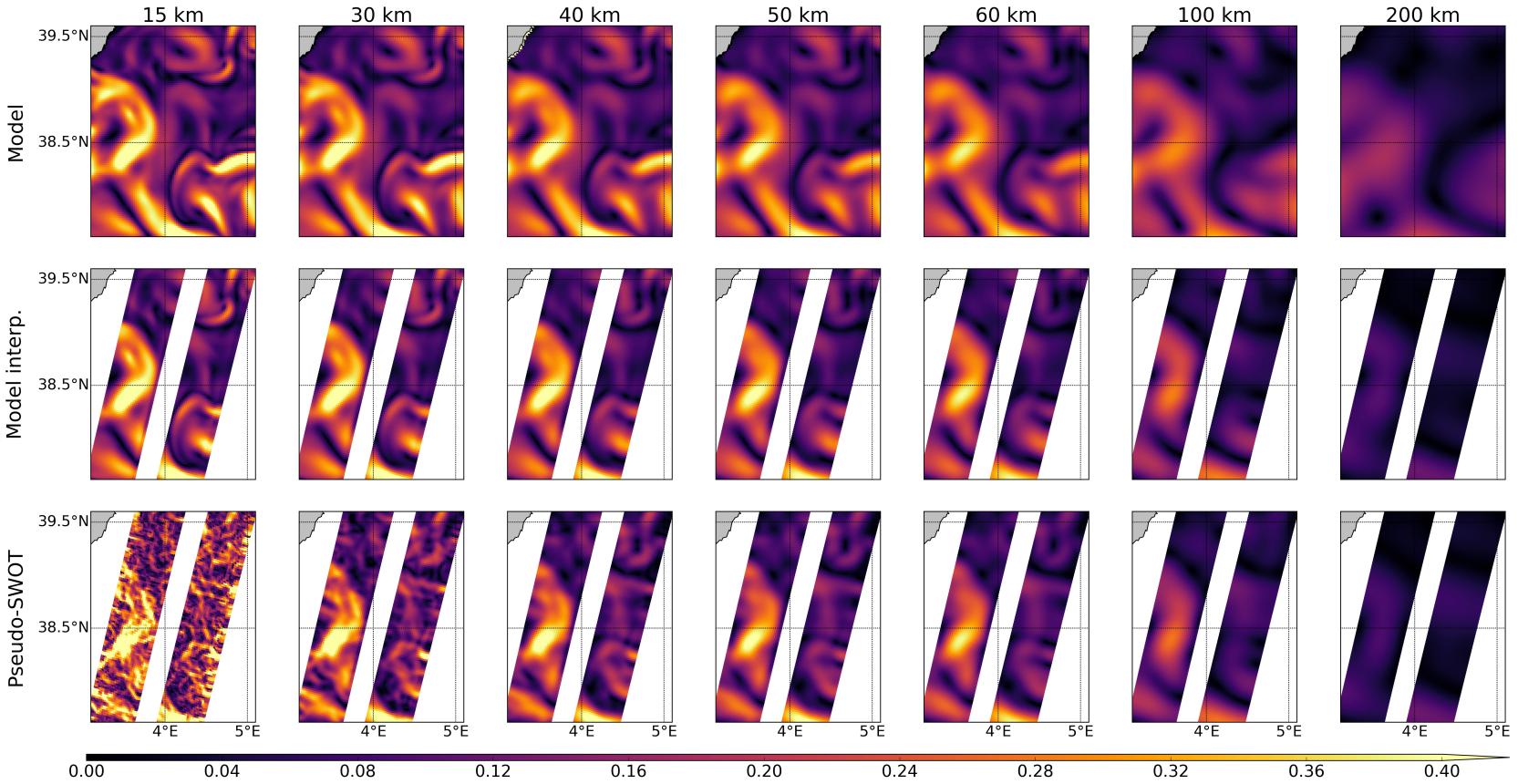

Figure 3.10: Absolute geostrophic velocity (m/s) on 3 February 2009 corresponding to pass 168 of cycle 2.

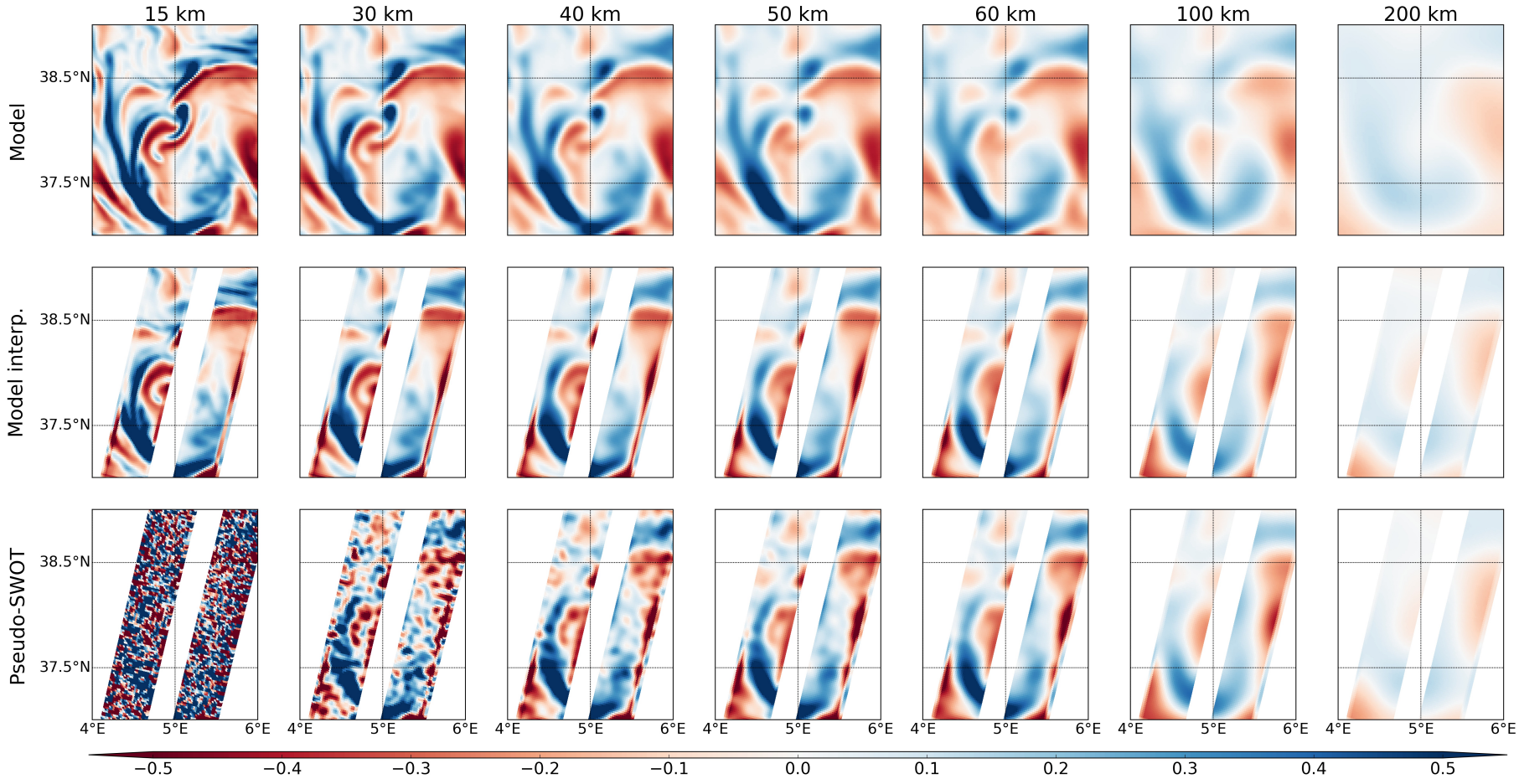

Figure 3.11: Relative vorticity normalized by f on 23 January 2009 corresponding to pass 15 of cycle 2.

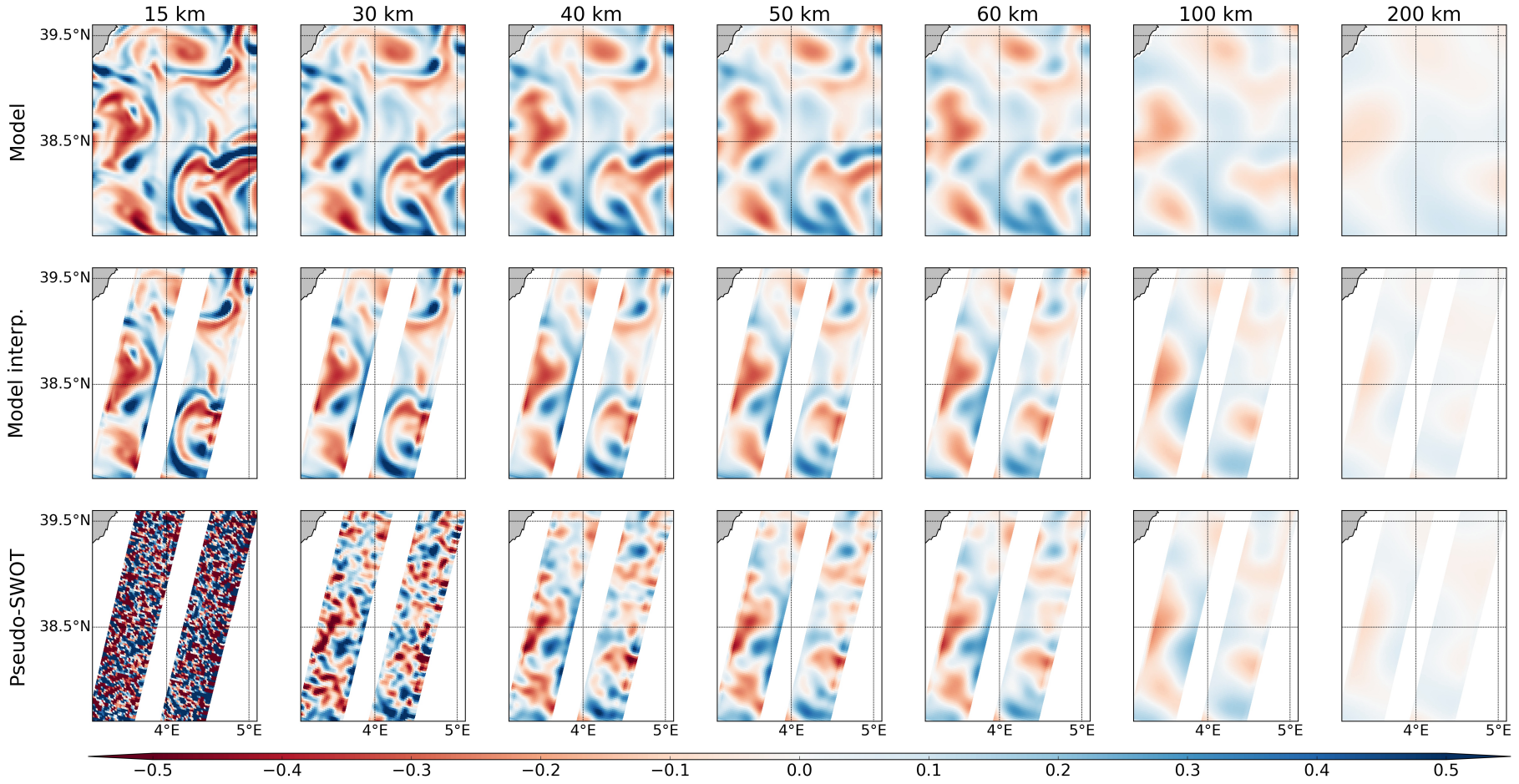

Figure 3.12: Relative vorticity normalized by f on 3 February 2009 corresponding to pass 168 of cycle 2.

After applying the Laplacian diffusion filter, we can now retrieve the structures present in the pseudo-SWOT SSH in the absolute geostrophic velocity plots (Figures 3.9 and 3.10). With a 15 km λ_c filter, the effect of the noise can be still clearly observed, especially for box 2 where smaller structures are present. As a result, although the main structures are recovered after filtering, their shapes are not accurately retrieved. Even if spurious structures remain, with a 30 km λ_c there is a large improvement with respect to the 15 km λ_c. This improvement seems greater for box 1 than box 2, as the noise seems to have a greater effect within box 2 than box 1. For a 40 km λ_c, in box 1, we can no longer qualitatively see any remaining noise, but we can see some in box 2. For $\lambda_c s$ greater than or equal to 50 km, the effect of the noise is no longer observed in either box 1 (Figure 3.9) or box 2 (Figure 3.10). On the other hand, we observe a large decrease of the magnitude of the velocities from the 15 to the 200 km λ_c. With this filtering method, the intensity of the structures present, and thus the signal, decreases with the increase of λ_c.

In the relative vorticity plots, the loss of signal with the increase of λ_c is even more evident. With no filtering, the relative vorticity of box 1 ranges from -1.82f to 1.66f for SSH_{model} and from -15.22f to 18.16f for SSH_{obs} (Figure 3.4). With a 200 km λ_c, this reduces to -0.23f to 0.14f for both SSH_{model} and SSH_{obs} (Figure 3.11). For box 2, with no filtering, the relative vorticity ranges from -0.71f to 1.50f for SSH_{model} and from -17.39f to 17.71f for SSH_{obs} (Figure 3.5). For 200 km, it reduces to-0.07f to 0.10f for SSH_{model} and from -0.09f to 0.06f for SSH_{obs} (Figure 3.12). There is approximately two orders of magnitude difference between the vorticity calculated from the original data, and that filtered at $\lambda_c = 200$ km. For box 1, the velocity appears to contain no further noise with $\lambda_c = 40$ km, but this filtering is not sufficient to properly reconstruct the relative vorticity. With a 50 km λ_c, some noise is still present, and with 60 km λ_c, there appears to be no remaining noise. For box 2, the velocity appears to have no further noise with a 50 km λ_c, and, similarly to box 1, we use a 60 km λ_c to qualitatively remove remaining noise in the relative vorticity plots. The relative vorticity fields present unrealistic small-scale structures at larger $\lambda_c s$ values than SSH and velocity. This is expected as the noise effects increase as higher order derivatives are reached. Nevertheless, the larger structures present in the images are recovered from the non-filtered image with a 60 km λ_c filter for both box 1 and 2. Not as much signal is lost with a 60 as with a 200 km λ_c, but some is still lost. For the mesoscale, given the relative vorticity and structures observed in Figures 3.11 and 3.12, this does not seem to have a large impact. However, there may be an impact when wanting to observe finer scales as we retrieve normalized relative vorticity much lower than 1.

Spectra were computed for $\lambda_c s$ of 30, 60 and 200 km to visualize these effects. The corresponding SNR is also calculated in two different ways by using two references. One is by dividing the filtered model-interpolated data by the filtered pseudo-SWOT data, and the other by dividing the non-filtered model-interpolated data by the filtered pseudo-SWOT data. This is shown in Figures 3.13 and 3.14.

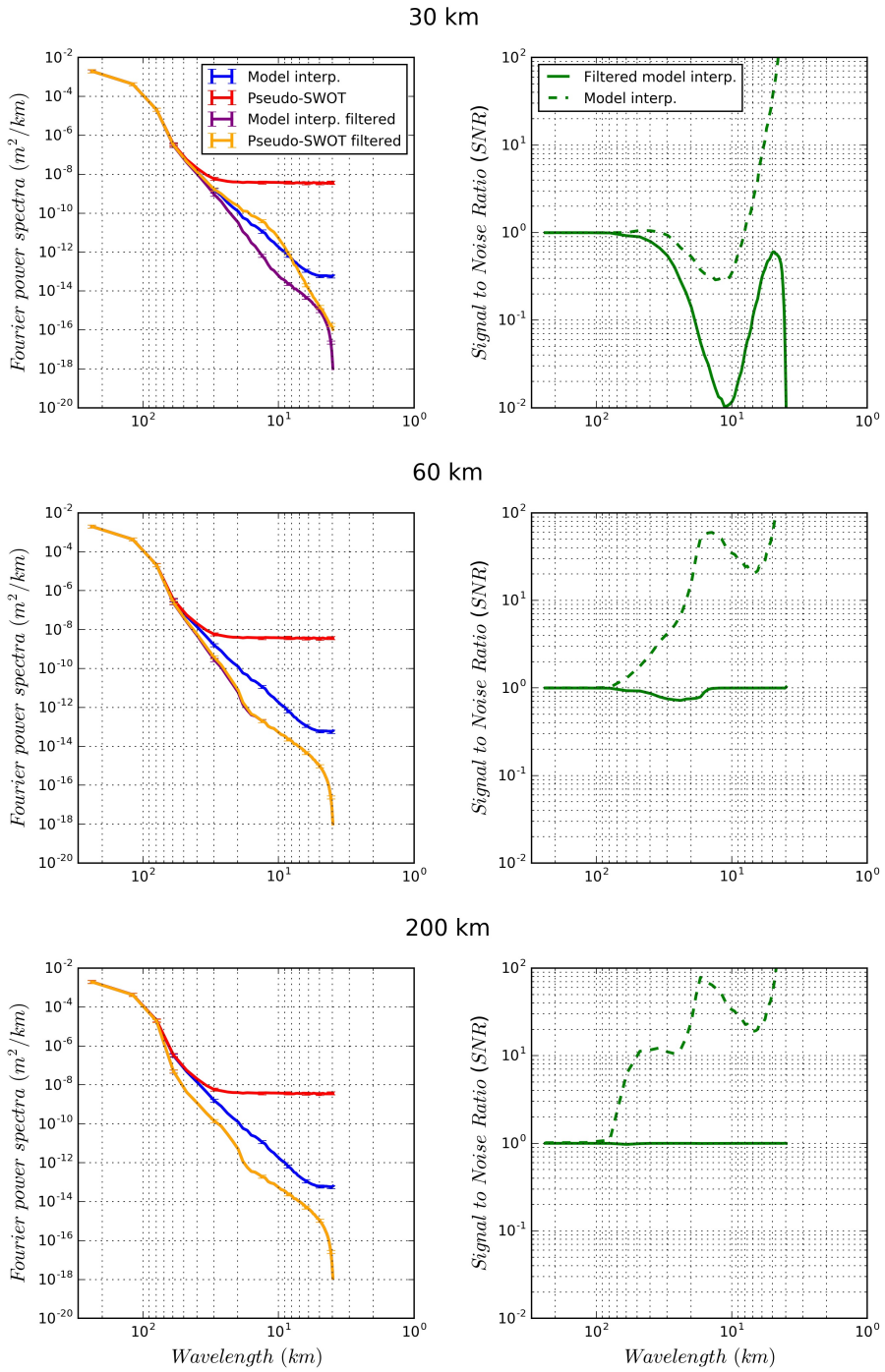

Figure 3.13: Box 1 region (pass 15) mean of cycles 1 to 122. **Left:** Spectra of SSH_{model} (blue) and SSH_{obs} (red) before filtering and after applying the different cut-off wavelengths shown in the different rows (30, 60 and 200 km) in purple and orange, respectively. Error bars denote 95% confidence intervals. **Right:** SNR of SSH_{model} and SSH_{obs}, both filtered (solid line) and of SSH_{model} non-filtered and filtered SSH_{obs} (dashed line).

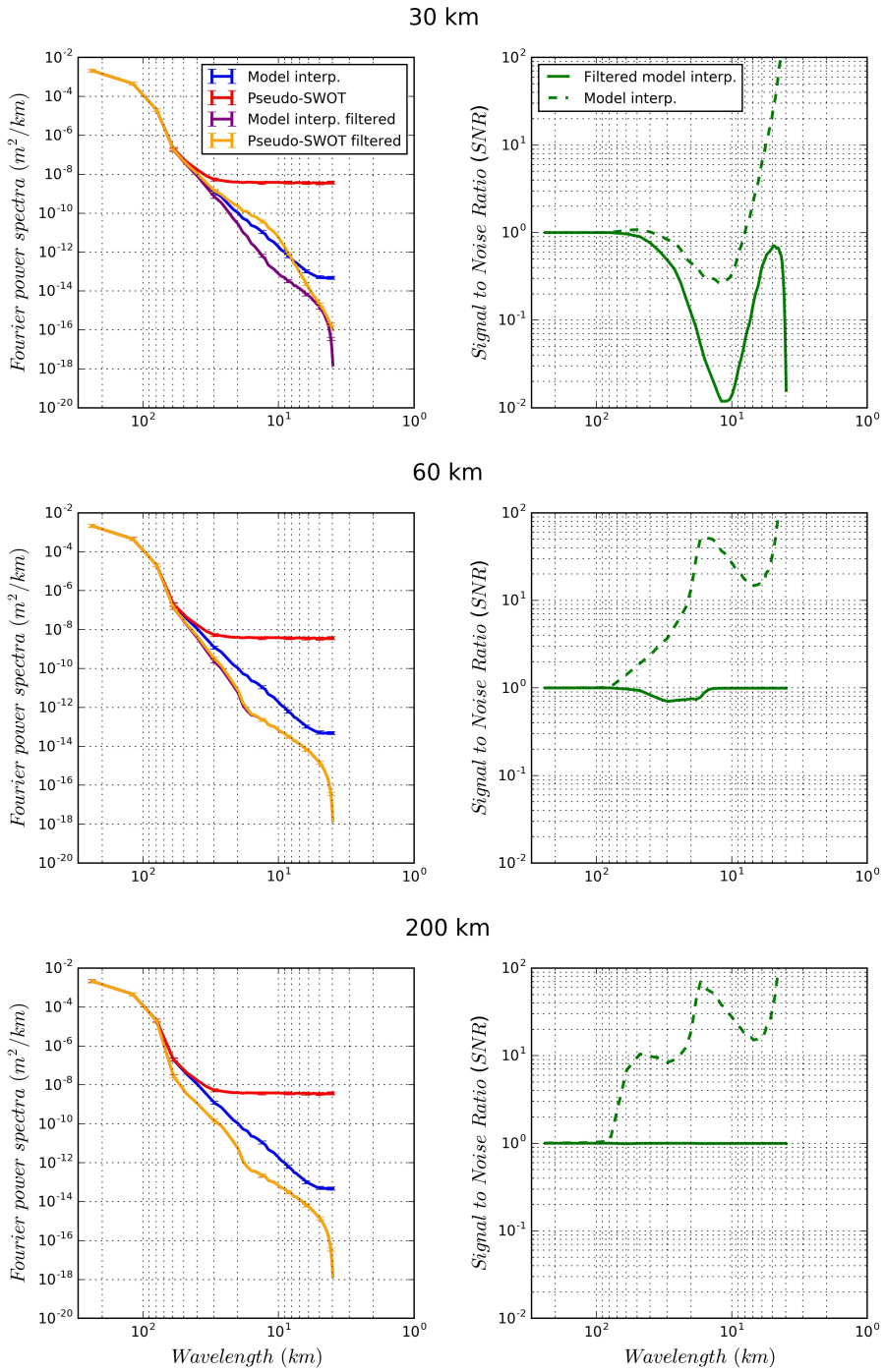

Figure 3.14: Box 2 region (pass 168) mean of cycles 1 to 122. **Left:** Spectra of SSH_{model} (blue) and SSH_{obs} (red) before filtering and after applying the different cut-off wavelengths shown in the different rows (30, 60 and 200 km) in purple and orange, respectively. Error bars denote 95% confidence intervals. **Right:** SNR of SSH_{model} and SSH_{obs}, both filtered (solid line) and of SSH_{model} non-filtered and filtered SSH_{obs} (dashed line).

As a consequence of the application of the filter, the separation of the spectral curves of SSH_{model} (model-interp.) and SSH_{obs} (pseudo-SWOT) is reduced. As seen in Figure 3.6, with no filter, the model-interp. (blue) and pseudo-SWOT (red) curves separate at a wavelength around 60 km. With a 30 km λ_c, the noise level is still high, as observed in Figures 3.7 to 3.12, but the power spectra difference at wavelengths smaller than 60 km between the pseudo-SWOT filtered (yellow) and the model-interp. (blue) curves is much smaller than it is between the model-interp (blue) and pseudo-SWOT (red) curves (top left panel of Figures 3.13 and

3.14). Moreover, the pseudo-SWOT filtered and the model-interp. curves separate at smaller wavelengths. If we look at the dashed line of the top right panel of Figures 3.13 and 3.14, we can more accurately determine this wavelength separation value by looking at where the dashed curve starts decreasing. This corresponds to 30 and 40 km wavelengths for box 1 and 2, respectively. Between wavelengths of 60 and 30 km (40 for box 2), the SNR (dashed line) is greater than 1, indicating some over-filtering/smoothing, but this value is very low (1.064 for box 1 and 1.088 for box 2). The pattern of the SNR of the filtered model-interp. over the filtered pseudo-SWOT data (solid line of top right panel of Figures 3.13 and 3.14) is similar to that of Figure 3.6. The noise gains importance as the wavelengths reduce from 60 km, but the SNR values of the 30 km λ_c are lower than the non-filtered ones. On the other hand, this indicates that, given that the filtered model-interp. and pseudo-SWOT spectra are still quite different, a larger λ_c is necessary. In both the left and right panels of the 30 km λ_c of Figures 3.13 and 3.14, anomalous patterns are observed below the 10 km wavelength. Not only are these spatial scales very small, but, if we look at the spectra values, they are about 10^{-12} m^2/km or lower. We consider these values to be too low for discussion.

With a 60 km λ_c, the noise is further reduced, but we lose more signal too. If we look at the continuous line of the right panel of Figures 3.13 and 3.14, we see that it remains approximately constant at 1. For box 1, it reaches a minimum SNR of 0.715 and for box 2 of 0.697. Looking at the dashed line, the SNR becomes larger than 1 at wavelengths lower than 80 km for both boxes. This means that, although we eliminate all the noise, we are also eliminating part of the signal that was initially present. At wavelengths greater than 10 km, the power spectra of the filtered pseudo-SWOT reach a maximum difference nearly two orders of magnitude smaller than the original model-interp. spectra.

Lastly, with a 200 km λ_c filtering, the model-interp. and pseudo-SWOT spectra curves are identical, and the SNR (solid line) is approximately 1 (Figures 3.13 and 3.14, bottom row): however, as observed in Figures 3.7 to 3.12, we lose a lot of signal. In the 20–80 km wavelength range, we can see how the SNR curves (dashed line) rapidly increase and the values are greater with a 200 km λ_c than with a 60 km λ_c. At wavelengths lower than 80 km, on average, there is about one order of magnitude difference between the filtered spectra and the original SSH_{model}. It is also interesting to note that the purple and yellow curves separate from the red and blue at 80 km instead of 60, showing that this cut-off exceeds that necessary to remove the noise. This also emphasizes how with SWOT a major advancement could be made as lower cut-off wavelengths will be possible, and thus the observation of smaller scale structures than with contemporary satellites. On the one hand, this result is expected thanks to the 2D swath instead of only 1D nadir data, but, on the other hand, it is important to remember that these are simulated from expected errors and that not all errors are implemented (see Appendix 3.B).

To further quantify the differences observed between the different $\lambda_c s$ in Figures 3.7 to 3.12, the RMSE between the interpolated model and pseudo-SWOT data shown in these Figures were calculated as described in Section 3.2.3.3.

In Figure 3.15, it is interesting to focus on the minimum points of the RMSE curves. Looking at the λ_c corresponding to the different minimum points, for both boxes, the minimum of the curve for SSH and the absolute geostrophic velocity (Vg) is found for a 30 km (29) λ_c. It is slightly higher, 40 km (41), for relative vorticity. This directly relates to the amplification of fine-scale structures, and thus the effect of the noise, in the computation of second-order derivatives. It is also in accordance with what is found in the SNR in Figure 3.6, which shows that we cannot recover the signal at wavelengths lower than 40–50 km. With the qualitative (Figures 3.7 to 3.12) and the spectra (Figures 3.13 and 3.14) plots, we saw that, for box 2, as the signal is lower than in box 1, the effect of the noise is greater, and larger $\lambda_c s$ are necessary. The RMSE plots show us another point of view. As the signal is not as intense in box 2 as in box 1, the over-smoothing (signal lost) due to the Laplacian diffusion filter is lower, and thus we observe lower RMSE values in Figure 3.15. Moreover, the improvement of the RMSE values is greater for box 2 than box 1. For SSH, the RMSE reduces by 0.05 and 0.07 m from the no filter (0 λ_c) to the minimum RMSE, for box 1 and box 2, respectively. For Vg, the RMSE reduces by 0.42 and 0.455 m/s, and for ζ/f by 3.2 and 3.35.

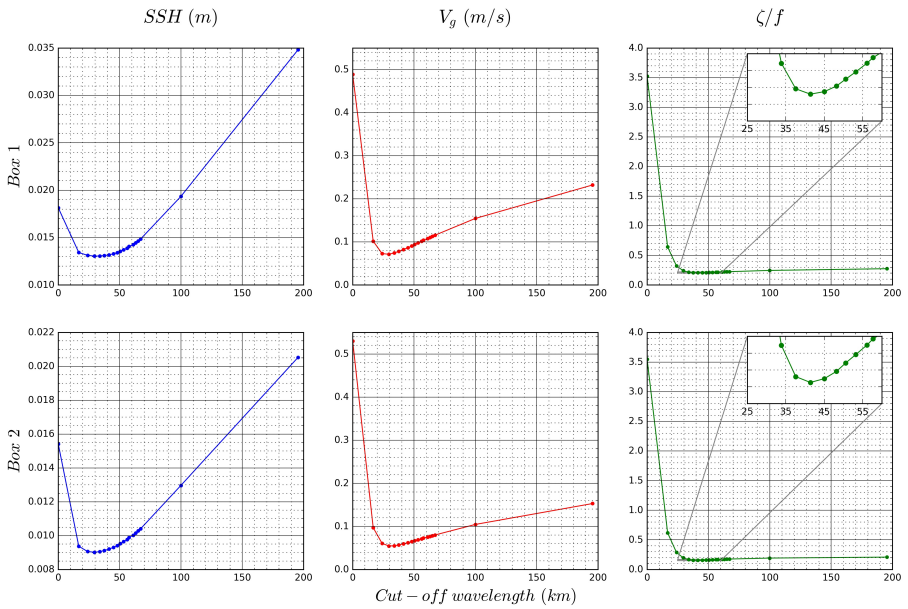

Figure 3.15: RMSEs of the different variables against the filter's cut-off wavelengths applied to SSH, for pass 15 (**top**) and pass 168 (**bottom**) of cycle 2. Insets show zoom of marked region for better observation of the curves' minimum points.

For SSH, we could say that with a 40 km λ_c it is sufficient, but if we do not want to see the effect of the noise in vorticity, we need a greater λ_c of 60 km. Therefore, together with what is observed in Figures 3.4–3.15, we consider that, with this filtering technique applied to this region, SWOT will be able to resolve wavelengths down to a 40 – 60 km wavelength range. This is the λ_c range where we found that there is a compromise between filtering out the noise of SSH and its derived variables (Vg and ζ/f), and over-smoothing the original image as little as possible. It is important to note that λ_c depends on the signal-to-noise ratio between SSH signals and instrument noise at fine scales. As such, it can be expected to change from region to region (and from season to season) depending on the energy levels at fine scales and on the noise level.

3.4 Discussion

We find that, by applying our filtering technique to pseudo-SWOT data in the western Mediterranean region, we cannot reach the 15 km wavelength argued for by *Fu and Ubelmann* (2014). We are however able to recover the signal within a swath down to wavelengths of 40 – 60 km. This wavelength range is close to the one found by *Dufau et al.* (2016) at the western boundary currents and nearly half the wavelength values found at the eastern basins by 1D altimeter data. In addition, with the characteristic of SWOT providing 2D SSH data, this will imply a large improvement on the 200 km wavelength resolved by present-day gridded altimetric fields (*Chelton et al.*, 2007). The SWOT resolved wavelengths found will make it possible to detect structures of 20-30 km in diameter (following *Klein et al.* (2015)) and therefore opens the possibility for observation of fine scales that are unobservable by contemporary altimetric products. This filter is a useful tool for studies comparing the capacities of pseudo-SWOT data with the present altimetric satellite constellation data. As this filter is particularly effective in removing the spatially uncorrelated KaRIn noise, it may allow the application of already developed techniques that more effectively remove other correlated errors (*Ruggiero et al.*, 2016).

We find that the presence of structures of different scales and regimes governing—for example, the mesoscale (Ro. order(0.1)) or submesoscale (Ro. order(1)) affects our results on the efficiency of the Laplacian diffusion filter. This filter is therefore sensitive to the presence of different patterns, depending on the region. To reach even smaller scales, it is important to use filtering techniques that conserve and/or retrieve the gradients and, thus, the intensity of the signal present in the observed field. Nonetheless, this sensitivity of the Laplacian

diffusion filter could also be due to the effects of noise, depending on the structure in question and its intensity. We also note that the differences between box 1 and 2 found in, for example, the qualitative plots (Figures 3.7–3.12) and the minimum RMSE values were not very large; this is not surprising when considering how close in time the two snapshots are.

With this improvement of individual swaths, gridded and possibly daily SWOT SSH maps could be obtained through different interpolation and/or reconstruction techniques. Current gridded altimetric products are obtained using optimal interpolation (OI) (*Pujol et al.*, 2016). OI may not be the best interpolation method. OI exploits a covariance model of the field to be interpolated. The specification of this covariance model typically relies on a trade-off between the space-time size of the missing data areas and the space-time scales of interest. A covariance model with a large correlation length may lead to an over-smoothing of fine-scale structures, whereas shorter correlation lengths result in filling large missing areas with the background field. From a computational point of view, OI requires a matrix inversion, whose complexity evolves as the cube of the number of observation points. The image-like structure of SWOT data may then be highly computationally-demanding when considering large correlation lengths to fill in large missing areas. Multi-scale OI may be an alternative. However, we expect dynamical interpolation and other data assimilation methods (*Ubelmann et al.*, 2015; *Lguensat et al.*, 2019; *Fablet et al.*, 2018) to be more adapted both in terms of computational complexity and in their ability to embed relevant dynamic priors to reconstruct horizontal scales down to a few tens of kilometres from SWOT data. On the other hand, SWOT data will greatly improve the present-day OI altimetric products (*Pujol et al.*, 2012). In addition, SWOT gridded data could be improved in the 40 – 60 km wavelength range by combining it with the data of a higher temporal resolution.

Dynamic interpolation is an example of a technique that has been investigated by *Ubelmann et al.* (2015) that could help to obtain gridded, daily SSH maps from SWOT. When they apply this method to the Gulf Stream region, they recover the SSH field down to 80 km wavelength. Data-driven schemes recently introduced by *Fablet et al.* (2018); *Lguensat et al.* (2019) are also of interest to better reconstruct horizontal scales below 100 km. Overall, for such approaches, it is important to recover the lowest wavelengths possible as spatial resolution loss is likely when producing the gridded maps. Moreover, this spatial resolution loss might be even higher when addressing gridded maps of derived variables. Therefore, the cut-off wavelength should be adjusted to the variables that are to be studied.

Another reconstruction technique that has been investigated in the context of SWOT is a 3D multivariate reconstruction of ocean state. *Durán-Moro et al.* (2017) do this by combining information from SSH and high resolution image structure observations. Once this is achieved, study of the capacity of SWOT to detect fine-scale structures could be improved by, for example, better characterizing eddies. As the dataset would be of a higher spatial and temporal resolution than the L2 product, it would then be possible to apply eddy-tracking algorithms like the *py-eddy tracker* (*Mason et al.*, 2014) or the code developed by *Conti et al.* (2016), which have already been implemented in this region to characterize the western Mediterranean eddy field. A comparison could then be made with the eddies characterized in data from the WMOP model, in the presently available altimetric data and in pseudo-SWOT data.

In future work, the effect of the inter- and intra-annual (or seasonal) variability in the region on the results obtained could be studied too. Although mean spectra were obtained, we focused on two dates in winter. *d'Ortenzio et al.* (2005); *Houpert et al.* (2015) found that there is a strong winter–summer difference in the upper ocean dynamics due to the change of stratification, with the mixed layer depth being deeper in winter. For example, the reconstruction of mesoscale structures in the upper ocean from pseudo-SWOT data in the Kuroshio Extension region has been studied. They found that the simulated and reconstructed vorticity correlation coefficients varied both inter- and intra-annually. (*Qiu et al.*, 2016)

The implementation of filtering techniques that take into account the first and second order SSH derivatives has been started. With this, we hope that in future studies we will be able to recover even smaller wavelengths and to conserve the intensity of the signal after having applied the filter.

New versions of the SWOT simulator will allow the simulation of pseudo-SWOT data during the fast-sampling phase. This makes it possible to start preparing for the calibration/validation phase including the comparison with high resolution in situ data collected during future intensive multi-platform experiments in the western Mediterranean Sea. On the other hand, the only source of geophysical error implemented in the SWOT simulator is still just that related to the wet troposphere. New releases of the SWOT simulator may include

the effects of sea state and internal tides (*Lindstrom et al.*, 2017). Internal tides and waves are important sources of geophysical errors because, at wavelengths shorter than 50 km, they can affect SWOT data (*Fu and Morrow*, 2016). Therefore, in future work, it would also be interesting to compare our results with an updated version of the SWOT simulator and other OGCMs, especially those that include tides.

3.5 Conclusions

We have generated simulated pseudo-SWOT data for the western Mediterranean Sea using a SWOT simulator and outputs from an ocean numerical model. To evaluate the output SWOT data, we derived absolute geostrophic velocities and relative vorticities from the pseudo-SWOT SSH data. We find that, due to the satellite's instrumental noise and geophysical errors, the features observed in the pseudo-SWOT SSH are lost in the derived dynamical variables. Looking at the spatial spectra, we find that noise dominates the signal at wavelengths smaller than 60 km. We applied a Laplacian diffusion filtering technique to attempt to remove the noise and hence observe finer scales. We estimated the appropriate cut-off wavelength for each parametrization. To filter out the noise, we applied a series of ascending cut-off wavelengths: 15, 30, 40, 50, 60, 100 and 200 km. We find that in this study region, using this technique, we cannot resolve the expected 15 km wavelength. On the other hand, we are able to recover the signal within a swath down to a 40 – 60 km wavelength range. This is still an improvement in comparison to wavelengths resolved by present-day 1D altimeters, especially at eastern basins. Robust swath-filtering is an important first step towards meeting our goals for reconstruction techniques that will enable us to combine SWOT and altimetric data in order to produce gridded SSH maps of significantly higher resolution than contemporary products. New versions of the SWOT simulator code include improved representation of instrumental and geophysical errors, and also give us the option to obtain pseudo-data for the SWOT fast-sampling phase. New pseudo-SWOT data will allow us to better refine the results of this study and to examine a wider range of scenarios.

3.A Appendix A

In order to know which number of iterations and lambda to set in the filter's parametrization, the filter was applied to a set of 100 randomly generated white noise fields. Spectra were then obtained and the cut-off wavelength was found by identifying the one that corresponded to where the energy was reduced to a half. An example is shown in Figure A1.

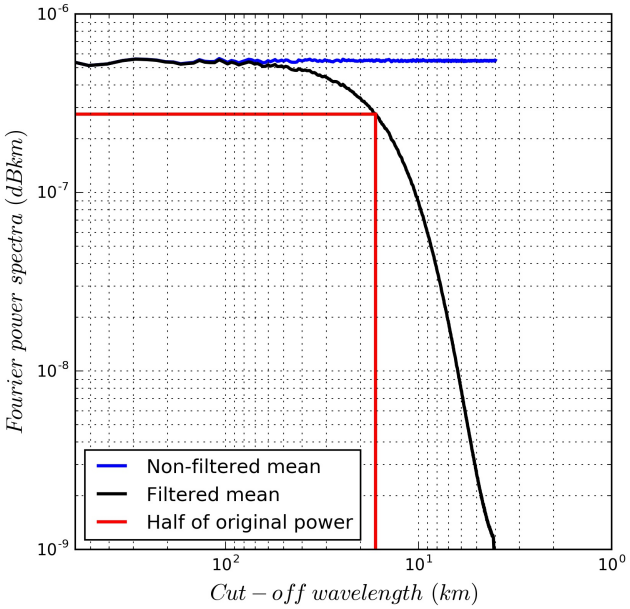

Figure A1: Illustration of how the parameterization corresponding to a 15 (16.72) km cut-off wavelength (λ_c) is estimated. The blue line represents the mean spectra of the 100 non-filtered white noise fields. The black line is the mean spectra of the 100 filtered white noise fields. The horizontal red line shows the half-power spectra of the blue line, and the vertical red line the corresponding wavelength value of the black line, and thus the cut-off wavelength.

In Table 3.1, we show the different λ_c obtained for a set of lambdas and number of iterations and in Figure A2 a plot of the values shown in Table 3.1 is presented. As can be observed in Table 3.1, in most cases, several combinations of lambdas and iterations can give the same cut-off wavelength. We decided to choose the combination corresponding to the smallest lambda, as the smaller the lambda, the smaller the over-smoothing.

Table 3.1: Cut-off wavelengths (λ_c) values and their corresponding lambda and number of iterations (iter) combinations. The cut-off wavelengths shown in Figures 3.7–3.12 are in bold.

Cut-off	**Lambda**	**Iter**	**Cut-off**	**Lambda**	**Iter**	**Cut-off**	**Lambda**	**Iter**	**Cut-off**	**Lambda**	**Iter**
16.72	0.05	50	71.88	0.10	450	105.09	0.20	500	141.41	0.35	500
23.95	0.05	100		0.15	300		0.25	400		0.40	450
	0.10	50		0.30	150		0.30	350		0.45	400
29.47	0.05	150		0.45	100		0.35	300		0.50	350
	0.15	50	74.5	0.10	500		0.40	250		0.55	350
33.85	0.05	200		0.20	250		0.50	200		0.60	300
	0.10	100		0.25	200		0.65	150		0.65	300
	0.20	50		0.50	100	110.78	0.25	450		0.70	250
37.58	0.05	250	77.31	0.15	350		0.45	250		0.75	250
	0.25	50		0.35	150		0.55	200	151.91	0.40	500
41.38	0.05	300		0.55	100		0.70	150		0.45	450
	0.10	150	83.63	0.15	400		0.75	150		0.50	400
	0.15	100		0.20	300	117.12	0.25	500		0.55	400
	0.30	50		0.25	250		0.30	400		0.60	350
45.02	0.05	350		0.30	200		0.35	350		0.70	300
	0.35	50		0.40	150		0.40	300		0.80	250
48.19	0.05	400		0.60	100		0.50	250	164.1	0.45	500
	0.10	200	87.19	0.15	450		0.60	200		0.50	450
	0.20	100		0.45	150		0.65	200		0.50	500
	0.40	50		0.65	100		0.80	150		0.55	450
50.58	0.05	450	91.07	0.15	500	124.24	0.30	450		0.60	400
	0.15	150		0.20	350		0.30	500		0.65	350
	0.45	50		0.25	300		0.35	400		0.65	400
53.2	0.05	500		0.30	250		0.40	350		0.70	350
	0.10	250		0.35	200		0.45	300		0.75	300
	0.25	100		0.50	150		0.50	300		0.75	350
	0.50	50		0.70	100		0.55	250		0.80	300
56.12	0.55	50		0.75	100		0.60	250	178.42	0.55	500
57.7	0.10	300	95.31	0.20	400		0.70	200		0.60	450
	0.15	200		0.40	200		0.75	200		0.60	500
	0.20	150		0.55	150	132.27	0.35	450		0.65	450
	0.30	100		0.80	100		0.40	400		0.70	400
	0.60	50	**99.96**	0.20	450		0.45	350		0.70	450
61.15	0.65	50		0.25	350		0.55	300		0.75	400
63.03	0.1	350		0.3	300		0.65	250		0.8	350
	0.35	100		0.35	250		0.80	200		0.80	400
	0.70	50		0.45	200				**195.49**	0.65	500
65.03	0.15	250		0.60	150					0.70	500
	0.25	150								0.75	450
	0.75	50								0.75	500
67.17	0.1	400								0.8	450
	0.20	200								0.8	500
	0.40	100									
	0.80	50									

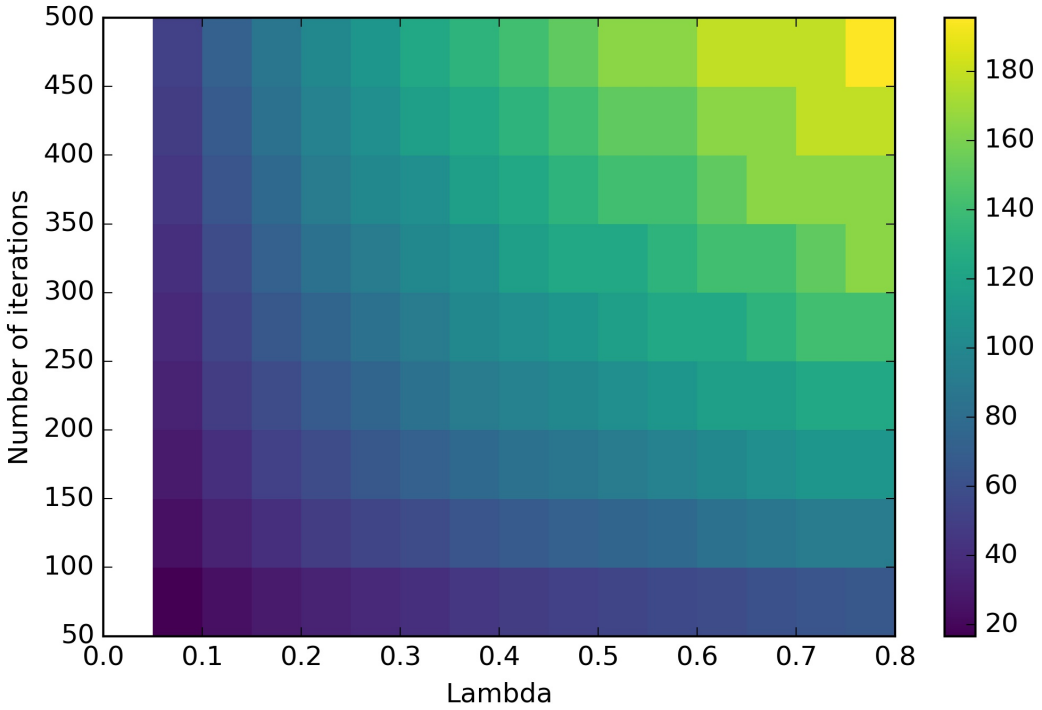

Figure A2: Laplacian diffusion cut-off wavelengths (km) for different combinations of the number of iterations and lambdas.

3.B Appendix B

The noise added by the SWOT simulator can be divided into two types:

- Instrument errors: There are the different types of noise that can affect the signal due to the satellite itself:
  - Ka-Band Radar Interferometer (`KaRIn`)
  - Roll
  - Timing
  - Phase
  - Baseline dilation

Below are two example cycles of the instrument errors added by the simulator to passes 15 and 168 (Figures B1 and B2). Please note that the color-scale has been adjusted for each error type.

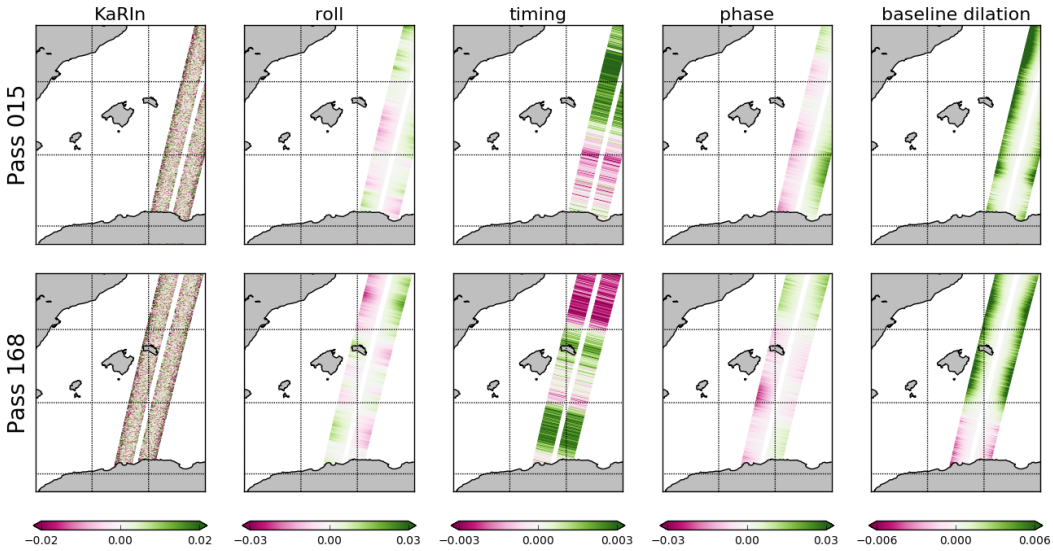

Figure B1: The different instrument noise types (m) for passes 15 pass 168 over cycle 2 are shown.

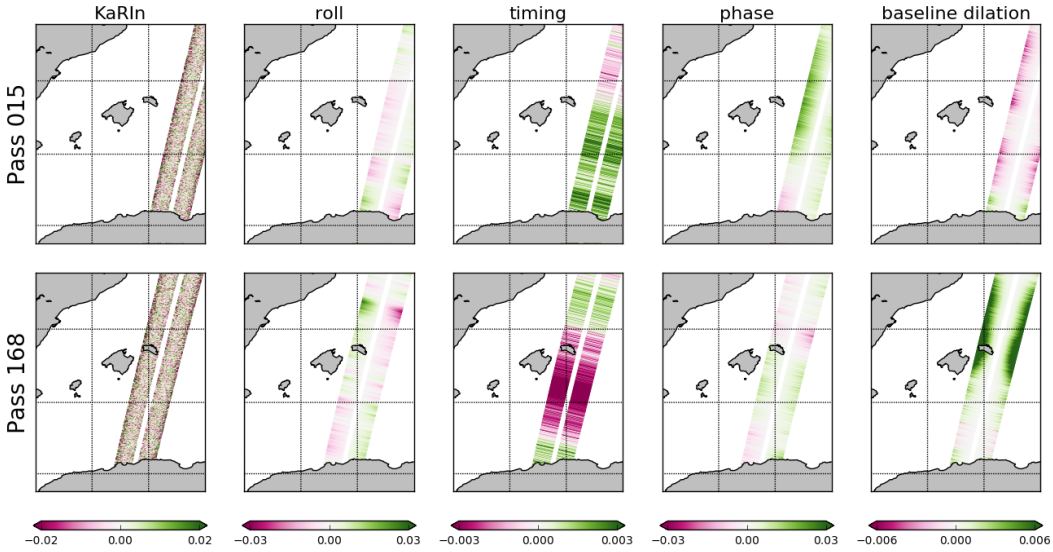

Figure B2: The different instrument noise types (m) for passes 15 and 168 over cycle 30 are shown.

- Geophysical errors: In version 1 of the simulator, only the geophysical error due to the wet troposphere is implemented. Other geophysical errors include those due to the dry troposphere, the ionosphere and the sea state bias (electromagnetic bias). However, the wet troposphere is a major source of geophysical errors and it is implemented via these following two variables:
  - Path delay (`pd`),
  - Residual path delay (`pd_err_1b`).

Below, we show two example cycles of the geophysical errors added by the simulator to passes 15 and 168 (Figures B3 and B4). Please note that the color-scale has been adjusted for each error type.

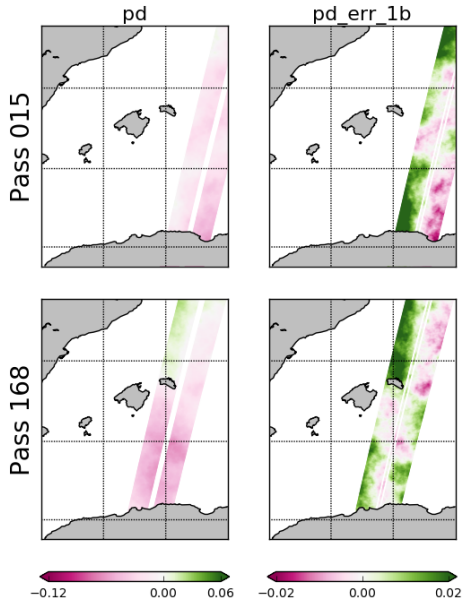

Figure B3: The different geophysical errors (m) for passes 15 and 168 over cycle 2 are shown.

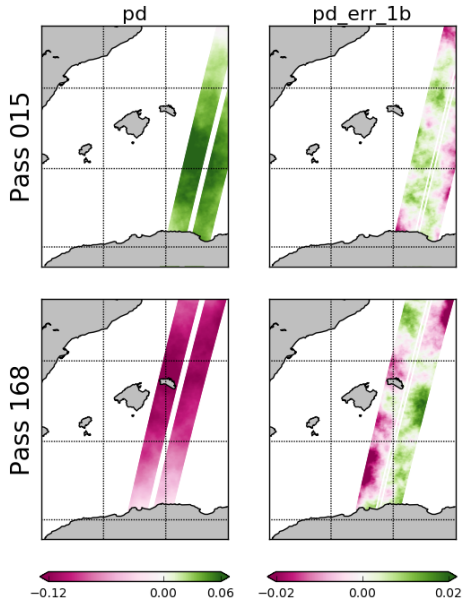

Figure B4: The different geophysical errors (m) for passes 15 and 168 over cycle 30 are shown.

For more details on instrument and geophysical errors, see *Gaultier et al.* (2016) and *Esteban-Fernandez* (2017).

Chapter 4

Development of an image de-noising method in preparation for the surface water and ocean topography satellite mission.

This chapter has been published as: Gómez-Navarro, L., Cosme, E., Sommer, J. L., Papadakis, N., & Pascual, A. (2020). Development of an Image De-Noising Method in Preparation for the Surface Water and Ocean Topography Satellite Mission. Remote Sensing, 12(4), 734.

Contents

4.1 Introduction

The Surface Water Ocean Topography (SWOT) (*Fu, Lee-Lueng and Alsdorf, Douglas and Morrow, Rosemary and Rodriguez, Ernesto and Mognard, Nelly*, 2012) mission will provide an unprecedented two-dimensional view of ocean surface topography at a pixel resolution of 2 km. The launch is scheduled for 2021. SWOT's wide-swath altimeter, based upon Synthetic Aperture Radar (SAR) interferometry technology, will measure Sea Surface Height (SSH) over a 120-km wide swath with a 20-km gap at the nadir. The satellite will also carry a conventional nadir altimeter. SWOT will evolve on two different orbits: the first 3 months of scientific data production will be dedicated to a fast-sampling phase, where the repeat cycle will be 1 day. Then, the satellite will be moved to its nominal orbit with a 20.86-day repeat cycle. SWOT is a multidisciplinary hydrology and oceanography mission, and here, we focus on the latter.

The main oceanographic objective of SWOT is to observe the geostrophic fine-scale circulation at the global scale (*Fu and Ferrari*, 2008; *Morrow et al.*, 2019). The measurement system is designed to resolve ocean circulation patterns at scales down to 15 km, whereas the present-day constellation of conventional altimeters only resolves scales of 150–200 km and above (*Morrow et al.*, 2019). In addition to potentially unexpected discoveries, this order-of-magnitude gain in resolution will help quantify several oceanic processes much more accurately than today. Among those processes are vertical motions, which are key to the vertical exchanges between the ocean surface and the atmosphere and between the ocean surface and the deep ocean (*Thomas et al.*, 2008; *Taylor and Ferrari*, 2011; *Lévy et al.*, 2012b; *Mahadevan*, 2016; *McGillicuddy Jr*, 2016; *Pascual et al.*, 2017), and the dissipation of kinetic energy, which partly determines the climatic role of the global ocean (*Sasaki et al.*, 2014; *Uchida et al.*, 2017).

The SWOT mission objectives will be reached if we can accurately estimate gridded maps of at least the first- and second-order horizontal derivatives of SSH. Altimetry describes the upper ocean dynamics through geostrophy, which involves the horizontal SSH gradients. Geostrophy is a fairly good approximation of mesoscale dynamics, i.e., at scales larger than the first Rossby deformation radius (about 10–15 km in our region (*Escudier et al.*, 2016b)), for which Rossby numbers are typically smaller than 1. Kinetic energy dissipation is driven by the horizontal strain rates of the ocean surface flow (*Capet et al.*, 2008a). Complete, gridded maps of SSH derivatives are required for climate studies and short-term operational applications. One way to make gridded maps from incomplete SSH observations (including SWOT, but not only) is to assimilate those data into dynamical models. The assimilation of SWOT is expected to be challenging because of the spatially correlated errors, and promising solutions to this rely upon the joint assimilation of SSH and its derivatives (*Ruggiero et al.*, 2016; *Yaremchuk et al.*, 2018). All these considerations compel the scientific community to strive for getting accurate estimates of SSH derivatives.

Unfortunately, SWOT data will very likely be contaminated by small-scale noise and errors that prevent the direct computation of SSH derivatives. The errors expected to contaminate SWOT measurements gather several components with different spatial coherences and different amplitudes. Details are provided in the SWOT mission performance and error budget document (*Esteban-Fernandez*, 2017). To be prepared to exploit the future SWOT data, the SWOT simulator for ocean science has been developed to simulate realistic realizations of SWOT uncertainties (*Gaultier et al.*, 2016). Some are illustrated at our study region (Figure 4.1) in Figure 4.2. Errors due to the satellite roll, the baseline dilation, and the path delay induced by atmospheric humidity exhibit significant spatial correlations with different characteristic patterns. The system timing error presents errors invariant across-track but with possible small-scale variations along-track. The KaRIn (Ka-band Radar Interferometer) noise is spatially uncorrelated, with higher amplitudes at nadir and near the edges of the swath. The path-delay component also exhibits small-scale variations due to sharp changes in air humidity. Efforts have already been undertaken to filter out SWOT's random, small-scale noise by *Gómez-Navarro et al.* (2018). The authors show that the implementation of a diffusion-based filter allows to retrieve the dynamical spectral signature down to 40–60 km scales (20–30 km in terms of dynamical pattern scales). However, the de-noising approach here is not specifically designed to retrieve SSH derivatives, and we believe there is room for improvement in the scales to be retrieved.

This paper presents a method designed to remove the random, small-scale noise of the future SWOT data, which explicitly relies upon the regularity (bounded variations) of the first three orders of SSH derivatives. Consequently, this approach is of interest as it has a direct impact on not only SSH but also on important oceanic variables like geostrophic velocity and vorticity. This de-noising method is rooted in image restoration

techniques of the variational type (*Rudin et al.*, 1992; *Chang et al.*, 2000; *Desbrun et al.*, 2000; *Chambolle*, 2004). The range of image restoration techniques is extremely wide and diversified. Testing all existing methods is out of reach and irrelevant here. Our approach is then to acknowledge that our image is a smooth physical field with relatively smooth derivatives and that the estimation of derivatives is an important issue. This consideration guides the design of the de-noising method presented in Section 4.2. The method involves a set of parameters that must be adjusted. An essential task is to identify optimal sets of parameters. This study suggests a methodology to identify them. The experimental setup is described in Section 4.3. Sections 4.4 and 4.5 present the results, and Section 4.6 summarizes the study, draws the most relevant conclusions, discusses them, and suggests possible future research paths.

4.2 Variational De-Noising of SWOT Images

4.2.1 Formulation of the Image De-Noising Problem

The purpose of image de-noising here is to allow the computation of first- and second-order SSH spatial derivatives of SWOT data as accurately as possible. The two reasons already mentioned in the introduction are (i) that these quantities represent geostrophic velocities and relative vorticity, respectively, of which the estimation is central to the success of SWOT mission, and (ii) that these quantities could be used to draw maximum benefits from the assimilation of SWOT data into ocean circulation models (*Ruggiero et al.*, 2016; *Yaremchuk et al.*, 2018). We therefore propose a method that explicitly constrains these derivatives.

The proposed de-noising model is formulated as a regularized least-square problem with a Tikhonov regularization. The de-noised SWOT image h is searched for by minimizing the following cost function:

$$J(h) = \frac{1}{2}\|m \circ (h - h_{obs})\|^2 + \frac{\lambda_1}{2}\|\nabla h\|^2 + \frac{\lambda_2}{2}\|\Delta h\|^2 + \frac{\lambda_3}{2}\|\nabla\Delta h\|^2 \tag{4.1}$$

where $\|\quad\|$ represents the L_2-norm, h^{obs} is the original noisy image (i.e., our observation, the pseudo-SWOT data), $\nabla = (\partial/\partial x, \partial/\partial y)$ is the gradient operator, and $\Delta = \partial^2/\partial x^2 + \partial^2/\partial y^2$ is the Laplacian operator. Letter m and sign $\circ$ represent a mask and the entrywise matrix product, respectively. They can be ignored for the present and the next subsection: their role is discussed in Section 4.2.3 below. The regularization terms impose regularity constraints on geostrophic velocity, vorticity, and vorticity gradient, respectively. Parameters λ_1, λ_2, and λ_3 must be prescribed. The search for their optimal values is reported in Section 4.3.3.

4.2.2 Resolution of the Variational Problem

The variational problem displayed in Equation (5.2) is solved using a gradient descent method (*Biemond et al.*, 1990). The gradient of J is written as follows:

$$\nabla J(h) = m \circ (h - h_{obs}) - \lambda_1\Delta h + \lambda_2\Delta\Delta h - \lambda_3\Delta\Delta\Delta h \tag{4.2}$$

so that the solution can be reached after convergence of the following iterations:

$$h^{k+1} = h^k + \tau\left(m \circ (h_{obs} - h^k) + \lambda_1\Delta h^k - \lambda_2\Delta\Delta h^k + \lambda_3\Delta\Delta\Delta h^k\right) \tag{4.3}$$

Stability of iterations is guaranteed if $\tau \leq (1 + 8\lambda_1 + 64\lambda_2 + 512\lambda_3)^{-1}$. In practice, it is taken equal to this value. Two improvements on the method's implementation accelerate the gradient descent: Firstly, iterations are started with a preconditioned image obtained by applying a Gaussian filter onto the original image, including inpainting as discussed in Sections 4.2.3 and 4.2.4 (note that h^{obs} remains the original, unfiltered image). Preconditioning considerably speeds up the algorithm convergence, in particular for the inpainted regions. Secondly, iterations are actually implemented with an acceleration of Scheme 5.3 based on the Fast Iterative Shrinkage-Thresholding Algorithm (FISTA) (*Beck and Teboulle*, 2009), detailed in Appendix 4.B.The Laplacian operator is discretized with finite differences using the five-point stencils of the

image pixels. As commonly done in image processing, the division by pixel size is ignored; this also reduces the probability of truncation errors due to operations with terms different by too many orders of magnitude. Pixels located at the boundaries, where the stencil is incomplete, must have a Laplacian value attributed; otherwise, the image would become smaller at each iteration of the gradient descent. The implementation of the Laplacian operator follows *Chambolle* (2004) and is detailed in Appendix 4.A.

4.2.3 Dealing with Gaps in the Image

An inpainting method is implemented to deal with islands, continents, and the 20-km wide gap at the SWOT nadir, which all represent obstacles to the calculation of the second derivatives of images. Inpainting consists of filling the gaps consistently with the neighbouring water pixels. This is done (i) by extending images h^{obs} and h with pixels in the gaps and (ii) by filling mask m with ones in the water pixels of the original image and zeros in the gaps. Differential operators can then be applied to every image pixel, and the gradient descent iterations are carried out smoothly. Mask m is applied to the resulting image to obtain the final, filtered image with islands, continents, and the nadir gap.

Inpainting should not only be considered as a complimentary step to facilitate the gradient descent implementation but also as an opportunity to fill the nadir gap for calibration, validation, and reconstruction purposes. In the gaps, the image resulting from the iterations is determined only by the neighbouring water pixels and regularity constraints. The gap width (20 km) appears reasonably small in comparison with spatial scales of SSH variations in most parts of the mid-latitude, open ocean. The image values obtained at nadir may thus be comparable to those collected by the nadir instrument carried by SWOT, allowing calibration of the radar interferometer, validation of data, and reconstruction of SSH in gap-free images. Such opportunities will be explored in a future work.

4.2.4 Comparison with Convolution-Based Filters

In Section 4.4, the image de-noising technique described above will be compared with standard-type filters, namely convolution-based filters. In our experiments, we test the two commonly used boxcar and Gaussian convolution kernels, with a large range of parameters, and we shortly refer to the boxcar filter and the Gaussian filter. Their parameters are the box size (or footprint) and the standard deviation for the Gaussian kernel (hereinafter referred to as σ). Gaps in the SWOT swath (lands, islands, and nadir gap) are inpainted to facilitate filtering and to ensure the smoothness of SSH fields. Then, SSH values created in gaps are removed for the evaluation of the methods using the mask m. Inpainting is implemented as follows: (i) Image gaps are filled with zeros; (ii) both the filled image and the mask m are filtered with the same kernel; and (iii) the filtered filled image is divided entrywise by the filtered mask. Note that, in an earlier study (*Gómez-Navarro et al.*, 2018), a Laplacian diffusion filter was experimented. It is not reproduced here, since it is equivalent to the Gaussian filter implemented in this study. For details on the software used to implement these methods see Appendix 4.E.

4.3 Experimental Setup

4.3.1 Simulated SWOT Dataset

The input of our database is a 15-month North Atlantic simulation at a resolution of 1/60°. We use the NEMO3.6 ocean model coupled to LIM2 ice model, with atmospheric forcing from a global ocean reanalysis at 1/4° (GLORYS-v3) and ocean-atmosphere boundary conditions of Drakkar Forcing Set (DFS5.2) based on European Centre for Medium-Range Weather Forecasts (ECMWF) Interim Re-Analysis (ERA-Interim). It has no high frequency forcing and thus does not include tides. The domain covers the North Atlantic from 25°N to 66°N. The horizontal resolution is between 0.8 and 1.6 km (depending on latitude), and the grid has 300 vertical levels. This NEMO (Nucleus for a European Model of the Ocean) model configuration is referred

to as NATL60, and the source files and codes are available in *Molines* (2018). The particular simulation used herein has been described in *Amores et al.* (2018); *Fresnay et al.* (2018); *Ajayi et al.* (2019). Lastly, the simulation time span is from mid-June 2012 to October 2013 (*Le Sommer et al.*, In prep.).

The SWOT simulator for Ocean Science (version 2.21) (*Gaultier et al.*, 2016) is run to generate pseudo-SWOT scenes from the NATL60 simulation. The SWOT simulator first builds the SWOT observation grid based on the provided satellite orbit. In this study, SWOT grid resolution is fixed at 1 km. After this work started, the resolution of the basic SWOT level 2 SSH data products has been fixed to 2 km, but this small mismatch does not modify the general approach. After building the grid, the simulator reads SSH data from NATL60 and linearly interpolates them from the model to the SWOT grid (rendering the variable SSH_model). In a last step, it computes random realizations of observation errors and adds them to the interpolated SSH data (rendering SSH_obs). Observation errors considered at the moment are KaRIn noise errors, roll errors, phase errors, baseline dilation errors, timing errors, and errors due to signal alternation by atmospheric humidity. Among these errors, only the KaRIn noise is expected to be spatially uncorrelated. Technically, the SWOT simulator provides simulations of the noise-free SSH observed by SWOT and of the noisy data that SWOT will actually yield (sum of the former and the noise: SSH_obs = SSH_model + errors). For the evaluation of image de-noising methods, it thus provides "true" noise-free images (h^{true}) along with the realistic SWOT data (h^{obs}) to process and compare with the truth.

A set of 543, 121 $\times$ 200 km^2 pseudo-SWOT scenes are generated in the western Mediterranean Sea, covering one winter and two summer seasons (choice limited by the model's time span). SWOT scenes are sampled from the fast-sampling phase satellite orbit, focusing on a cross-over region, i.e., where an ascending pass crosses a descending pass, therefore providing 2 passes per day. The SWOT data simulation is carried out over three 3-month periods: July to September 2012 and 2013 (JAS12 and JAS13 hereafter), representing the summer season, and February to April 2013 (FMA13), representing the winter season. The summer periods provide 92 (resp. 91) of ascending (resp. descending) passes; the winter period provides 89 (resp. 88) passes. The selected region belongs to the fast-sampling phase crossover in the western Mediterranean Sea. This is one of the regions selected for calibration/validation (Cal/Val) (*d'Ovidio et al.*, 2019) in which *in situ* measurements have been made in the frame of SWOT (*Barceló-Llull et al.*, 2018). To mitigate the computational complexity of the study and to avoid the presence of continents and islands, limited subregions of the SWOT swaths are sampled. These subregions are 121-km wide (the width of 2 SWOT swaths plus the gap) and 200-km long. The region, the SWOT passes, and the subregions are shown in Figure 4.1. It is worth noting that each scene is affected by a unique realization of the SWOT error.

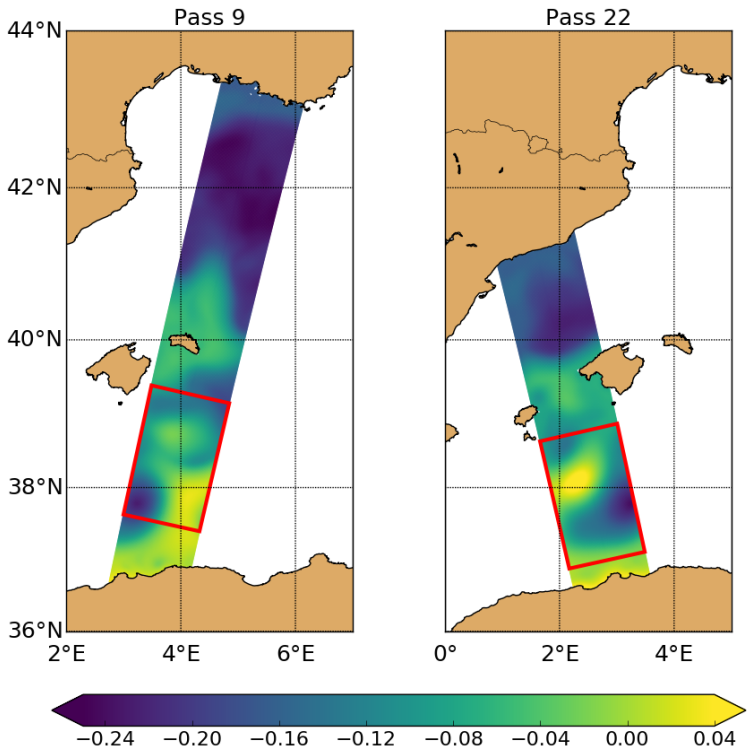

Figure 4.1: SSH_model outputs (m) for cycle 1 of pass 9 (**left**) and 22 (**right**) of the July to September 2012 (JAS12) dataset: In red is the subregions selected.

In this work, image de-noising techniques are first applied to the pseudo-SWOT scenes affected by the KaRIn noise only (SSH_obs_K) and then to the scenes containing all errors (SSH_obs). This approach allows to discriminate the effects and the performance of image de-noising in the presence of the spatially correlated SWOT errors.

A few realizations of the different components of the SWOT error are shown in Figure 4.2, where we can observe how most errors exhibit strong and long-range correlations, whilst the KaRIn error does not show any correlation at all.

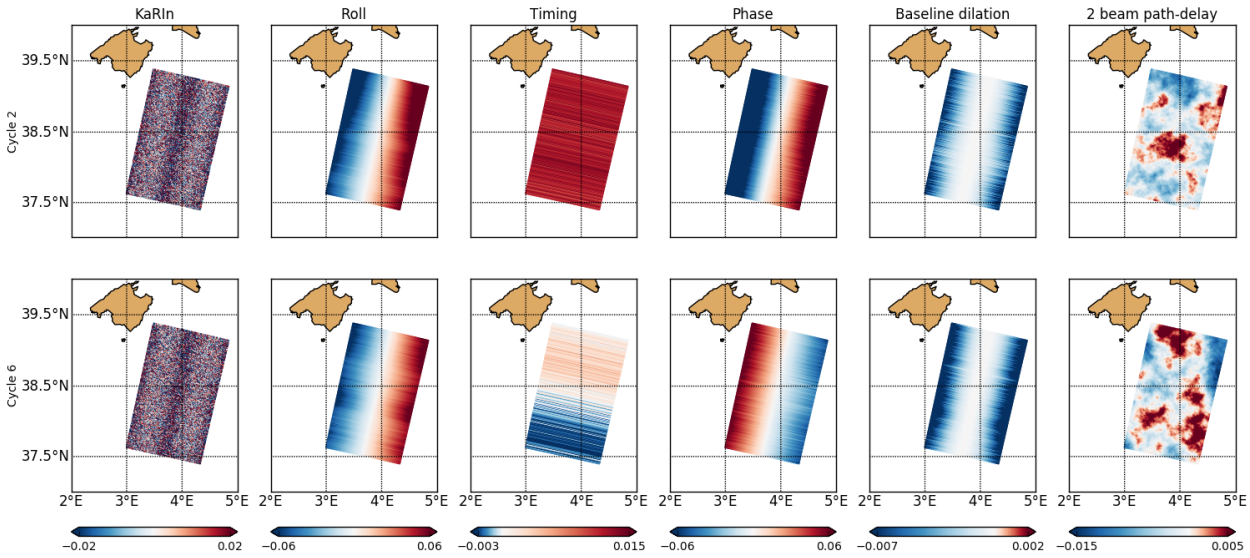

(**a**)

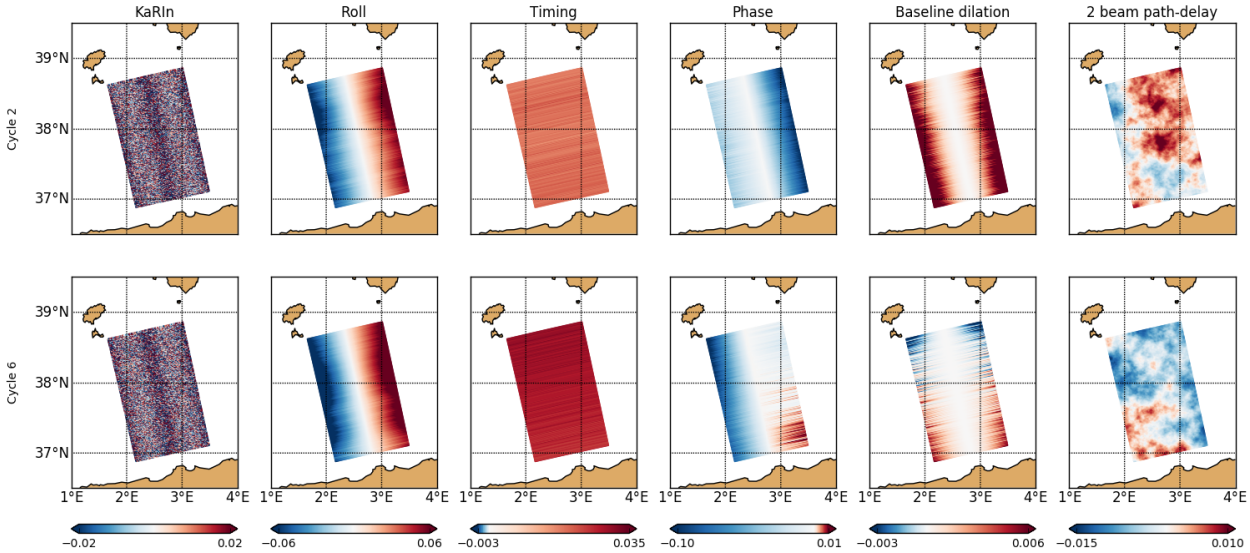

(**b**)

Figure 4.2: Examples of errors (m) added by this Surface Water Ocean Topography (SWOT) simulator version 2.21 to our study region fast-sampling phase for JAS12 pass 9 (**a**) and 22 (**b**): Note that these simulations are performed without the 20-km gap at nadir.

4.3.2 Diagnostics for Evaluation

The quantitative evaluation of de-noising methods is carried out by computing Root Mean Square Errors (RMSE) and Mean Spectral Ratios (MSR). RMSE for a single de-noised SWOT field h is computed as the Euclidean distance to the corresponding original, noise-free field h^{true}:

$$RMSE(h) = \sqrt{\frac{1}{N}\sum_{i=1}^{N}(h_i - h_i^{\text{true}})^2} \tag{4.4}$$

where N is the number of pixels and i a pixel index. Single image RMSEs are then averaged out by season for the 3 seasons considered and are computed for SSH, $|\nabla \text{SSH}|$ and ΔSSH. Thus, the test of a de-noising

method with a specific set of parameters results in 9 RMSE values. To evaluate the improvement after the application of the different de-noising techniques and parameters, we also calculate the percentage of the initial RMSE left. We calculate this RMSE residual ($RMSE_r$) as follows:

$$RMSE_r(h) = \frac{RMSE(h)}{RMSE(h^{obs})} \times 100, \tag{4.5}$$

where h is the de-noised field and h^{obs} is the original noisy field (SSH_obs_K or SSH_obs).

The spatial spectra of the de-noised SWOT SSH are compared with the spectra of the noise-free and the noisy SWOT SSH. For each pass, we calculate the cross-track averaged and along-track power spectrum. The spectra are then averaged out over each season, leading to one spectrum per season. Information on the wavenumber spectrum calculations is given in Appendix 4.C. Again, to evaluate the improvement after the application of the different de-noising techniques and parameters, we compare the noise-free and de-noised fields. To do so, the Mean Spectral Ratio (MSR) is computed from the Power Spectral Densities (PSD) of SSH. For each season, MSR is computed as follows:

$$MSR = \sqrt{\frac{1}{\sum_{j=1}^{N_k} \delta k_j} \sum_{j=1}^{N_k} \left(\left(\log_{10} \left(\frac{PSD_j(h^{\text{true}})}{PSD_j(h)} \right) \right)^2 \times \delta k_j \right)}, \tag{4.6}$$

where N_k is the number of wavelengths considered and where $PSD_j(h^{\text{true}})$ and $PSD_j(h)$ are the power spectral density values at wavelength j for the original, noise-free SWOT field and the de-noised SWOT field, respectively.

4.3.3 Exploring Parameters of the De-Noising Methods

For all de-noising methods, a wide range of parameters are tested to identify optimal parameters according to the diagnostics presented in Section 4.3.2. The convolution-based methods use a single parameter that can easily be compared with the image dimensions in pixels. For the boxcar kernel, the tested parameter values go from 3 to 200 km and correspond to the size of the box in pixels (1 km in our case). For the Gaussian kernel, the tested parameters go from 0.25 to 300 and correspond to the standard deviation, in pixels (we test up to a big sigma to have a highly oversmoothed image to reach the limit of the method). On the contrary, the geometric interpretation of the parameters of the variational method is not straightforward, and a wide exploration of the parameter space must be undertaken. However, due to computation time limitations, this cannot be performed in a strictly systematic manner. The adopted procedure is detailed below.

4.3.3.1 Orders of Magnitude of the Cost Function Terms

The orders of magnitude of the terms $\|\nabla h\|^2$, $\|\Delta h\|^2$, and $\|\nabla \Delta h\|^2$ composing the cost function (Equation (5.2)) are estimated to coarsely scale the parameters λ_1, λ_2, and λ_3. The rationale is that, for one of these terms (with its weight) to have some impact on the solution, it must be of an order of magnitude not too different from the background term $\|m \circ (h - h^{obs})\|^2$. Figure 4.3 shows the seasonal evolution of the derivative terms, computed from the model in a $2° \times 2°$ region containing the SWOT passes used in this study. The relative ratios between $\|\nabla h\|^2$, $\|\Delta h\|^2$, and $\|\nabla \Delta h\|^2$ are approximately 1000:10:1. Therefore, if we want to include all three terms in the cost function, the ratios between λ_1, λ_2, and λ_3 should coarsely be 1:100:1000. Those ratios must be only considered as a guideline to start the investigation, not a strict rule. Note that the order of magnitude of the background term after minimization of the cost function is thought to be in the range 1 to 100 in the same region. This has been estimated using the noise-free field.

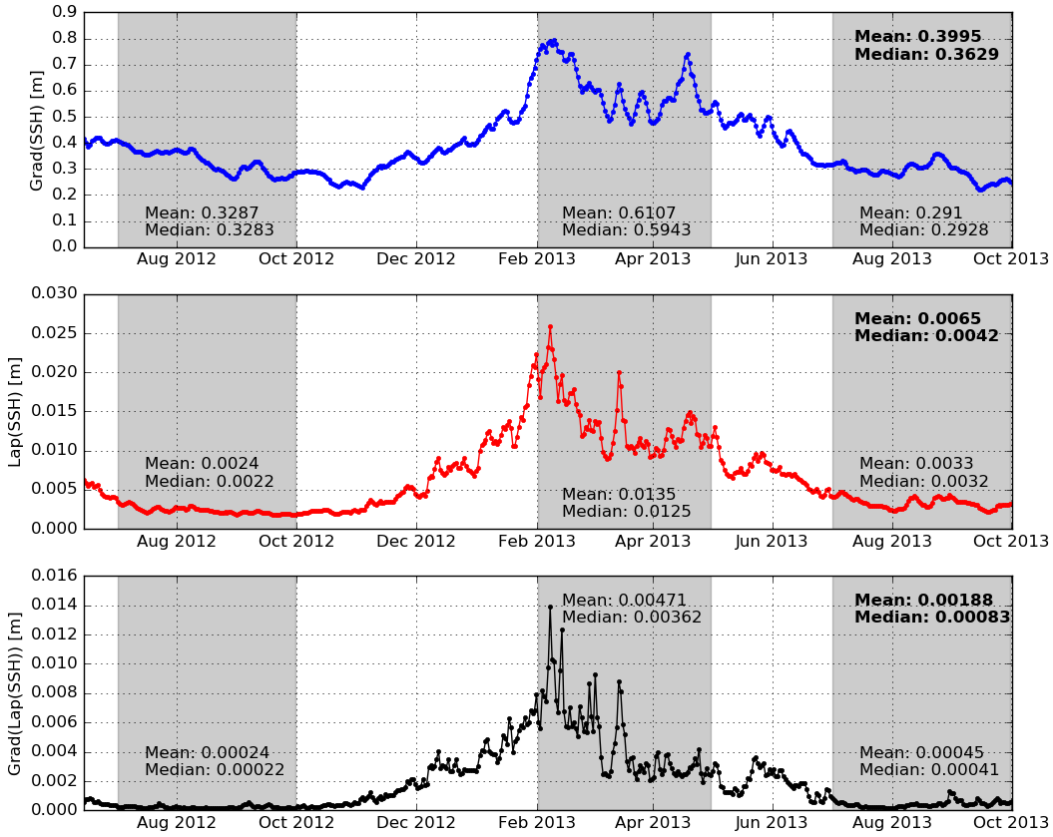

Figure 4.3: Seasonal variations of the cost function terms $\|\nabla h\|^2$, $\|\Delta h\|^2$, and $\|\nabla \Delta h\|^2$, from top to bottom: Shaded areas indicate the JAS12, February to April 2013 (FMA13), and July to September 2013 (JAS13) periods from left to right, respectively. The mean and median values are printed for each period and for the whole year (upper right corners, in bold).

4.3.3.2 Finding Optimal Sets of Parameters

First, we created an exponential series of values to be tested for the three lambdas, consistently with the previously estimated relative ratios. For λ_1, the series is chosen as $\{4^n, n = 0, ..., 7\}$. For λ_2 and λ_3, the series are $\{10 \times 4^n, n = 0, ..., 7\}$ and $\{100 \times 4^n, n = 0, ..., 7\}$, respectively. With these, six scenarios of Derivatives Penalization (DP) de-noising are investigated, including one, two, or three penalization terms in the cost function of Equation (5.2). Three scenarios out of the six considered include a single penalization term (mono-parametric) of orders 1, 2 and 3, successively. The other scenarios are made of terms of orders 1 and 2 and of 2 and 3, and the last one includes the three orders. For conciseness, particularly in the next section, we refer to the variational method with the first-order term only as the λ_1 method. We similarly refer to the λ_2 method and to the $(\lambda_1 + \lambda_2)$ method when the first two penalization terms are considered, and so on.

For each scenario, a two-step procedure is implemented to identify an optimal set of parameters. In a first step, de-noising of the full set of images is performed with all possible combinations of parameters permitted by the scenario and the parameter series defined previously. RMSEs and MSR are computed for all the combinations. In a second step, refined series of parameters are created in the neighborhood of the combination of parameters that yields the minimum RMSE and MSR scores. Image de-noising is then carried out again with all possible combinations of these series.

4.4 Optimal De-Noising Method

In this section, the optimal de-noising method is searched for based on the RMSE and MSR scores described in Section 4.3. We investigate the KaRIn-noise-only scenario and then the all errors scenario and finally have a closer look at the method identified as optimal. As it becomes clear in what follows, the notion of optimality does not only refer to quantitative measures. The design of a single index summarizing the performance of the method for the different RMSEs is indeed subjective. Moreover, we take into account the ease of implementation and parameterization as a criteria in the final decision.

Minimum values of RSME and MSR for each season, method, and variable are reported in Tables 4.1 and 4.2 for the KaRIn-only and all errors scenarios, respectively. RMSE scores are actually expressed as the percentage of the original RMSEs (RMSE_r), i.e., those of the original, noisy data. For SSH, $|\nabla \mathrm{SSH}|$, and ΔSSH RMSE and MSR of each de-noising configuration and parameterization, the scores do not necessarily correspond to the same optimal parameter (box size, σ, or λ).

Table 4.1: Scores summary of boxcar, Gaussian and Derivatives Penalization (DP) de-noising methods for the just KaRIn (Ka-band Radar Interferometer) dataset.

Season	De-noising method		$\mathbf{RMSE}_r$			Minimum MSR
			SSH	**$\lvert\nabla$SSH$\rvert$**	**ΔSSH**	
JAS12	**Boxcar**		12.43	0.094	0.300	0.2010
	Gaussian		11.23	0.067	0.250	0.1111
	DP	**1**	12.55	0.084	0.279	0.2028
		2	08.71	0.050	0.247	0.0143
		3	09.06	0.051	0.247	0.1021
		1 + 2	08.72	0.050	0.247	0.0192
		2 + 3	08.68	0.049	0.247	0.0205
		1 + 2 + 3	08.66	0.049	0.246	0.0259
FMA13	**Boxcar**		15.04	0.177	0.511	0.1066
	Gaussian		12.97	0.133	0.424	0.0746
	DP	**1**	15.41	0.173	0.483	0.1498
		2	10.92	0.115	0.420	0.0178
		3	10.86	0.113	0.416	0.0682
		1 + 2	10.92	0.115	0.420	0.0208
		2 + 3	10.79	0.113	0.416	0.0168
		1 + 2 + 3	10.82	0.113	0.416	0.0255
JAS13	**Boxcar**		11.98	0.086	0.326	0.1796
	Gaussian		10.99	0.063	0.276	0.0911
	DP	**1**	12.78	0.083	0.309	0.2031
		2	08.96	0.053	0.274	0.0216
		3	09.11	0.053	0.273	0.1010
		1 + 2	08.97	0.053	0.274	0.0394
		2 + 3	08.84	0.052	0.272	0.0243
		1 + 2 + 3	08.84	0.052	0.272	0.0269

4.4.1 RMSE and MSR Scores with KaRIn Noise Only

For all variables (h, ∇h, and Δh), all seasons, and all de-noising methods, minimum RMSEs are smaller in summer than in winter (Table 4.1). This is expected because the oceanic surface features in winter are smaller than in summer (*Escudier*, 2014), so their observation is more affected by the KaRIn noise. Also, smaller structures are more affected by the smoothing due to the de-noising.

For all three seasons and all three variables, RMSEs and MSRs from the convolution-based methods and from the λ_1 method are larger than RMSEs and MSRs from all other variational methods. Also, the λ_3

method provides MSRs significantly higher than the other variational methods. None of these methods is the optimal de-noising one in this KaRIn-only noise configuration and are not further discussed in the following.

In terms of both RMSEs and MSRs and among the methods still on course, no method outperforms the others systematically and distinctly. For all three variables, RMSEs are close to each other, with differences less than a very few percents. MSRs are a bit more scattered but without any clear predominance of a specific method in all seasons. However, the λ_2 method exhibits the lowest MSR values in summer and the second lowest value in winter, close to the $\lambda_2 + \lambda_3$ method.

Finally, this analysis persuades us to further examine the λ_2 method for the KaRIn-only scenario (see Section 4.4.3). This choice is supported by the RMSE and MSR analysis above, which shows that other methods do not beat it clearly, and by the fact that it is much easier to parametrize a single-parameter method rather than a two- or three-parameter method.

4.4.2 RMSE and MSR Scores with All Errors

Normalized minimum RMSEs for h and $|\nabla h|$ are higher than in the KaRIn-only scenario by factors of 6–12 for h and 1.5–4 for $|\nabla h|$ (Table 4.2). This is obviously due to the spatially correlated component of the errors (see Figure 4.2), which is not filtered out by any of the methods used here. Other approaches must be used to remove the correlated errors in order to obtain more accurate estimates (*Metref et al.*, 2019, 2020).

Contrary to h and ∇h, RMSEs for Δh are comparable with those obtained in the KaRIn-only case. They are 5% higher only. This slight increase in RMSE is the signature of the nonlinear component of the correlated error. In the across-track direction, this nonlinear (quadratic, more precisely) component is due to the baseline dilation (*Gaultier et al.*, 2016; *Esteban-Fernandez*, 2017). The other components are constant, linear, or piecewise linear and thus are removed by the second-order derivatives. The spatial errors' signal in the along-track direction is supposed to vary less with the satellite attitude (except timing errors) and the local environmental constraints on the satellite (baseline dilation). This is reflected as small but not null second-order derivatives of errors that may slightly affect the RMSE. In reality, the spatial decorrelation of such errors might be short and combined with geophysical variations (waves and atmosphere).

Considering only RMSEs on Δh, except for the boxcar and the λ_1, no method performs significantly better than the others, and RMSEs are higher in winter than in summer. This is similar to the KaRIn-only scenario. The Gaussian filter performs comparatively better than in the KaRIn-only scenario.

In terms of MSRs, the methods involving λ_2 perform significantly better than the others, including the λ_3 and the Gaussian methods. These last two exhibit MSRs larger than the others by factors of 1.5 to 4. In winter, the λ_2 method is a little less effective than the multi-parameter methods, with a MSR twice as large.

The de-noising experiments with all errors, like those with the KaRIn noise only, lead us to favor the λ_2 method. The reasons are similar: based on RMSEs and MSRs, the method compares favorably with the others, and a single-parameter method is much easier to parametrize. The only result speaking against this choice is the MSR in winter, for which the multi-parameter methods perform better than the λ_2 method. Considering the score value though and after the examination of the wavenumber spectra (see Section 4.5) this point hardly justifies discarding the λ_2 method as the optimal one.

4.4.3 A Focus on the Second-Order Variational Method

This section investigates the sensitivity of the λ_2 de-noising to the parameter value. Figure 4.4 shows the RMSEs for h, $|\nabla h|$, and Δh and the MSR for h as functions of λ_2. On each graph, the three seasons are shown for both KaRIn-only (solid lines) and all errors (dashed lines) scenarios, making a total of 6 curves.

Except for h and $|\nabla h|$ RMSEs in the all errors scenario, all RMSE and MSR curves exhibit a clear minimum point, which indicates the existence of an optimal or a range of close-to-optimal λ_2 values for the de-noising. These optimal values are larger in summer than in winter. This is very likely because small-scale dynamics

are amplified in winter (*Sasaki et al.*, 2014). Large λ_2 values tend to over-smooth the SSH field in winter, leading to higher residual errors. The seasonal difference in optimal λ_2 values is particularly evident with MSR, with values of ∼100 in winter and of ∼400 in summer. In Figure 4.4, the impact of applying the optimal λ_2 value for winter to summer (or viceversa) can be observed. RMSEs are not very sensitive to λ_2 near the optimal values, contrary to MSRs. For instance, using the winter value in summer (or vice versa) barely changes RMSEs but affects MSR more significantly. RMSEs for h and ∇h in the all errors scenario are dominated by the correlated SWOT errors, which remain present after de-noising. Consistently with the analysis of the previous section, those RMSEs are much higher in the all errors than in the KaRIn-only scenario.

Table 4.2: Scores summary of boxcar, Gaussian and Derivatives Penalization (DP) de-noising methods for the all errors dataset.

Season	**De-noising method**		**RMSE$_r$**			**Minimum MSR**
			SSH	**|∇SSH|**	**ΔSSH**	
JAS12		**Boxcar**	90.31	0.171	0.303	0.2024
		Gaussian	90.10	0.156	0.264	0.1181
	DP	**1**	87.60	0.159	0.281	0.1922
		2	90.57	0.174	0.261	0.0307
		3	90.22	0.156	0.265	0.1359
		1 + 2	87.61	0.158	0.262	0.0328
		2 + 3	90.22	0.156	0.261	0.0391
		1 + 2 + 3	87.40	0.156	0.261	0.0395
FMA13		**Boxcar**	90.88	0.250	0.511	0.1274
		Gaussian	90.76	0.221	0.435	0.0515
	DP	**1**	89.89	0.237	0.484	0.1415
		2	91.11	0.226	0.432	0.0314
		3	90.96	0.226	0.432	0.0868
		1 + 2	89.90	0.223	0.435	0.0160
		2 + 3	91.00	0.226	0.430	0.0177
		1 + 2 + 3	89.82	0.220	0.430	0.0203
JAS13		**Boxcar**	89.73	0.137	0.328	0.1792
		Gaussian	89.18	0.126	0.289	0.1152
	DP	**1**	84.30	0.131	0.310	0.1895
		2	90.36	0.142	0.287	0.0254
		3	89.66	0.127	0.290	0.1251
		1 + 2	84.19	0.131	0.287	0.0237
		2 + 3	89.66	0.127	0.286	0.0285
		1 + 2 + 3	83.75	0.127	0.286	0.0267

Finally, the optimal λ can be defined within a range that is a compromise between the RMSE and MSR results, for each season. In Figure 4.4, horizontal bars indicate the range of λ_2 values that provide scores higher than the minimum by less than 5%. For each season, the overlap of all horizontal bars defines a range of optimal λ_2 values. Not detailed here, the results from the other (single or multiple-parameter) configurations of variational de-noising also exhibit such overlaps, except for λ_1. Based on this information and on MSR scores, we propose λ_2 intervals of [300–400] and [400–500] in summer for the KaRIn-only and all errors cases, respectively. With λ_2 in these intervals, MSR scores remain close to their minima. Note that the two summer seasons' results render slightly different optimal values, suggesting that the optimal λ_2 choice is inevitably subject to a part of subjectivity if no additional information on the ocean surface dynamics is available. In winter, the optimal λ_2 interval is [90–120]. Due to more energetic dynamics that make the signal-to-noise ratio higher, the MSR optimal λ_2 values in the KaRIn and all errors scenarios are much closer to each other than in summer.

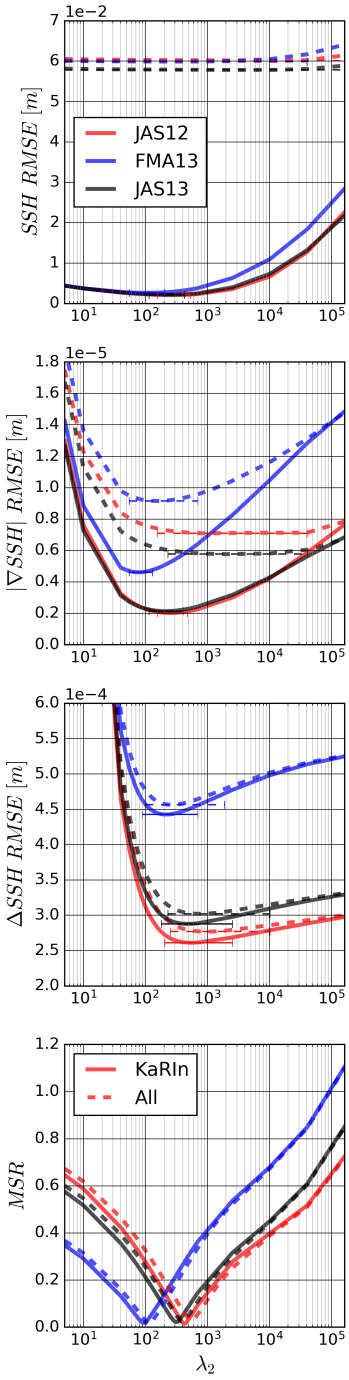

Figure 4.4: Scores of RMSE and MSR of the λ_2 method from just KaRIn (solid line) and all errors (dashed line) for all 3 seasons: Horizontal bars in the RMSE plots show the range of λ_2 values that provide scores higher than the minimum RMSE by less than 5%.

4.5 Retrieved SWOT Fields and Spatial Spectra

Figures 4.5 and 4.6 illustrate the de-noising with the λ_2 method on SWOT passes and are presented in the same format: h on the top panel, $|\nabla h|$ on the central panel, and Δh on the bottom panel. The first panel shows, from left to right, the original, noise-free h field, h with KaRIn noise only, h with all sources of errors, the de-noised KaRIn-only h, and the de-noised all errors h. The de-noised data have been obtained with the λ_2 method with parameter values chosen within the intervals identified in Section 4.4.3 and indicated on each graph. The second and third panels show the corresponding $|\nabla h|$ and Δh, respectively. Figures 4.5a,b exhibit summer time scenes with high and low correlated SWOT errors, respectively. Figures 4.6a,b are the corresponding winter plots.

In all cases, de-noising leads to correct orders of magnitude for all fields and particularly for $|\nabla h|$ and Δh. This is not the case for the conventional convolution-based methods (see Appendix 4.D). As expected and already shown by *Gómez-Navarro et al.* (2018) and *Chelton et al.* (2019), the original SWOT data affected by random, small-scale noise does not provide any useful information about SSH derivatives. The de-noising method corrects this efficiently and makes it possible to identify the main structural characteristics of the fields.

A strong spatially correlated error shows strong signatures on h, moderate signatures on $|\nabla h|$, and low signatures on Δh, except at the outer boundaries of the swath. The low signature on Δh was already observed in the RMSEs and is due to the specific spatial structure of the errors. Most components are linear in the across-track direction. In the along-track direction, the impact is lower because for the wavelengths impacted by the filtering, the error correlation is high (Figure 4.2). Therefore, the correlated errors have a low effect on the second-order derivatives. The remaining noise at the outer boundaries is due to the finite difference method used to compute the derivatives described in Appendix 4.A.

Although the resulting fields of Δh fall in correct orders of magnitude and capture the structure of the true fields at the scale of the swath, the kilometric-scale fronts and filaments are smoothed out by the de-noising. Solving this issue would require the development of more sophisticated de-noising techniques or a post-processing of the present result including, for example, some ocean dynamics through data assimilation techniques. This will be a natural step forward, since the first motivation for developing a de-noising technique constraining Δh is precisely the combined assimilation of h and its first two derivatives, as stated in the introduction.

Figure 4.7 shows Power Spectral Densities (PSD) of h. The rows distinguish the just KaRIn noise added and the all errors cases. The columns are for summer 2012, winter 2013, and summer 2013. On each graph, the spectra are shown for the noise-free data (SSH_model), the noisy data (SSH_obs), the de-noised data (SSH_obs_f), the pre-de-noising noise (noise), and post-de-noising noise (noise_f). The de-noised data have been obtained with the same λ_2 values as in Figures 4.5 and 4.6. Each spectra has an envelope showing PSD values between the 5th and 95th percentile, representing the PSD variability. This envelope reduces with the PSD values and with wavelength. At small scales, SSH_obs_f's envelope is narrower than SSH_model's, very likely because a fine-scale part of the physical signal is removed along with the noise.

From this spectral viewpoint, the de-noised data matches the noise-free data well at all scales down to $\sim$15 km. In the noisy data, the noise amplitude approaches the signal amplitude at wavelengths of 50 km in summer and 40 km in winter and dominates the signal at shorter wavelengths. This is efficiently corrected by the de-noising. The process seems more efficient in winter than in summer, probably because of higher PSDs in winter related to more intense ocean surface processes.

Following the definition proposed by *Wang et al.* (2019a) for the spatial scale resolved by SWOT, the de-noising reduces this scale by a factor of 2, leading to resolved scales between 20 and 30 km approximately. *Wang et al.* (2019a) define the spatial scale resolved by SWOT by the wavelength at which the SWOT noise spectrum intersects the spectrum of the true signal (SSH_model here). Figure 4.7 indicates resolved scales of 50, 40, and 50 km in the JAS12, FMA13, and JAS13 scenarios, respectively, in both just KaRIn and all errors cases. After de-noising, the resolved scales are reduced to approximately 25, 20, and 25 km in the KaRIn-only case and to 30, 20, and 30 km in the all errors case. Even below these scales, the noise left is very low and within the variability of SSH_model (red envelope in Figure 4.7). At wavelengths near 10 km, the noise is reduced by 10^4 in the JAS scenarios and 10^3 in the FMA scenario.

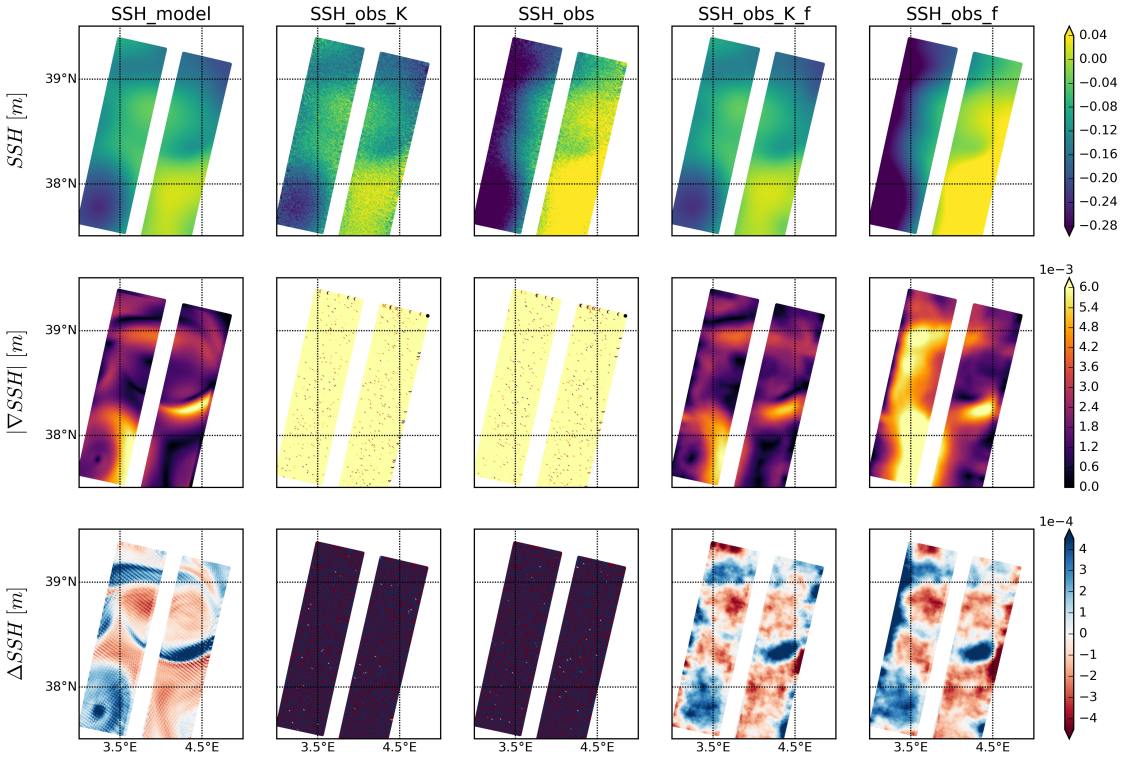

(**a**)

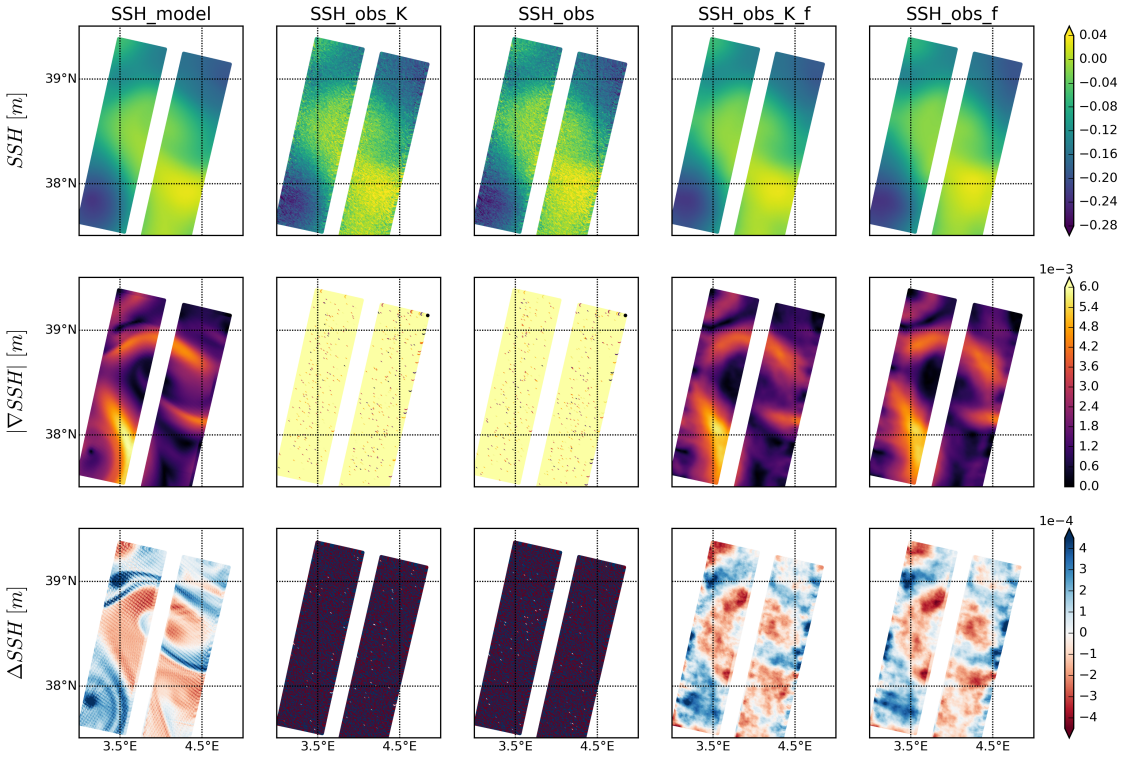

(**b**)

Figure 4.5: Fields of pass 09, cycle 2 (**a**) and 6 (**b**) of the JAS12 dataset compared to the fields filtered with $\lambda_2 = 355$ (455) for SSH_obs_K_f (SSH_obs_f). From top to bottom: SSH, gradient of SSH and Laplacian of SSH. From left to right: model interpolated to SWOT grid (SSH_model), SSH_model + KaRIn noise (SSH_obs_K), SSH_model + all errors (SSH_obs), filtered SSH_obs_K (SSH_obs_K_f), and filtered SSH_obs (SSH_obs_f).

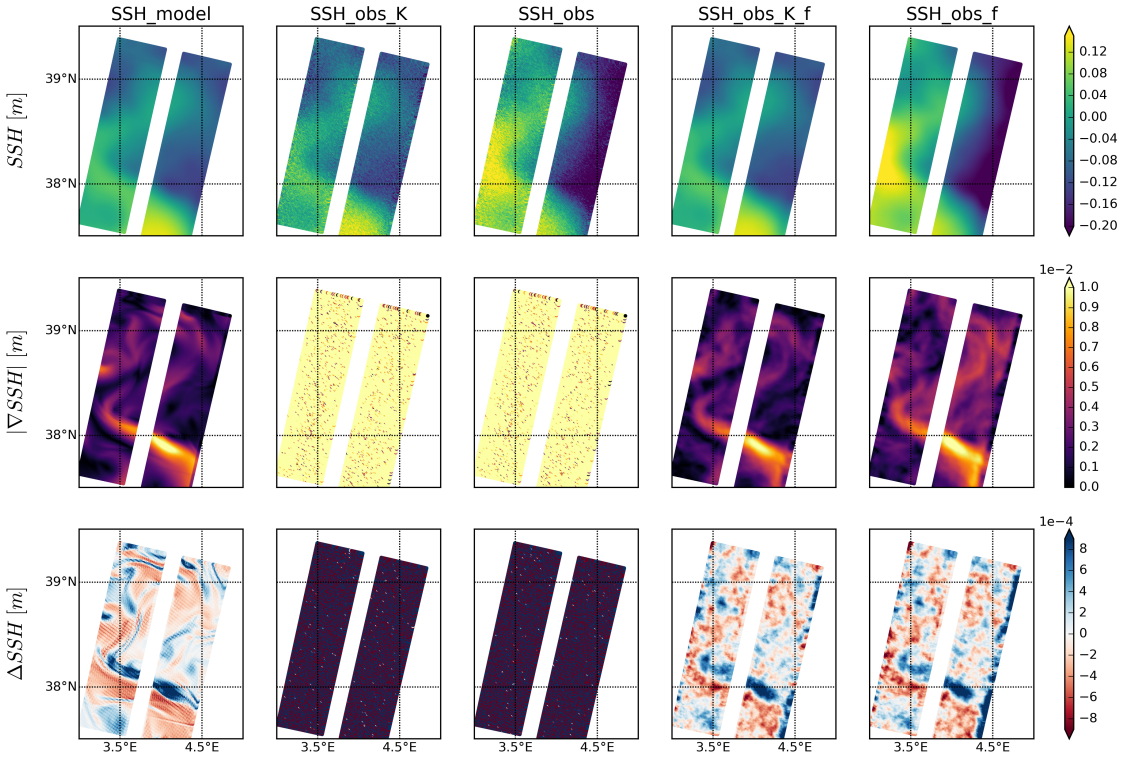

(**a**)

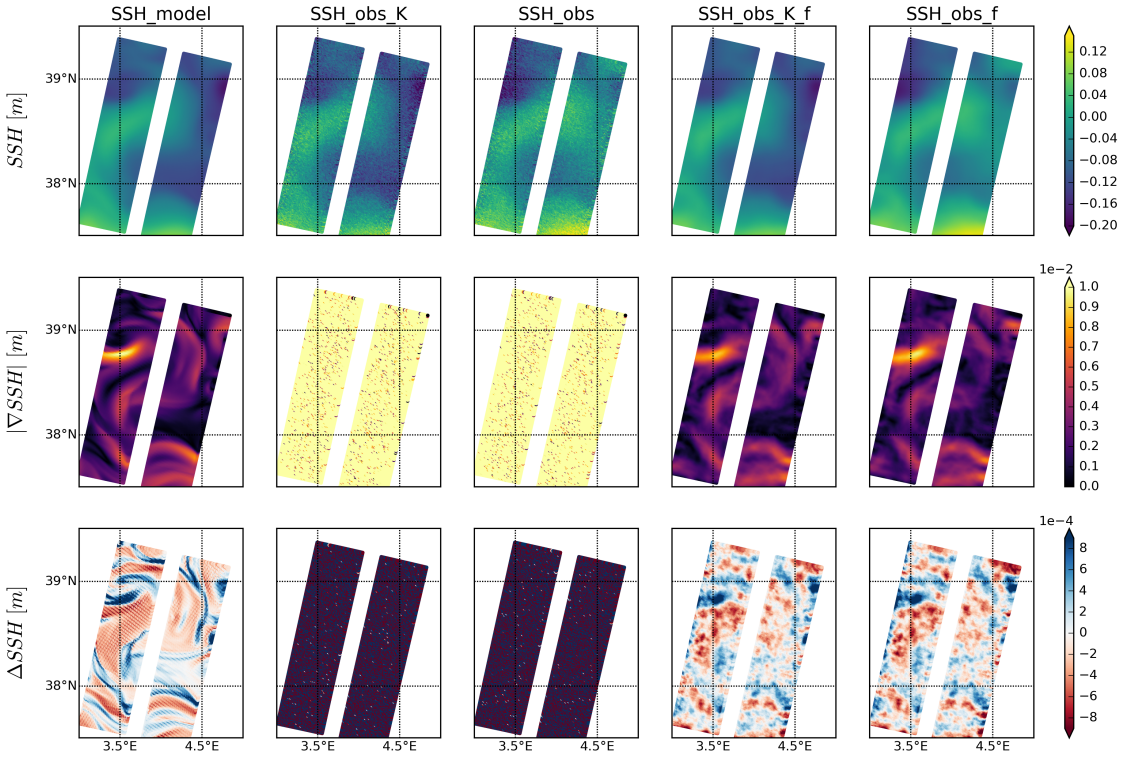

(**b**)

Figure 4.6: Fields of pass 09, cycle 2 (**a**) and 6 (**b**) of the FMA13 dataset compared to the fields filtered both with $\lambda_2 = 105$. From top to bottom: SSH, gradient of SSH and Laplacian of SSH. From left to right: model interpolated to SWOT grid (SSH_model), SSH_model + KaRIn noise (SSH_obs_K), SSH_model + all errors (SSH_obs), filtered SSH_obs_K (SSH_obs_K_f), and filtered SSH_obs (SSH_obs_f).

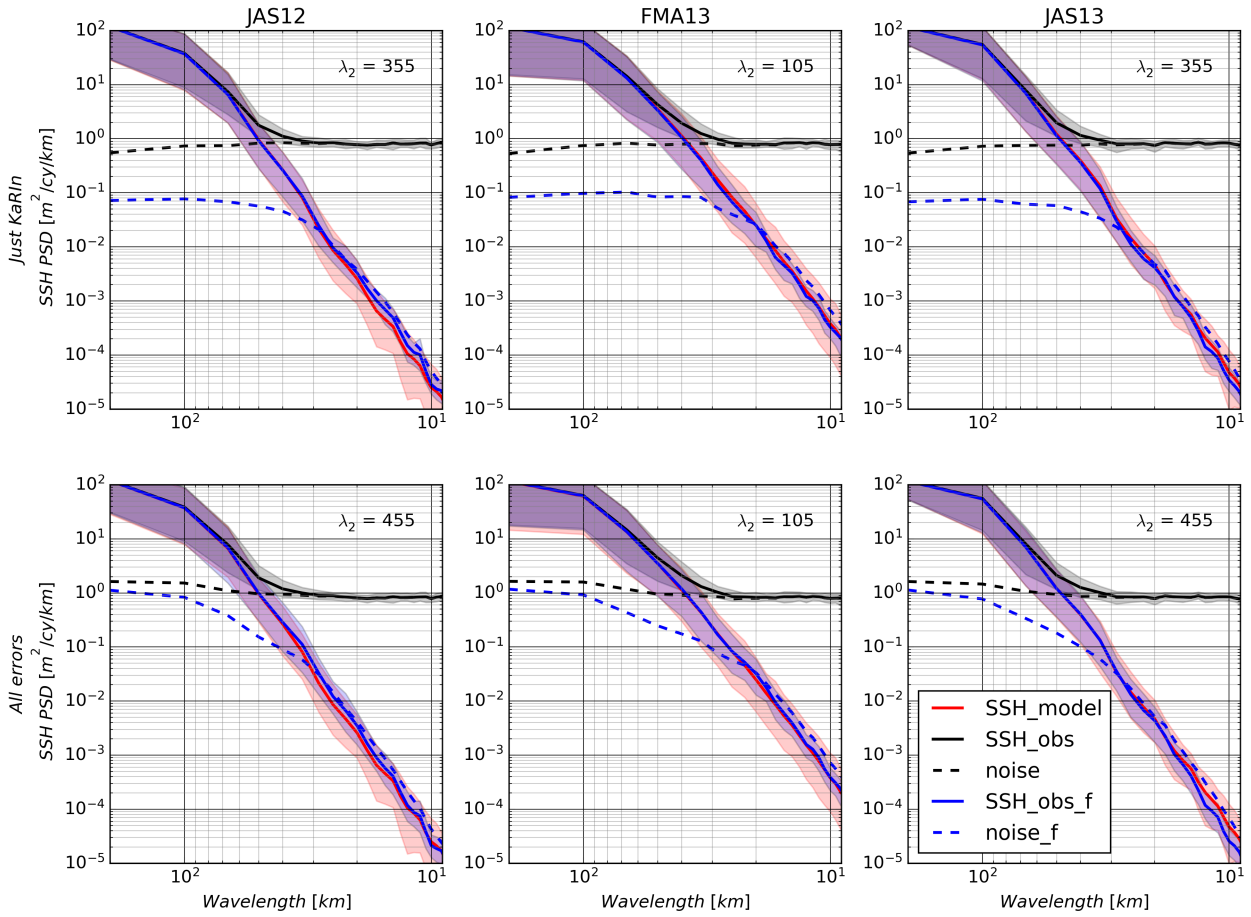

Figure 4.7: Spatial spectra of the model interpolated data (SSH_model) are shown in red, and that of the pseudo-SWOT data (SSH_obs) is in black. Blue lines indicate the filtered pseudo-SWOT spectra (SSH_obs_f) obtained with the same λ_2 as in Figures 4.5 and 4.6. The dashed lines are the noise spectra of SSH_obs (noise) and SSH_obs_f (noise_f). Shaded areas show values between the 5th and 95th percentiles, showing the Power Spectral Density (PSD) variability. Top row shows pseudo-SWOT data with just KaRIn noise added and bottom row shows all errors. Columns represent the different seasonal datasets from left to right: summer 2012 (JAS12), winter 2013 (FMA13), and summer 2013 (JAS13).

4.6 Discussion and Conclusions

Several objectives of the SWOT mission will be met only if the random, small-scale noise and errors affecting the data can be efficiently removed. Small-scale noise, in particular the spatially uncorrelated KaRIn instrument noise, prevents the computation of horizontal SSH derivatives. This limits both the direct estimation of relevant oceanic variables on the SWOT swath and the use of SWOT data to build gridded products of altimetry.

To remove the small-scale SWOT noise, we propose a de-noising method that performs better than conventional convolution-based methods both in terms of RMSE (physical space diagnostic) and spectra. The method, which originates from image processing applications, is based on the regularization of the SWOT SSH data by the penalization of its derivatives of orders 1 to 3 in a variational, optimization framework. This approach is chosen because it is in close connection with the oceanic variables of interest, namely geostrophic velocity and vorticity. After a thorough evaluation based on a large number of simulated SWOT scenes, the variational de-noising method exhibits better performance than standard, boxcar, and Gaussian filters. We find the method performs best when only the second-order derivative (λ_2) is considered in the cost function. Only one parameter needs to be set, which makes the parameterization of the method as simple as a

convolution-based method. We find that this parameter can be set smaller or larger in function of the characteristics of our field: the higher the intensity of the signal, the lower the derivatives penalization needed and thus the value of the parameter (as we find in the FMA13 λ_2 values in contrast to JAS12). Also, if the noise level in our fields is higher (all errors scenario), the more we need to penalize and the larger the parameter value. In other words, the higher the signal-to-noise ratio (SNR), the less we need to penalize our field, and so the smaller λ_2.

The method will require further investigations before operational applications, since we have focused our attention to one particular region (the western Mediterranean Sea), with an ocean circulation free of tidal forcing and a prescribed Significant Wave Height (SWH) of 2 m. The present study shows that, in one single region, the range of optimal parameters changes with the season due to seasonal changes in the ocean surface dynamics. Similar conclusions are certainly expected with respect to regional and dynamical regimes. The NATL60 simulation used here does not include tidal forcing. The behavior and efficiency of the de-noising method may be questioned in the presence of tidal motions and particularly tide-generated internal waves. Finally, the SWH prescribed in the SWOT simulator to compute the KaRIn error amplitude is prescribed to 2 m. As the SWH varies geographically and according to the atmospheric regime, KaRIn errors smaller or larger than those computed for the present study with the SWOT simulator can be expected (*Wang et al.*, 2019a). The first two aspects (geographic variations of ocean dynamics and internal tides) are presently under study using data from several high-resolution simulations that include tidal forcing: the HYbrid Coordinate Ocean Model (HYCOM) (*Chassignet et al.*, 2009), the Massachusetts Institute of Technology general circulation model (MITgcm) (*Marshall et al.*, 1997), and the recent extended NATL60 (eNATL60) simulation (not yet published). This greater range of scenarios will help provide a more generic set of λ_2s to use in function of the ocean dynamics.

The method should also benefit from additional developments to reconstruct more realistic fields of relative vorticity on the SWOT swath and could ultimately lead to the estimation of vertical velocities. The de-noising process inevitably smooths out the very fine-scale, elongated structures usually visible in surface relative vorticity fields (*Sasaki et al.*, 2014). Restoring these structures should be investigated, for example using appropriate image processing techniques (*Deledalle et al.*, 2009; *Yan et al.*, 2013) or methods already developed in the oceanographic community such as Lagrangian advection (*Rogé et al.*, 2015; *Berti and Lapeyre*, 2014). Dynamical models could also be used in a data assimilation framework.

To conclude, this de-noising method opens the way to several relevant applications using the SWOT data, possibly including SWOT data validation, assimilation, and SSH mapping. We mention SWOT data validation due to the inpainting capability of the variational de-noising method, i.e., the fact that the process naturally fills the 20-km gap of the SWOT swath (here the gap is inpainted and emptied again after de-noising to restore SWOT data in the original shape). In other words, the SWOT data are interpolated on the track of the SWOT nadir altimeter. This is obviously relevant for data comparison and validation. De-noising is also interesting to preprocess the SWOT data before their assimilation in ocean circulation models. This actually was a primary motivation for the method development. Computing spatial derivatives of the SWOT data allows the implementation of data assimilation methods that account for SWOT error correlations (*Ruggiero et al.*, 2016; *Yaremchuk et al.*, 2018). Alternatively, the relative vorticity derived from the de-noising can be directly assimilated. This option has not been explored yet to our knowledge. This de-noising method can also be combined with other techniques to improve the assimilation. We particularly think about combining it with the technique recently developed by *Metref et al.* (2019) to significantly reduce the impact of the geometrically structured, highly correlated SWOT errors (roll, phase, timing, and baseline errors). Finally, this study has been done using the noise and errors simulated by the SWOT simulator version 2.21, and these will very likely be different. We anticipate that the method is simple and flexible enough to be easily adapted to more realistic noise and errors.

4.A Calculation of the Laplacian

Laplacian are computed using finite differences, following the method proposed by Reference *Chambolle* (2004). We note h, the image of size $N_x \times N_y$. In a first step, the two components of the gradient are computed as follows ($i = 1, ..., N_x$; $j = 1, ..., N_y$):

$$\begin{array}{rll} (\nabla h)^x_{i,j} & = h_{i+1,j} - h_{i,j} & \text{if} \quad i < N_x \\ & = 0 & \text{if} \quad i = N_x \\ (\nabla h)^y_{i,j} & = h_{i,j+1} - h_{i,j} & \text{if} \quad j < N_y \\ & = 0 & \text{if} \quad j = N_y \end{array}$$

In a second step, Laplacian is computed as the divergence of the gradient. Divergence of vector $\mathbf{a} = (a^x, a^y)$ is computed as follows:

$$\text{div}(\mathbf{a}) = b^x_{i,j} + b^y_{i,j}$$

where:

$$b^x_{i,j} = \begin{array}{ll} a^x_{i,j} - a^x_{i-1,j} & \text{if} \quad 1 < i < N_x \\ a^x_{i,j} & \text{if} \quad i = 1 \\ -a^x_{i-1,j} & \text{if} \quad i = N_x \end{array}$$

and

$$b^y_{i,j} = \begin{array}{ll} a^y_{i,j} - a^y_{i,j-1} & \text{if} \quad 1 < j < N_y \\ a^y_{i,j} & \text{if} \quad j = 1 \\ -a^y_{i,j-1} & \text{if} \quad j = N_y \end{array}$$

The scheme implemented at the boundaries preserves the image size, contrary to what a standard five-point stencil Laplacian operator would do. Preservation of image size is essential in the gradient descent iterations to end up with a final image of size similar to the initial image.

4.B FISTA

To speed up the gradient descent iterations, the Fast Iterative Shrinkage-Thresholding Algorithm (FISTA) algorithm (*Beck and Teboulle*, 2009) is implemented. Setting $t_0 = 1$ and introducing an auxiliary variable y initialized as $y^0 = h^0$, the iterative algorithm of Equation (5.3) becomes the following :

$$\begin{aligned} h^{k+1} &= h^k + \tau \left(m \circ (h_{obs} - y^k) + \lambda_1 \Delta y^k - \lambda_2 \Delta\Delta y^k + \lambda_3 \Delta\Delta\Delta y^k \right) \\ t_{k+1} &= (1 + \sqrt{1 + 4t_k^2})/2 \\ y^{k+1} &= h^{k+1} + \frac{t_k - 1}{t_{k+1}} (h^{k+1} - h^k) \end{aligned} \tag{4.7}$$

4.C Calculation of Spatial Spectra

The spatial spectra used as one of the scores for the de-noising parameterizations are calculated as follows:

1. Apply a linear detrending;
2. Remove the spatial mean;
3. Apply a Tukey window with a 0.5 fraction of the window inside the cosine tapered region;
4. Compute the 1D spatial Fourier power spectra along-track for each SSH swath across-track dimension.

4.D Qualitative Figures of Different Methods

To better illustrate the advantage of our de-noising approach, we show in Figures 4.8 and 4.9 the fields provided by the boxcar and Gaussian methods, corresponding to the λ_2 experiments presented in Figures 4.5 and 4.6. We only show the all errors scenario. Boxcar derivatives fields are very noisy, as it is specially visible for the Laplacian fields. With the Gaussian method, the Laplacian is less noisy than with our method, but the gradient is over-smoothed.

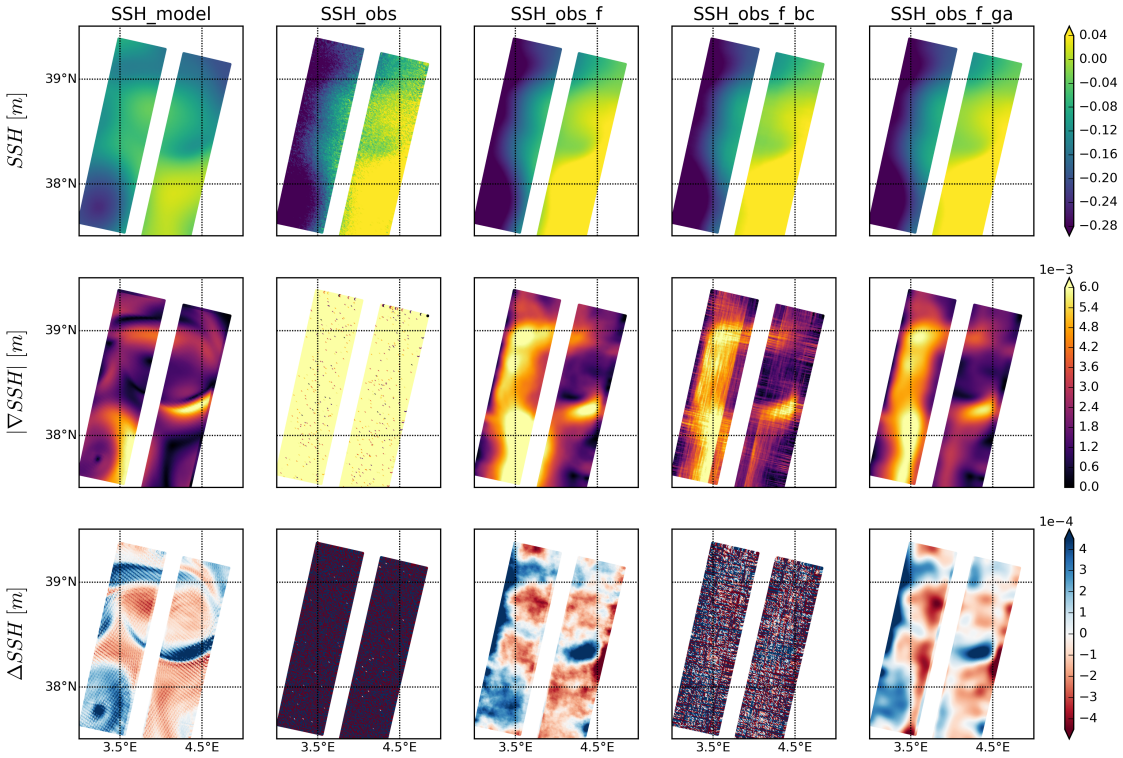

(**a**)

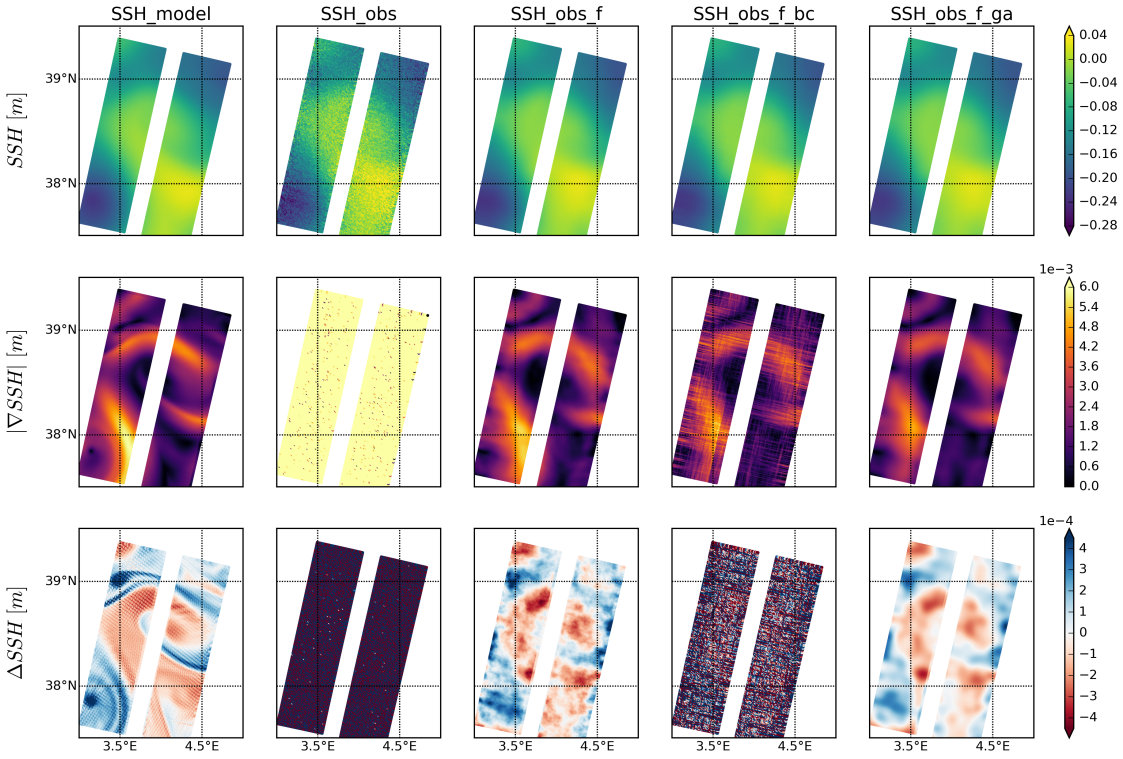

(**b**)

Figure 4.8: Fields of pass 09, cycle 2 (**a**) and 6 (**b**) of the JAS12 all errors dataset. From left to right: comparison between the SSH_model, SSH_obs, SSH_obs filtered with our approach and $\lambda_2 = 455$ (SSH_obs_f), with the optimal boxcar (SSH_obs_f_bc), and with the optimal Gaussian (SSH_obs_f_ga) methods. From top to bottom: SSH, gradient of SSH and Laplacian of SSH.

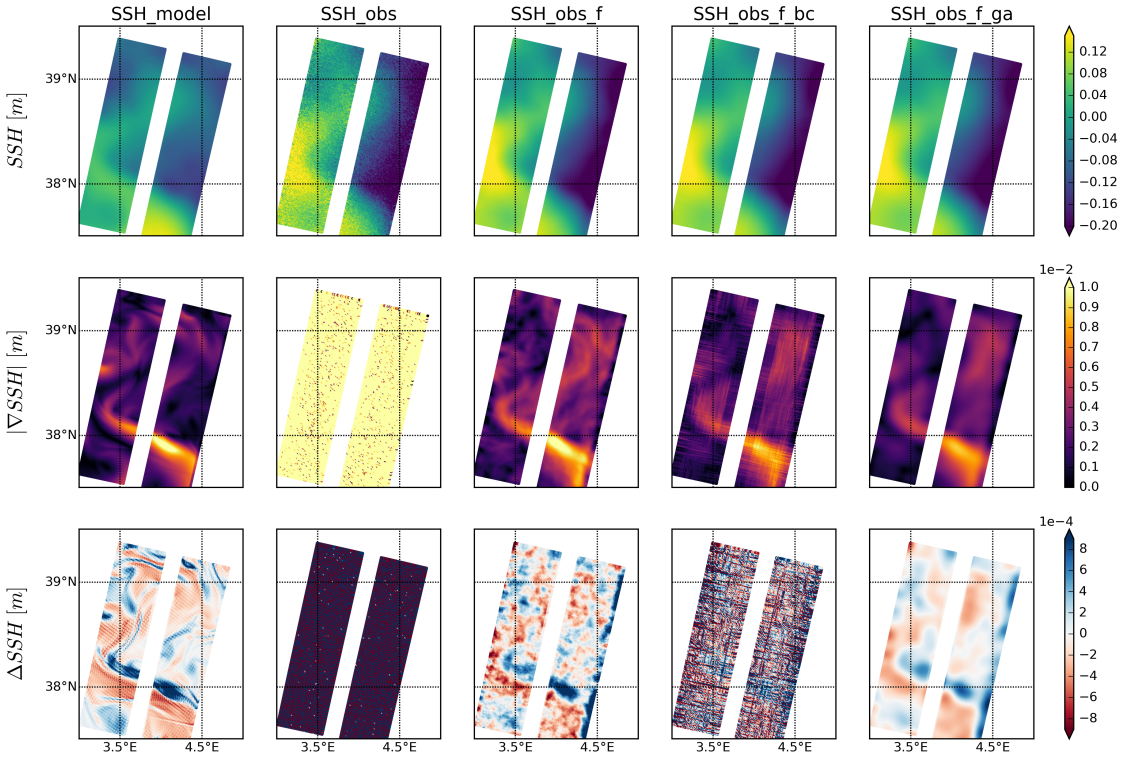

(**a**)

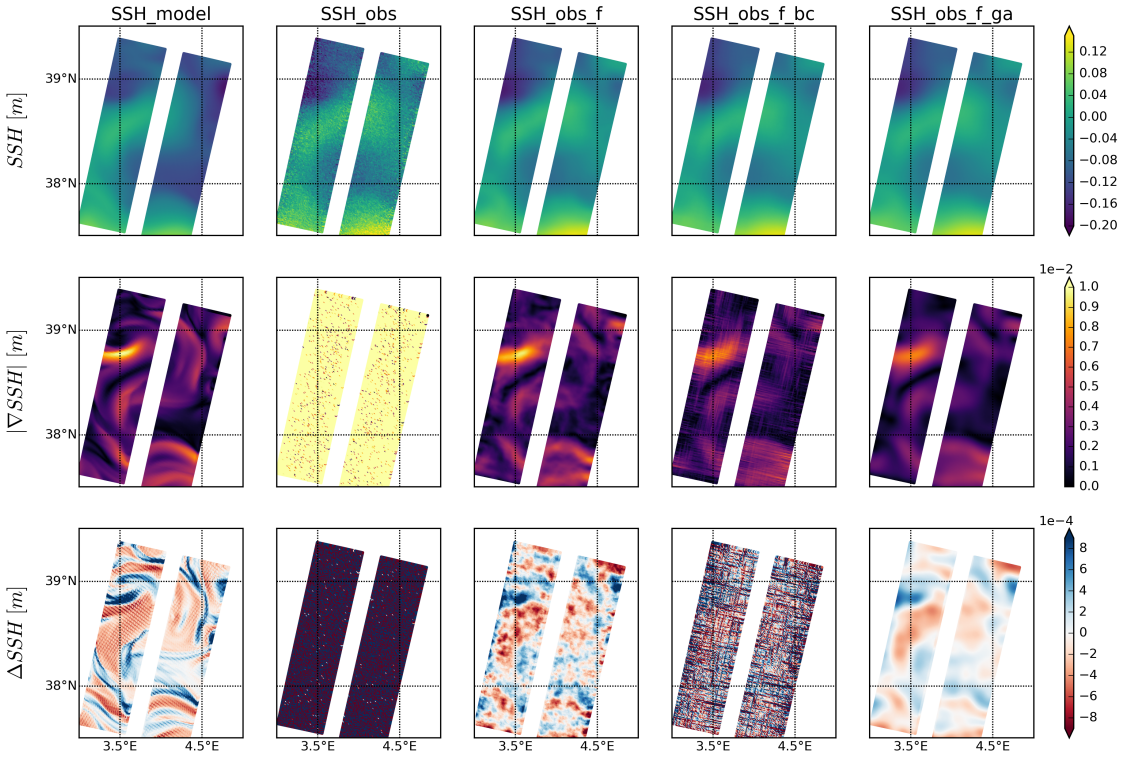

(**b**)

Figure 4.9: Fields of pass 09, cycle 2 (**a**) and 6 (**b**) of the FMA13 all errors dataset. From left to right: comparison between the SSH_model, SSH_obs, SSH_obs filtered with our approach and $\lambda_2 = 105$ (SSH_obs_f), with the optimal boxcar (SSH_obs_f_bc), and with the optimal Gaussian (SSH_obs_f_ga) methods. From top to bottom: SSH, gradient of SSH and Laplacian of SSH.

4.E Softwares

- Standard image techniques: For both boxcar and Gaussian kernel python's scipy.ndimage module was used with the following specific functions:
  - Boxcar filter: $scipy.ndimage.generic\_filter()$
  - Gaussian: $scipy.ndimage.gaussian()$
- Variational regularization method:

  `https://github.com/LauraGomezNavarro/SWOTmodule`

Chapter 5

What will be the finest resolved scale of SWOT SSH data under different dynamical conditions?

Contents

5.1 Introduction

In this chapter, we investigate the finest spatial scale that SWOT could resolve after de-noising, in several regions, seasons and using different OGCMs. In Chapter 4, a method is found to mitigate the impact of SWOT instrumental noise and errors, but large uncertainties remain due to the incomplete understanding of the impact of fast unbalanced motions (e.g. internal gravity waves) on SSH signals, and therefore the impact on the performance of the de-noising algorithm. The surface signature of these oceanic features appears as we move down to small spatial wavelengths, at which previous altimeter missions did not resolve with enough resolution to detect them. Previous chapters show how after applying image de-noising techniques, in some cases, SWOT can resolve spatial scales down to the expected 15 km wavelength (*Fu and Ubelmann*, 2014), whilst preserving the SSH gradients present. This is only tested for the western Mediterranean Sea, so this chapter focuses on different regions and seasons in order to document the variety of regimes that SWOT will sample. Like in the previous chapter, pseudo-SWOT observations are studied for the 3-months long fast-sampling phase in which the satellite's repeat-cycle will be of one day, but with less passes per cycle. In those areas where passes are present, Calibration and Validation (Cal/Val) of the SWOT data will take place (*d'Ovidio et al.*, 2019).

The satellite mission's objective is to resolve wavelengths down to 15 km. *Fu and Ubelmann* (2014), obtained this resolved wavelength by extrapolating a Jason-1 power spectra and seeing where it crossed the baseline requirement defined by the SWOT project team (see fig. 5.1). At this wavelength, one can say that the SSH signal is of the same order as the noise signal. The SWOT spatial resolved wavelength (Ls) can be defined as the wavelength at which the signal and the noise spatial power spectral densities are of the same magnitude (PSD(SSH) $\sim$ PSD(noise)). This has been defined as such in previous studies such as *Fu and Ubelmann* (2014); *Dufau et al.* (2016); *Wang et al.* (2019a).

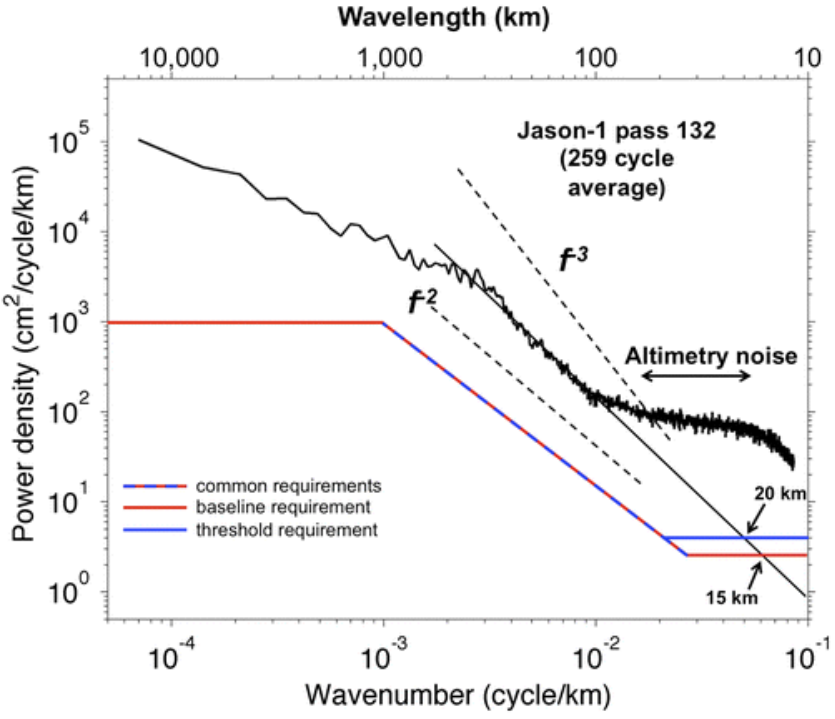

Figure 5.1: The black curve is the wavenumber spectrum of SSH from a Jason-1 descending pass from the central North Pacific to the southeastern Pacific based on 7 years' worth of altimeter data. The black dashed lines represent two power laws (where f denotes wavenumber). The red line represents the SSH baseline accuracy requirement for the SWOT mission. The blue line represents the threshold requirement, which differs from the baseline in the noise performance. The intersection of the accuracy requirement with the SSH signal spectrum represents the expected wavelength resolution of the SWOT observations. (From *Fu and Ubelmann* (2014))

Ls has been previously explored globally by *Dufau et al.* (2016) and *Wang et al.* (2019a). They found that *Ls* will vary geographically and seasonally. *Ls* depends on the SSH spatial spectral level, which as found by *Xu and Fu* (2012), has a high regional variability. This reflects then on the geographical variability of *Ls* from 15 km at low latitudes to around 30 - 45 km at mid and high latitudes (fig. 5.2 (*Wang et al.*, 2019a)). As observed in fig. 5.2, its seasonal variability depends on the region, being higher at high latitudes than low latitudes.

The objective of *Dufau et al.* (2016) was to investigate the mesoscale resolution capabilities of present altimeters and SWOT from SSH spectral slopes. They define this resolution as the intersection of the satellite's error level and the mesoscale band spectral slope. To do this, they assume linearity of the spectral slope, which breaks down in regions where there are high internal tide or other high-frequency signals. For the SWOT error level they use the values from *Peral et al.* (2015) and they take into account seasonal variations like the ones due to the Sea Wave Height (SWH). They derive SWH from Jason-2 over the March to October 2013 period. To obtain the SWOT SSH spectral slope, they assume that current altimeters' SSH spectral slopes are realistic, and use Jason-2's spectra after noise removal. Lastly, they obtain a mean global map of *Ls*, which is a mean from March to October. They find that compared to present altimeters, SWOT will be able to provide better observations of the meso- and submesoscale processes, specially at the western boundary currents.

Wang et al. (2019a) do take into account the non-linearity of the SWOT spectral SSH slope due to the presence of IGWs. They generate noise-free SWOT data from the MITgcm48 LLC4320 simulation, and compare their spectra to the KaRIn noise's. This is the only SWOT error they consider, but like *Dufau et al.* (2016), they do not use a unique noise level, but obtain the KaRIn noise level in function of each region's SWH (more realistically derived from a SWH climatology by *Queffeulou* (2004). They obtain global maps of *Ls* values for the Winter and Summer months by looking at where the pseudo-SWOT noise-free data spectra crosses that of the KaRIn noise. They also look at the monthly and latitudinal variability of *Ls* (fig. 5.2) and find that both eddies and IGWs affect *Ls*.

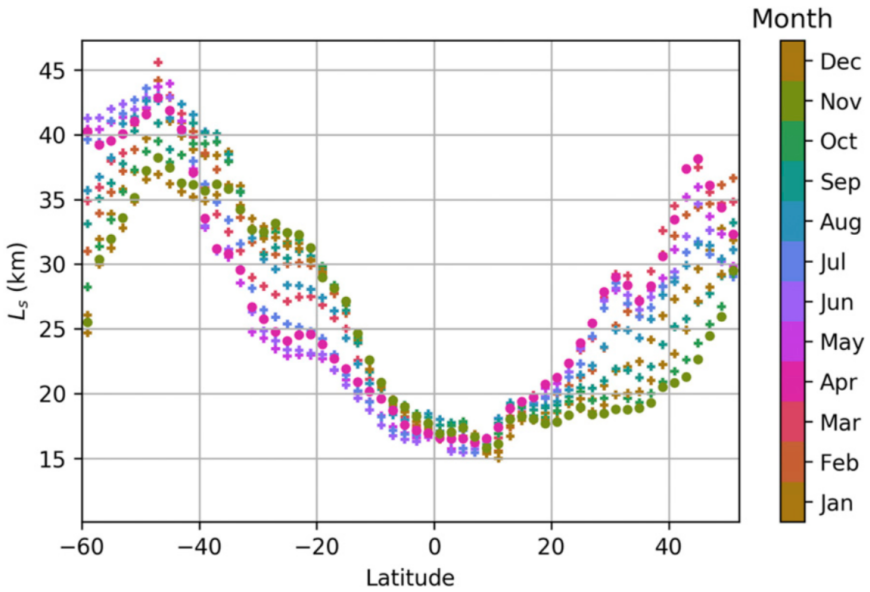

Figure 5.2: Longitudinal median *Ls* [km] as a function of latitude (x axis) and month of year (colour). (From *Wang et al.* (2019a)).

Previous studies like *Torres et al.* (2018) have found that Internal Gravity Waves (IGWs) can have a significant impact on SSH, and that this a major challenge for SWOT. The presence of IGWs can be evaluated using the transition scale (*Lt*), defined as the wavelength at which the SSH signal goes from being dominated by balanced motions to unbalanced wave motions (*Qiu et al.*, 2017). If *Lt* is larger than *Ls*, it means SWOT could observe IGWs (*Wang et al.*, 2019a). This brings insight on which regions the disentanglement of the balanced and unbalanced motions (*Torres et al.*, 2018) could be necessary. It is important because they have different

impacts on the ocean KE budget (*Klein et al.*, 2019), and by separating them, the shear production from SWOT data can be calculated to better understand KE transfers. *Qiu et al.* (2018) argue that removing the signal of IGWs, like internal tides, is crucial to better detect and understand submesoscale balanced motions. Moreover, it is important to know if Lt is greater than Ls as geostrophy is no longer valid below it, which is relevant when deriving variables from SSH, like velocity. (*Torres et al.*, 2019) More complex formulations need to be implemented like for example quasi-geostrophy or a wave-averaged geostrophic balance (*Kafiabad et al.*, 2020). The relationship between Ls and Lt depends not only on the SSH variance, but also on the SWOT noise and error present, specially at small scales. However, de-noising of SWOT data has not been considered in previous studies which compare Ls and Lt (*Qiu et al.* (2017, 2018); *Wang et al.* (2019a)).

The ocean submesoscale remains quite unknown due to the resolution and sampling limitations of oceanographic data. Recent advances in *in situ* and satellite measurements have allowed to improve the data's resolution, but in many cases the temporal or spatial sampling is not enough. For now, the source of data that can provide the best submesoscale information both in terms of resolution and sampling are Ocean General Circulation Models (OGCMs). This is key as OGCMs are necessary to generate pseudo-SWOT data, and because, as found in previous studies (e.g. (*Gómez-Navarro et al.*, 2018; *Wang et al.*, 2019a; *Gómez-Navarro et al.*, 2020)), the smallest resolved wavelength by SWOT will highly depend on the SNR at scales below approximately 50 - 60 km. Unfortunately, a large uncertainty in SWOT Ls exists because of OGCMs discrepancies at these small spatial scales. *Savage et al.* (2017a); *Ajayi et al.* (2020) found how different OGCMs were capable to resolve the submesoscales, but that discrepancies existed between them, specially at the submesoscale. To account for the uncertainty of the SSH variance at small wavelengths, three different high-resolution OGCMs including tidal forcing are used here which provide a range of scenarios. The models are presented in Section 5.3, where a brief comparison is made to characterize them.

In this context, this study's motivation is to investigate SWOT's smallest resolved wavelength (Ls). *Fu and Ubelmann* (2014); *Dufau et al.* (2016); *Wang et al.* (2019a) used extrapolated SSH spectra from current altimeters or model SSH outputs. Except *Wang et al.* (2019a), they did not generate pseudo-SWOT data and none considered any de-noising algorithms. This study revisits the estimation of Ls, focusing on:

- including all the known sources of errors (from SWOT simulator),
- the use of most recent noise-filtering algorithm for SWOT data explored in previous chapters,
- the uncertainty associated to the choice of a specific model.

5.2 Study regions

Four study regions are chosen. The two main criteria for selecting them are:

• Range of oceanic dynamical regimes:

As Ls depends on the SSH spectral level, regions with contrasted dynamical regimes need to be chosen. One of the dynamics considered is if it is a high or low eddying region. Then, as the presence of IGWs have a high impact on the SSH spectral energy levels, specially at small scales, regions with a high and low IGWs signal are selected. To decide which regions present a high IGWs signal, the results found by *Ray and Zaron* (2016); *Savage et al.* (2017b) are used. In fig. 5.3 (adapted from *Savage et al.* (2017b)), the black boxes show some of the regions with a high presence of IGWs. These are near the Azores Islands and Cape Verde Islands in the North Atlantic Ocean, and near the French Polynesian Islands in the South Pacific Ocean.

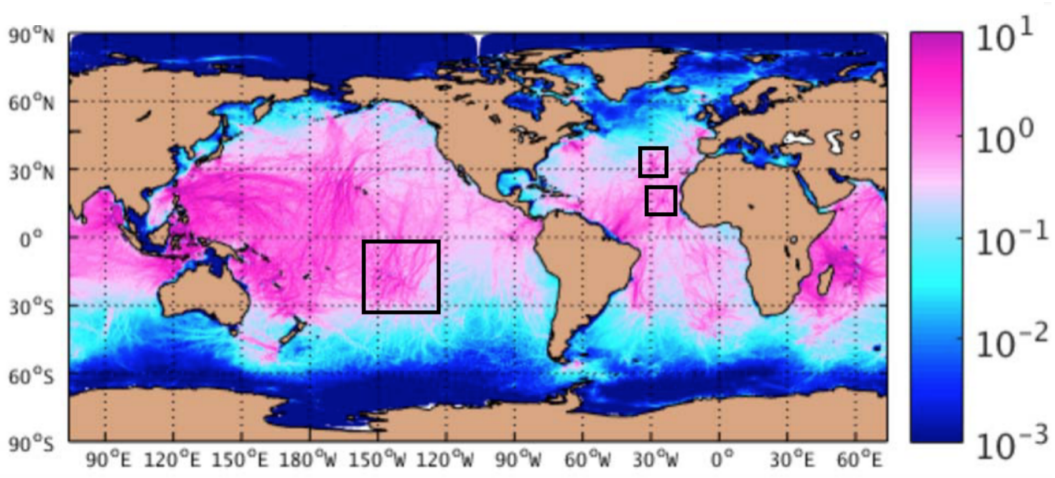

Figure 5.3: Global steric SSH variance (cm^2) in the semidiurnal band (frequencies 1.86-2.05 cpd). Black boxes show some of the regions with a high internal waves signal (adapted from *Savage et al.* (2017b)).

• Fast-sampling (Cal/Val) phase cross-overs:

In this study, the focus is on the fast-sampling phase, so another criterion for the selection of the study regions is the presence of a fast-sampling phase cross-over. The focus is on this phase as, in addition to helping prepare for the Cal/Val phase and the *in situ* campaigns being prepared for it (*d'Ovidio et al.*, 2019), its 1 day repeat-cycle allows to better capture IGWs' signal (if present). The phase's nadir tracks are shown in fig. 5.4 in black.

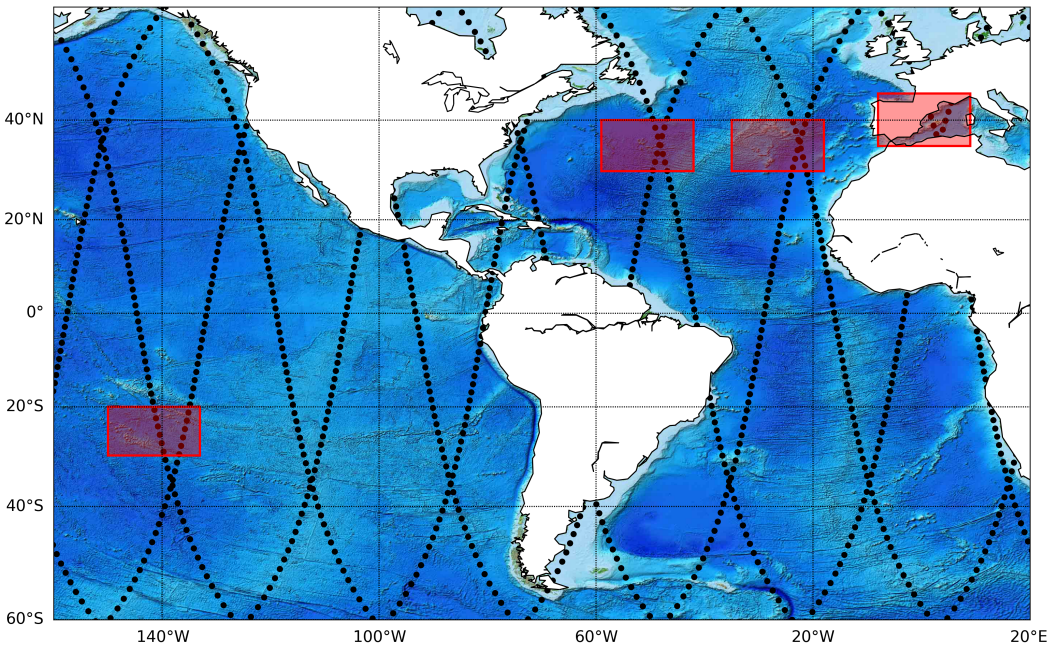

Figure 5.4: Black dotted lines show fast-sampling phase nadir tracks. Red boxes are the selected study regions, from west to east: PAC, GST, AZO and WMED.

Considering the above stated points, the region shown by red boxes in fig. 5.4 are selected. These regions are:

- Western Mediterranean (WMED): This region has a low presence of IGWs (fig. 5.3) and low energetics (in comparison to other regions like the Gulf Stream). It includes the presence of a cross-over site. In addition, it provides continuity to previous chapters of this PhD.
- Gulf Stream (GST): Although the selected region is a bit east from the Gulf Stream jet itself, the cross-over region selected (fig. 5.4) is on its high-eddying region. It is region with a medium presence of IGWs as observed in fig. 5.3.
- Azores (AZO): This region has a lower signal of IGWs than the south Pacific region, but has one of the highest signals in the North Atlantic. It has lower energetics than the Gulf Stream region (eddy kinetic energy-wise). Moreover, the Azores region is selected instead of the Cape Verde region shown in fig. 5.3, as it includes a fast-sampling phase cross-over (fig. 5.4).
- South Pacific (PAC): This is one of the regions shown in fig. 5.3 with the highest signal of IGWs. In order to capture their signal as much as possible, the selected box is a bit north from the exact SWOT cross-over (fig. 5.4).

5.3 Pseudo-SWOT data generation from OGCMs

5.3.1 OGCMs description

The dataset of this study consists of hourly SSH outputs of three tide-resolving OGCMs available to the SWOT Science Team. They are used to generate pseudo-SWOT data (via the SWOT simulator (version 3; *Gaultier et al.* (2016)). Three different OGCMs are used because they provide a range of scenarios to account for the uncertainty of the SSH variance at small wavelengths. Two of them are global simulations (HYCOM25 and MITgcm48) and one basin scale (eNATL60). eNATL60, in addition to providing continuity to previous studies (NATL60 used in *Gómez-Navarro et al.* (2020)), it has the highest spatial resolution, but is not global. HYCOM25 and MITgcm48 both are global and include tidal forcing, but one does better at lower frequencies (HYCOM25) and the other at higher frequencies (MITgcm48). MITgcm48 simulates more energetic super-tidal motions than HYCOM25 (*Savage et al.*, 2017a), but can produce too much energy at low frequencies. Table 5.1 below summarizes some of the main characteristics of these OGCMs (for more details on these OGCMs see Section 2.1).

Table 5.1: OGCMs main characteristics.

Model	eNATL60	HYCOM25	MITgcm48
Domain	N. Atlantic	Global	Gobal
Time-span	mid-June 2012 to October 2013	January to December 2014	September 2011 to November 2012
Horizontal grid	1/60° : 0.9km - 1.6km	1/25° : $\sim$ 4 km	1/48° : 0.75 - 2.3 km
Vertical coord.	Z partial cells	Hybrid (Z, isopycnal and sigma)	Z-levels
Vertical grid	300 levels : 1m - 50m	41 levels	90 levels : 1m - 480m
Tidal forcing	Yes	Yes	Yes

Table 5.1 shows how the three OGCMs have different numerics, like horizontal and vertical resolutions. They also have different integration periods and spin-up strategies. Nevertheless, they are all a priori able to

simulate scales down to 20 km adequately. A variety of plausible levels of SSH variance is then provided with these 3 OGCMs at the study sites.

5.3.2 OGCMs comparison: RMS and spatial spectra

For each region, the Winter and Summer months are explored. A 3 month period is chosen, the expected duration of the fast-sampling phase. As in Wang et al. (2019), February, March and April (FMA) months and August, September and October (ASO) are selected respectively for the northern hemisphere Winter and Summer. The same 3 months periods were chosen for the 3 simulations, but the year is not the same, as they all have different time-spans (see table 2.1). Although the simulations do not include data assimilation, and as so do not really represent the year the simulation is said to run for, it is important to note that the forcings (e.g. atmospheric forcing) will have been chosen corresponding to that year, and this could affect the larger mesoscale conditions. After having decided the regions and temporal periods for this study, hourly SSH data is extracted from each OGCM for the red-bordered boxes shown in fig. 5.4, for the FMA and ASO months. This in total renders 22 scenarios (recall the PAC region is not available for eNATL60).

Before generating the pseudo-SWOT data, a minimum exploration and comparison of the OGCMs' outputs in the different scenarios is done. For this a land-free (for simplicity) subregion of the red boxes shown in fig. 5.4 is used. For all regions except WMED it is chosen to be 5° by 5°. Limited by the presence of land, the WMED region is 2° by 2°. The subregions are chosen so that the SWOT fast-sampling phase passes fall within them as much as possible. Root Mean Square (RMS) and spatial spectra are calculated for each scenario. This allows to compare the energetics and its variability between regions, seasons and OGCMs.

Then the RMS for N hourly SSH snapshots is calculated as:

$$RMS = \sqrt{\frac{1}{N}\sum_{i=1}^{N}(SLA - \overline{SLA})^2} \tag{5.1}$$

; where SLA (Sea Level Anomaly) is $SSH - \overline{SSH}$, being $\overline{SSH}$ the area-weighted spatial average for each snapshot.

The RMS FMA and ASO months results are shown in figures 5.5 and 5.6, respectively. They show the range of dynamics between the four selected regions, and the differences between seasons and OGCMs. The WMED region presents the lowest RMS values and GST the highest due to intense eddying activity, except in Summer for PAC HYCOM25 and AZO MITgcm48. In this case, PAC and AZO are the regions with the highest RMS due to the strong presence of IGWs. The OGCMs RMS differences in terms of magnitude are low during FMA in all regions except AZO. In terms of structure positions, the AZO region is the only one with similar RMS between the three OGCMs, being lowest at the centre of the subregion and increasing towards the borders. In the ASO months, there is higher OGCM differences in each region, both in RMS magnitude and structure. At WMED ASO, MITgcm48 is the least energetic, and at GST ASO, eNATL60 has the highest RMS values. At AZO ASO, MITgcm48 RMS has a higher magnitude than the other OGCMs. The difference between MITgcm48 and the other OGCMS is higher in ASO than FMA, which is when the IGWs signal is expected to be larger. The overenergetics found by *Savage et al.* (2017a) in MITgcm48 shows here. Finally, at PAC ASO, HYCOM25 shows higher values than MITgcm48. The overenergetics found in AZO due to IGWs doesn't show in this region, although it has a high IGWs signal too (fig. 5.3). The RMS confirm some OGCMs characteristics stated in Section 5.3.1 and show that in the presence of IGWs, larger differences amongst OGCMs are observed. The RMS differences give insight on which scenarios we can expect to have higher or lower Ls. Nevertheless, these differences could be affected by the SWOT spatial sampling. Red boxes in figures 5.5 and 5.6 show the fast-sampling phase passes, and for example in the FMA GST scenario, the HYCOM25 SWOT passes fall less within the high RMS areas than for the other OGCMs.

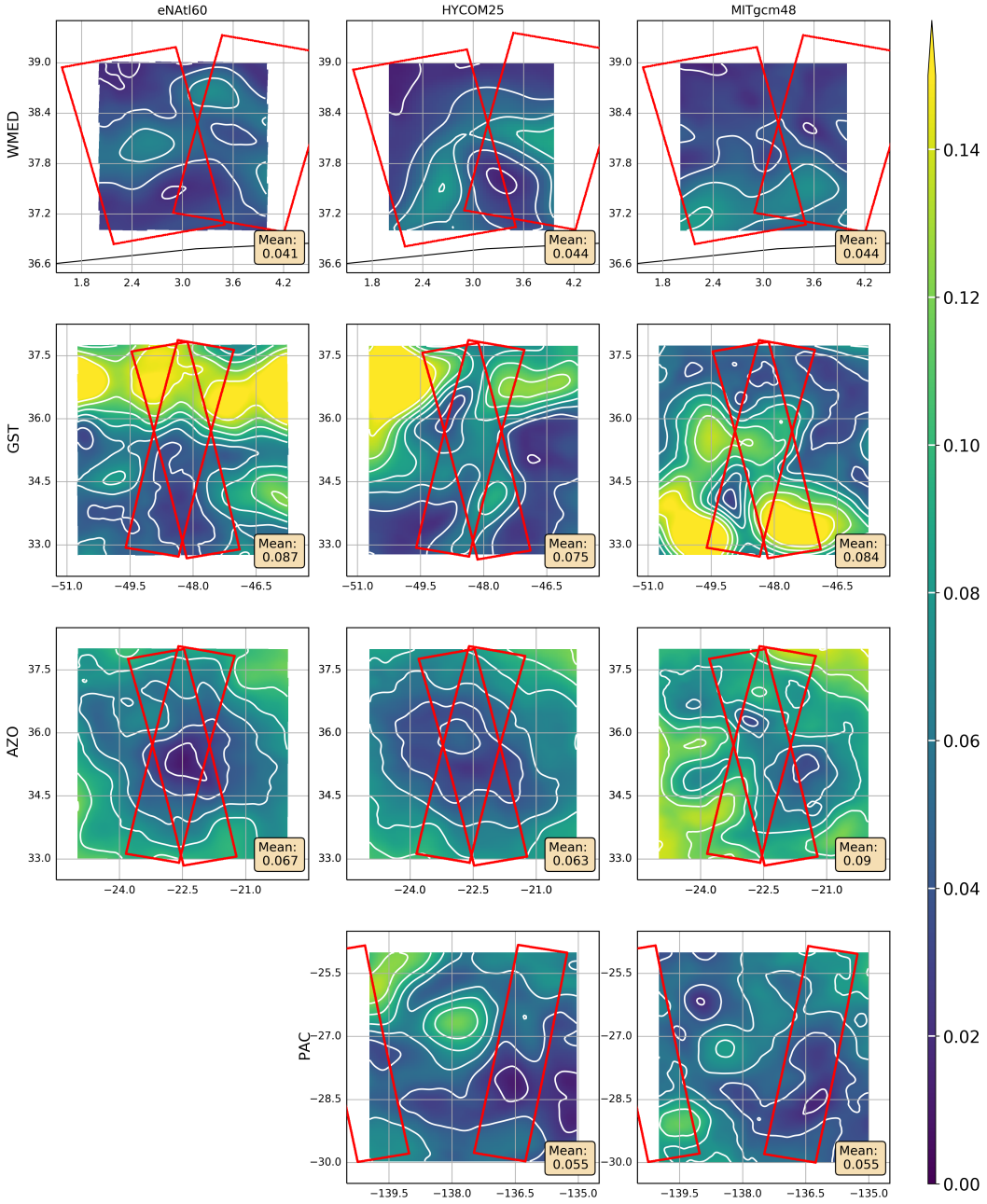

Figure 5.5: RMS [m] for the FMA months. Red boxes show the fast-sampling phase pass subregions. The mean RMS is shown at the bottom right of each subplot.

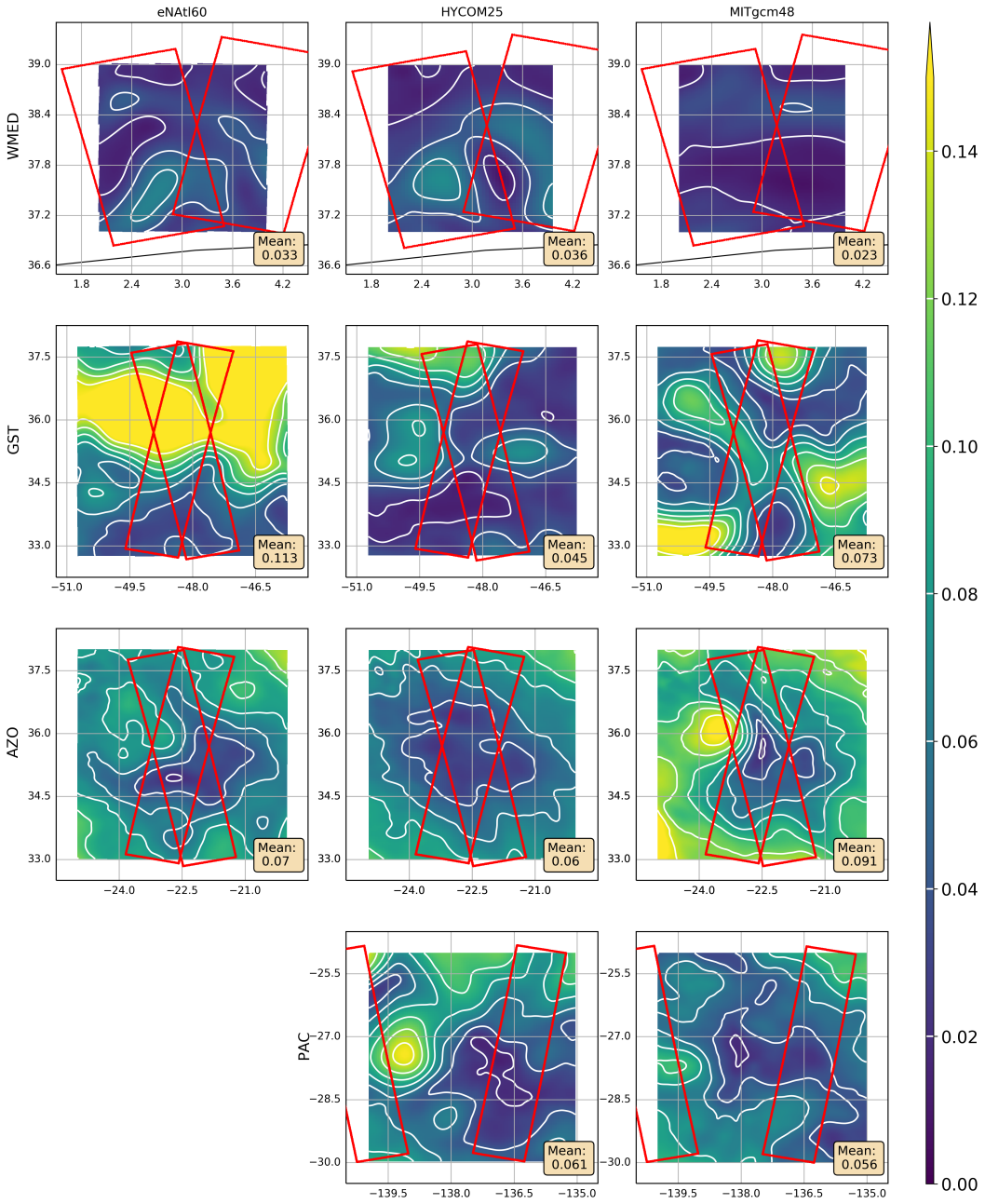

Figure 5.6: RMS [m] for the ASO months. Red boxes show the fast-sampling phase pass subregions. The mean RMS is shown at the bottom right of each subplot.

Spatial spectra of the OGCM SSH hourly outputs are calculated for each scenario. Like RMS, this allows to have a preliminary idea of the dynamics of each scenario and the differences between the OGCMs. Firstly, 2D spatial spectra of the regions shown in fig. 5.4 are obtained and compared to the estimated noise level as specified by *Esteban-Fernandez* (2017). The specific noise level used here corresponds to a KaRIn noise level for a 2 m SWH following *Wang et al.* (2019a). In fig. 5.7, two scenarios are shown: GST FMA and AZO ASO. The first one being a scenario with high-energy, eddying dynamics and the second with a high presence of IGWs. Fig. 5.7 shows that for both scenarios, at large-scales some similarities exist between the models, showing very similar spectral slopes. Below wavelengths of about 100 km, all show different SSH variance levels. This reflects the need of using these 3 different OGCMs. The AZO ASO scenario was also chosen because it is one of the expected regions where the SSH signal diverges between the models. The SSH field is specially different in MITgcm48 due to the higher IGWs signal (at the supertidal band) as explained by *Savage et al.* (2017a). Figure 5.7 shows how at all wavelengths, MITgcm48 shows a higher energy level.

Moreover, in the AZO ASO spectra, although the energy levels differ between OGCMs, energy peaks are very well aligned (i.e., found at the same wavelengths). These peaks can be observed at 120 km, 70 and 30 km wavelengths, and are probably due to IGWs. In the GST FMA spectra, at large-scales, MITgcm48 and eNATL60 are similar, then they diverge, specially below 70 km. HYCOM25 shows a lower signal at all wavelengths probably due to its horizontal resolution, which is about half that of the other two OGCMs. (It is important to note that the spectral results should only be considered below 300 km). Lastly, fig. 5.7 shows the uncertainty of the SSH variance at small wavelengths. As one can see, this consequently has an effect on the wavelength at at which the SWOT noise levels becomes larger than the SSH variance level (PSD). This justifies the importance of using different OGCMs to evaluate Ls.

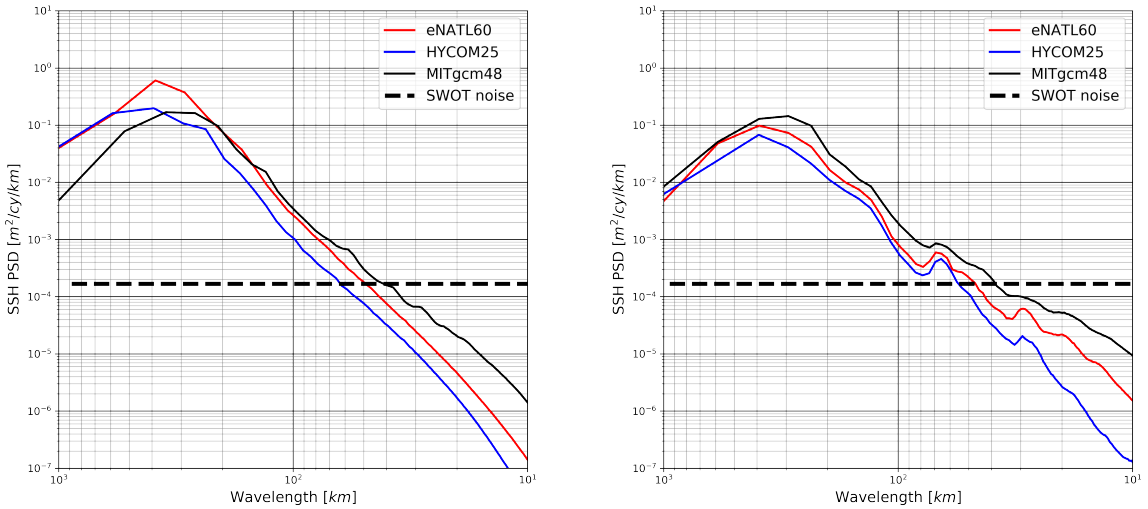

Figure 5.7: Comparison of OGCMs' 2D spatial Power Spectral Densities (PSD) for two scenarios. Left: Gulf Stream in Winter (GST FMA). Right: Azores in Summer (AZO ASO). The black line shows the SWOT KaRIn noise level for a Significant Wave Height (SWH) of 2 m from *Wang et al.* (2019a).

Secondly, the OGCMs' spatial spectra are compared to nadir altimeter data. OGCMs render different energy levels, specially at small wavelengths. At present it is difficult to validate spatial SSH spectra at small wavelengths, but the OGCM spectra can be compared with the satellite altimeter spectra. The models' spectra are compared to spatial spectra from SARAL-Altika and Sentinel3. Fig. 5.8 shows the results of SARAL-Altika data compared to eNATL60 SSH interpolated in space and time to the altimeter's tracks for the same scenarios as fig. 5.7. Down till where the altimeter noise starts to become significant, i.e., when the spectra flattens, both spectra are very similar. Lastly, fig. 5.8 AZO ASO eNATL60 spectrum doesn't capture the IGWs energy peaks as clearly as in fig. 5.7. This shows how the satellite sampling strategies are important in adequately capturing these phenomena. Moreover, due to these differences in spatial coverage of the two-dimensional model outputs and the altimeter tracks' one-dimensional data, and its effect on the spectral calculations, it is relevant to show figures 5.7 and 5.8 separately.

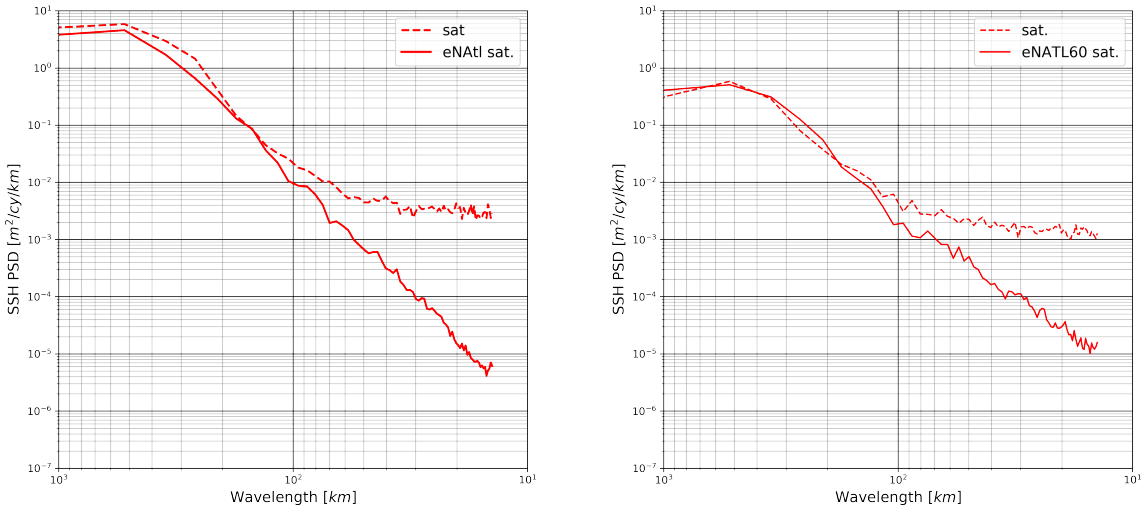

Figure 5.8: Power Spectral Densities (PSD) of SARAL-Altika altimeter (sat.) compared to eNATL60 interpolated to the satellite's tracks (eNATL60 sat.). Left: Gulf Stream (GST) region for Winter (FMA) months. Right: Azores (AZO) region for Summer (ASO) months.

5.3.3 Pseudo-SWOT data

The SWOT simulator for Ocean Science (version 3; *Gaultier et al.* (2015)) is used to generate pseudo-SWOT data in the 22 scenarios. The SWOT swath sections analyzed are shown in red in figures 5.5 and 5.6, and have a 2 km gridsize. The SWOT simulator renders two SSH output variables: the model data interpolated onto the SWOT grid (SSH_model) and with added noise (SSH_obs). The residual noise can be obtained by calculating the difference from these two fields. An initial SWOT resolved spatial scale (Ls_i) can be obtained from these. The 1D spatial spectra (averaged across-track and in time for each scenario) of SSH_model is compared to the spectra of the residual noise of SSH_obs (noise_o). These spectra are shown in fig. 5.9. (Please note that the western Mediterranean region is 2° by 2° while the rest are 5° by 5°, due to the presence of land). The different OGCMs present different SSH_model spectra, with different energy levels, and sometimes different slopes. Like in fig. 5.7, within each scenario the OGCMs' spectra specially differ at small wavelengths. This again shows the importance of using different OGCMs in this study. Indeed, one particular model may get closer to observations in one specific region, but it is unclear at this stage whether one model stands out compared to observations in all cases. Although random realizations of the noise are used to generate SWOT noise and errors in the SWOT simulator, this results in very similar residual noise spectra at all wavelengths for all OGCMs and scenarios. As between figures 5.7 and 5.8, differences between fig. 5.7 and the GST FMA and AZO ASO subplots in fig. 5.9 exist. Specially in the AZO ASO scenario, where the IGWs peaks are less pronounced than in fig. 5.7. The SWOT fast-sampling phase sampling also has an effect on spectrally capturing the ocean dynamics.

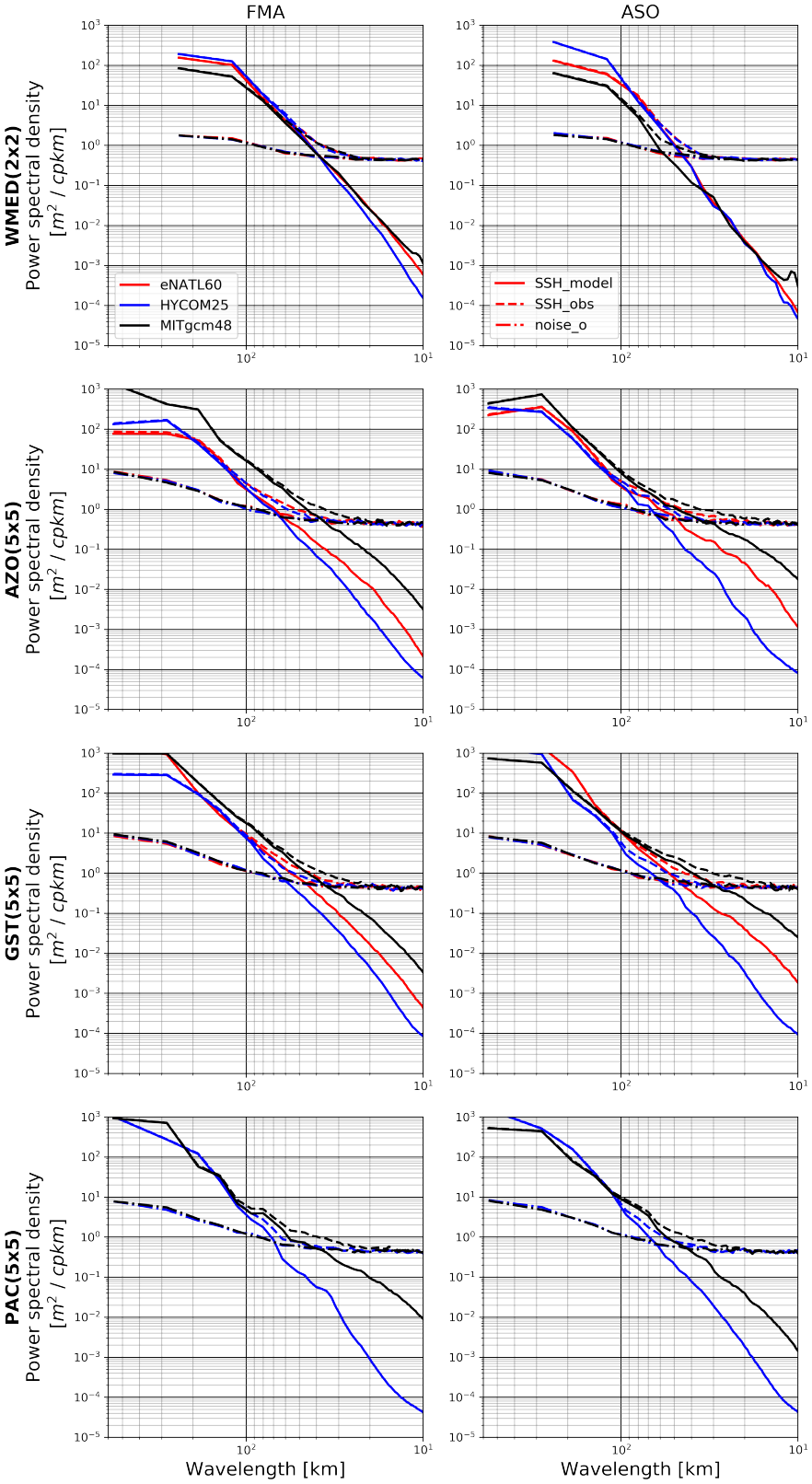

Figure 5.9: Spatial spectra comparison of eNATL60 (red), HYCOM25 (blue) and MITgcm48 (black) for each region and season. In each subplot, the SSH_model (noise and error free pseudo-SWOT data), SSH_obs (pseudo-SWOT data) and noise_o (SSH_obs residual noise) spectra corresponding to each model are shown. Spectra shown are the mean of all passes and cycles of each scenario. Top to bottom: western Mediterranean (WMED) 2° by 2° subregion size (2x2), Azores (AZO) 5° by 5° (5x5), Gulf Stream (GST) 5x5 and Pacific (PAC) 5x5. The regions are shown in fig. 5.5. FMA months are shown on the left column and ASO on the right.

5.4 De-noising of pseudo-SWOT data

5.4.1 Derivatives penalization de-noising method

In this study, the derivatives penalization de-noising method presented in Chapter 4 (*Gómez-Navarro et al.*, 2020) is used. The objective of this method is to remove the small scale, uncorrelated SWOT noise and error components. Few other techniques have been applied to remove this small scale noise. *Chelton et al.* (2019) and *Gómez-Navarro et al.* (2018) apply a convolutional kernel to smooth the signal and *Pujol et al.* (2012); *Gaultier et al.* (2016); *Qiu et al.* (2016) use optimal interpolation. These manage to remove the small scale noise, but remove part of the signal too, which specially affects the retrieved fields of current velocity and vorticity (derived from SSH). A first implementation of the derivatives penalization method on fast-sampling phase pseudo-SWOT data in the western Mediterranean (from NATL60 SSH daily outputs) by *Gómez-Navarro et al.* (2020), allowed the retrieval of the SSH spectral signal down to the mission's objective, 15 km. To efficiently remove the SWOT uncorrelated noise and error components and achieve these results, a second order penalization (a Laplacian regularization) of an image, h (SWOT SSH field here) is applied by minimizing the cost function. The cost function (J(h)) is expressed as:

$$J(h) = \frac{1}{2}\|h - h_{obs}\|^2 + \frac{\lambda_2}{2}\|\Delta h\|^2 \tag{5.2}$$

This is implemented iteratively as:

$$h^{k+1} = h^k + \tau(h_{obs} - h^k + \lambda_2 \Delta\Delta h^k) \tag{5.3}$$

; where $\tau = 1/(1 + 64\lambda_2)$ to guarantee the stability of the iterations.

This technique is parameterized by setting λ_2 and the number of iterations (by a maximum number of iterations or a convergence criterion). The latter has been previously parameterized by *Gómez-Navarro et al.* (2020), so only λ_2 is left to parameterize. Unfortunately, from equation 5.2 only the order of magnitude of λ_2 can be estimated. Moreover, in practice the optimal λ_2 parameterization will vary with SWOT's Signal to Noise Ratio (SNR). Therefore, the optimal values found in *Gómez-Navarro et al.* (2020) cannot be used here, even for the western Mediterranean region, as the signal and noise levels are different. The signal differs because a simulation with tidal forcing is used here and the noise level differs due to different SWOT grid sizes. As explained by *Chelton* (2019), the noise level increases as the SWOT grid decreases in size. Nevertheless, the optimal λ_2 values found in *Gómez-Navarro et al.* (2020) are used to choose an initial range of λ_2 values to test. The same procedure is then used to find the optimal λ_2 value for each scenario. It consists of comparing the filtered pseudo-SWOT data with the noise-free SWOT data generated by the SWOT simulator by using Root Mean Squared Error (RMSE) on SSH, its gradient and Laplacian; and SSH spatial spectra. RMSEs give information on the correct representation of the oceanographic structures present, whilst SSH spatial spectra give information on the energy conservation and wavelengths resolved. It was found that when all errors were included in the simulations, only the RMSE on the Laplacian of SSH was of use to parametrize the optimal λ_2, given the small impact of the correlated errors on the Laplacian. Consequently, two scores can be used to determine the optimal λ_2: RMSE on the Laplacian of SSH and the Mean Spectral Ratio (MSR), based on SSH spatial spectra. As the main interest here is Ls, which is calculated from SSH spatial spectra, the MSR diagnostic is the score which will be used to find the optimal λ_2. RMSEs of the Laplacian of SSH are shown to assess the performance of the optimal λ_2 found from MSR on the SSH signal phase. Lastly, although not the main motivation of this study, from a methodological perspective, implementing this method is interesting to test if it is still effective under the presence of IGWs.

5.4.2 Optimal de-noising parameterization

The de-noising algorithm penalizing the Laplacian of SSH is applied to the pseudo-SWOT data (SSH_obs) of all scenarios. The de-noised SSH_obs variable obtained is referred to as SSH_obs_f. The same initial range of λ_2s is applied to each scenario. The MSR score is used to then find the optimal λ_2 for each scenario. This parameter, as it depends on the SSH signal, can vary depending on the OGCM, region and season. A systematic investigation is performed in order to find the optimal λ_2, and the results are shown in fig. 5.10. The optimal λ_2 is found at the minimum MSR value. The smaller the value of MSR, the closer the spectra from the filtered field (SSH_obs_f) is to the true spectra (SSH_model). Fig. 5.10 shows that the minimum MSR score obtained in all scenarios and OGCMs are very good. All values are below 0.075, except for MITgcm48 WMED ASO where it's about 0.1 (here an anomalous energy peak is observed at 10 km in fig. 5.9).

A set of optimal λ_2s (one for each OGCM) is obtained for each scenario and shown in table 5.2. The values go from 1 to 54. This is in accordance with the range of dynamics investigated here, varying between regions, seasons and OGCMs. As MITgcm48 is the most energetic model, it has the lowest λ_2 in all cases, followed by eNATL60 and then HYCOM25. As the latter is less energetic, the noise has a greater effect on it (small SNR), and so needs a larger λ_2. The values are quite close for all three OGCMs in the WMED region, which as shown in fig. 5.9, the three models exhibit similar SSH variances. A seasonal difference can be observed too. In WMED, the optimal λ_2 values are smaller in Winter than in Summer, which makes sense with the higher energy levels observed in the region during Winter. In the AZO region, the opposite happens. Due to the presence of IGWs, Summer presents higher energetics than Winter. The high IGW signal in AZO in Summer brings up the energy level at the small scales (flattening the SSH spectra), where the SWOT noise starts to dominate. At GST, the optimal λ_2 is slightly smaller for Summer in eNATL60 and MITgcm48, but smaller in Winter for HYCOM25. In the GST region, there is also a IGW signal in Summer like in AZO, but it is much lower. What seems to happen is that the IGW signal is still important in the eNATL60 and MITgcm48 models, but relatively lower in HYCOM25. Nevertheless, the seasonal optimal λ_2 difference is low in this region. Lastly, for PAC, the optimal λ_2 is smaller in Winter for HYCOM25 and in Summer for MITgcm48. The signal of IGWs in the FMA HYCOM25 spectra are below the energy level of the ASO spectra, whilst in MITgcm48, the flattening of the SSH spectra in FMA by IGWs increases above the ASO SSH spectra at small scales. This could be explained by the results found by (*Savage et al.*, 2017a), where HYCOM25 performs better at the low frequencies (large wavelengths) and MITgcm48 at high frequencies (small wavelengths). Overall, the optimal λ_2 values found agree well with the results found in Section 5.3 on the energetic differences between regions, OGCMs and seasons.

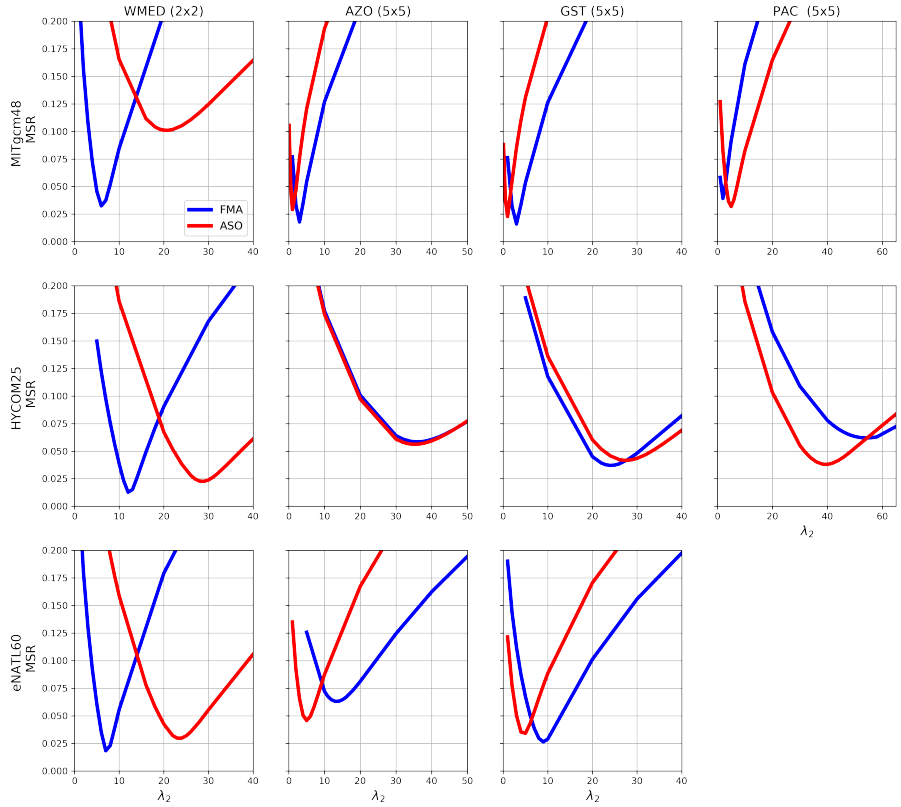

Figure 5.10: Mean Spectral Ratio (MSR) in function of λ_2 comparison for the different scenarios. Top to bottom: Outputs from MITgcm48, HYCOM25 and eNATL60 simulations. From left to right: western Mediterranean (WMED 2x2), Açores (AZO 5x5), Gulf Stream (GST 5x5) and Pacific (PAC 5x5) regions. FMA and ASO months are shown in blue and red, respectively.

Table 5.2: Optimal λ_2 for each scenario. Blue for FMA and red for ASO.

		OGCM		
		eNATL60	HYCOM25	MITgcm48
Regions	WMED	7 | 24	12 | 29	6 | 21
	AZO	13 | 5	36 | 35	3 | 1
	GST	9 | 5	24 | 28	3 | 1
	PAC	-	54 | 39	2 | 5

All subregions studied are 5° by 5° except for WMED, which to not include land, it is limited to 2° by 2°. To check if the results found above on the optimal λ_2 depend on the subregion size, the results obtained for the 5° by 5° subregions are compared to those rendered by a 2° by 2° size. For eNATL60 and MITgcm48, the same optimal λ_2 is obtained for both subregion sizes. For HYCOM25 the values differ, but are still close. As an example, in fig. 5.11 the results for the Gulf Stream region are shown. The optimal λ_2 values are exactly the same for both sizes for eNATL60 and MITgcm48. The HYCOM25 values differ by only 1 and 6 for FMA and ASO, respectively. This is beneficial as it implies λ_2 does not have to be re-tuned. Fig. 5.11 shows too

that MSR values for 2° by 2° regions are systematically higher than for the 5° by 5°, specially moving away from the optimal λ_2 value. Consequently, although the optimal λ_2 values does not seem to be very affected by the region size, the impact of choosing an non-optimal λ_2 on the MSR score, does. If the selected region is much larger than 5° by 5°, different oceanic structures could be present and thus maybe have an impact on the optimal λ_2 value. Even though it may differ, if it remains the same region, it should not vary much from the one found with a 5° by 5° region or smaller. In a more technical sense, this result supports the robustness of the de-noising method and the MSR score used for its evaluation.

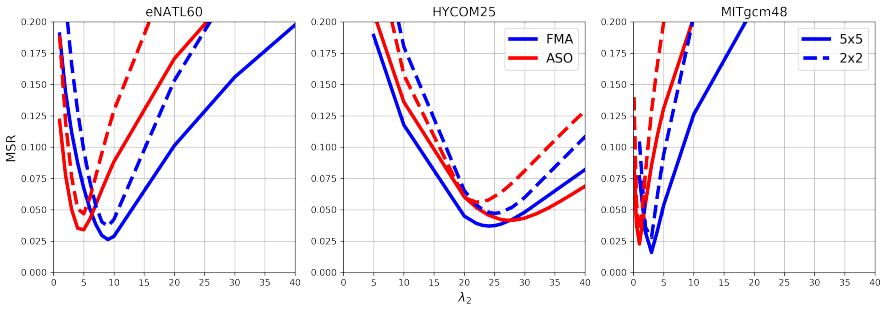

Figure 5.11: MSR comparison for different subregion sizes, 5x5 (bold) and 2x2 (dashed) in the Gulf Stream region. FMA (blue) and ASO (red) months are plotted for the eNATL60, HYCOM25 and MITgcm48 (left to right).

The optimal λ_2 values from MSR scores are compared to those obtained from the Laplacian of SSH RMSE. This allows to asses how well the de-noising method does regarding the phase of the signal, or in other words, how accurately it recovers the oceanic structures present. The results of the RMSE residual of the Laplacian of SSH (RMSE of SSH_obs_f as a percentage of RMSE of SSH_obs) are shown in fig. 5.12. In all scenarios the RMSE residual is very low, being less than 10% in most scenarios. No matter the oceanic dynamics of the scenario, the de-noising algorithm correctly retrieves the Laplacian of SSH. The optimal λ_2 found with the MSR diagnostic is systematically lower than the optimal value found with the Laplacian RMSE. This is expected as the effect of the noise is amplified in SSH derivatives. Nevertheless, in most cases it is within the 5% range shown in fig. 5.12, so the RMSE residual increment due to using the optimal λ_2 from MSR is less than 5%. In this particular study, as the main focus is on obtaining Ls from SSH spectra, no adjustments in the λ_2 parameterization need to be done. If the use of the SWOT de-noised data was different and needed better de-noised SSH derivatives, like for example deriving vertical velocities, the λ_2 value could be adjusted, and chosen slightly higher than that obtained with the MSR score.

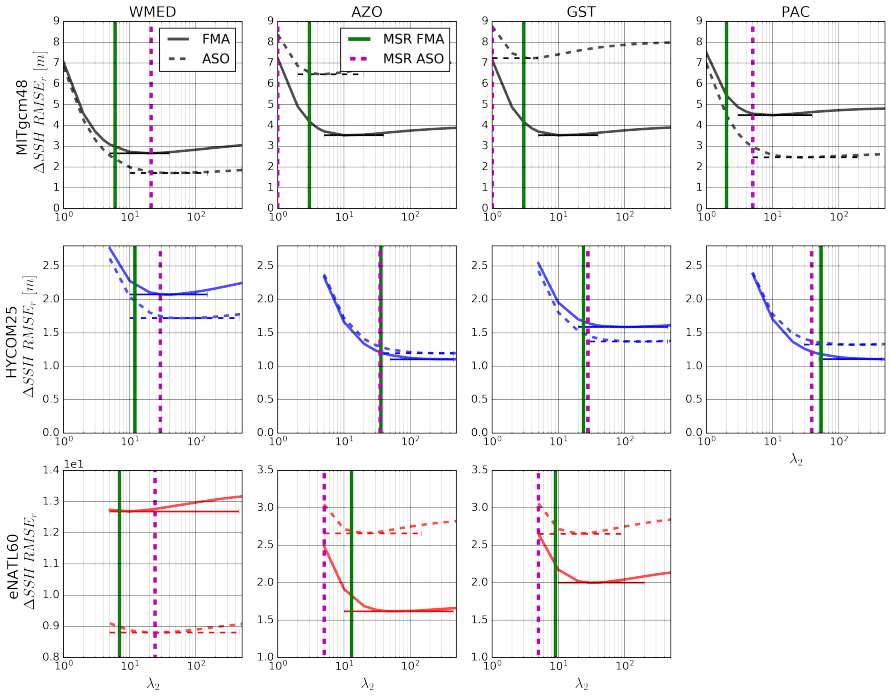

Figure 5.12: RMSE residuals for the Laplacian (ΔSSH) for FMA (bold) and ASO months (dashed). From top to bottom: MITgcm48, HYCOM25 and eNATL60 results. From left to right: western Mediterranean 2x2 (WMED), Açores 5x5 (AZO), Gulf Stream 5x5 (GST) and Pacific 5x5 (PAC) regions. Horizontal bars show the range of λ_2 values that provide scores higher than the minimum RMSE by less than 5%. For comparison the vertical lines show the MSR optimal λ_2 for FMA (bold green) and ASO months (dashed magenta).

5.5 SWOT resolved scales

Once the optimal λ_2s were found, all the elements to re-evaluate Ls after de-noising (Ls_f) were available. This is done by obtaining the spatial spectra of the residual noise of SSH_obs_f (noise_f); where SSH_obs_f is the SSH_obs field filtered with the optimal λ_2 obtained from the MSR score. Then, Ls_f is found by finding the wavelength at which the spectra of SSH_model and noise_f intersect. This is implemented for the mean spectra of each scenario and OGCM. As an example, the results of the GST FMA scenario are shown in fig. 5.13 (the figures of the other scenarios are shown in Appendix 5.A). Fig. 5.13 on the left shows SSH_model with the PSDs of SSH_obs and SSH_obs_f and on the right SSH_model with the respective noise residuals. On the left subplots the value of Ls_i and Ls_f are indicated. The SNR and the Percentage of Noise Removed (PNR) are evaluated at Ls_i and Ls_f and shown on the right subplots. These diagnostics help to evaluate the SSH signal at these 2 wavelengths. The SNR is calculated for SSH_obs (SNR_o) and SSH_obs_f (SNR_f) as SSH_model over noise_o and noise_f, respectively. The PNR is also calculated as:

$$PNR = \left(1 - \frac{noise\_f}{noise\_o}\right) * 100 \tag{5.4}$$

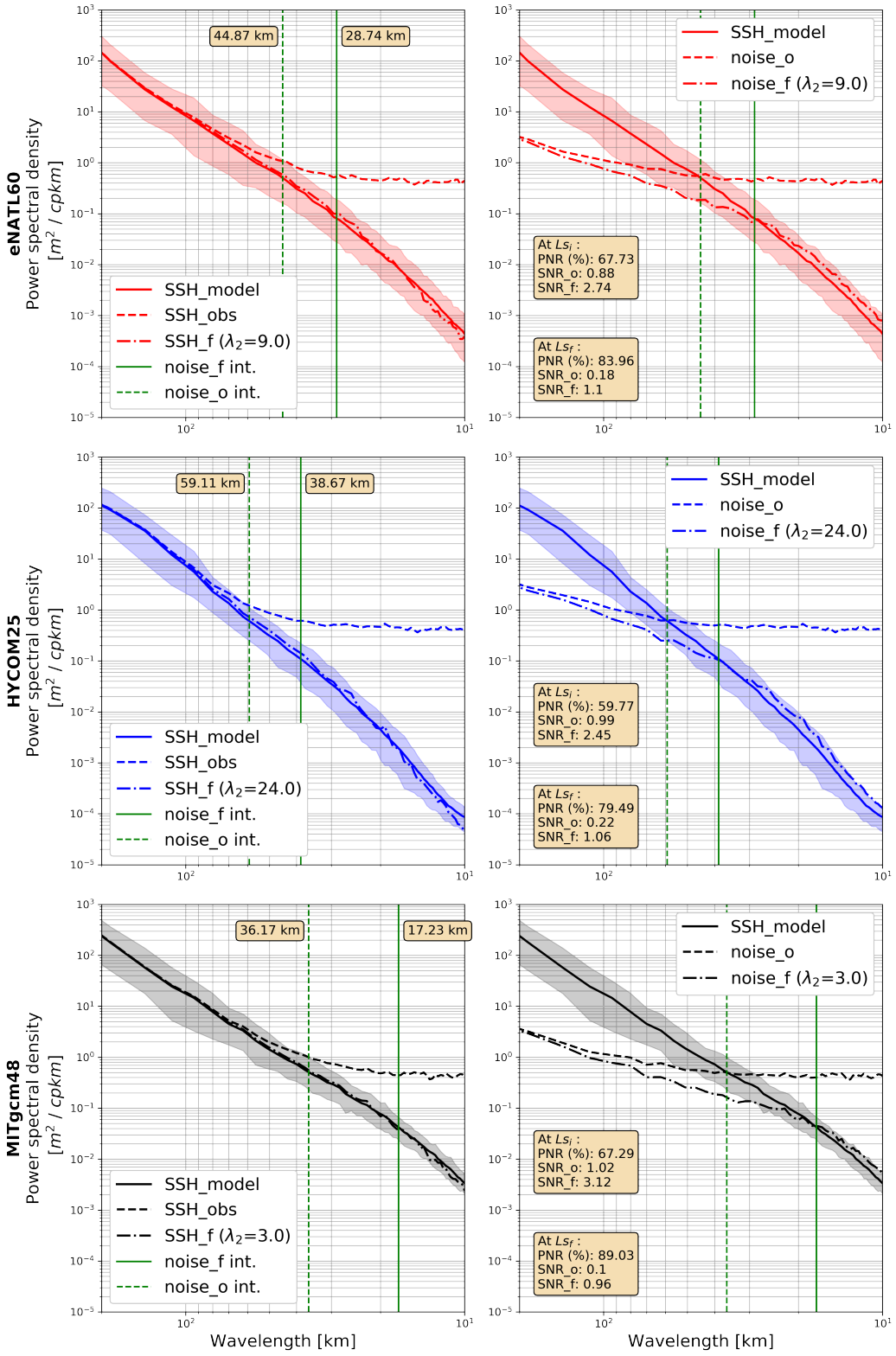

Figure 5.13: Spatial spectra for the Gulf Stream Winter scenario (GST FMA). SSH_model is compared to SSH_obs and SSH_obs_f (left) and to noise_o and noise_f (right) spectra. The shaded areas show values between the 5th and 95th percentiles of SSH_model, showing its Power Spectral Density (PSD) variability. Top to bottom: eNATL60, HYCOM25 and MITgcm48 OGCMs outputs shown. Green dashed (bold) lines show Ls_i (Ls_f). In the left panels the exact Ls values are shown and in the right panel the values of SNR_o, SNR_f and PNR at Ls_i and Ls_f.

Ls_i and Ls_f values are retrieved from fig. 5.13-like figures (see Appendix 5.A) and summarized in table 5.3 and fig. 5.14. Ls_i values predicted by MITgcm48 are systematically the smallest, followed by eNATL60 and HYCOM25, except for WMED ASO. This again is in accordance with the higher energetics observed in the MITgcm48 outputs in all scenarios except in WMED ASO as observed in figures 5.6 and 5.9. Overall, there is a good agreement between the OGCMs' Ls in the WMED region, but there is a large difference across OGCMs in the other regions. In WMED FMA the same Ls are obtained for all OGCMs, but in fig. 5.21 it can be observed that actually small differences do exist. These are not captured due to the discrete wavelengths rendered by the spectral method. Table 5.3 and fig. 5.14 show that there is a systematic reduction of Ls_i thanks to the de-noising algorithm. This reduction goes from 10 km in MITgcm48 WMED ASO to 30 km in eNATL60 AZ0 FMA. The reduction seems to be affected by the energy level at small-scales. This can clearly be observed in the AZO FMA scenario, where eNATL60 and HYCOM25 have the same Ls_i, but Ls_f is greater for HYCOM25 than eNATL60. Looking at fig. 5.9, eNATL60 has higher PSD values at small wavelengths than HYCOM25. The same happens in PAC MITgcm48 between FMA and ASO. In FMA (Summer) IGWs are present, making the energy level at small-scales higher than in ASO (Winter), and thus a smaller Ls_f in FMA than ASO. Lt values derived from *Vergara et al.* (2020) are also shown in table 5.3 and fig. 5.14 for all scenarios except WMED for which data is not available. Comparing Ls_i to Lt, some HYCOM25 values are above Lt, and some other values are quite close (e.g. eNATL60 GST FMA). After de-noising, all the OGCMs predict an Ls (Ls_f) clearly below Lt in all regions and seasons.

Table 5.3: SWOT resolved wavelengths pre-filtering (Ls_i) and post-filtering (Ls_f) for each scenario in km. Blue for FMA and red for ASO. Last column shows the transition scale (Lt) in km found by *Vergara et al.* (2020).

		OGCM						Lt
		eNATL60		HYCOM25		MITgcm48		
		Ls_i	Ls_f	Ls_i	Ls_f	Ls_i	Ls_f	
Region	WMED	37	**23**	37	**23**	37	**23**	-
		44	**32**	44	**32**	54	**44**	-
	AZO	66	**36**	66	**53**	36	**18**	76
		49	**26**	66	**45**	34	**15**	62
	GST	45	**29**	59	**39**	36	**17**	48
		45	**27**	59	**34**	27	**12**	53
	PAC	-	-	66	**53**	42	**20**	128
		-	-	59	**42**	42	**27**	96

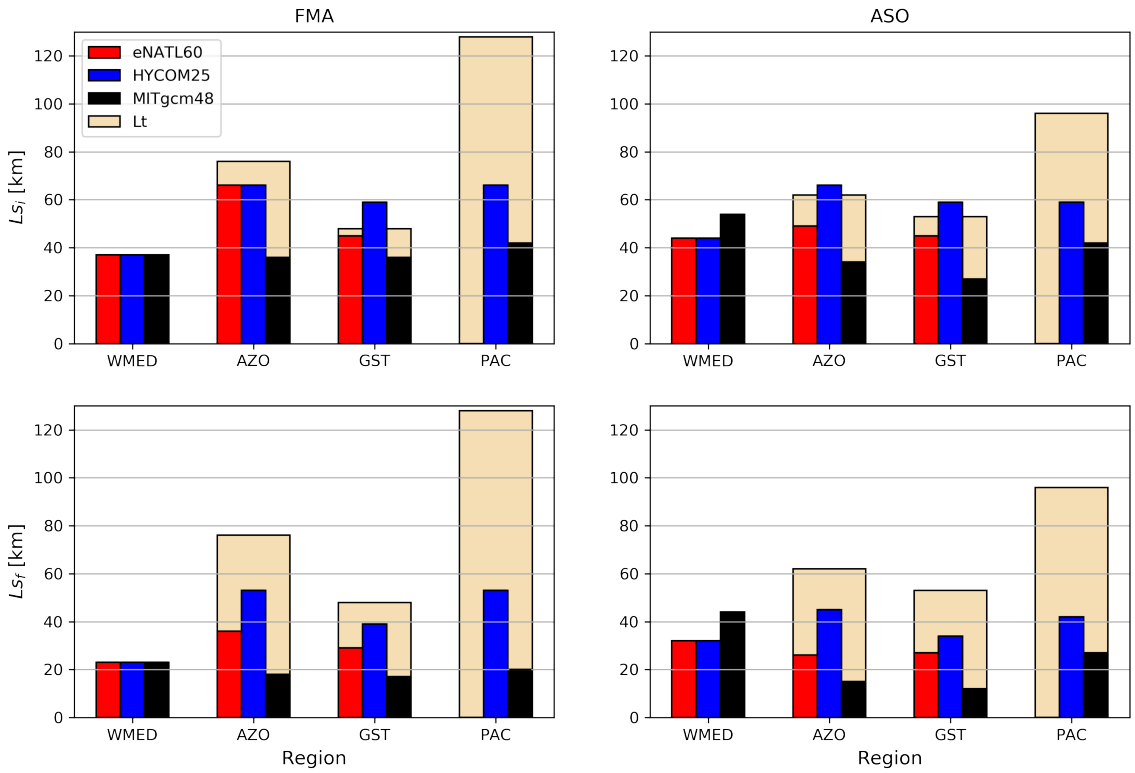

Figure 5.14: SWOT resolved scale (Ls) [km] values pre-filtering (Ls_i) (top) and post-filtering (Ls_f) (bottom), for the FMA (left) and ASO (right) months. Mean transition scale (Lt) of each region for FMA and ASO months obtained from *Vergara et al.* (2020) is shown .

The improvements of the de-noising method on the SWOT data are not only reflected on the reduction of Ls, but also on the high percentage of noise removed. Looking at the PNR values at Ls_i, these go from 51% to 77% (table 5.4); and at Ls_f from 66% to 93% (table 5.5). The PNR values at Ls_i are lower than at Ls_f probably because the SNR values at Ls_i are better (higher) than at Ls_f. In other words, there is more noise to remove at Ls_f than Ls_i, so more space for improvement. It is important to note, that the PNR values are calculated at different Ls for each OGCM in each scenario. For example, looking at the scenario GST FMA shown in fig. 5.13, HYCOM25 has the lowest PNR at Ls_i, but it is not because it has the highest SSH spectra level (as observed in fig. 5.9, but because PNR is calculated at a higher wavelength (HYCOM25 has a higher Ls_i value as shown in fig. 5.14). Therefore, the comparison between OGCMs and scenarios becomes complex, but the relevant information provided by tables 5.4 and 5.5 is that their values are above 50% in all cases.

Table 5.4: Percentage of Noise Removed (PNR) at Ls_i for each scenario. Blue for FMA and red for ASO months.

		OGCM		
		eNATL60	HYCOM25	MITgcm48
Regions	WMED	72% | 76%	75% | 77%	73% | 64%
	AZO	51% | 59%	57% | 57%	67% | 56%
	GST	68% | 63%	60% | 59%	67% | 63%
	PAC	-	56% | 64%	61% | 65%

Table 5.5: Percentage of Noise Removed (PNR) at Ls_f for each scenario. Blue for FMA and red for ASO months.

		OGCM		
		eNATL60	HYCOM25	MITgcm48
Regions	WMED	89% | 89%	93% | 90%	88% | 73%
	AZO	79% | 80%	66% | 78%	87% | 82%
	GST	84% | 78%	79% | 89%	89% | 87%
	PAC	-	73% | 83%	80% | 81%

5.6 Retrieved SWOT Fields and Spatial Spectra

The high PNR values reflect on the fields of SSH derivatives. Figures 5.15 and 5.16 show an example of an eNATL60 AZO FMA pass with a high and low presence of correlated errors, respectively. Even in the example with a high presence of correlated errors (fig. 5.15), the most energetic features observed in the gradient of SSH_model can be observed in SSH_obs_f. The retrieved field of the Laplacian is quite good except for the signal of the correlated errors remaining in the right outer border of the swath. This KaRIn noise is the highest across-track at the swath's outer borders, but it could also be due to the residual of the uncorrelated component along-track of the correlated errors. When the presence of correlated errors is low, like in fig. 5.16, the retrieved results of SSH and its gradients are visually close to the SSH_model fields. The magnitude and the shape of the oceanic structures are well retrieved with the de-noising method.

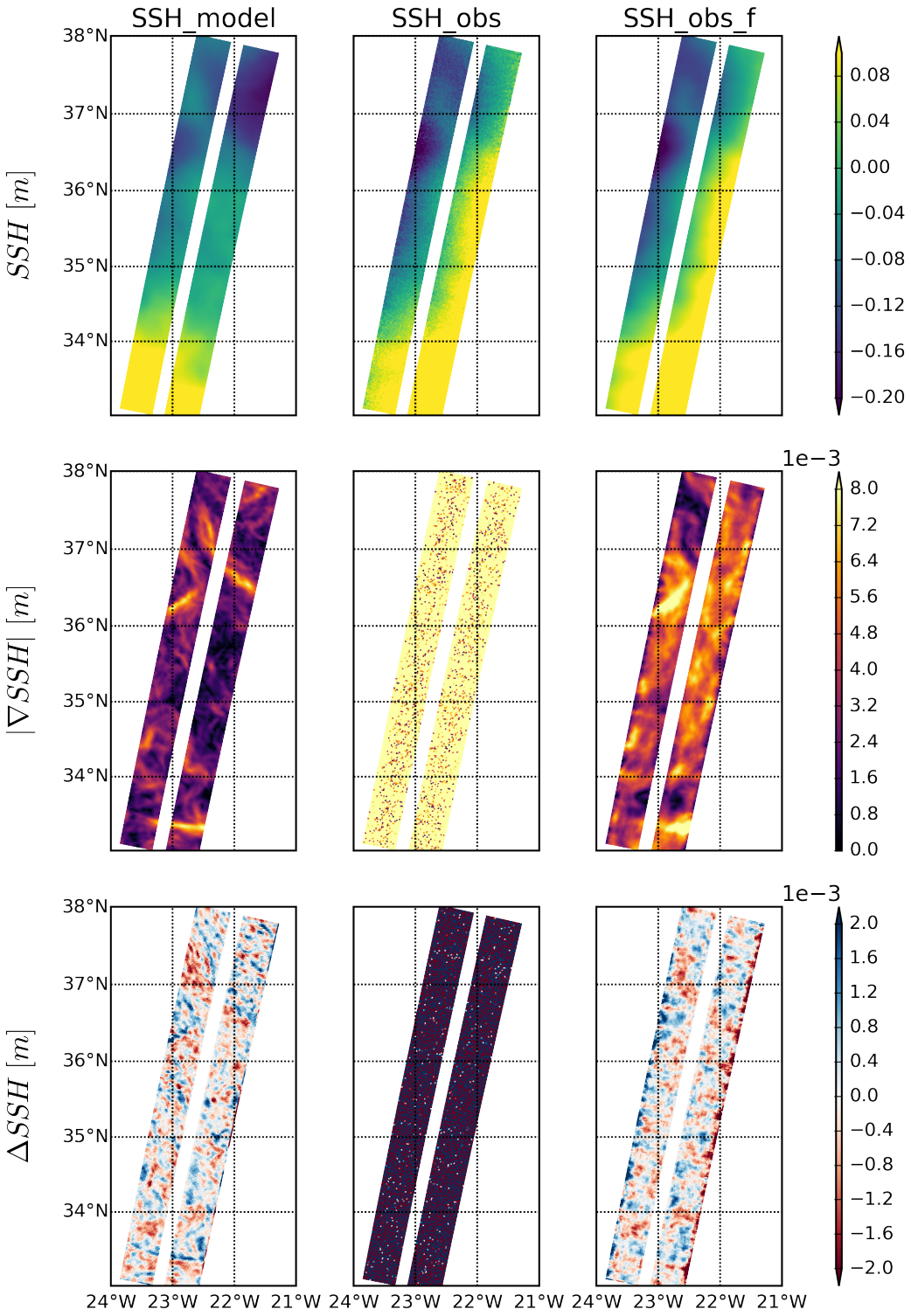

Figure 5.15: Fields of pass 11, cycle 83 of the FMA AZO eNATL60 dataset. From left to right, model data interpolated to SWOT grid (SSH_model), SSH_model with noise and errors added (SSH_obs) and SSH_obs filtered with the optimal λ_2, 13 (SSH_obs_f). From top to bottom: SSH, gradient of SSH and Laplacian of SSH.

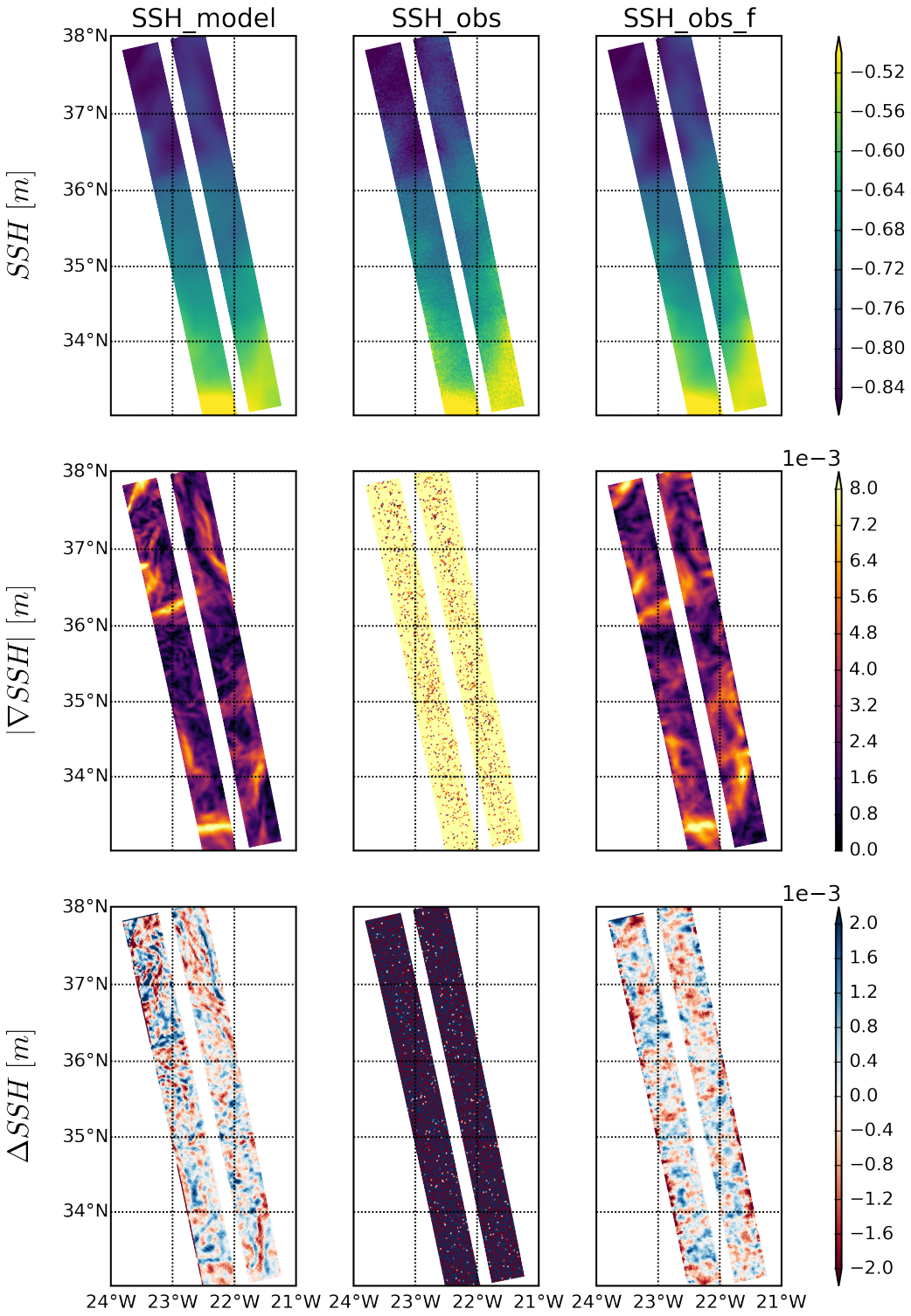

Figure 5.16: Fields of pass 24, cycle 83 of the FMA AZO eNATL60 dataset. From left to right, model data interpolated to SWOT grid (SSH_model), SSH_model with noise and errors added (SSH_obs) and SSH_obs filtered with the optimal λ_2, 13 (SSH_obs_f). From top to bottom: SSH, gradient of SSH and Laplacian of SSH.

Adding to fig. 5.9 the spectra of each scenario filtered with its optimal λ_2 value renders figures 5.17 and 5.18. Both figures show that even below Ls_f, SSH_obs_f is very close to the SSH_model spectra and inside its envelope of variability. Although Ls_f might be higher, for all scenarios the SSH spectral signal is very well

recovered down to the initial SWOT mission's objective, 15 km (*Fu and Ubelmann*, 2014). The presence of IGWs does not seem to pose a problem in applying the de-noising method. Focusing on scenarios with a high presence of IGWs, like AZO ASO and PAC FMA, the de-noising method works efficiently there too. There is room left for improvement in order to better represent the IGWs' energy peaks post-filtering. Moreover, work is to be done to further understand if their complete signal is correctly captured after de-noising.

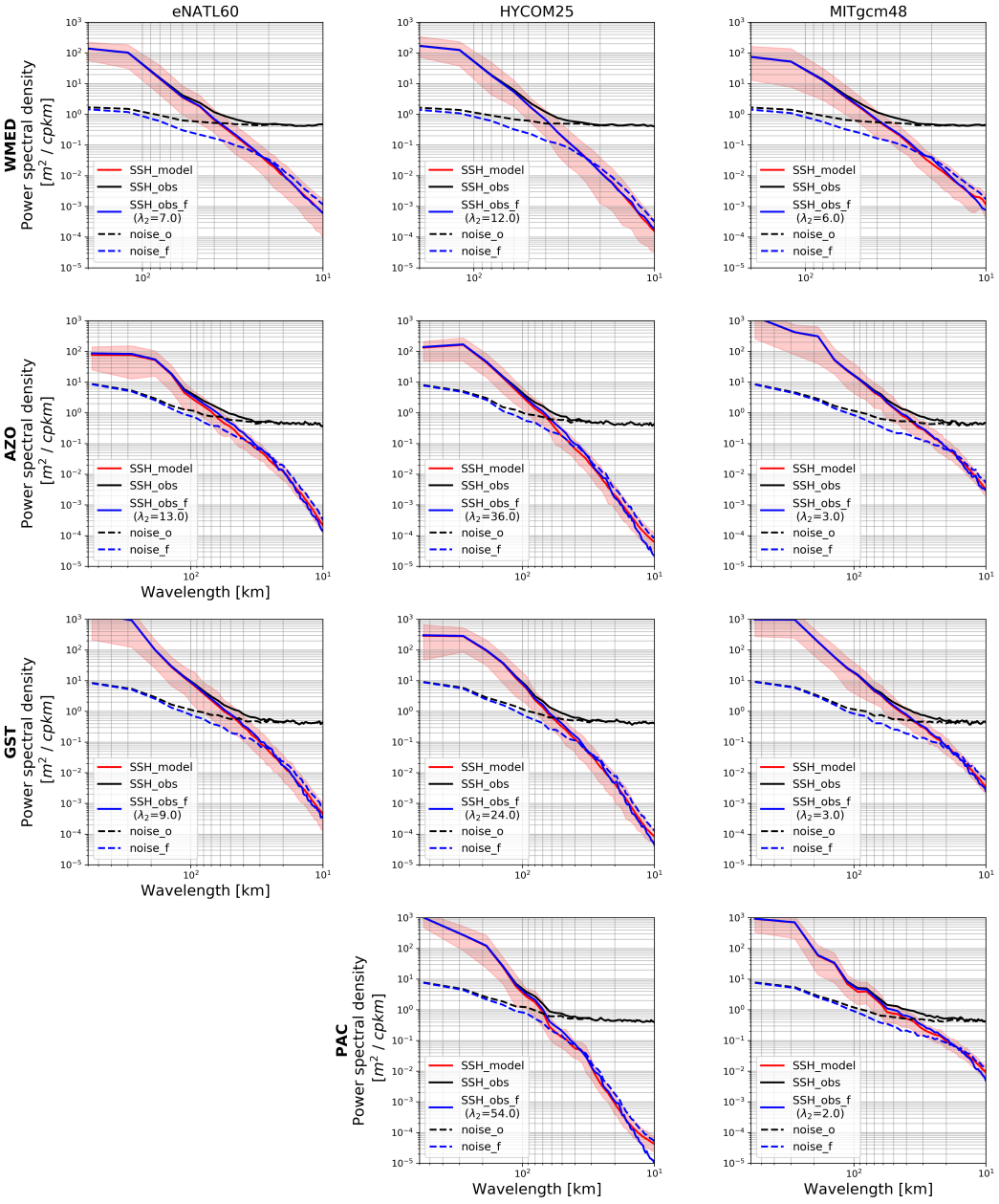

Figure 5.17: Mean of all passes and cycles of spatial spectra for each OGCM and regions in the selected sub-boxes of each pass (see fig. 5.5) for the Winter season (FMA). Spatial spectra of the model interpolated data (SSH_model) are shown in red, and that of the pseudo-SWOT data (SSH_obs) is in black. Blue lines indicate the filtered pseudo-SWOT spectra (SSH_obs_f) obtained with its optimal λ_2. The dashed lines are the residual noise spectra of SSH_obs (residual) and SSH_obs_f (residual_f). The red shaded area show values between the 5th and 95th percentiles of SSH_model, showing its Power Spectral Density (PSD) variability.

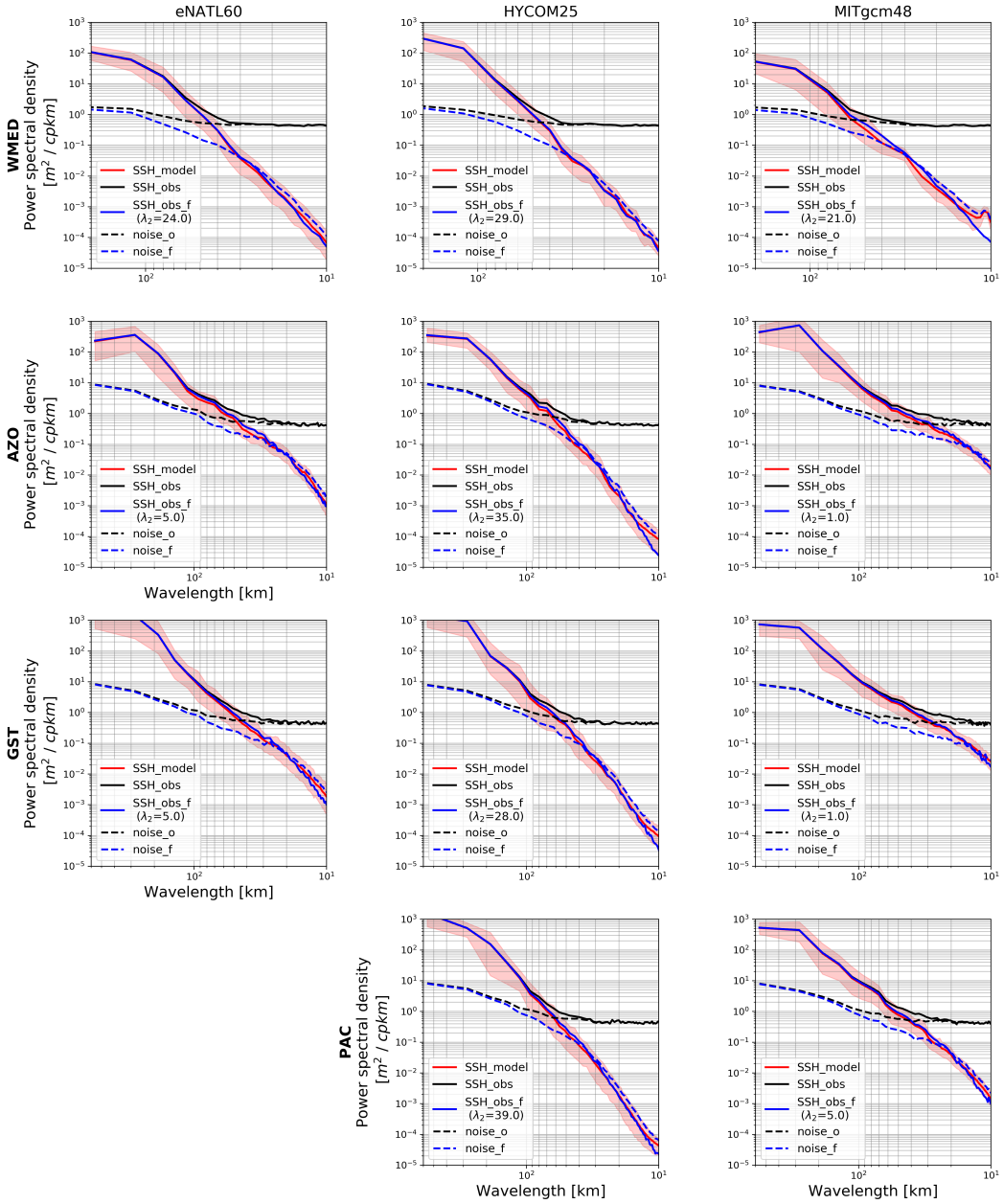

Figure 5.18: Mean of all passes and cycles of spatial spectra for each OGCM and regions in the selected sub-boxes of each pass (see fig. 5.6) for the Summer season (ASO). Spatial spectra of the model interpolated data (SSH_model) are shown in red, and that of the pseudo-SWOT data (SSH_obs) is in black. Blue lines indicate the filtered pseudo-SWOT spectra (SSH_obs_f) obtained with its optimal λ_2. The dashed lines are the residual noise spectra of SSH_obs (residual) and SSH_obs_f (residual_f). The red shaded area show values between the 5th and 95th percentiles of SSH_model, showing its Power Spectral Density (PSD) variability.

5.7 Calibration of the de-noising method

Here λ_2 was calibrated from MSR scores, finding the λ_2 which rendered the minimum value for each OGCM in each scenario. Obtaining these scores is only possible when the "true" SSH (SSH_model here) is known. Moreover, in practice the optimal λ_2 parameterization will vary with the SNR. Preliminary tests were done to see if a relationship could actually be obtained between the SNR and the optimal λ_2. The mean PSD values of each of the 22 scenarios was used. As in general the noise starts to dominate at wavelengths of 60

km or below (see table 5.3), the relationship at 60 km is explored, as well as at a smaller wavelength, 30 km. The relationship between the optimal λ_2 obtained in the different scenarios and the PSD value of SSH at these two wavelengths is shown in fig. 5.19.

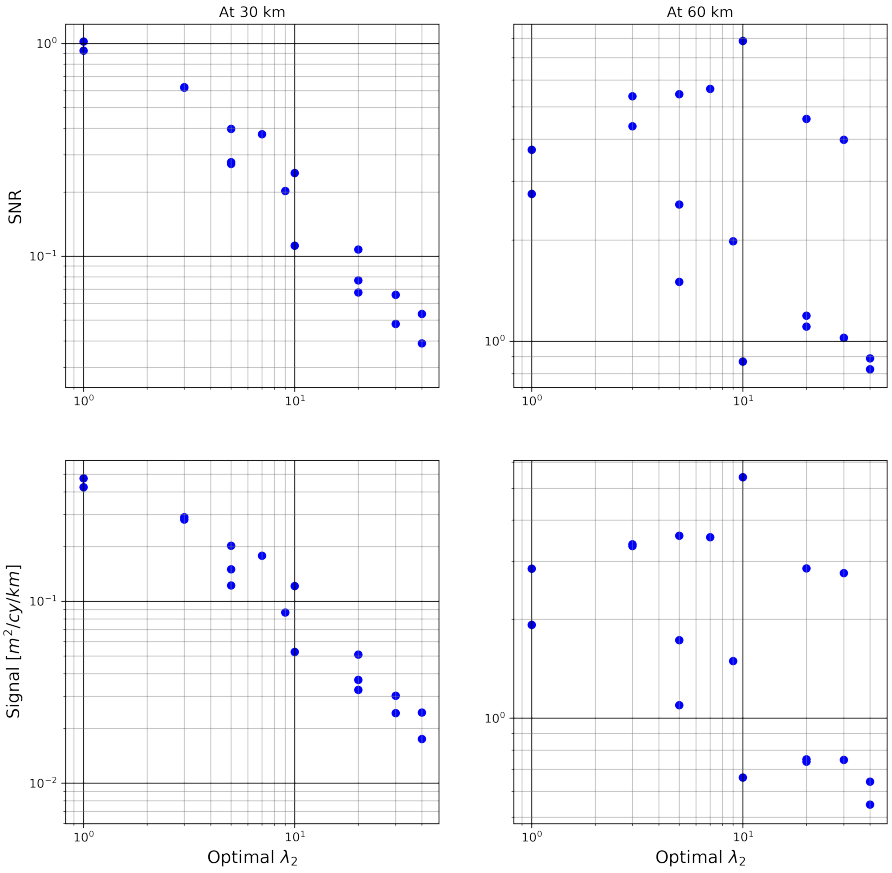

Figure 5.19: Relation between optimal λ_2 found and the Signal to Noise Ratio (SNR) (top) and just the signal $[m^2/cy/km]$ (PSD(SSH_model)) (bottom). The SNR and Signal values are at a wavelength of 30 km (left) and 60 km (right). Each of the points in every subplot represent the mean spectral value of each scenario (for example, eNATL60 AZO ASO).

In fig. 5.19, no clear relation is observed at 60 km, but a linear relationship (in log-log scale) is observed at 30 km. Although SWOT errors and noise estimates exist from the SWOT project team, their exact values are not known. A very similar relationship is obtained for the top and bottom plots of fig. 5.19. Therefore, a calibration method is presented here where the signal, the SSH variance level at 30 km, is used. The relationship between the optimal λ_2 and the PSD value of SSH at 30 km is further explored. The plot is repeated including all the PSD values within each scenario, i.e., all scenarios' passes and cycles (fig. 5.20) which in total renders 4002 points. The probability density function of this cloud of points is calculated via a gaussian kernel density estimation. Fig. 5.20 shows how the points cluster in a quite structured cloud and around the mean points.

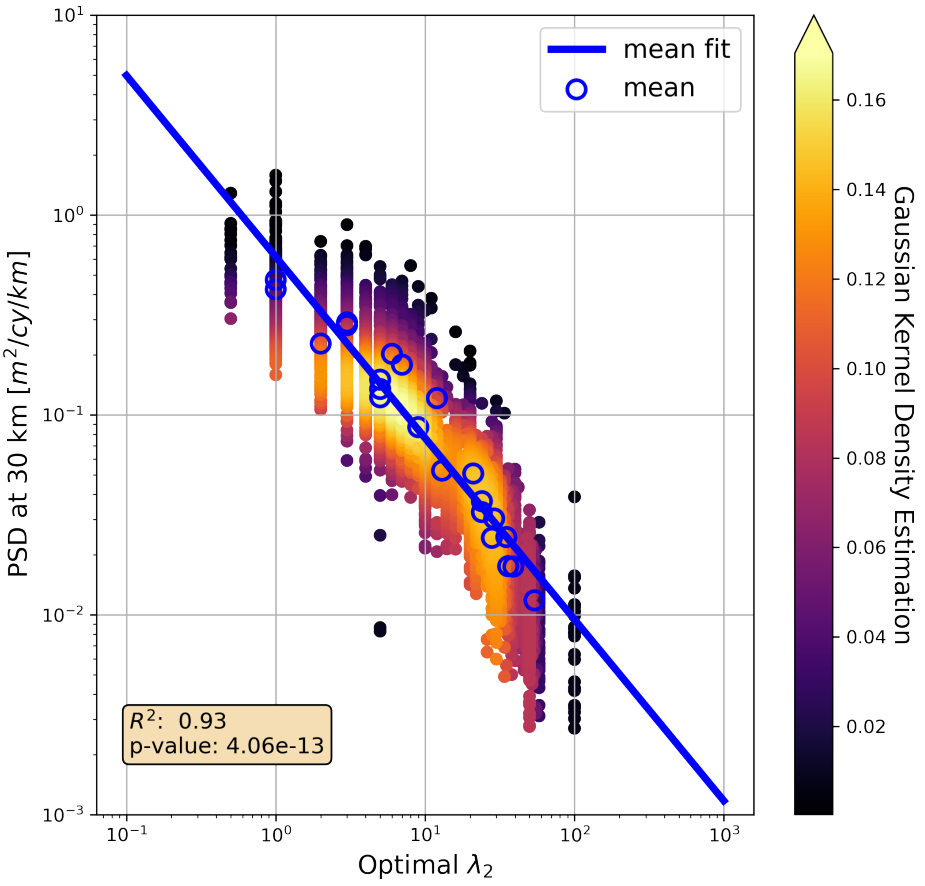

Figure 5.20: Relation between optimal λ_2 found and PSD(SSH_model) $[m^2/cy/km]$ at 30 km. Each point represnts a single pass, cycle, season, region and OGCM. The points' probability density function is shown by a gaussian kernel density estimation. The blue circles are the mean values of the passes and cycles available for each OGCM, region and season (the bottom left subplot of fig. 5.19). The blue line is a linear fit of the blue points (in log-log scale).

Fig. 5.20 further confirms that a relation between the optimal λ_2 and the PSD(SSH) at 30 km can be drawn from the experiments presented here. The blue line shows a linear least-squares regression fit (in log-log scale) of the mean PSD points (blue circles in fig. 5.20). The fit is good as R^2 (the correlation coefficient squared) is above 0.9 and the p-value is less than 0.05. The linear fit on the cloud of points is very similar (see fig. 5.29). The differences between the optimal λ_2 of the two fits is less than 50%. The SSH variance at 30 km wavelengths can be obtained from current nadir altimeters. Their noise is better known than for SWOT, and methodologies exist to obtain the PSD down to this wavelength. For example the work carried out by *Vergara et al.* (2020), allows to retrieve the PSD(SSH) at 30 km from altimeters like Jason-2. Therefore, all the elements are available to calibrate the de-noising algorithm. Here, only the MSR score is considered to determine the optimal λ_2, as the RMSE score on the Laplacian is the only reliable RMSE. To calibrate the method with the RMSE of the Laplacian, vorticity observations would be needed. Unfortunately, these measurements are not as easy to obtain as SSH spatial PSDs. Nevertheless, maybe this could be possible during the *in situ* campaigns planned at the fast-sampling phase cross-over regions (*d'Ovidio et al.*, 2019).

5.8 Discussion and Conclusions

In this study, the smallest spatial scale to be resolved by the future satellite SWOT (Ls) is re-explored. As found in previous chapters and studies (e.g. *Gómez-Navarro et al.* (2018); *Wang et al.* (2019a); *Gómez-Navarro et al.* (2020)), the smallest resolved wavelength by SWOT will highly depend on the SNR at scales below approximately 50 - 60 km. Unfortunately, a large uncertainty in SWOT Ls exists because of OGCMs discrepancies at these small spatial scales. This is taken into account by using three different, high-resolution OGCMs including tidal forcing. SSH hourly data is extracted from each. 4 different dynamical regions are chosen for the Winter and Summer months. Pseudo-SWOT data for the fast-sampling phase are generated for each scenario via the SWOT simulator. Independent realizations of the SWOT noise and errors are included. A specific SWOT de-noising technique developed by *Gómez-Navarro et al.* (2020) is then applied. This technique is parametrized by setting the optimal λ_2, which penalizes the Laplacian of SSH. The optimal λ_2 is found via the MSR score, and applied for each scenario. Applying this de-noising algorithm with its optimal parameters, leads to a reduction of Ls by approximately 10 - 30 km. This allows to observe spatial scales below the transition scale in all the scenarios explored. Lastly, a practical solution for calibrating the de-noising algorithm with existing altimetric data is proposed.

In all scenarios Ls is reduced to below 60 km thanks to the de-noising algorithm. Current 1D along-track SSH data can resolve wavelengths down to 30 - 50 km (*Pujol et al.*, 2012). Here not only are wavelengths in some regions below 30 km (fig. 5.14), but the data is 2D instead of 1D. Moreover, this could imply a huge improvement from the approximately 150 km or above resolved wavelengths of two-dimensional gridded products from current altimeters (*Ducet et al.*, 2000). The resolved wavelength of SWOT gridded products might probably be lower than the swath Ls, but its 2D characteristic allows it to sample mesoscale variability like 2 - 4 nadir altimeters (*Pascual et al.*, 2006; *Pujol et al.*, 2012). A Ls, i.e., a resolved wavelength of 60 km, implies observing eddies of 30 km in diameter. This implies a great breakthrough for the study of small-scale eddies, which have been found to be very important in vertical transports (*Lapeyre and Klein*, 2006) and in understanding energy transfers and balance in the Ocean (*Capet et al.*, 2008a). (*Fu and Ubelmann*, 2014)

The results show an improvement of some of the Ls values found in the same regions in other previous studies. For example, in the Azores region Ls is recovered down to about 20 km, while in *Dufau et al.* (2016) the Ls there was found around 35 - 50 km and about 25 - 40 km by *Wang et al.* (2019a). Nevertheless, it is important to note that the Ls found by *Wang et al.* (2019a) takes into account the variability of the KaRIn noise level with the sea wave height (SWH), while here only a KaRIn noise level in a 2 m SWH scenario is considered. Similarities are found when comparing tables 5.2 and 5.3 at WMED with the results found in *Gómez-Navarro et al.* (2020). Both results show smaller Ls in Winter than Summer, and a higher λ_2 necessary in Summer than Winter. The optimal λ_2 values here are smaller than in *Gómez-Navarro et al.* (2020) due to NATL60 being slightly less energetic at small scales and because a higher SWOT footprint is used here of 2 km instead of 1 km. A smaller footprint implies a higher noise level as shown by *Chelton* (2019). Ls_f values are very close to the resolved scales post-filtering found in *Gómez-Navarro et al.* (2020). Therefore this study further confirm the conclusions reached in *Gómez-Navarro et al.* (2020).

In all cases, after de-noising all Ls are lower than Lt. As explained in Section 5.1, this implies that unbalanced motions could be detectable in the SWOT SSH signal, at least down to Ls and perhaps the spectral slope in the unbalanced regime. On the one hand, this will allow to derive interesting quantities like the shear production to better understand KE transfers (*Torres et al.*, 2019). On the other hand, the disentanglement of balanced and unbalanced motions might be necessary, which is not evident. Furthermore, below Lt it becomes very questionable to use geostrophy to derive velocities and vorticities, theory which is very commonly used in present altimetry. Compared with the results found by *Wang et al.* (2019a), the de-noising method allows to resolve scales below Lt in regions like the Gulf Stream and Azores during Summer. It is important to note that the Lt values used in *Wang et al.* (2019a) are calculated from MITgcm48 simulation outputs (*Qiu et al.*, 2018), while the estimates of Lt here come from altimetry data (*Vergara et al.*, 2020). Moreover, the regions where *Wang et al.* (2019a) find $Ls > Lt$ (and thus IGWs not observed by SWOT), are regions with weak IGWs or with a high SWH, specially in Winter. In regions where the latter is relevant, this may change the results found here as the SWH considered is constant and equal to 2 m.

Different high-resolution OGCMs including tides have been analyzed and compared, allowing to minimally assess the still relatively unknown Ocean fine-scale dynamics. It has been confirmed, via the RMS and spatial

spectra analyses, that depending on the region and season, large discrepancies between OGCMs can exist, for example in AZO ASO. This leads to a range of SSH variance levels which lead to a range of optimal λ_2s and Ls values for the same region and season. Ls values reach differences of around 30 km. Nevertheless, all Ls values coincide in being below the Lt values estimated by *Vergara et al.* (2020). Having more and better data to assess OGCMs, and the future SWOT data, at the fine scales is important to reduce the uncertainty at these scales.

The de-noising algorithm used here, not only allowed to improve Ls, but also the SSH derivatives fields. These improvements can be observed in figures 5.15 and 5.16. The recovery of the SSH gradients is necessary to derive other oceanographic variables like vertical velocities (*Mahadevan et al.*, 2020), and to apply data assimilation methods to remove the correlated errors and/or interpolate the swaths onto a gridded map. Even in the presence of IGWs, the de-nosing method has rendered promising results towards effective removal of the uncorrelated, small scale noise and errors on the SWOT swath. Nevertheless, there is probably still space for optimization of the method, for example taking more into account the IGWs' dynamics and other fine-scale dynamics. The latter has been found to be important too in the parameterization of the method. The Ocean dynamics which have an impact on the small wavelengths of the SSH spatial spectra are more important than those which have a signal at large wavelengths, as it is where the SNR is lower.

A clear perspective of this study, would be to expand it to other cross-over regions of the fast-sampling phase. Then, repeating the procedure for the Science phase would be interesting, as the spatial and temporal sampling would vary and that could have an impact on capturing the SSH variance levels and the signal of IGWs. To better understand the signal of IGWs captured by SWOT data, the influence of its spatial and temporal sampling on the strength of the IGWs in SSH spatial spectra could be studied. Moreover, to investigate the sensitivity of the SWOT SSH spectra to temporal and spatial sampling regionally because as found by *Xu and Fu* (2012), spectra present a high variability. For example, in regions with a high presence of IGWs, these can create a change of slope or peak in the SSH spatial spectra.

In summary, this work helps to bring insight onto the spatial scales SWOT might be able to resolve in the future. The use of relatively recent high-resolution OGCM simulations including tides, has helped to better understand the possible SWOT observations of the Ocean fine-scale dynamics. This is partly thanks to the use of a SWOT swath de-noising method that renders promising results on the uncorrelated, small-scale noise and errors removal. The SWOT resolved scale found in the 4 regions studied is below Lt, opening new opportunities to better understand the balanced and unbalanced motions and their interaction. Finally, together with the SWOT resolved scales results, a solution to calibrate the SWOT de-noising method is proposed, which may allow to map the optimal λ_2 in the global ocean and thus allow the SWOT Ocean community to practically implement the method.

5.A Spatial spectra results

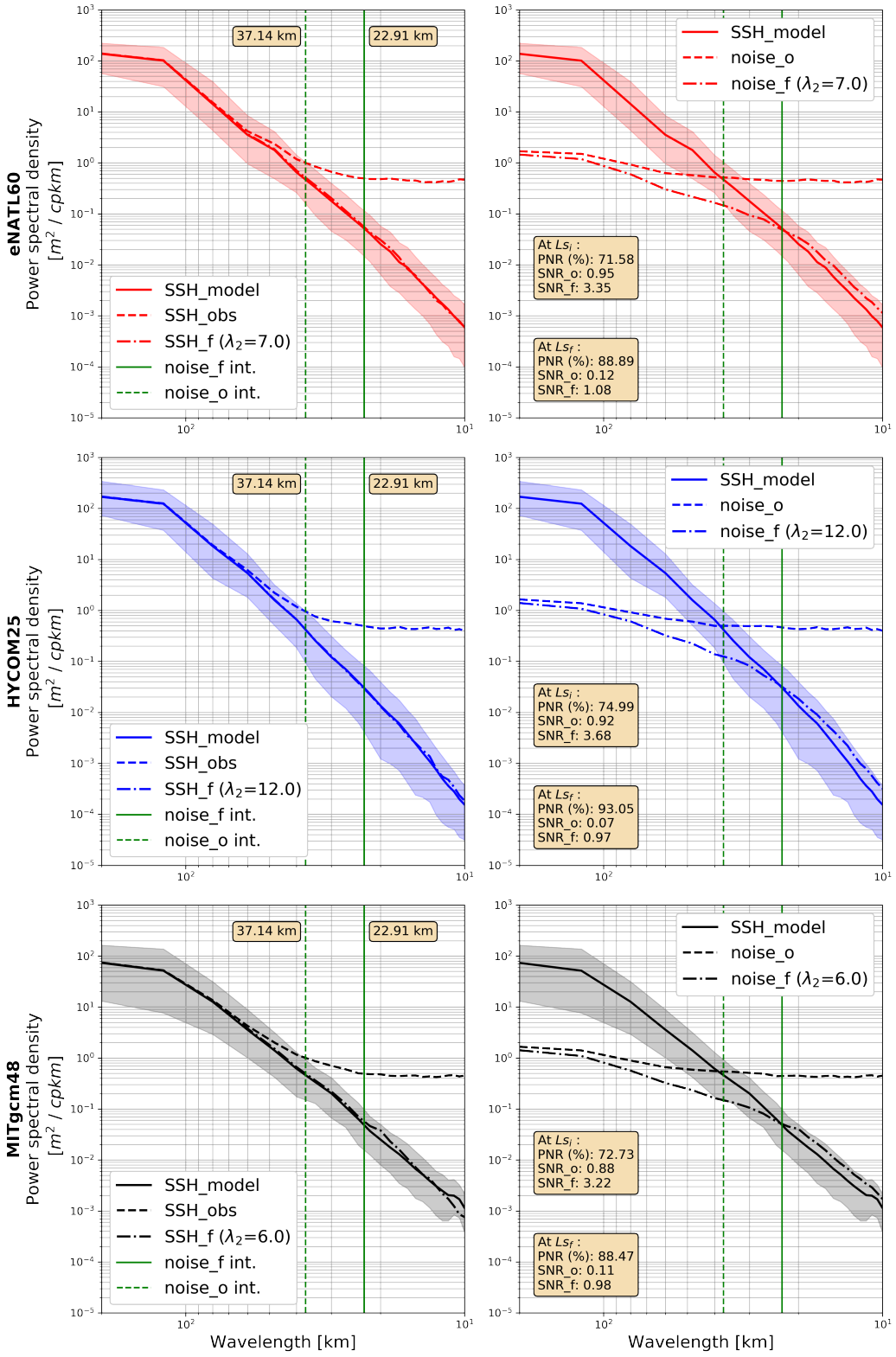

Figure 5.21: Spatial spectra for the western Mediterranean Winter scenario (WMED FMA). SSH_model is compared to SSH_obs and SSH_obs_f (left) and to noise_o and noise_f (right) spectra. Top to bottom: eNATL60, HYCOM25 and MITgcm48 OGCMs outputs shown. Green dashed (bold) lines show Ls_i (Ls_f). In the left panels the exact Ls values are shown and in the right panel the values of SNR_o, SNR_f and PNR at Ls_i and Ls_f.

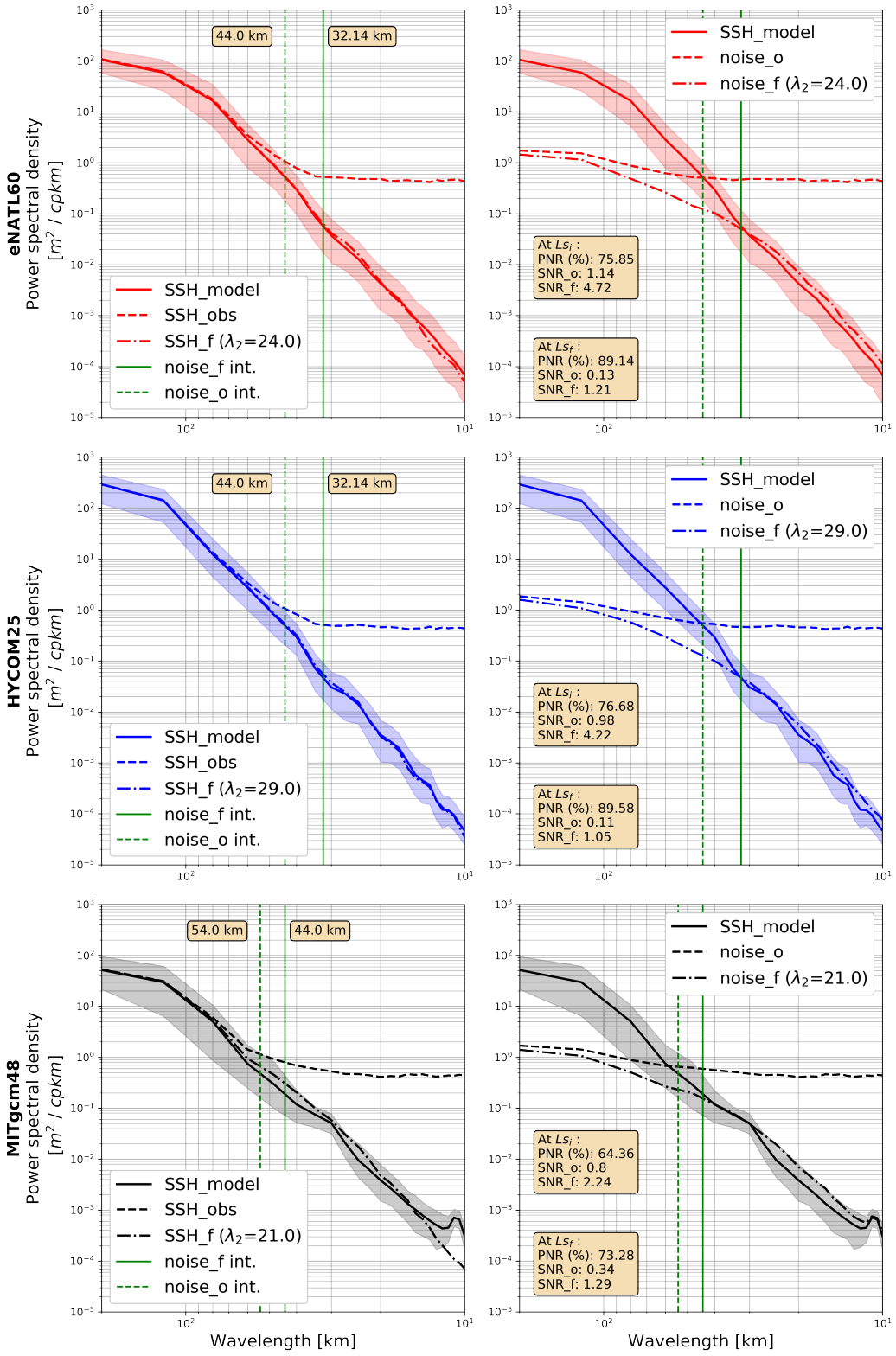

Figure 5.22: Spatial spectra for the western Mediterranean Summer scenario (WMED ASO). SSH_model is compared to SSH_obs and SSH_obs_f (left) and to noise_o and noise_f (right) spectra. Top to bottom: eNATL60, HYCOM25 and MITgcm48 OGCMs outputs shown. Green dashed (bold) lines show Ls_i (Ls_f). In the left panels the exact Ls values are shown and in the right panel the values of SNR_o, SNR_f and PNR at Ls_i and Ls_f.

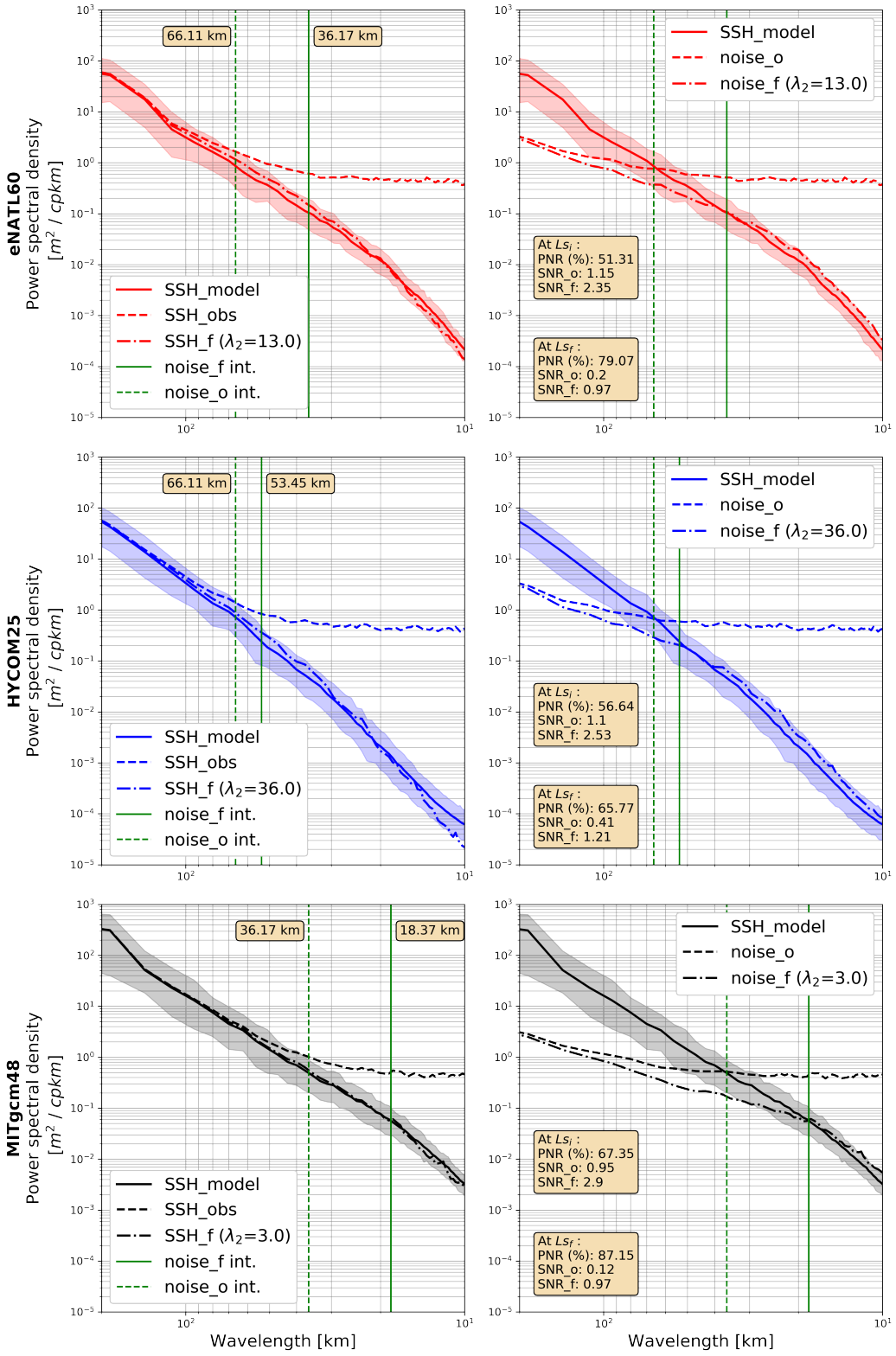

Figure 5.23: Spatial spectra for the Azores Winter scenario (AZO FMA). SSH_model is compared to SSH_obs and SSH_obs_f (left) and to noise_o and noise_f (right) spectra. Top to bottom: eNATL60, HYCOM25 and MITgcm48 OGCMs outputs shown. Green dashed (bold) lines show Ls_i (Ls_f). In the left panels the exact Ls values are shown and in the right panel the values of SNR_o, SNR_f and PNR at Ls_i and Ls_f.

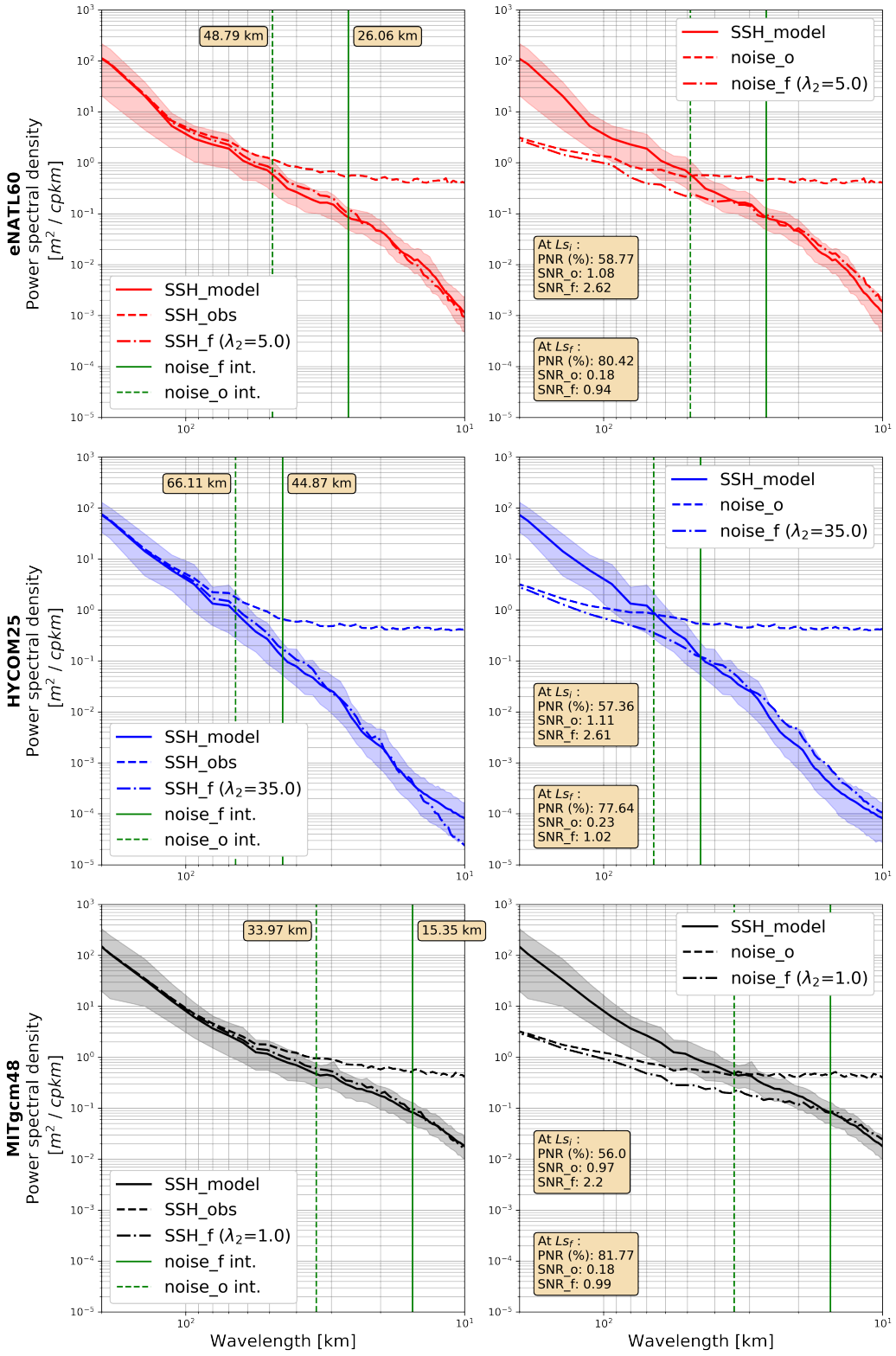

Figure 5.24: Spatial spectra for the Azores Summer scenario (AZO ASO). SSH_model is compared to SSH_obs and SSH_obs_f (left) and to noise_o and noise_f (right) spectra. Top to bottom: eNATL60, HYCOM25 and MITgcm48 OGCMs outputs shown. Green dashed (bold) lines show Ls_i (Ls_f). In the left panels the exact Ls values are shown and in the right panel the values of SNR_o, SNR_f and PNR at Ls_i and Ls_f.

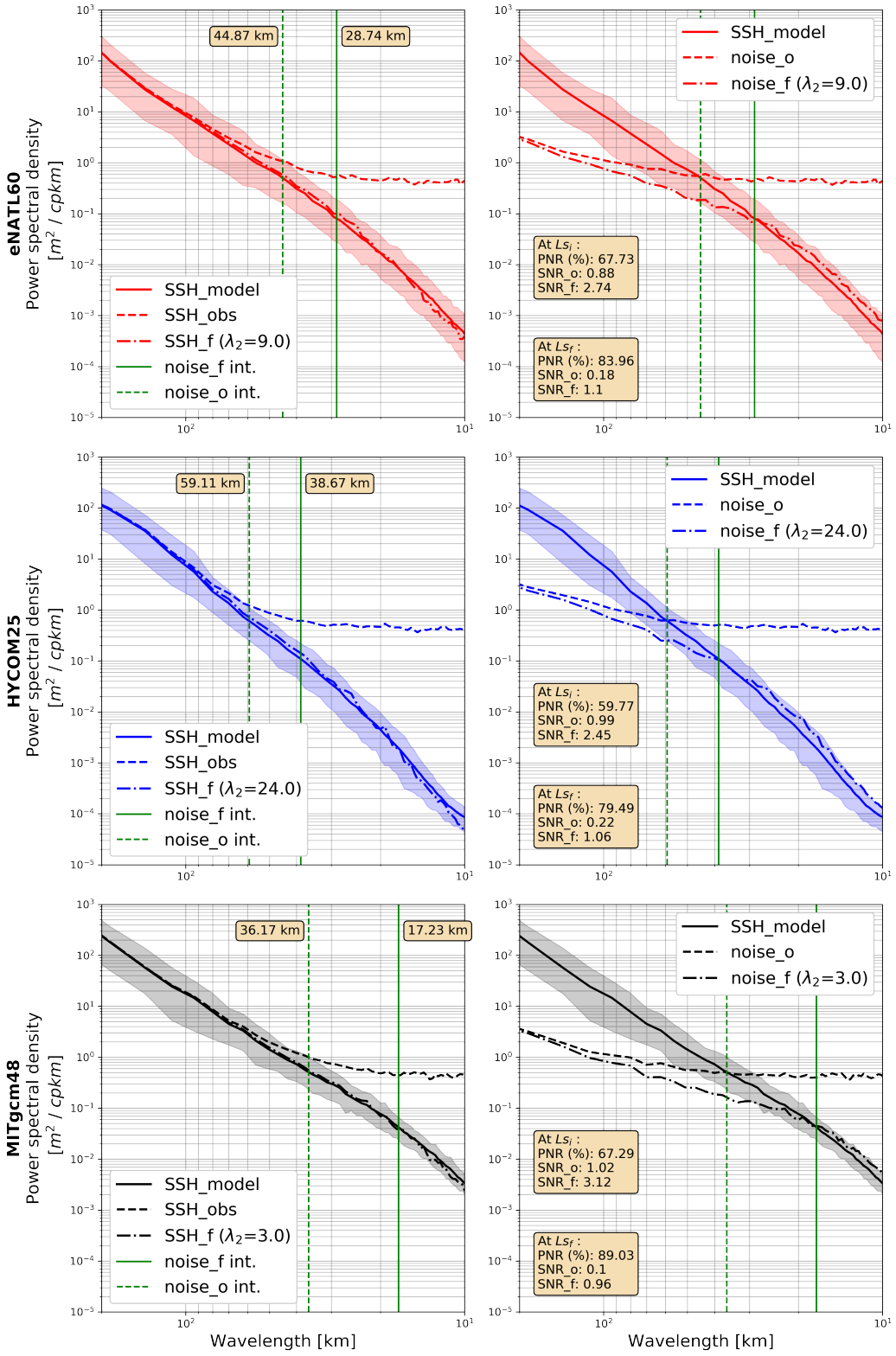

Figure 5.25: Spatial spectra for the Gulf Stream Winter scenario (GST FMA). SSH_model is compared to SSH_obs and SSH_obs_f (left) and to noise_o and noise_f (right) spectra. Top to bottom: eNATL60, HYCOM25 and MITgcm48 OGCMs outputs shown. Green dashed (bold) lines show Ls_i (Ls_f). In the left panels the exact Ls values are shown and in the right panel the values of SNR_o, SNR_f and PNR at Ls_i and Ls_f.

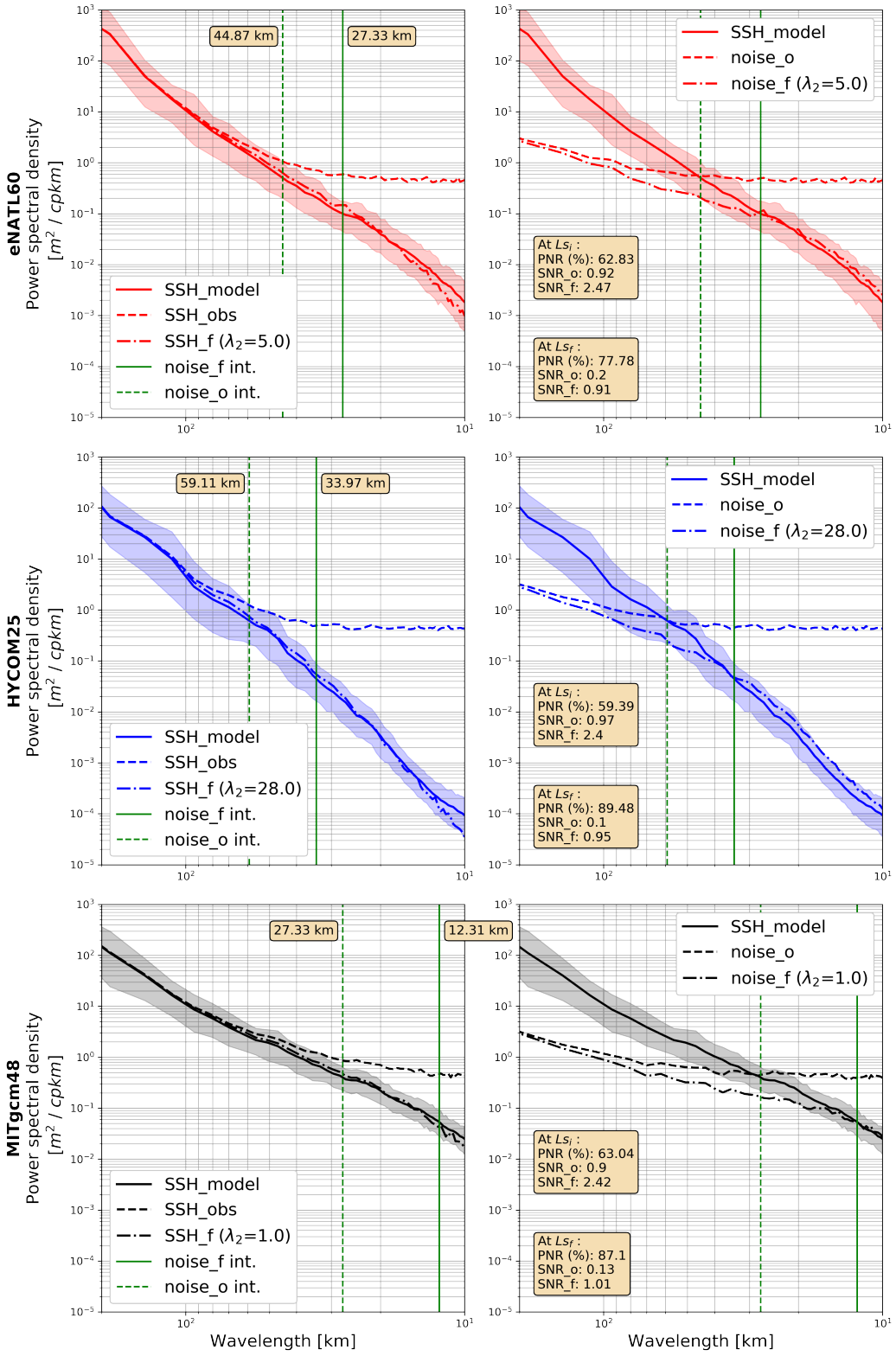

Figure 5.26: Spatial spectra for the Gulf Stream Summer scenario (GST ASO). SSH_model is compared to SSH_obs and SSH_obs_f (left) and to noise_o and noise_f (right) spectra. Top to bottom: eNATL60, HYCOM25 and MITgcm48 OGCMs outputs shown. Green dashed (bold) lines show Ls_i (Ls_f). In the left panels the exact Ls values are shown and in the right panel the values of SNR_o, SNR_f and PNR at Ls_i and Ls_f.

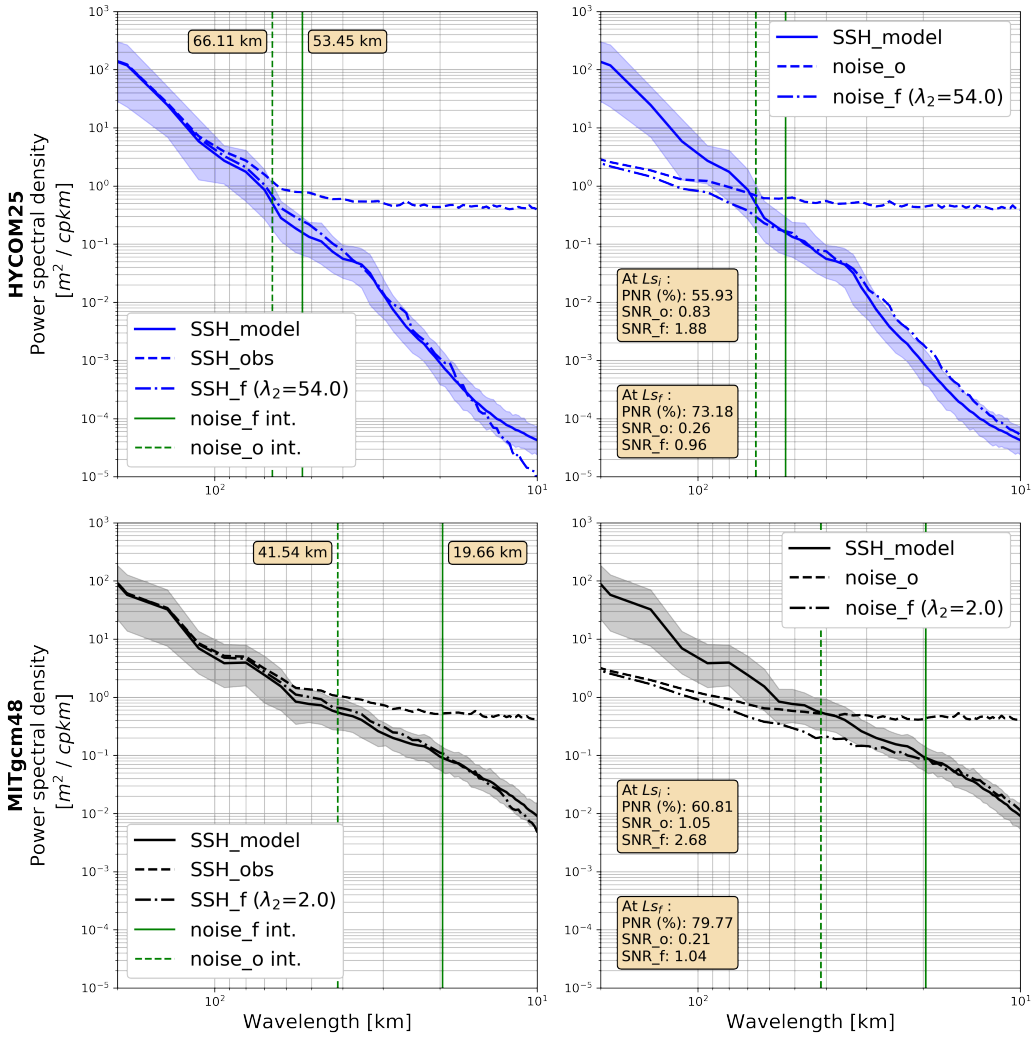

Figure 5.27: Spatial spectra for the Pacific Winter scenario (PAC FMA). SSH_model is compared to SSH_obs and SSH_obs_f (left) and to noise_o and noise_f (right) spectra. Top to bottom: eNATL60, HYCOM25 and MITgcm48 OGCMs outputs shown. Green dashed (bold) lines show Ls_i (Ls_f). In the left panels the exact Ls values are shown and in the right panel the values of SNR_o, SNR_f and PNR at Ls_i and Ls_f.

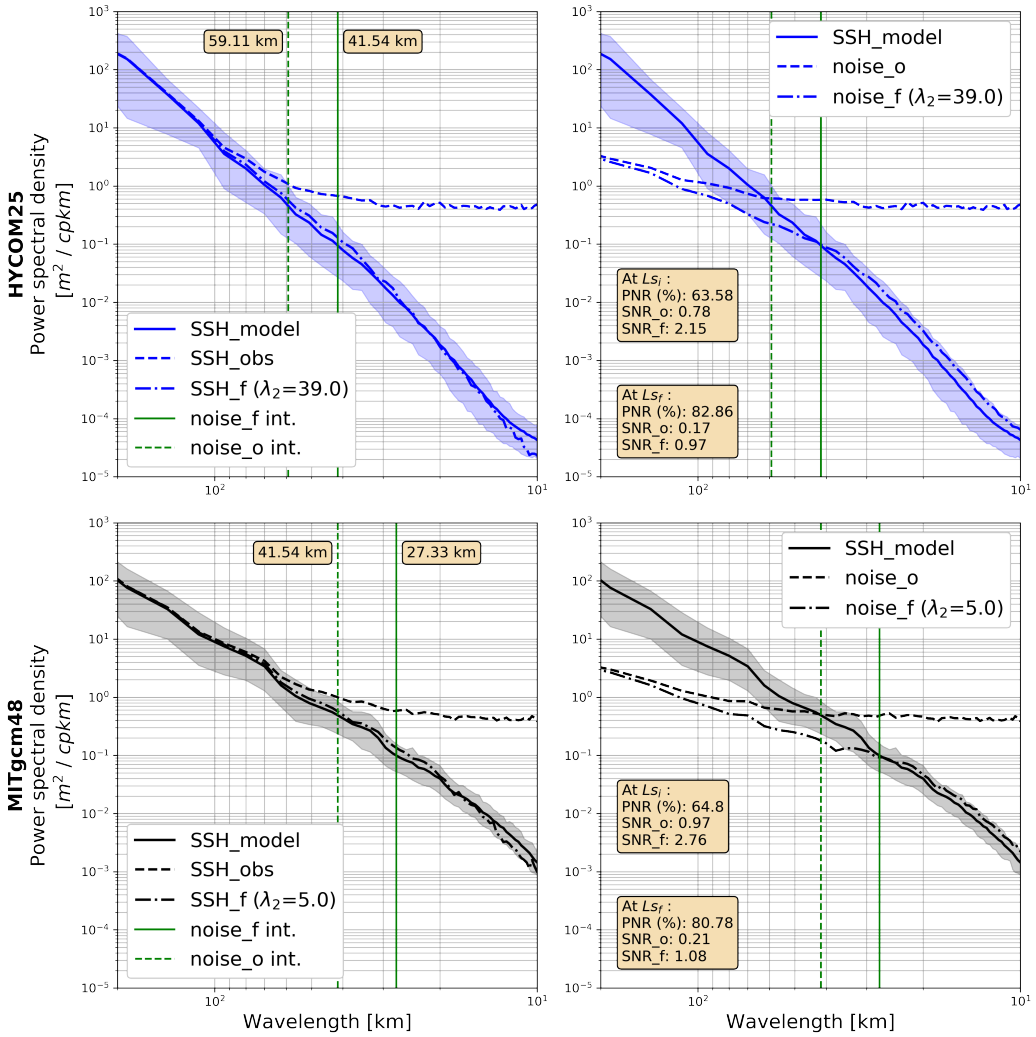

Figure 5.28: Spatial spectra for the Pacific Summer scenario (PAC ASO). SSH_model is compared to SSH_obs and SSH_obs_f (left) and to noise_o and noise_f (right) spectra. Top to bottom: eNATL60, HYCOM25 and MITgcm48 OGCMs outputs shown. Green dashed (bold) lines show Ls_i (Ls_f). In the left panels the exact Ls values are shown and in the right panel the values of SNR_o, SNR_f and PNR at Ls_i and Ls_f.

5.B Supplementary material on the de-noising method calibration

Fig. 5.29 compares the linear fits on the cloud and mean points.

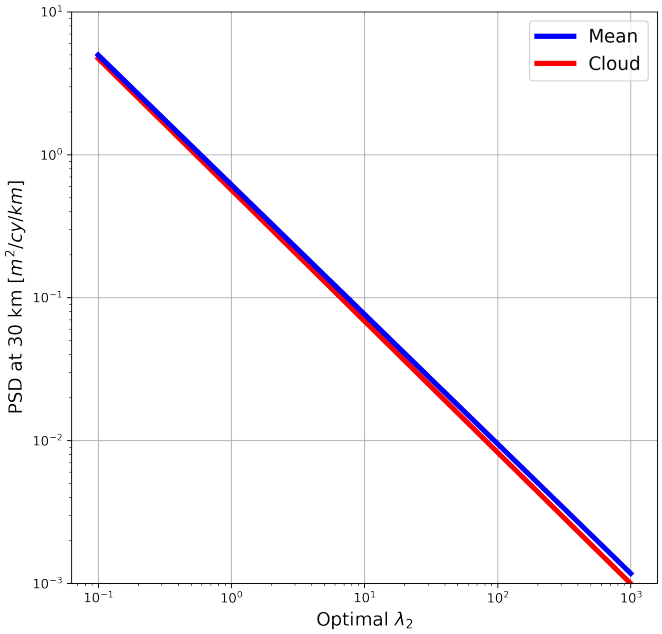

Figure 5.29: Comparison of the linear fits of the mean points (blue) and the cloud of points (red).

Chapter 6

Conclusions and perspectives

6.1 Conclusions

The aim of this study was to investigate the observation of the oceanic fine scales by the future SWOT satellite. The observation of the fine scales has been limited by the spatial and temporal resolution of the observations and model data available. SWOT is expected to break this barrier, but firstly, SWOT-specific processing algorithms need to be developed to maximize the benefits of this data. One of the main SWOT data processing steps is removing the uncorrelated noise and error components. These completely mask the signal when first (velocity) and second (vorticity) order derivatives of SSH are calculated. The de-noising is explored in Chapters 3 and 4, and in Chapter 5 the de-noising is applied to investigate the finest spatial scales to be resolved by SWOT. Below, the details of the main findings of these chapters:

- Chapter 3 explores the SWOT outputs in the western Mediterranean during the Science phase and their spatial scales. In this region SWOT will provide a very high spatial coverage with up to 2 passes per day, but there will be big temporal gaps of 7 days. The scales observed in the swath's SSH fields are lower than with the present 2D gridded altimetric product which resolves wavelengths of $\sim$200 km, but the derived geostrophic velocity and relative vorticity are completely masked by the satellite's noise and errors. After applying a Laplacian diffusion filter, geostrophic velocity and vorticity fields can be robustly estimated from SSH data allowing to reconstruct spatial scales down to 40 - 60 km wavelength. This is equivalent to resolving structures of 20 - 30 km in diameter, but the intensity of these is smoothed by the filtering.

- A new de-noising algorithm based in penalizing the derivatives of the SSH fields is explored and implemented in Chapter 4. As a test scenario, three seasonal datasets of the western Mediterranean for the fast-sampling phase are used. Compared to conventional convolution-based de-noising methods, the derivatives penalization is found to render better results. The best parameterization of the method is found. This allowed to recover the SSH spectral signals and the fields of SSH and its first and second order derivatives (velocity and vorticity). Together with this, a methodology to evaluate the de-noising of the SWOT data has been also developed which can be useful to evaluate our method as well as other. This de-noising technique reduces the spatial scale resolved by SWOT by a factor of 2, and at 10 km wavelengths, the noise level is reduced by factors of 10^4 and 10^3 for summer and winter, respectively. The de-noised SWOT SSH fields resolve wavelengths down to 20 - 30 km (structures of 10 - 15 km in diameter).

- In Chapter 5 the finest resolved scale of SWOT SSH under different dynamical conditions is investigated. These include four regions of the global ocean (WMED, AZO, GST and PAC), during Winter and Summer months and three OGCMs. They represent a range of dynamics, with high/low eddying regime and a high/low presence of IGWs. The SWOT spatial resolved wavelength (Ls) for the fast-sampling phase is found for each scenario, pre and post-filtering. The de-noising reduces Ls, making it lower than the transition scale (Lt) in all scenarios. The large uncertainty between OGCMs at small

scales is observed, and reflects in a range of Ls found in each region and season. This range is smallest in low IGWs and eddying regimes like the western Mediterranean and highest when there's a high signal of IGWs at Azores and the South Pacific region. The de-noising algorithm was found to appropriately work in all scenarios. A calibration solution for the de-noising method is proposed based on existing altimetric SSH spectral values, where the optimal λ_2 value can be obtained from the SSH spatial Power Spectral Density (PSD) at a 30 km wavelength from current nadir altimeters.

These results have allowed to answer the two main questions of this PhD study:

1. What is the best method to remove this small-scale noise, whilst conserving the SSH signal and structures?

The best method refers here to the one which renders the best results out of the limited amount of methods explored in this study, together with its optimal parameterization. The derivatives penalization de-noising method proved to be better than convolution-based methods such as, a moving average, Gaussian and Laplacian Diffusion. The results obtained from the derivatives penalization de-noising allowed to recover the oceanic structures present in the SWOT swath, whilst conserving the magnitude of the SSH signal and its first and second order derivatives. This allows to recover not only SWOT SSH, but current velocity and relative vorticity. Although other methods could be explored, this method was found to efficiently attain our objectives.

2. What will be the spatial resolution of the de-noised SWOT swath data in different dynamic regimes?

The spatial resolution of the SWOT swath data (Ls) was obtained for the fast-sampling phase in four different regions, Winter and Summer and from three different OGCMs. The Ls values found for each region after applying the derivatives penalization de-noising (Ls_f) are shown in table 6.1. The range of values found from the different OGCMs are shown and compared to the transition scale (Lt). All Ls_f were found to be below Lt. At this scale the oceanic regime goes from being dominated by geostrophic, balanced motions to dominated by wave, unbalanced motions. Consequently, with the de-noising algorithm, SWOT observations are able to resolve, at least partially, wave, unbalanced motions.

Table 6.1: SWOT resolved wavelengths post-filtering (Ls_f, km) ranges for each region compared to the transition scale (Lt, km) found by *Vergara et al.* (2020). Blue for FMA and red for ASO.

		Ls_f		Lt	
Regions	WMED	23	32 - 44	-	-
	AZO	18 - 53	15 - 45	76	62
	GST	17 - 39	12 - 34	48	53
	PAC	20 - 53	27 - 42	128	96

Lastly, the results found in this study contribute to attaining the SWOT mission objective: to better understand the meso- and submesoscale ocean circulation down to 15 km wavelengths (*Morrow et al.*, 2018).

6.2 Perspectives

The studies carried out during this PhD have contributed to shed light on the new surface ocean observations that the SWOT satellite will provide. Thanks to the results found, a door has been opened to different aspects of the SWOT data processing and analysis. Concerning the processing, the development of an effective image de-noising technique to remove the small-scale, uncorrelated noise and error components has been accomplished and made available on Github and soon on the CNES data server (HAL). Nevertheless, there is space for improvement and possible next steps. These are:

- Improvements of the de-noising method:
  - the results shown render two de-noised half-swaths, but the possibility of in-painting is included in our algorithm. Taking advantage of the SWOT nadir, the in-painting could be improved to render a full 120 km-wide, de-noised swath,
  - given that the KaRIn noise level varies across-track, an across-track varying λ_2 could be explored,
- Making the method more operational by better adapting it to the real data that will be measured by SWOT by:
  - exploring the effect of using a KaRIn noise level non-based on a constant SWH. Furthermore, based on a changing wave steepness,
  - investigating further the relationship between the optimal de-noising parameter and the PSD at 30 km to produce a set of optimal λ_2 values based on nadir altimeters' PSD.
- Combining our method with other SWOT-specific processing algorithms to:
  - remove the correlated errors (e.g. *Metref et al.* (2019); *Yaremchuk et al.* (2020)),
  - further improve the refinement of the oceanic structures present in the swath (for example filaments), especially the SSH second order derivative fields (relative vorticity), by for example using the techniques presented by *Rogé et al.* (2015) and *Durán-Moro et al.* (2017),
  - obtain 2D gridded SSH products (e.g. via data assimilation methods (*Metref et al.*, 2020)).

With respect to the analysis of SWOT data, another natural step to this study would be to expand the study regions presented in Chapter 5. Then, to repeat the study for the Science phase to see the effect of the different temporal and spatial sampling and if it would make the SWOT resolved spatial scales vary from the fast-sampling phase's. As SWOT's spatial coverage will vary regionally, increasing with latitude, SWOT data will present strong regional variations, specially during the Science phase.

The image de-noising methods explored in this study are of great importance for the SWOT mission as they allow to retrieve the SWOT SSH fields and its derivatives at scales significantly smaller than accessible with the raw data. The de-noising technique presented here makes it possible to retrieve the SSH gradients originally masked by the noise. These are necessary to derive other oceanographic variables and to apply other data assimilation methods to remove the correlated errors and/or interpolate the swaths onto a gridded map. One of these oceanographic variables is the surface current. Many present studies look at what percentage of the total velocity is represented by geostrophic velocity. The geostrophic velocity derived from current altimeter constellations is used, and it is found that only in certain parts of the ocean it is above 50%. This a very important result, but it is highly dependent on how well the current (and past) altimeter constellations manage to capture geostrophic velocities. Spatial gaps in space for example can greatly affect this. SWOT data will help shed some light on this issue, but before that, velocities need to be retrieved from the noisy SWOT SSH data. Moreover, SWOT's 2D swath motivates the exploration and development of new methods (or/and the improvement of old ones) to better retrieve ocean surface currents. This knowledge is of great relevance for the SWOT mission, but also for new satellite missions that aim to directly measure surface currents using Doppler radar measurements (*European Space Agency*, 2019).

The information of SSH and its derivatives at a higher spatial resolution than present altimeters, will allow not only to better study fine-scale oceanic features, but also their interaction. This is one of the challenges that is expected to be better understood thanks to the future SWOT data (*Müller and Melnichenko*, 2020). The estimations of kinetic energy could also be improved with SWOT data, specially if the contribution of unbalanced motions can be taken into account (*Torres et al.*, 2019). This was found possible in all studied regions and seasons after de-noising. The derivation of vertical velocities will also benefit from the 2D aspect of the SWOT data (*Qiu et al.*, 2016), especially after an effective de-noising of the swath which allows to retrieve the vorticity fields. As shown in Chapter 5, the de-noising allowed to improve the resolved SWOT spatial scale, but opens the door to other studies and research fields. For example, the effective de-noising of the SWOT data is also beneficial for the inversion of the marine gravity field (*Wan et al.*, 2020).

An accurate estimate of SWOT SSH derivatives allows to better estimate the oceanic three-dimensional circulation and vertical exchanges. Combining horizontal velocity gradient maps derived from SWOT data with

climatological data (for example, SST gradient data), vertical velocities could be inferred via the Omega equation (*Klein and Lapeyre*, 2009; *Fu, Lee-Lueng and Alsdorf, Douglas and Morrow, Rosemary and Rodriguez, Ernesto and Mognard, Nelly*, 2012). The de-noised SSH fields and its derivatives are thus a valuable product for physical and also interdisciplinary oceanographic studies (*Qiu et al.*, 2016). This has a big impact on the biogeochemical applications of the SWOT mission. An improved field of the oceanic flow at the fine scales helps to improve the study of the exchanges of heat, freshwater, carbon, nutrients and more, between different oceanic basins and layers. This affects biogeochemical cycles, biomass evolution, plankton diversity, ice-margin dynamics and socioeconomic applications like pollution monitoring (*Morrow et al.*, 2018; *d'Ovidio et al.*, 2019; *Morrow et al.*, 2019). Information on vertical velocities are especially strong at oceanic fronts, where a lot of nutrients can come up to the surface enhancing primary production, which then has an impact on higher trophic levels (*Morrow et al.*, 2019). Consequently, this three-dimensional ocean dynamics data is also relevant to better understand marine ecosystems. For example, combining SWOT with animal-bourne telemetry data can provide important information for marine protected areas' spatial planning (*d'Ovidio et al.*, 2019).

Removing the small-scale noise and error components will allow to use the SSH derivatives information to apply data assimilation techniques that exploit this to remove the correlated errors (*Ruggiero et al.*, 2016; *Metref et al.*, 2019). Also, to use data assimilation techniques to combine the swaths to obtain 2D gridded SSH maps. At present optimal interpolation is used to combine altimeter data, but for SWOT data, more complex techniques are necessary which need filtered SWOT SSH fields. Introducing SWOT data to obtain the 2D gridded product is expected to improve the product's resolution and also to reduce the present coarsening effect in which small eddies are merged together (*Amores et al.*, 2018; *Müller and Melnichenko*, 2020). Fulfilling all these steps of the SWOT data processing helps to better meet the mission's objectives, like understanding the formation, evolution, and dissipation of eddy variability (*Morrow et al.*, 2019). Several studies have mentioned the advantages of incorporating SWOT data to obtain 2D gridded SSH products, e.g. *Pujol et al.* (2012); *Amores et al.* (2018). The improvements the de-noising algorithm could provide to the SSH field's mapping, namely the eddy field, could be explored. More specifically, to see to what extent the eddy observability and tracking is improved if de-noised SWOT data is used.

This work has highly depended on diagnostics on wavenumber spectra. The SWOT mission error specifications are defined as wavenumber spectra, so this tool has become indispensable for the oceanographic scientific community. Nevertheless, I believe there is space for improvement and a better consensus of the wavenumber spectra calculation within the community. For example, seeing how to better consider the presence of land in the calculations and implementing other methods like auto regressive spectral analysis. The latter has no windowing effect and needs less segments for averaging (*Mailhes et al.*, 2016). Also, in relation with wavenumber spectra, a better understanding of spectral slopes would greatly benefit studies related to the SWOT mission.

To further evaluate SWOT data, new technologies and methodologies are important. At the small spatial scales SWOT might reach, there are not many observations available. New observational arrays like saildrones and HF radars can provide fine-scale information on surface currents. Recent methodologies which take advantage of the drifting information of different observational datasets can also provide fine-scale information not provided by other instruments. For example, using drifting data of ships and seabirds (*Miyazawa et al.*, 2015; *Sánchez-Román et al.*, 2019) and of Argo floats and gliders when they are transmitting data at the surface. An advantage of methodologies that exploit this type of drifting data is that it's "green", recycled data. All these new data sources which can observe the fine scales should be further studied to use them for validation of SWOT data and to explore how to best combine them.

To conclude, I hope this study provides results and tools that will contribute to obtaining improved SWOT data and a better understanding of it. Furthermore, that this small sand grain contributes to improving our knowledge of the ocean dynamics and circulation, helping to better preserve and protect the marine environment.

Appendix A

Thesis valorization

A.1 Publications

First author publications included in the Results chapters.

- Gomez-Navarro, L., Cosme, E., Le Sommer, J., Papadakis, N., Molines, J.-M., Pascual, A. Arbic, B.K., Ajayi, A.O., Albert, A., Brodeau, L., Menemenlis, D., Shriver, J. F., Richman, J. G., Savage, A. And Ye, J. (*in prep.*) What will be the finest resolved scale of SWOT SSH data under different dynamical conditions?
- Gómez-Navarro, L., Cosme, E., Le Sommer, J., Papadakis, N. and Pascual, A. (2020). Development of an image de-noising method in preparation for the Surface Water and Ocean Topography satellite mission. *Remote Sensing*, 12(4), 734. doi:10.3390/rs12040734.
- Gómez-Navarro, L., Fablet, R., Mason, E., Pascual, A., Mourre, B., Cosme, E., & Le Sommer, J. (2018). SWOT Spatial Scales in the Western Mediterranean Sea Derived from Pseudo-Observations and an Ad Hoc Filtering. Remote Sensing, 10(4), 599. doi:10.3390/rs10040599.

Co-authored publications include:

- Metref, S., Cosme, E., Le Sommer, J., Poel, N., Brankart, J.M., Verron, J., **Gómez-Navarro**, L. (2019). Reduction of spatially structured errors in wide-swath altimetric satellite data using data assimilation. *Remote Sensing*, 11(11), 1336. doi:10.3390/rs11111336.
- López-Radcenco, M., Pascual, A., **Gómez-Navarro, L.**, Aïssa-El-Bey, A., Chapron, B., & Fablet, R. (2019). Analog Data Assimilation of Along-Track Nadir and Wide-Swath SWOT Altimetry Observations in the Western Mediterranean Sea. *IEEE Journal of Selected Topics in Applied Earth Observations and Remote Sensing*, 11(11), 1336. doi:10.1109/JSTARS.2019.2903941.
- Sánchez-Román, A., **Gómez-Navarro, L.**, Fablet, R., Oro, D., Mason, E., Arcos, J. M., ... & Pascual, A. (2019). Rafting behaviour of seabirds as a proxy to describe surface ocean currents in the Balearic Sea. *Scientific reports*, 9(1), 17775. doi:10.1038/s41598-018-36819-w.
- Barceló-Llull, B., Pascual, A., Díaz-Barroso, L., Sánchez-Román, A., Casas, B., Muñoz, C., Torner, M., Alou-Font, E., Cutolo, E., Mourre, B., Allen, J.T., Aulicino, G., Carbonero, A., Calafat, N., Capó, E., Cotroneo, Y., Cyr, F., Doglioli, A. M., D'Ovidio, F., Dumas, F., Fernández, J. G., **Gómez-Navarro, L.**, Gregori, G., Hernández-Lasheras, J., Mahadevan, A., Mason, E., Miralles, A., Roque, D., Rubio, M., Ruiz, I., Ruiz, S., Ser-Giacomi, E., Toomey, T. (2018). PRE-SWOT Cruise Report. Mesoscale and submesoscale vertical exchanges from multi-platform experiments and supporting modeling simulations: anticipating SWOT launch (CTM2016-78607-P). doi:10.20350/digitalCSIC/8584.
- López-Radcenco, M., Pascual, A., **Gómez-Navarro, L.**, Aïssa-El-Bey, A., Chapron, B., & Fablet, R. (2018). Can SWOT Improve the Reconstruction of Sea Level Anomaly Fields? Insights for Data-driven Approaches in the Western Mediterranean Sea. hal-01891689.

A.2 Works presented in conferences

- As first author:
  - Gómez-Navarro, L., Cosme, E., Le Sommer, J.*, Papadakis, N., Molines, J.M., Pascual, A., Arbic, B. K., Ajayi, A. O., Albert, A., Menemenlis, D. and others. What will be the finest resolved scale of SWOT SSH data under different dynamical conditions? Ocean Sciences Meeting, San Diego (USA), February 16-21, 2020. Oral presentation.
  - Gómez-Navarro, L., Cosme, E., Le Sommer, J., Papadakis, N., Molines, J.M. and Pascual, A. SWOT resolved wavelengths in different oceanic dynamic regimes after small scale noise removal. SWOT Science Meeting, Bordeaux (France), June 16-20, 2019. Poster presentation.
  - Gómez-Navarro, L., Cosme, E., Le Sommer, J., Metref, S., Lguensat, R., Papadakis, N. Exploring de-noising and reconstruction methods for SWOT. SWOT Science Meeting, Montreal (Canada), June 26-29, 2018. Oral presentation.
  - Gómez-Navarro, L., Cosme, E., Le Sommer, J., Papadakis, N., Molines, J. M. and Pascual, A. Filtering SWOT noise: First experiments in the western Mediterranean 2 Sea. Ocean Sciences Meeting, Portland (USA), February 12-16, 2018. Poster presentation.
  - Gómez-Navarro, L., Sánchez-Román, A., Pascual, A., Fablet, R., Hernández-Carrasco, I., Mason, E., Arcos, J. M. and Oro, D. (2017). Seabird drift as a proxy to estimate surface currents in the western Mediterranean? GODAE OceanView International School, Pollença, Balearic Islands (Spain), October 1-13, 2017. Poster presentation.
  - Gómez-Navarro, L., Sánchez-Román, A., Pascual, A., Fablet, R., Hernández-Carrasco, I., Mason, E., Arcos, J. M. and Oro, D. Seabird drift as a proxy to estimate surface currents in the western Mediterranean? EGU General Assembly, Vienna (Austria), April 23-28, 2017. Poster presentation.
  - Gómez-Navarro, L., Pascual, A., Fablet, R. and Mason, E. Investigating SWOT's capabilities to detect meso and submesoscale eddies in the western Mediterranean. EGU General Assembly, Vienna (Austria), April 23-28, 2017. Oral communication.
- As co-author:
  - Pascual, A., Ruiz, S., Barceló-Llull, B., Sanchez-Roman, A., Mason, E., Cutolo, E., Tarry, D. R., Antich, H., **Gómez-Navarro, L.**, Ouala, S., Mourre, B., Faugere, Y., Fablet, R., Tintore, J., Mahadevan, A. and d'Ovidio, F. Finescale horizontal and vertical currents from in-situ observations in preparation for SWOT altimeter mission, Abstract PS42B-02, presented at 2020 Ocean Sciences Meeting, San Diego CA, February 16-21, 2020. Oral presentation.
  - Metref, S., Cosme, E., Le Sommer, J., Poel, N., Brankart, J. M., Verron, J., **Gómez-Navarro, L.** and Le Guillou, F. Dealing with spatially structured errors in SWOT data. SWOT Science Team meeting. 16-20 June 2019. Bordeaux, France. Oral presentation.
  - Pascual, A., Barceló-Llull, B., Cutolo, E., Sánchez Román, A., Díaz-Barroso, L., Alou, E., Mourre, B., Allen, J., Muñoz, C., Fernández, J.-G., Antich, H., **Gómez-Navarro, L.,** Torner, M., Ruiz, S., Mason, E., Ser-Giacomi, E., Cyr, F., Doglioli, A., Dumas, F., D'Ovidio F. The Pre-SWOT experiment. SWOT Science Meeting, Bordeaux (France), June 16-20, 2019. Oral presentation.
  - Pascual, A., Barceló-Llull, B., **Gómez-Navarro, L.**, Díaz-Barroso, L., Casas, B., Muñoz, C., Mourre, B., Torner, M., Ruiz, S., Allen, J., D'Ovidio, F., Doglioli, A. and Dumas F. PRE-SWOT multi-platform experiment in the SouthWest Mediterranean Sea. SWOT Science Meeting, Bordeaux (France), June 16-20, 2019. Poster presentation.
  - Pascual, A., Ruiz, S., Sanchez-Roman, A., **Gómez-Navarro, L.**, Barcelo-Llull, B., Diaz-Barroso, L., Chabert, P., Cutolo, E., Freilich, M. A., Heslop, E., Casas, B., Torner, M., Mourre, B., Alou, E., Cotroneo, Y., Aulicino, G., Mason, E., Mahadevan, A., Tintore, J., D'Ovidio, F., Fablet, R., Allen, J. Overview of Fine-scale Multiplatform Experiments in the Southwest Mediterranean Sea: Lessons Learnt in the Last Five Years. 25 Years of Progress in Radar Altimetry Symposium, Ponta Delgada, Açores Islands (Portugal), September 24-29, 2018. Oral presentation.
  - Cosme, E., Poel, N., **Gómez-Navarro, L.**, Brankart, J.M., Le Sommer, J., Pascual, A., Molines, J.M. On the assimilation of high-resolution wide-swath altimetric data. 25 Years of Progress in Radar Altimetry Symposium, Ponta Delgada, Açores Islands (Portugal), September 24-29, 2018. Poster presentation.

- Pascual, A., Barceló-Llull, B., **Gómez-Navarro, L.**, Díaz-Barroso, L., Casas, B., Muñoz, C., Mourre, B., Torner, M., Ruiz, S., Allen, J., D'Ovidio, F., Doglioli, A. and Dumas F. PRE-SWOT multi-platform experiment in the SouthWest Mediterranean Sea. GODAE-OceanView COSS-TT workshop, Madrid (Spain), September 2018. Poster presentation.
- Lopez-Radcenco, M., Pascual, A., **Gómez-Navarro, L.**, Aissa-El-Bey, A., Fablet, R. Analog data assimilation for along-track nadir and SWOT altimetry data in the western Mediterranean Sea. IGARSS, Valencia (Spain), July 2018. Poster presentation.
- Lopez-Radcenco, M., Pascual, A., **Gómez-Navarro, L.**, Aissa-El-Bey, A., Fablet, R. Assimilation par Analogues de Données Altimétriques Nadir et SWOT dans la Mer Méditerranée Occidentale. Conférence Française de Photogrammétrie et de Télédétection, Marne-la-Vallée (France), June 2018. Oral presentation.
- Pascual, A., Barceló-Llull, B., **Gómez-Navarro, L.***, Díaz-Barroso, L., Casas, B., Muñoz, C., Mourre, B., Torner, M., Ruiz, S., Allen, J., D'Ovidio, F., Doglioli, A. and Dumas F. PRE-SWOT multi-platform experiment in the SouthWest Mediterranean Sea. SWOT Science Meeting, Montreal (Canada), June 26-29, 2018. Poster presentation.
- Sánchez-Román, A., Mason, E., **Gómez-Navarro, L.**, Pascual, A., Fablet, R., Arcos, J. M., Oro, D. and Ruiz, S. Rafting behavior of Scopoli's shearwaters: a proxy to describe surface currents in the western Mediterranean Sea? VI International Symposium on Marine Sciences, Vigo Spain, June 20-22, 2018. Poster presentation.
- Barceló-Llull, B., Díaz-Barroso, L., Casas, B., **Gómez-Navarro, L.**, Cutolo, E., Sánchez-Román, A., Escudier, E., Carbonero, A., Calafat, N., Capó, E., Ser-Giacomi, E., Mason, E., Mourre, B., Muñoz, C., Ruiz, I., Alou, E., Ruiz, S., Torner, M., Miralles, A., Rubio, M., Vizoso, G., Tintoré, J., Allen, J., Pascual, A. Characterizing the SouthWest Mediterranean Sea to anticipate the SWOT satellite launch. V Encuentro Oceanografía Física, Vigo Spain, June 20-22, 2018. Poster presentation.
- Lopez-Radcenco, M., Pascual, A., **Gómez-Navarro, L.**, Aissa-El-Bey, A. and Fablet, R. Analog data assimilation of along-track nadir and SWOT altimetry observations in the Western Mediterranean Sea. EGU General Assembly, Vienna (Austria), May 8-13, 2018. Poster presentation. Vol. 20 EGU2018-18111.
- Lguensat, R., **Gómez-Navarro, L.**, Cosme, E. and Le Sommer, J. Data-Driven methods for the restoration of SWOT data. EGU General Assembly, Vienna (Austria), May 8-13, 2018. Oral presentation. Vol. 20, EGU2018-12750.
- Pascual, A., **Gómez-Navarro, L.***, Ruiz, S., Mahadevan, A., Farrar, J. T., Freilich, M., Chabert, P., Allen, J., Tintore, J. and d'Ovidio, F. (2018). Multi-platform experiments in the SouthWest Mediterranean Sea to study fine-scale ocean vertical exchanges: anticipating SWOT launch, Abstract PS51A-06, presented at 2018 Ocean Sciences Meeting, Portland, OR, February 12-16, 2018. Oral presentation.
- Sánchez-Román, A., Mason, E., **Gómez-Navarro, L.**, Pascual, A., Fablet, R., Arcos, J. M. and Oro, D., Ruiz, S. Rafting behavior of Scopoli's shearwaters: a proxy to describe surface currents in the western Mediterranean Sea? OSTST meeting, Miami (USA), 2017. Poster presentation.
- Cosme, E., **Gómez-Navarro, L.**, Monsimer, A., Le Sommer, J., Albert, A., Papadakis, N. and Deledalle, C. (2017). Processing SWOT data with image restoration techniques. NASA/CNES SWOT Science Team Meeting 2017, 26-28 June, Toulouse (France). Oral communication.

* presenting author

A.3 Seminars given

- *Observabilité de la turbulence océanique de surface par la mission SWOT*. January 30th 2017, IGE (Grenoble, France).
- Observability of oceanic turbulence by the SWOT mission. October 24th 2017, IGE (Grenoble, France).
- Observability of oceanic turbulence by the SWOT mission. Seminar given on February 5th 2019, IMEDEA (Esporles, Spain).
- Observability of oceanic fine-scales by the SWOT mission. Doctoriades: Journée de la jeune recherche, October 17th-18th 2019, Université de Toulon (Toulon, France).

A.4 Participation in summer schools and courses followed

- OceanHackweek (Seattle (USA), 2019)
- Becoming a Researcher (Grenoble (France), 2019)
- *La santé des étudiants : formation diplômante au secourisme, sensibilisation au mal-être étudiant et au handicap* (Grenoble (France), 2019)
- Grenoble Software Carpentry (Grenoble (France), 2018)
- GODAE OceanView International School (Pollença, Mallorca (Spain), 2017)
- Introduction to Data Assimilation (Grenoble (France), 2017)

A.5 Participation in scientific projects

- PRE-SWOT: Mesoscale and sub-mesoscale vertical exchanges from multiplatform experiments and supporting modeling simulations: anticipating SWOT launch (2016 - 2019). PI: Ananda Pascual. Principal organization, Spanish National Research Council (CSIC).

`https://digital.csic.es/handle/10261/172644`

- Ocean Modelling and Data-Assimilation for SWOT mission: preparing the inversion of SWOT ocean data (2016-2019). PIs: Emmanuel Cosme and Julien Le Sommer. SWOT Science Team (SWOT-ST).

`https://meom-group.github.io/projects/swot-st/`

- MOMOMS: Merging Ocean Models and Observations at Mesoscale and Submesoscale (2017-2020). PI: Emmanuel Cosme. Ocean Surface Topography Science Team (OST-ST, CNES-NASA-EUMETSAT-NOAA).

`https://sealevel.jpl.nasa.gov/science/ostscienceteam/scientistlinks/scientificinvestigations2017/cosme/`

- MULTI-SUB: Mesoscale and Sub-mesoscale Vertical Exchanges from Multi-platform Experiments and Supporting Modeling Simulations (2015 - 2019). PI: Ananda Pascual. SWOT Science Team (SWOT-ST).

`https://swot.jpl.nasa.gov/documents/1529/?list=projects`

- MANATEE: Multi-platform experiments, numerical simulations ANd dATa sciEnce techniques for generation of new altimEtric products: focus on mesoscale and sub-mesoscale variability in the Western Mediterranean Sea (2017 - 2020). PI: Ananda Pascual. Ocean Surface Topography Science Team (OST-ST, CNES).

`https://sealevel.jpl.nasa.gov/science/ostscienceteam/scientistlinks/scientificinvestigations2017/pascual/`

- BOOST-SWOT: Building Of Ocean Surface Topography maps from SWOT (2018 - 2021). PI. Emmanuel Cosme. Project funded by the French National Research Agency (ANR).

`https://anr.fr/Project-ANR-17-CE01-0009`.

A.6 Participation in oceanographic cruises

- Pre-SWOT cruise: May 2018. The results of this PhD helped plan the oceanographic campaign sampling and contributed to the Pre-SWOT project.

A.7 Outreach activities

During my PhD I have organized and participated in different outreach activities at both institutions:

- IGE
  - World Ocean Day event on 8th June 2018, Saint Martin d'Heres (France).
  - *Tribulations savantes* 2018 and 2019 at *Université Grenoble Alpes*, Saint Martin d'Heres (France).
  - *Fête des tuiles* ocean circulation and plastic pollution stand, June 2019, Grenoble (France).
- IMEDEA
  - Organization of an Ocean circulation workshop during *Semana de la Ciencia y la Tecnología*, November 2017 and 2018, Esporles (Spain).
  - Participation in *Balears Fa Ciència* radio programme on the 11F platform (https://11fbalears.org/), February 2019, Palma de Mallorca (Spain).
  - Gave a presentation on an ocean circulation workshop at Palma aquarium, February 2019, Palma de Mallorca (Spain).

A.8 Other activities

- Teaching: I taught in the Ocean-Climate-Atmosphere course of L3 *Sciences de la Terre* undergraduate degree at the University Grenoble Alpes in 2018, 2019 and 2020.
- Short research stay at the University of Michigan under the supervision of B. K. Arbic to work on the effect of internal tides and waves on the SWOT satellite during January 2019.

Appendix B

List of Abbreviations

ADCP : Acoustic Doppler Current Profiler)

AE : Anticyclonic Eddy

ASO : August September October

AZO : AZOres islands region

BMs : Balanced Motions

CE : Cyclonic Eddy

CMEMS : Copernicus Marine Environment Monitoring Service

CNES : *Centre National d'Études Spatiales*

CTD : Conductivity–Temperature–Depth

DFS : Drakkar Forcing Set

DUACS : Data Unification and Altimeter Combination System

ECMWF : European Centre for Medium-Range Weather Forecasts

eNATL60 : extended North ATLantic simulation of $\frac{1}{60}^\circ$ resolution

FISTA : Fast Iterative Shrinkage-Thresholding Algorithm

FMA : February March April

GLORYS : GLobal Ocean ReanalYsiS

GST : Gulf STream region

HF : High Frequency radar

HYCOM25 : HYbrid COordinate Model simulation of $\frac{1}{25}^\circ$ resolution

IGWs : Internal Gravity Waves

KaRIn : Ka-band Radar Interferometer

Ls : spatial resolved wavelength

Lt : Transition scale

MITgcm48: Massachusetts Institute of Technology general circulation model simulation of $\frac{1}{48}^\circ$ resolution

MLD : Mixed Layer Depth

MSR : Mean Spectral Ratio

NASA : National Aeronautics and Space Administration

NATL60 : North ATLantic simulation of $\frac{1}{60}^\circ$ resolution

NEMO : Nucleus for European Modeling of the Ocean

OGCMs : Ocean General Circulation Models

OI : Optimal Interpolation

OOS : Ocean Observing Systems

OSMOSIS : Ocean Surface Mixing, Ocean Submesoscale Interaction Study

OSSEs : Observing System Simulation Experiments

PAC : south PACific region

PNR : Percentage of Noise Removed

PSD : Power Spectral Density

Ri : Richardson number

RMS : Root Mean Square

RMSE : Root Mean Square Error

Ro : Rossby number

ROMS : Regional Oceanic Modeling System

SAR : Synthetic Aperture Radar

SLA : Sea Level Anomaly

SMOS : Soil Moisture and Ocean Salinity satellite

SNR : Signal to Noise Ratio

SSH : Sea Surface Height

SSS : Sea Surface Salinity

SST : Sea Surface Temperature

SWH or Hs : Significant Wave Height

SWOT : Surface Water Ocean Topography

Tp : wave period

UMs : Unbalanced Motions

WaCM : Winds and Currents Mission

WMED : Western MEDiterranean region

Bibliography

Aguiar, E., B. Mourre, M. Juza, E. Reyes, J. Hernández-lasheras, E. Cutolo, E. Mason, and J. Tintoré (2019), Multi-platform model assessment in the Western Mediterranean Sea : impact of downscaling on the surface circulation and mesoscale activity, *Ocean Dynamics*, doi:10.1007/s10236-019-01317-8.

Ajayi, A., J. L. Sommer, E. Chassignet, J.-M. Molines, X. Xu, A. Albert, and W. Dewar (2019), Diagnosing cross-scale kinetic energy exchanges from two submesoscale permitting ocean models., *Earth and Space Science Open Archive*, doi:10.1002/essoar.10501077.1.

Ajayi, A., J. Le Sommer, E. Chassignet, J. Molines, X. Xu, A. Albert, and E. Cosme (2020), Spatial and temporal variability of the North Atlantic edd y field from two kilometric-resolution ocean models, *Journal of Geophysical Research: Oceans*, *125*, doi:10.1029/2019JC015827.

Allen, J. T., D. A. Smeed, J. Tintoré, and S. Ruiz (2001), Mesoscale subduction at the Almeria - Oran front Part 1 : Ageostrophic flow, *Journal of Marine Systems*, *30*(3), 263–285, doi:10.1016/S0924-7963(01)00062-8.

Alsdorf, D. E., N. M. Mognard, D. P. Lettenmaier, and SWOT Virtual Mission Team (2011), Remote sensing of surface water and recent developments in the swot mission, in *AGU Fall Meeting Abstracts*, vol. 2011, pp. H21J–06, available at `https://ui.adsabs.harvard.edu/abs/2011AGUFM.H21J..06A`.

Alvarez-Berastegui, D., L. Ciannelli, A. Aparicio-Gonzalez, P. Reglero, M. Hidalgo, J. L. López-Jurado, J. Tintoré, and F. Alemany (2014), Spatial scale, means and gradients of hydrographic variables define pelagic seascapes of bluefin and bullet tuna spawning distribution, *PLoS One*, *9*(10), doi:10.1371/journal.pone.0109338.

Alvarez-Berastegui, D., M. Hidalgo, M. P. Tugores, P. Reglero, A. Aparicio-González, L. Ciannelli, M. Juza, B. Mourre, A. Pascual, J. L. López-Jurado, A. García, J. M. Rodríguez, J. Tintoré, and F. Alemany (2016), Pelagic seascape ecology for operational fisheries oceanography: Modelling and predicting spawning distribution of Atlantic bluefin tuna in Western Mediterranean, *ICES Journal of Marine Science*, doi:10.1093/icesjms/fsw041.

Amores, A., G. Jordà, T. Arsouze, and J. L. Sommer (2018), Up to What Extent Can We Characterize Ocean Eddies Using Present-Day Gridded Altimetric Products ?, *Journal of Geophysical Research: Oceans*, *123*(10), 7220–7236, doi:10.1029/2018JC014140.

Amores, A., G. Jordà, and S. Monserrat (2019), Ocean Eddies in the Mediterranean Sea From Satellite Altimetry : Sensitivity to Satellite Track Location, *Frontiers in Marine Science*, *6*(November), 703, doi:10.3389/fmars.2019.00703.

Ansong, J. K., B. K. Arbic, M. C. Buijsman, J. G. Richman, J. F. Shriver, and A. J. Wallcraft (2015), Indirect evidence for substantial damping of low-mode internal tides in the open ocean, *Journal of Geophysical Research: Oceans*, *120*(9), 6057–6071, doi:10.1002/2015jc010998.

Ansong, J. K., B. K. Arbic, M. H. Alford, M. C. Buijsman, J. F. Shriver, Z. Zhao, J. G. Richman, H. L. Simmons, P. G. Timko, A. J. Wallcraft, and L. Zamudio (2017), Semidiurnal internal tide energy fluxes and their variability in a global ocean model and moored observations, *Journal of Geophysical Research: Oceans*, *122*(3), 1882–1900, doi:10.1002/2016JC012184.

Ansong, J. K., B. K. Arbic, D. Menemenlis, A. J. Wallcraft, R. Bourdalle-Badie, J. Chanut, F. Briol, M. Schindelegger, R. Ray, E. P. Chassignet, et al. (2020), Importance of damping in comparison of internal tides in several global hydrodynamical models with altimetry, in *Ocean Sciences Meeting. 16 to 21 February 2020, San Diego, USA*, AGU, available at `https://agu.confex.com/agu/osm20/meetingapp.cgi/Paper/651707`.

Apel, J. R., H. M. Byrne, J. R. Proni, and R. L. Charnell (1975), Observations of oceanic internal and surface waves from the Earth Resources Technology Satellite, *Journal of Geophysical Research*, *80*(6), 865–881, doi:10.1029/jc080i006p00865.

Arbic, B. K., and W. Brechner Owens (2001), Climatic warming of Atlantic intermediate waters, *Journal of Climate*, *14*(20), 4091–4108, doi:10.1175/1520-0442(2001)014<4091:CWOAIW>2.0.CO;2.

Arbic, B. K., A. J. Wallcraft, and E. J. Metzger (2010), Concurrent simulation of the eddying general circulation and tides in a global ocean model, *Ocean Modelling*, *32*(3-4), 175–187, doi:10.1016/j.ocemod.2010.01.007.

Arbic, B. K., M. H. Alford, J. K. Ansong, M. C. Buijsman, R. B. Ciotti, J. T. Farrar, R. W. Hallberg, C. E. Henze, C. N. Hill, C. A. Luecke, D. Menemenlis, E. J. Metzger, M. Müller, A. D. Nelson, B. C. Nelson, H. E. Ngodock, R. M. Ponte, J. G. Richman, A. C. Savage, R. B. Scott, J. F. Shriver, H. L. Simmons, I. Souopgui, P. G. Timko, A. J. Wallcraft, L. Zamudio, and Z. Zhao (2018), A Primer on Global Internal Tide and Internal Gravity Wave Continuum Modeling in HYCOM and MITgcm, in *New frontiers in operational oceanography*, edited by E. P. Chassignet, A. Pascual, J. Tintoré, and J. Verron, pp. 307–392, GODAE Oceanview, doi:10.17125/gov2018.ch13.

Aubert, G., and P. Kornprobst (2006), *Mathematical problems in image processing: partial differential equations and the calculus of variations*, vol. 147, Springer Science & Business Media: Berlin, Germany.

Ballarotta, M., C. Ubelmann, M.-I. Pujol, G. Taburet, F. Fournier, J.-f. Legeais, Y. Faugère, A. Delepoulle, D. Chelton, G. Dibarboure, and N. Picot (2019), On the resolutions of ocean altimetry maps, *Ocean Science*, *15*(4), 1091–1109, doi:10.5194/os-15-1091-2019.

Banks, H. T., R. A. Wood, J. M. Gregory, T. C. Johns, and G. S. Jones (2000), Are observed decadal changes in intermediate water masses a signature of anthropogenic climate change?, *Geophysical Research Letters*, *27*(18), 2961–2964, doi:10.1029/2000gl011601.

Barceló-Llull, B., A. Pascual, L. Día-Barroso, A. Sánchez-Román, B. Casas, C. Muñoz, M. Torner, E. Alou-Font, E. Cutolo, B. Mourre, et al. (2018), PRE-SWOT Cruise Report. Mesoscale and sub-mesoscale vertical exchanges from multi-platform experiments and supporting modeling simulations: anticipating SWOT launch, *(CTM2016-78607-P)*, doi:10.20350/digitalCSIC/8584.

Barceló-Llull, B., A. Pascual, S. Ruiz, R. Escudier, M. Torner, and J. Tintoré (2019), Temporal and spatial hydrodynamic variability in the mallorca channel (western mediterranean sea) from 8 years of underwater glider data, *Journal of Geophysical Research: Oceans*, *124*(4), 2769–2786, doi:10.1029/2018JC014636.

Batteen, M. L. (1997), Wind-forced modeling studies of currents, meanders, and eddies in the california current system, *Journal of Geophysical Research: Oceans*, *102*(C1), 985–1010, doi:10.1029/96jc02803.

Beck, A., and M. Teboulle (2009), A fast iterative shrinkage-thresholding algorithm for linear inverse problems, *SIAM Journal on Imaging Sciences*, *2*(1), 183–202, doi:10.1137/080716542.

Benveniste, J. (2011), *Coastal Altimetry*, chap. Radar Altimetry: Past, Present and Future, pp. 1–17, Springer Berlin Heidelberg, Berlin, Heidelberg, doi:10.1007/978-3-642-12796-0_1.

Beron-vera, F. J., A. Hadjighasem, Q. Xia, M. J. Olascoaga, and G. Haller (2019), Coherent Lagrangian swirls among submesoscale motions, *Proceedings of the National Academy of Sciences*, *116*(37), 18,251–18,256, doi:10.1073/pnas.1701392115.

Berti, S., and G. Lapeyre (2014), Lagrangian reconstructions of temperature and velocity in a model of surface ocean turbulence, *Ocean Modelling*, *76*, 59–71, doi:10.1016/j.ocemod.2014.02.003.

Bethoux, J. P., B. Gentili, J. Raunet, and D. Tailliez (1990), Warming trend in the western mediterranean deep water., *Nature*, *347*(6294), 660–662, doi:10.1038/347660a0.

Bethoux, J. P., B. Gentili, P. Morin, E. Nicolas, C. Pierre, and D. Ruiz-Pino (1999), The Mediterranean Sea : a miniature ocean for climatic and environmental studies and a key for the climatic functioning of the North Atlantic, *Progress in Oceanography*, *44*(1), 131–146, doi:10.1016/s0079-6611(99)00023-3.

Biemond, J., R. L. Lagendijk, and R. M. Mersereau (1990), Iterative methods for image deblurring, *Proceedings of the IEEE*, *78*(5), 856–883, doi:10.1109/5.53403.

Bonaduce, A., M. Benkiran, E. Remy, P. Yves, L. Traon, and G. Garric (2018), Contribution of future wide-swath altimetry missions to ocean analysis and forecasting, *Ocean Science*, *14*(6), 1405–1421, doi:10.5194/os-14-1405-2018.

Brannigan, L., D. P. Marshall, A. C. Naveira Garabato, A. G. Nurser, and J. Kaiser (2017), Submesoscale Instabilities in Mesoscale Eddies, *Journal of Physical Oceanography*, *47*(12), 3061–3085, doi:10.1175/JPO-D-16-0178.1.

Buckingham, C. E., A. C. Naveira Garabato, A. F. Thompson, L. Brannigan, A. Lazar, D. P. Marshall, A. J. George Nurser, G. Damerell, K. J. Heywood, and S. E. Belcher (2016), Seasonality of submesoscale flows in the ocean surface boundary layer, *Geophysical Research Letters*, *43*(5), 2118–2126, doi:10.1002/2016GL068009.

Buijsman, M. C., B. K. Arbic, J. Green, R. W. Helber, J. G. Richman, J. F. Shriver, P. Timko, and A. Wallcraft (2015), Optimizing internal wave drag in a forward barotropic model with semidiurnal tides, *Ocean Modelling*, *85*, 42–55, doi:10.1016/j.ocemod.2014.11.003.

Buijsman, M. C., J. K. Ansong, B. K. Arbic, J. G. Richman, J. F. Shriver, P. G. Timko, A. J. Wallcraft, C. B. Whalen, and Z. Zhao (2016), Impact of parameterized internal wave drag on the semidiurnal energy balance in a global ocean circulation model, *Journal of Physical Oceanography*, *46*(5), 1399–1419, doi:10.1175/jpo-d-15-0074.1.

Callies, J., R. Ferrari, J. M. Klymak, and J. Gula (2015), Seasonality in submesoscale turbulence, *Nature communications*, *6*(1), 1–8, doi:10.1038/ncomms7862.

Capet, X., P. Klein, B. L. Hua, G. Lapeyre, and J. C. McWilliams (2008a), Surface kinetic energy transfer in surface quasi-geostrophic flows, *Journal of Fluid Mechanics*, *604*, 165–174, doi:10.1017/S0022112008001110.

Capet, X., J. C. McWilliams, M. J. Molemaker, and A. Shchepetkin (2008b), Mesoscale to Submesoscale Transition in the California Current System . Part I : Flow Structure , Eddy Flux , and Observational Tests, *Journal of Physical Oceanography*, *38*(1), 29–43, doi:10.1175/2007JPO3671.1.

Capó, E., A. Orfila, E. Mason, and S. Ruiz (2019), Energy Conversion Routes in the Western Mediterranean Sea Estimated from Eddy - Mean Flow Interactions, *Journal of Physical Oceanography*, *49*(1), 247–267, doi:10.1175/JPO-D-18-0036.1.

Carret, A. (2019), Étude de la variabilité spatio-temporelle de la circulation en méditerranée nord-occidentale: apport de l'altimétrie spatiale, Ph.D. thesis, Université Paul Sabatier-Toulouse III, available at `https://tel.archives-ouvertes.fr/tel-03104033`.

Carton, X., M. Morvan, J. N. Reinaud, M. A. Sokolovskiy, and P. L'Hegaret (2017), Vortex Merger near a Topographic Slope in a Homogeneous Rotating Fluid, *Regular and Chaotic Dynamics*, *22*(5), 455–478, doi:10.1134/S156035471705001X.

Castelao, R. M., T. P. Mavor, J. A. Barth, and L. C. Breaker (2006), Sea surface temperature fronts in the California Current System from geostationary satellite observations, *Journal of Geophysical Research*, *111*(June), 1–13, doi:10.1029/2006JC003541.

Chambolle, A. (2004), An Algorithm for Total Variation Minimization and Applications, *Journal of Mathematical Imaging and Vision*, *20*(2), 89–97, doi:10.1023/B:JMIV.0000011325.36760.1e.

Chang, S. G., B. Yu, and M. Vetterli (2000), Spatially adaptive wavelet thresholding with context modeling for image denoising, *IEEE Transactions on Image Processing*, *9*(9), 1522–1531, doi:10.1109/83.862630.

Chassignet, E. P., H. E. Hurlburt, E. J. Metzger, O. M. Smedstad, J. A. Cummings, G. R. Halliwell, R. Bleck, R. Baraille, A. J. Wallcraft, C. Lozano, et al. (2009), US GODAE: global ocean prediction with the HYbrid Coordinate Ocean Model (HYCOM), *Oceanography*, *22*(2), 64–75, available at `www.jstor.org/stable/24860960`.

Chelton, D. B. (2019), The wavenumber spectra and standard deviations of uncorrelated errors in swot measurements of sea-surface height for various footprint sizes, available at `https://swot.jpl.nasa.gov/system/documents/files/2253_2253_Chelton_2019_SWOT_Measurement_Noise_190523.pdf`.

Chelton, D. B., R. A. Deszoeke, M. G. Schlax, K. El, N. And, and N. Siwertz (1998), Geographical Variability of the First Baroclinic Rossby Radius of Deformation, *Journal of Physical Oceanography*, *28*, 433–460, doi:10.1175/1520-0485(1998)028<0433:GVOTFB>2.0.CO;2.

Chelton, D. B., M. G. Schlax, R. M. Samelson, and R. A. de Szoeke (2007), Global observations of large oceanic eddies, *Geophysical Research Letters*, *34*(15), doi:10.1029/2007GL030812.

Chelton, D. B., M. G. Schlax, R. M. Samelson, J. T. Farrar, M. J. Molemaker, J. C. McWilliams, and J. Gula (2019), Prospects for future satellite estimation of small-scale variability of ocean surface velocity and vorticity, *Progress in Oceanography*, *173*, 256–350, doi:10.1016/j.pocean.2018.10.012.

Ciani, D., M.-H. Rio, M. Menna, and R. Santoleri (2019), A synergetic approach for the space-based sea surface currents retrieval in the Mediterranean Sea, *Remote Sensing*, *11*(11), 1285, doi:10.3390/rs11111285.

Cipollini, P., F. M. Calafat, S. Jevrejeva, A. Melet, and P. Prandi (2017), Monitoring Sea Level in the Coastal Zone with Satellite Altimetry and Tide Gauges, *Surveys in Geophysics*, *38*(1), 33–57, doi:10.1007/s10712-016-9392-0.

Colling, A., and Oceanography Course Team Open University (2001), *Ocean Circulation*, vol. 1, Open University, Walton Hall, Milton Keynes MK7 6AA and Butterworth-Heinemann, second edition.

Conti, D., A. Orfila, E. Mason, J. M. Sayol, G. Simarro, and S. Balle (2016), An eddy tracking algorithm based on dynamical systems theory, *Ocean Dynamics*, *66*(11), 1415–1427, doi:10.1007/s10236-016-0990-7.

Criado-Aldeanueva, F., J. Del Río Vera, and J. García-Lafuente (2008), Steric and mass-induced Mediterranean Sea level trends from 14 years of altimetry data, *Global and Planetary Change*, doi:10.1016/j.gloplacha.2007.07.003.

Da Silva, J., S. Ermakov, I. Robinson, D. Jeans, and S. Kijashko (1998), Role of surface films in ERS SAR signatures of internal waves on the shelf: 1. Short-period internal waves, *Journal of Geophysical Research: Oceans*, *103*(97), 8009–8031, doi:10.1029/97JC02725.

d'Addezio, J. M., S. Smith, G. A. Jacobs, R. W. Helber, C. Rowley, I. Souopgui, and M. J. Carrier (2019), Quantifying wavelengths constrained by simulated SWOT observations in a submesoscale resolving ocean analysis / forecasting system, *Ocean Modelling*, *135*(June 2018), 40–55, doi:10.1016/j.ocemod.2019.02.001.

Davidson, F., A. Alvera-azcárate, A. Barth, G. B. Brassington, E. P. Chassignet, E. Clementi, P. D. Meyfrémaux, P. Divakaran, C. Harris, F. Hernandez, P. Hogan, L. R. Hole, J. Holt, G. Liu, Y. Lu, P. Lorente, A. Moore, P. Oddo, A. Pascual, A.-C. Pequignet, H. Burchard, et al. (2019), Synergies in Operational Oceanography : The Intrinsic Need for Sustained Ocean Observations, *Frontiers in Marine Science*, *6*(450), doi:10.3389/fmars.2019.00450.

Delandmeter, P., J. Lambrechts, G. O. Marmorino, V. Legat, E. Wolanski, J.-F. Remacle, W. Chen, and E. Deleersnijder (2017), Submesoscale tidal eddies in the wake of coral islands and reefs: satellite data and numerical modelling, *Ocean Dynamics*, *67*(7), 897–913, doi:10.1007/s10236-017-1066-z.

Deledalle, C.-A., L. Denis, and F. Tupin (2009), Iterative weighted maximum likelihood denoising with probabilistic patch-based weights, *IEEE Transactions on Image Processing*, *18*(12), 2661–2672, doi:10.1109/tip.2009.2029593.

Desbrun, M., M. Meyer, P. Schröder, and A. H. Barr (2000), Anisotropic feature-preserving denoising of height fields and bivariate data., in *Proceedings of the Graphics Interface 2000 Conference, May 15-17, 2000, Montréal, Québec, Canada*, vol. 11, pp. 145–152, Citeseer, doi:10.20380/GI2000.20.

Dibarboure, G., and C. Ubelmann (2014), Investigating the performance of four empirical cross-calibration methods for the proposed SWOT mission, *Remote Sensing*, *6*(6), 4831–4869, doi:10.3390/rs6064831.

d'Ortenzio, F., D. Iudicone, C. D. B. Montegut, P. Testor, D. Antoine, S. Marullo, R. Santoleri, and G. Madec (2005), Seasonal variability of the mixed layer depth in the Mediterranean Sea as derived from in situ profiles, *Geophysical Research Letters*, *32*(12), 2–5, doi:10.1029/2005GL022463.

d'Ovidio, F., A. Pascual, J. Wang, A. M. Doglioli, Z. Jing, S. Moreau, G. Grégori, S. Swart, and S. Speich (2019), Frontiers in Fine-Scale in situ Studies : Opportunities During the SWOT Fast Sampling Phase, *Frontiers in Marine Science*, *6*(April), 1–7, doi:10.3389/fmars.2019.00168.

Drushka, K., W. E. Asher, J. Sprintall, S. T. Gille, and C. Hoang (2019), Global Patterns of Submesoscale Surface Salinity Variability, *Journal of Physical Oceanography*, *49*(7), 1669–1685, doi:10.1175/JPO-D-19-0018.1.

Ducet, N., P. Y. Le Traon, and G. Reverdin (2000), Global high-resolution mapping of ocean circulation from TOPEX/Poseidon and ERS-1 and -2, *Journal of Geophysical Research: Oceans*, *105*(C8), 19,477–19,498, doi:10.1029/2000JC900063.

Dufau, C., M. Orsztynowicz, G. Dibarboure, R. Morrow, and P. Y. Le Traon (2016), Mesoscale resolution capability of altimetry: Present and future, *Journal of Geophysical Research : Oceans*, *121*(7), 4910–4927, doi:10.1002/2015JC010904.

Durán-Moro, M. (2017), Reconstruction de la circulation océanique à partir d'observations satellitaires à très haute résolution, Ph.D. thesis, Université Grenoble Alpes, available at `http://www.theses.fr/2017GREAU037/document`.

Durán-Moro, M., J.-M. Brankart, P. Brasseur, and J. Verron (2017), Exploring image data assimilation in the prospect of high-resolution satellite oceanic observations, *Ocean Dynamics*, *67*(7), 875–895, doi:10.1007/s10236-017-1062-3.

Egbert, G. D., and R. D. Ray (2000), Significant dissipation of tidal energy in the deep ocean inferred from satellite altimeter data, *Nature*, *405*(6788), 775–778, doi:10.1038/35015531.

Escudier, R. (2014), Eddies in the western Mediterranean Sea: characterization and understanding from satellite observations and model simulations, Ph.D. thesis, Universitat de les Illes Balears and Université Grenoble Alpes, available at `https://www.tdx.cat/handle/10803/310417#page=1`.

Escudier, R., B. Mourre, M. Juza, and J. Tintoré (2016a), Subsurface circulation and mesoscale variability in the Algerian subbasin from altimeter-derived eddy trajectories, *Journal og Geophysical Research : Oceans*, *121*, 6310–6322, doi:10.1002/2016JC011760.

Escudier, R., L. Renault, A. Pascual, P. Brasseur, D. Chelton, and J. Beuvier (2016b), Eddy properties in the Western Mediterranean Sea from satellite altimetry and a numerical simulation, *Journal of Geophysical Research : Oceans*, *121*(6), 3990–4006, doi:10.1002/2015JC011371.

Esteban-Fernandez, D. (2017), Swot project: mission performance and error budget document, Jet Propulsion Laboratory, California Institute of Technology, JPL D-79084, 117 pp. Available at `https://swot.jpl.nasa.gov/system/documents/files/2178_2178_SWOT_D-79084_v10Y_FINAL_REVA__06082017.pdf`.

European Space Agency, T. N., Noordwijk (2019), Report for Mission Selection: SKIM, *ESA-EOPSM-SKIM-RP-3550*, p. 264, available at `https://skim-ucm.oceandatalab.com/rfms.html`.

Fablet, R., J. Verron, B. Mourre, B. Chapron, and A. Pascual (2018), Improving mesoscale altimetric data from a multitracer convolutional processing of standard satellite-derived products, *IEEE Transactions on Geoscience and Remote Sensing*, *56*(5), 2518–2525, doi:10.1109/TGRS.2017.2750491.

Ferry, N., L. Parent, G. Garric, C. Bricaud, C. Testut, O. Le Galloudec, J. Lellouche, M. Drevillon, E. Greiner, B. Barnier, et al. (2012), GLORYS2V1 global ocean reanalysis of the altimetric era (1992–2009) at meso scale, *Mercator Ocean–Quaterly Newsletter*, *44*, 28–39, available at `https://www.mercator-ocean.fr/wp-content/uploads/2015/05/Mercator-Ocean-newsletter-2012_44.pdf#page=28`.

Flexas, M. M., A. F. Thompson, H. S. Torres, P. Klein, J. T. Farrar, H. Zhang, and D. Menemenlis (2019), Global estimates of the energy transfer from the wind to the ocean, with emphasis on near-inertial oscillations, *Journal of geophysical research. Oceans*, *124*(8), 5723, doi:10.1029/2018JC014453.

Foltz, G. R., P. Brandt, I. Richter, B. Rodriguez-Fonseca, F. Hernandez, M. Dengler, R. R. Rodrigues, J. O. Schmidt, L. Yu, N. Lefevre, et al. (2019), The tropical atlantic observing system, *Frontiers in Marine Science*, *6*, 206, doi:10.3389/fmars.2019.00206.

Font, J., A. Camps, A. Borges, M. Martín-Neira, J. Boutin, N. Reul, Y. H. Kerr, A. Hahne, and S. Mecklenburg (2009), Smos: The challenging sea surface salinity measurement from space, *Proceedings of the IEEE*, *98*(5), 649–665, doi:10.1109/JPROC.2009.2033096.

Forget, G., J. Campin, P. Heimbach, C. N. Hill, R. M. Ponte, and C. Wunsch (2015), ECCO version 4 : an integrated framework for non-linear inverse modeling and global ocean state estimation, *Geoscientific Model Development*, (8), 3071–3104, doi:10.5194/gmd-8-3071-2015.

Frenger, I., M. Münnich, and N. Gruber (2018), Imprint of Southern Ocean mesoscale eddies on chlorophyll, *Biogeosciences*, *15*, 4781–4798, doi:10.5194/bg-15-4781-2018.

Fresnay, S., A. L. Ponte, S. Le Gentil, and J. Le Sommer (2018), Reconstruction of the 3-D Dynamics FromSurface Variables in a High-Resolution Simulation of North Atlantic, *Journal of Geophysical Research : Oceans*, *123*, 1–19, doi:10.1002/2017JC013400.

Fu, L.-L., and R. Ferrari (2008), Observing Oceanic Submesoscale Processes From Space, *Eos, Trans. Am. Geophys. Union*, *89*(48), 488–488, doi:10.1029/2008EO480003.

Fu, L.-L., and B. Holt (1984), Internal waves in the Gulf of California: Observations from a spaceborne radar, *Journal of Geophysical Research: Oceans*, *89*(C2), 2053–2060, doi:10.1029/JC089iC02p02053.

Fu, L.-L., and R. Morrow (2016), A next generation altimter for mapping the sea surface variability: Opportunities and challenges, in *48th International Liège Colloquium on Ocean Dynamics*, Liège, Belgium.

Fu, L.-L., and C. Ubelmann (2014), On the transition from profile altimeter to swath altimeter for observing global ocean surface topography, *Journal of Atmospheric and Oceanic Technology*, doi:10.1175/JTECH-D-13-00109.1.

Fu, L.-L., and V. Zlotnicki (1989), Observing oceanic mesoscale eddies from Geosat altimetry: Preliminary results, *Geophysical Research Letters*, *16*(5), 457–460, doi:10.1029/GL016i005p00457.

Fu, Lee-Lueng and Alsdorf, Douglas and Morrow, Rosemary and Rodriguez, Ernesto and Mognard, Nelly (2012), SWOT : The Surface Water and Ocean Topography Mission: wide-swath altimetric elevation on Earth, *Tech. rep.*, Pasadena, CA, USA: Jet Propulsion Laboratory, National Aeronautics and Space Administration, available at `http://hdl.handle.net/2014/41996`.

Gaultier, L., J. Verron, J.-M. Brankart, O. Titaud, and P. Brasseur (2013), On the inversion of submesoscale tracer fields to estimate the surface ocean circulation, *Journal of Marine Systems*, *126*, 33–42, doi:10.1016/j.jmarsys.2012.02.014.

Gaultier, L., C. Ubelmann, and L.-L. Fu (2015), SWOT Simulator Documentation, *Tech. rep.*, 1.0.0, Jet Propulsion Laboratory, California Institute of Technology, Pasadena, CA, USA. Available at `https://swot.odyseallc.net/docs/documentation_swotsimulator.pdf`.

Gaultier, L., C. Ubelmann, and L. L. Fu (2016), The challenge of using future SWOT data for oceanic field reconstruction, *Journal of Atmospheric and Oceanic Technology*, *33*, 119–126, doi:10.1175/JTECH-D-15-0160.1.

Gómez-Navarro, L., R. Fablet, E. M. Id, A. Pascual, B. Mourre, E. Cosme, and J. Le Sommer (2018), SWOT Spatial Scales in the Western Mediterranean Sea Derived from Pseudo-Observations and an Ad Hoc Filtering, *Remote Sensing*, *10*(4), 599, doi:10.3390/rs10040599.

Gómez-Navarro, L., E. Cosme, J. Le Sommer, N. Papadakis, and A. Pascual (2020), Development of an image de-noising method in preparation for the surface water and ocean topography satellite mission, *Remote Sensing*, *12*(4), doi:10.3390/rs12040734.

González-Haro, C., and J. Isern-Fontanet (2014), Global ocean current reconstruction from altimetric and microwave sst measurements, *Journal of Geophysical Research: Oceans*, *119*(6), 3378–3391, doi:10.1002/2013JC009728.

Good, S. A., M. J. Martin, and N. A. Rayner (2013), EN4: Quality controlled ocean temperature and salinity profiles and monthly objective analyses with uncertainty estimates, *Journal of Geophysical Research : Oceans*, doi:10.1002/2013JC009067.

Gould, J., B. Sloyan, and M. Visbeck (2013), Chapter 3 - in situ ocean observations: A brief history, present status, and future directions, in *Ocean Circulation and Climate*, *International Geophysics*, vol. 103, edited by G. Siedler, S. M. Griffies, J. Gould, and J. A. Church, pp. 59 – 81, Academic Press, doi:https://doi.org/10.1016/B978-0-12-391851-2.00003-9.

Gula, J., M. J. Molemaker, and J. C. McWilliams (2016), Topographic generation of submesoscale centrifugal instability and energy dissipation, *Nature Communications*, *7*(1), 1–7, doi:10.1038/ncomms12811.

Gunturk, B. K., and X. Li (2012), *Image restoration: fundamentals and advances*, CRC Press: Boca Raton, FL, USA.

Hallberg, R. (2013), Using a resolution function to regulate parameterizations of oceanic mesoscale eddy effects, *Ocean Modelling*, *72*, 92–103, doi:10.1016/j.ocemod.2013.08.007.

Harcourt, R., A. M. M. Sequeira, X. Zhang, F. Roquet, K. Komatsu, M. Heupel, C. R. McMahon, F. G. Whoriskey, M. Meekan, G. Carroll, et al. (2019), Animal-Borne Telemetry : An Integral Component of the Ocean Observing Toolkit, *Frontiers in Marine Science*, *6*, 326, doi:10.3389/fmars.2019.00326.

Hernández-Carrasco, I., A. Orfila, V. Rossi, and V. Garçon (2018), Effect of small scale transport processes on phytoplankton distribution in coastal seas, *Scientific reports*, *8*(1), 1–13, doi:10.1038/s41598-018-26857-9.

Heslop, E., A. Sánchez-Román, A. Pascual, D. Rodríguez, K. Reeve, Y. Faugère, and M. Raynal (2017), Sentinel-3A views ocean variability more accurately at finer resolution, *Geophysical Research Letters*, *44*(24), 367–374, doi:10.1002/2017GL076244.

Houpert, L., P. Testor, X. D. D. Madron, S. Somot, F. d'Ortenzio, C. Estournel, and H. Lavigne (2015), Seasonal cycle of the mixed layer , the seasonal thermocline and the upper-ocean heat storage rate in the Mediterranean Sea derived from observations, *Progress in Oceanography*, *132*, 333–352, doi:10.1016/j.pocean.2014.11.004.

Juza, M., B. Mourre, L. Renault, S. Gómara, K. Sebastián, S. Lora, J. P. Beltran, B. Frontera, B. Garau, C. Troupin, M. Torner, E. Heslop, B. Casas, R. Escudier, G. Vizoso, and J. Tintoré (2016), SOCIB operational ocean forecasting system and multi-platform validation in the Western Mediterranean Sea, *Journal of Operational Oceanography*, *9*(sup1), s155–s166, doi:10.1080/1755876X.2015.1117764.

Kafiabad, H. A., J. Vanneste, and W. R. Young (2020), Wave-averaged geostrophic balance, *arXiv preprint arXiv:2003.03389*, doi:10.1017/jfm.2020.1032.

Klein, P., and G. Lapeyre (2009), The oceanic vertical pump induced by mesoscale and submesoscale turbulence, *Annual Review of Marine Science*, *1*, 351–375, doi:10.1146/annurev.marine.010908.163704.

Klein, P., R. Morrow, R. Samelson, D. Chelton, G. Lapeyre, L. Fu, B. Qiu, C. Ubelmann, P.-Y. Le Traon, X. Capet, A. Ponte, H. Sasaki, F. D 'ovidio, T. Farrar, B. Chapron, E. D 'asaro, R. Ferrari, J. Mcwilliams, S. Smith, and A. Thompson (2015), Mesoscale / sub-mesoscale dynamics in the upper ocean, *NASA Surface Water and Ocean Topography (SWOT)*, available at `http://www.aviso.altimetry.fr/fileadmin/documents/missions/Swot/WhitePaperSWOTSubmesoscale.pdf`.

Klein, P., G. Lapeyre, L. Siegelman, B. Qiu, L.-l. Fu, H. S. Torres, Z. Su, D. Menemenlis, and S. Le Gentil (2019), Ocean-Scale Interactions From Space, *Earth and Space Science*, *6*(5), 795–817, doi:10.1029/2018EA000492.

Lapeyre, G., and P. Klein (2006), Impact of the small-scale elongated filaments on the oceanic vertical pump, *Journal of Marine Research*, *64*(6), 835–851, doi:10.1357/002224006779698369.

Le Guillou, F., S. Metref, E. Cosme, C. Ubelmann, M. Ballarotta, J. Le Sommer, and J. Verron (2020), Mapping altimetry in the forthcoming swot era by back-and-forth nudging a one-layer quasi-geostrophic model, *Earth and Space Science Open Archive*, p. 15, doi:10.1002/essoar.10504575.2.

Le Sommer, J., E. P. Chassignet, and A. J. Wallcraft (2018), Ocean circulation modeling for operational oceanography: Current status and future challenges, in *New frontiers in operational oceanography*, edited by E. P. Chassignet, A. Pascual, J. Tintoré, and J. Verron, pp. 289–308, GODAE Oceanview, doi:10.17125/gov2018.ch12.

Le Sommer, J., J. Molines, A. Albert, L. Brodeau, A. Ajayi, L. Gómez-Navarro, E. Cosme, T. Penduff, B. Barnier, J. Verron, P. Brasseur, P. Rampal, and E. Chassignet (In prep.), NATL60: A North Atlantic ocean circulation model dataset based on NEMO for preparing SWOT altimeter mission., *Geoscientific Model Development*.

Le Traon, P.-Y. (2018), Satellites and operational oceanography, in *New frontiers in operational oceanography*, edited by E. P. Chassignet, A. Pascual, J. Tintoré, and J. Verron, pp. 161–190, GODAE Oceanview, doi:10.17125/gov2018.ch07.

Lee, H., S. Biancamaria, D. Alsdorf, K. Andreadis, E. Clark, M. Durand, H. C. Jung, D. Lettenmaier, N. Mognard, E. Rodriguez, Y. Sheng, and C. K. Shum (2010), Capability of SWOT to Measure Surface Water Storage Change, in *Proceedings of the Towards high-resolution of oceans dynamics and terrestrial water from space meeting, Lisbon, Portugal*, pp. 21–22.

Lévy, M., P. Klein, and A.-M. Treguier (2001), Impact of sub-mesoscale physics on production and subduction of phytoplankton in an oligotrophic regime, *Journal of Marine Research*, *59*(4), 535–565, doi:10.1357/002224001762842181.

Lévy, M., R. Ferrari, P. J. S. Franks, A. P. Martin, and P. Rivière (2012a), Bringing physics to life at the submesoscale, *39*(July), 1–13, doi:10.1029/2012GL052756.

Lévy, M., D. Iovino, L. Resplandy, P. Klein, G. Madec, A. Tréguier, S. Masson, and K. Takahashi (2012b), Large-scale impacts of submesoscale dynamics on phytoplankton : Local and remote effects, *Ocean Modelling*, *43-44*, 77–93, doi:10.1016/j.ocemod.2011.12.003.

Lguensat, R., P. H. Viet, M. Sun, G. Chen, T. Fenglin, B. Chapron, and R. Fablet (2019), Data-driven interpolation of sea level anomalies using analog data assimilation, *Remote Sensing*, *11*(7), doi:10.3390/rs11070858.

Lima, I. D., and J. P. Castello (1995), Distribution and abundance of South-west Atlantic anchovy spawners (Engraulis anchoita) in relation to oceanographic processes in the southern Brazilian shelf, *Fisheries Oceanography*, *4*(1), 1–16, doi:10.1111/j.1365-2419.1995.tb00057.x.

Lindstrom, E., S. Cherchal, L.-L. Fu, R. Morrow, T. Pavelsky, J.-F. Cretaux, P. Vaze, T. Lafon, S. Coutin-Faye, L. Amen, N. Bellefond, E. Bronner, E. Picot, Nicolas and R. Morrow (2017), Summary Report of the 2nd SWOT Science Team Meeting 2017, *Tech. Rep. June 2017*, Météo-France Conference Centre: Toulouse, France, available at `https://spark.adobe.com/page/iuFI7X6PBlVYT`.

Lopez-Radcenco, M., A. Pascual, L. Gomez-Navarro, A. Aissa-El-Bey, B. Chapron, and R. Fablet (2019), Analog Data Assimilation of Along-Track Nadir and Wide-Swath SWOT Altimetry Observations in the Western Mediterranean Sea, *IEEE Journal of Selected Topics in Applied Earth Observations and Remote Sensing*, *12*(7), 2530–2540, doi:10.1109/JSTARS.2019.2903941.

Luecke, C. A., B. K. Arbic, J. G. Richman, J. F. Shriver, M. H. Alford, J. K. Ansong, S. L. Bassette, M. C. Buijsman, D. Menemenlis, R. B. Scott, P. G. Timko, G. Voet, A. J. Wallcraft, and L. Zamudio (2020), Statistical comparisons of temperature variance and kinetic energy in global ocean models and observations: Results from mesoscale to internal wave frequencies, *Journal of Geophysical Research: Oceans*, *125*(5), e2019JC015,306, doi:10.1029/2019JC015306.

Ma, Z., and G. Han (2019), Reconstruction of the Surface Inshore Labrador Current from SWOT Sea Surface Height Measurements, *Remote Sensing*, *11*(11), 1264, doi:10.3390/rs11111264.

Mahadevan, A. (2016), The Impact of Submesoscale Physics on Primary Productivity of Plankton., *Annual Review of Marine Science*, *8*, 161–184, doi:10.1146/annurev-marine-010814-015912.

Mahadevan, A., and A. Tandon (2006), An analysis of mechanisms for submesoscale vertical motion at ocean fronts, *Ocean Modelling*, *14*(3-4), 241–256, doi:10.1016/j.ocemod.2006.05.006.

Mahadevan, A., A. Pascual, D. L. Rudnick, S. Ruiz, J. Tintoré, and E. d'Asaro (2020), Coherent pathways for vertical transport from the surface ocean to interior, *Bulletin of the American Meteorological Society*, *101*(11), E1996–E2004, doi:10.1175/BAMS-D-19-0305.1.

Mailhes, C., D. Bonacci1, O. Besson, A. Guillot, S. Le Gac, N. Steunou, C. Cheymol, and N. Picot (2016), Review of spectral analysis methods applied to sealevel anomaly signals, in *OSTST Meeting*, La Rochelle, France, available at `https://www.tesa.prd.fr/documents/26/2016-11-03-9h-tesa-cnes-ostst-uncertaintiessession_compressed.pdf`.

Malanotte-Rizzoli, P., V. Artale, G. L. Borzelli-Eusebi, S. Brenner, A. Crise, M. Gacic, N. Kress, S. Marullo, M. Ribera d'Alcalà, S. Sofianos, T. Tanhua, A. Theocharis, M. Alvarez, Y. Ashkenazy, A. Bergamasco, V. Cardin, S. Carniel, G. Civitarese, F. d'Ortenzio, J. Font, E. Garcia-Ladona, J. M. Garcia-Lafuente, A. Gogou, M. Gregoire, D. Hainbucher, H. Kontoyannis, V. Kovacevic, E. Kraskapoulou, G. Kroskos, A. Incarbona, M. G. Mazzocchi, M. Orlic, E. Ozsoy, A. Pascual, P. M. Poulain, W. Roether, A. Rubino, K. Schroeder, J. Siokou-Frangou, E. Souvermezoglou, M. Sprovieri, J. Tintoré, and G. Triantafyllou (2014), Physical forcing and physical/biochemical variability of the Mediterranean Sea: A review of unresolved issues and directions for future research, *Ocean Science*, *10*(3), 281, doi:10.5194/os-10-281-2014.

March, D., L. Boehme, J. Tintoré, P. Joaquín, and V.-b. B. J. Godley (2019), Towards the integration of animal-borne instruments into global ocean observing systems, *Global change biology*, pp. 1–11, doi:10.1111/gcb.14902.

Marshall, J., and R. Plumb (2008), The general circulation of the atmosphere, *Atmosphere, ocean, and climate dynamics–an introductory text (eds) Dmowska R, Hrtmann D and Rossby HT, Inter. Geophys. Union, Ser. Monogr*, *93*, 319.

Marshall, J., A. Adcroft, C. Hill, L. Perelman, and C. Heisey (1997), A finite-volume, incompressible navier stokes model for studies of the ocean on parallel computers, *Journal of Geophysical Research: Oceans*, *102*(C3), 5753–5766, doi:10.1029/96JC02775.

Mason, E., A. Pascual, and J. C. McWilliams (2014), A new sea surface height-based code for oceanic mesoscale eddy tracking, *Journal of Atmospheric and Oceanic Technology*, *31*(5), 1181–1188, doi:10.1175/JTECH-D-14-00019.1.

McClain, Charles R (2009), A decade of satellite ocean color observations, *Annual Review of Marine Science*, *1*, 19–42, doi:10.1146/annurev.marine.010908.163650.

McGillicuddy, D. J., L. A. Anderson, N. R. Bates, T. Bibby, K. O. Buesseler, C. A. Carlson, C. S. Davis, C. Ewart, P. G. Falkowski, S. A. Goldthwait, et al. (2007), Eddy/wind interactions stimulate extraordinary mid-ocean plankton blooms, *Science*, *316*(5827), 1021–1026, doi:10.1126/science.1136256.

McGillicuddy Jr, D. J. (2016), Mechanisms of physical-biological-biogeochemical interaction at the oceanic mesoscale, *Annual Review of Marine Science*, *8*, 125–159, doi:10.1146/annurev-marine-010814-015606.

McWilliams, J. C. (2016), Submesoscale currents in the ocean, *Proceedings of the Royal Society A: Mathematical, Physical and Engineering Sciences*, *472*, doi:10.1098/rspa.2016.0117.

McWilliams, J. C., and B. Fox-Kemper (2013), Oceanic wave-balanced surface fronts and filaments, *Journal of Fluid Mechanics*, *730*, 464–490, doi:10.1017/jfm.2013.348.

Mémery, L., and F. Olivier (2003), Primary production and export fluxes at the Almeria-Oran front: A numerical study, in *EGS-AGU-EUG Joint Assembly, Nice, France, 6-11 April, 2003*, p. 5886, available at `https://ui.adsabs.harvard.edu/abs/2003EAEJA.....5886M`.

Metref, S., E. Cosme, J. Le Sommer, N. Poel, J.-M. Brankart, J. Verron, and L. Gómez Navarro (2019), Reduction of spatially structured errors in wide-swath altimetric satellite data using data assimilation, *Remote Sensing*, *11*(11), 1336, doi:10.3390/rs11111336.

Metref, S., E. Cosme, F. Le Guillou, J. Le Sommer, J.-M. Brankart, and J. Verron (2020), Wide-swath altimetric satellite data assimilation with correlated-error reduction, *Frontiers in Marine Science*, *6*, 822, doi:10.3389/fmars.2019.00822.

Minnett, P. J., A. Alvera-Azcárate, T. Chin, G. Corlett, C. Gentemann, I. Karagali, X. Li, A. Marsouin, S. Marullo, E. Maturi, et al. (2019), Half a century of satellite remote sensing of sea-surface temperature, *Remote Sensing of Environment*, *233*, 111,366, doi:10.1016/j.rse.2019.111366.

Miyazawa, Y., X. Guo, S. M. Varlamov, T. Miyama, K. Yoda, K. Sato, T. Kano, and K. Sato (2015), Assimilation of the seabird and ship drift data in the north-eastern sea of Japan into an operational ocean nowcast/forecast system, *Scientific Reports*, *5*, 17,672, doi:10.1038/srep17672.

Molemaker, M. J., J. C. McWilliams, and W. K. Dewar (2015), Submesoscale Instability and Generation of Mesoscale Anticyclones near a Separation of the California Undercurrent, *Journal of Physical Oceanography*, *45*(3), 613–629, doi:10.1175/JPO-D-13-0225.1.

Molines, J.-M. (2018), meom-configurations/NATL60-CJM165: NATL60 code used for CJM165 experiment, doi:10.5281/zenodo.1210116.

Mordy, C. W., E. D. Cokelet, A. De Robertis, R. Jenkins, C. E. Kuhn, N. Lawrence-Slavas, C. L. Berchok, J. L. Crance, J. T. Sterling, J. N. Cross, et al. (2017), Advances in ecosystem research: Saildrone surveys of oceanography, fish, and marine mammals in the Bering Sea, *Oceanography*, *30*(2), 113–115, doi:10.5670/oceanog.2017.230.

Morrow, R., and P.-Y. Le Traon (2012), Recent advances in observing mesoscale ocean dynamics with satellite altimetry, *Advances in Space Research*, *50*(8), 1062–1076, doi:10.1016/j.asr.2011.09.033.

Morrow, R., F. Birol, D. Griffin, and J. Sudre (2004), Divergent pathways of cyclonic and anti-cyclonic ocean eddies, *Geophysical Research Letters*, *31*(24), 1–5, doi:10.1029/2004GL020974.

Morrow, R., D. Blumstein, and G. Dibarboure (2018), Fine-scale Altimetry and the Future SWOT Mission, in *New frontiers in operational oceanography*, edited by E. P. Chassignet, A. Pascual, J. Tintoré, and J. Verron, pp. 191–226, GODAE Oceanview, doi:10.17125/gov2018.ch08.

Morrow, R., L.-L. Fu, F. Ardhuin, M. Benkiran, B. Chapron, E. Cosme, F. d'Ovidio, J. T. Farrar, S. T. Gille, G. Lapeyre, P.-Y. Le Traon, A. Pascual, A. Ponte, B. Qiu, N. Rascle, C. Ubelmann, J. Wang, and E. D. Zaron (2019), Global Observations of Fine-Scale Ocean Surface Topography With the Surface Water and Ocean Topography (SWOT) Mission, *Frontiers in Marine Science*, *6*, 232, doi:10.3389/fmars.2019.00232.

Morvan, M., P. L. Hégaret, X. Carton, J. Gula, C. Vic, and C. de Marez (2019), The life cycle of submesoscale eddies generated by topographic interactions, *Ocean Science*, *15*(6), 1531–1543, doi:10.5194/os-15-1531-2019.

Mouffe, M., A. Getirana, S. M. Ricci, C. Lion, S. Biancamaria, A. Boone, N. M. Mognard, and P. Rogel (2011), Towards SWOT data assimilation for hydrology : automatic calibration of global flow routing model parameters in the Amazon basin, in *AGU Fall Meeting Abstracts*, vol. 2011, pp. H23G–1364, available at `https://ui.adsabs.harvard.edu/abs/2011AGUFM.H23G1364M`.

Müller, M., B. K. Arbic, J. G. Richman, J. F. Shriver, E. L. Kunze, R. B. Scott, A. J. Wallcraft, and L. Zamudio (2015), Toward an internal gravity wave spectrum in global ocean models, *Geophysical Research Letters*, *42*(9), 3474–3481, doi:10.1002/2015GL063365.

Müller, V., and O. Melnichenko (2020), Decadal Changes of Meridional Eddy Heat Transport in the Subpolar North Atlantic Derived From Satellite and In Situ Observations, *Journal of Geophysical Research: Oceans*, *125*(5), e2020JC016,081, doi:10.1029/2020JC016081.

Nikurashin, M., and R. Ferrari (2010), Radiation and dissipation of internal waves generated by geostrophic motions impinging on small-scale topography: Theory, *Journal of Physical Oceanography*, *40*(5), 1055–1074, doi:10.1175/2009jpo4199.1.

Nurser, A. J. G., and S. Bacon (2013), The Rossby radius in the Arctic Ocean, *Ocean Science*, *10*, 1807–1831, doi:10.5194/osd-10-1807-2013.

Olmedo, E., J. Martínez, M. Umbert, N. Hoareau, M. Portabella, J. Ballabrera-Poy, and A. Turiel (2016), Improving time and space resolution of smos salinity maps using multifractal fusion, *Remote Sensing of Environment*, *180*, 246–263, doi:10.1016/j.rse.2016.02.038.

Omand, M. M., E. A. d'Asaro, C. M. Lee, M. J. Perry, N. Briggs, I. Cetinić, and A. Mahadevan (2015), Eddy-driven subduction exports particulate organic carbon from the spring bloom, *Science*, *348*(6231), 222–225, doi:10.1126/science.1260062.

Paduan, J. D., and I. Shulman (2004), HF radar data assimilation in the Monterey Bay area, *Journal of Geophysical Research*, *109*(C7), doi:10.1029/2003jc001949.

Pascual, A., Y. Faugère, G. Larnicol, and P.-Y. Le Traon (2006), Improved description of the ocean mesoscale variability by combining four satellite altimeters, *Geophysical Research Letters*, *33*(2), 2–5, doi:10.1029/2005GL024633.

Pascual, A., M.-I. Pujol, G. Larnicol, P.-Y. Le Traon, and M.-H. Rio (2007), Mesoscale mapping capabilities of multisatellite altimeter missions: First results with real data in the Mediterranean Sea, *Journal of Marine Systems*, *65*(1), 190–211, doi:10.1016/j.jmarsys.2004.12.004.

Pascual, A., S. Ruiz, A. Olita, C. Troupin, M. Claret, B. Casas, B. Mourre, P.-m. Poulain, A. Tovar-sanchez, A. Capet, et al. (2017), A Multiplatform Experiment to Unravel Meso- and Submesoscale Processes in an Intense Front (AlborEx), *Frontiers in Marine Science*, *4*, 39, doi:10.3389/fmars.2017.00039.

Peral, E., E. Rodríguez, and D. Esteban-Fernández (2015), Impact of surface waves on SWOT's projected ocean accuracy, *Remote Sensing*, *7*(11), 14,509–14,529, doi:10.3390/rs71114509.

Pietri, A., and J. Karstensen (2018), Dynamical Characterization of a Low Oxygen Submesocale Coherent Vortex in the Eastern North Atlantic Ocean, *Journal of Geophysical Research: Oceans*, *123*(3), 2049–2065, doi:10.1002/2017JC013177.

Ponte, A. L., and P. Klein (2013), Reconstruction of the upper ocean 3d dynamics from high-resolution sea surface height, *Ocean Dynamics*, *63*(7), 777–791, doi:10.1007/s10236-013-0611-7.

Pörtner, H., D. Roberts, V. Masson-Delmotte, P. Zhai, M. Tignor, E. Poloczanska, K. Mintenbeck, M. Nicolai, A. Okem, J. Petzold, B. Rama, and N. e. Weyer (2019), IPCC Special Report on the Ocean and Cryosphere in a Changing Climate, *IPCC Intergovernmental Panel on Climate Change: Geneva, Switzerland*.

Pujol, M.-I., and G. Larnicol (2005), Mediterranean sea eddy kinetic energy variability from 11 years of altimetric data, *Journal of Marine Systems*, *58*(3), 121–142, doi:10.1016/j.jmarsys.2005.07.005.

Pujol, M.-I., G. Dibarboure, P. Y. Le Traon, and P. Klein (2012), Using high-resolution altimetry to observe mesoscale signals, *Journal of Atmospheric and Oceanic Technology*, *29*, 1409–1416, doi:10.1175/JTECH-D-12-00032.1.

Pujol, M.-I., Y. Faugère, G. Taburet, S. Dupuy, C. Pelloquin, M. Ablain, and N. Picot (2016), DUACS DT2014 : the new multi-mission altimeter data set reprocessed over 20 years, *Ocean Science*, *12*, 1067–1090, doi:10.5194/os-12-1067-2016.

Pujol, M.-I., P. Schaeffer, Y. Faugère, M. Raynal, G. Dibarboure, and N. Picot (2018), Gauging the improvement of recent mean sea surface models: a new approach for identifying and quantifying their errors, *Journal of Geophysical Research: Oceans*, *123*(8), 5889–5911, doi:10.1029/2017JC013503.

Qiu, B., S. Chen, P. Klein, C. Ubelmann, L.-L. Fu, and H. Sasaki (2016), Reconstructability of Three-Dimensional Upper-Ocean Circulation from SWOT Sea Surface Height Measurements, *Journal of Physical Oceanography*, *46*(3), 947–963, doi:10.1175/JPO-D-15-0188.1.

Qiu, B., T. Nakano, S. Chen, and P. Klein (2017), Submesoscale transition from geostrophic flows to internal waves in the northwestern Pacific upper ocean., *Nature Communications*, *8*(1), 1–10, doi:10.1038/ncomms14055.

Qiu, B., S. Chen, P. Klein, J. Wang, H. S. Torres, L.-L. Fu, and D. Menemenlis (2018), Seasonality in transition scale from balanced to unbalanced motions in the world ocean, *Journal of Physical Oceanography*, *48*(3), 591–605, doi:10.1175/JPO-D-17-0169.1.

Queffeulou, P. (2004), Long-term validation of wave height measurements from altimeters, *Marine Geodesy*, *27*(3-4), 495–510, doi:10.1080/01490410490883478.

Ramos, R. J., B. Lund, and H. C. Graber (2009), Determination of internal wave properties from X-Band radar observations, *Ocean Engineering*, *36*(14), 1039–1047, doi:10.1016/j.oceaneng.2009.07.004.

Ray, R. D., and E. D. Zaron (2016), M2 Internal Tides and Their Observed Wavenumber Spectra from Satellite Altimetry, *Journal of Physical Oceanograph*, *46*(1), 3–22, doi:10.1175/JPO-D-15-0065.1.

Reul, N., S. Fournier, J. Boutin, O. Hernandez, C. Maes, B. Chapron, G. Alory, Y. Quilfen, J. Tenerelli, S. Morisset, et al. (2014), Sea surface salinity observations from space with the smos satellite: A new means to monitor the marine branch of the water cycle, *Surveys in Geophysics*, *35*(3), 681–722, doi:10.1007/s10712-013-9244-0.

Richardson, P. L. (1983), Eddy Kinetic Energy in the North Atlantic From Surface Drifters, *Journal of Geophysical Research: Ocean*, *88*(C7), 4355–4367, doi:10.1029/jc088ic07p04355.

Rio, M.-H., and the CLS altimetry team. (2013), The state of the art in the study of ocean circulation with satellite altimetry., in *IMEDEA-EUMETSAT Workshop, Palma de Mallorca, Spain.*

Rio, M.-H., S. Mulet, and N. Picot (2014a), Beyond GOCE for the ocean circulation estimate: Synergetic use of altimetry, gravimetry, and in situ data provides new insight into geostrophic and Ekman currents, *Geophysical Research Letters*, *41*(24), 8918–8925, doi:10.1002/2014GL061773.

Rio, M.-H., A. Pascual, P. M. Poulain, M. Menna, B. Barceló, and J. Tintoré (2014b), Computation of a new mean dynamic topography for the Mediterranean Sea from model outputs , altimeter measurements and oceanographic in situ data, *Ocean Science*, *10*(4), 731–744, doi:10.5194/os-10-731-2014.

Rixen, M., J.-M. Beckers, S. Levitus, J. Antonov, T. Boyer, C. Maillard, M. Fichaut, E. Balopoulos, S. Iona, H. Dooley, M. Garcia, B. Manca, A. Giorgetti, G. Manzella, N. Mikhailov, N. Pinardi, and M. Zavatarelli (2005), The Western Mediterranean Deep Water : A proxy for climate change, *Geophysical Research Letters*, *32*(12), 2–5, doi:10.1029/2005GL022702.

Robinson, A. R., W. G. Leslie, A. Theocharis, and A. Lascaratos (2001), Mediterranean sea circulation, in *Encyclopedia of Ocean Sciences*, edited by J. H. Steele, pp. 1689–1705, Academic Press, Oxford, doi:10.1006/rwos.2001.0376.

Rocha, C. B., T. K. Chereskin, S. T. Gille, and D. Menemenlis (2016), Mesoscale to Submesoscale Wavenumber Spectra in Drake Passage, *Journal of Physical Oceanography*, *46*(2), 601–620, doi:10.1175/JPO-D-15-0087.1.

Rodriguez, E. (2010), The Surface Water and Ocean Topography (SWOT) Mission, in *OSTST Meeting*, Lisboa, Portugal.

Rodríguez, E. (2016), Surface Water and Ocean Topography Mission Project Science Requirement Document, Revision A, *Jet Propulsion Laboratory, California Institute of Technology, JPL D-61923*, p. 28.

Rodriguez, E., D. E. Fernandez, E. Peral, C. W. Chen, J.-w. D. Bleser, and B. Williams (2017), Wide-Swath Altimetry: a review, in *Satellite Altimetry Over Oceans and Land Surfaces*, pp. 71–112, CRC Press, doi:10.1201/9781315151779.

Roemmich, D., and W. Owens (2000), The argo project: Observing the global ocean with profiling floats, *Oceanography*, *13*, 45–50, doi:10.5670/oceanog.2009.36.

Rogé, M. (2018), Etudes de cartographie altimétrique pour l'observation de la dynamique méso-échelle dans le contexte swot: application à la mer méditerranée occidentale, Ph.D. thesis, Université Paul Sabatier-Toulouse III, available at `https://tel.archives-ouvertes.fr/tel-02146019/`.

Rogé, M., R. A. Morrow, and G. Dencausse (2015), Altimetric Lagrangian advection to reconstruct Pacific Ocean fine-scale surface tracer fields, *Ocean Dynamics*, *65*(9-10), 1249–1268, doi:10.1007/s10236-015-0872-4.

Rogé, M., R. Morrow, C. Ubelmann, and G. Dibarboure (2017), Using a dynamical advection to reconstruct a part of the SSH evolution in the context of SWOT , application to the Mediterranean Sea, *Ocean Dynamics*, *67*(8), 1047–1066, doi:10.1007/s10236-017-1073-0.

Rubio, A., J. Mader, L. Corgnati, C. Mantovani, A. Griffa, A. Novellino, C. Quentin, L. Wyatt, J. Schulz-Stellenfleth, J. Horstmann, P. Lorente, E. Zambianchi, M. Hartnett, C. Fernandes, V. Zervakis, P. Gorringe, A. Melet, and I. Puillat (2017), HF radar activity in European coastal seas: Next steps toward a pan-European HF radar network, *Frontiers in Marine Science*, *4*, 8, doi:10.3389/fmars.2017.00008.

Rudin, L. I., S. Osher, and E. Fatemi (1992), Nonlinear total variation based noise removal algorithms, *Physica D: nonlinear phenomena*, *60*(1-4), 259–268, doi:10.1016/0167-2789(92)90242-f.

Ruggiero, G., E. Cosme, J. Brankart, J. L. Sommer, and C. Ubelmann (2016), An efficient way to account for observation error correlations in the assimilation of data from the future SWOT High-Resolution altimeter mission, *Journal of Atmospheric and Oceanic Technology*, *33*(12), 2755–2768, doi:10.1175/JTECH-D-16-0048.1.

Ruiz, S., A. Pascual, B. Garau, Y. Faugère, A. Alvarez, and J. Tintoré (2009), Mesoscale dynamics of the Balearic Front, integrating glider , ship and satellite data, *Journal of Marine Systems*, *78*, S3–S16, doi:10.1016/j.jmarsys.2009.01.007.

Ruiz, S., M. Claret, A. Pascual, A. Olita, C. Troupin, A. Capet, A. Tovar-Sánchez, J. Allen, P.-M. Poulain, J. Tintoré, and A. Mahadevan (2019), Effects of Oceanic Mesoscale and Submesoscale Frontal Processes on the Vertical Transport of Phytoplankton, *Journal of Geophysical Research: Oceans*, *124*(8), 5999–6014, doi:10.1029/2019JC015034.

Ruiz-Villarreal, M., C. González-Pola, G. D. del Río, A. Lavin, P. Otero, S. Piedracoba, and J. Cabanas (2006), Oceanographic conditions in North and Northwest Iberia and their influence on the Prestige oil spill, *Marine Pollution Bulletin*, *53*(5-7), 220–238, doi:10.1016/j.marpolbul.2006.03.011.

Sánchez-Román, A., L. Gómez-Navarro, R. Fablet, D. Oro, E. Mason, J. Arcos, S. Ruiz, and A. Pascual (2019), Rafting behaviour of seabirds as a proxy to describe surface ocean currents in the balearic sea, *Scientific reports*, *9*(1), 1–11, doi:10.1038/s41598-018-36819-w.

Sasaki, H., P. Kleinand, B. Qiu, and Y. Sasai (2014), Impact of oceanic-scale interactions on the seasonal modulation of ocean dynamics by the atmosphere, *Nature Communications*, *5*, 5636, doi:10.1038/ncomms6636.

Savage, A. C. (2017), Sea surface height signatures of internal gravity waves, Ph.D. thesis, University of Michigan, available at `https://deepblue.lib.umich.edu/handle/2027.42/138555`.

Savage, A. C., B. K. Arbic, M. H. Alford, J. K. Ansong, J. T. Farrar, D. Menemenlis, A. K. O'Rourke, J. G. Richman, J. F. Shriver, G. Voet, et al. (2017a), Spectral decomposition of internal gravity wave sea surface height in global models, *Journal of Geophysical Research: Oceans*, *122*(10), 7803–7821, doi:10.1002/2017JC013009.

Savage, A. C., B. K. Arbic, J. G. Richman, J. F. Shriver, M. H. Alford, M. C. Buijsman, J. Thomas Farrar, H. Sharma, G. Voet, A. J. Wallcraft, et al. (2017b), Frequency content of sea surface height variability from internal gravity waves to mesoscale eddies, *Journal of Geophysical Research: Oceans*, *122*(3), 2519–2538, doi:10.1002/2016JC012331.

Schaeffer, P., Y. Faugere, J. F. Legeais, A. Ollivier, T. Guinle, and N. Picot (2012), The CNES_CLS11 global mean sea surface computed from 16 years of satellite altimeter data, *Marine Geodesy*, *35*(sup1), 3–19, doi:10.1080/01490419.2012.718231.

Schroeder, K., J. Chiggiato, S. Josey, M. Borghini, S. Aracri, and S. Sparnocchia (2017), Rapid response to climate change in a marginal sea., *Scientific reports*, *7*, 4065, doi:10.1038/s41598-017-04455-5.

Shchepetkin, A. F., and J. C. McWilliams (2005), The regional oceanic modeling system (ROMS): a split-explicit, free-surface, topography-following-coordinate oceanic model., *Ocean Modelling*, *9*, 347–404, doi:10.1016/j.ocemod.2004.08.002.

Shriver, J. F., B. K. Arbic, J. G. Richman, R. D. Ray, E. J. Metzger, A. J. Wallcraft, and P. G. Timko (2012), An evaluation of the barotropic and internal tides in a high-resolution global ocean circulation model, *Journal of Geophysical Research: Oceans*, *117*(C10), 1–14, doi:10.1029/2012JC008170.

Simoncelli, S., C. Fratianni, N. Pinardi, A. Grandi, M. Drudi, P. Oddo, and S. Dobricic (2014), Mediterranean Sea physical reanalysis (MEDREA 1987-2015) (Version 1) [Data set], *Copernicus Monitoring Environment Marine Service (CMEMS)*, doi:10.25423/medsea_reanalysis_phys_006_004.

Smith, R., E. Johns, G. Goni, J. Trinanes, R. Lumpkin, A. Wood, C. Kelble, S. Cummings, J. Lamkin, and S. Privoznik (2014), Oceanographic conditions in the gulf of mexico in july 2010, during the deepwater horizon oil spill, *Continental Shelf Research*, *77*, 118–131, doi:10.1016/j.csr.2013.12.009.

Sonka, M., V. Hlavac, and R. Boyle (2014), *Image processing, analysis, and machine vision*, Cengage Learning: Boston, MA, USA, 2014.

Soufflet, Y., P. Marchesiello, F. Lemarié, J. Jouanno, X. Capet, L. Debreu, and R. Benshila (2016), On effective resolution in ocean models, *Ocean Modelling*, *98*, 36–50, doi:10.1016/j.ocemod.2015.12.004.

Stewart, R. H., et al. (2008), *Introduction to physical oceanography*, Texas A & M University College Station.

Sudre, J., H. Yahia, O. Pont, and V. Garçon (2015), Ocean turbulent dynamics at superresolution from optimal multiresolution analysis and multiplicative cascade, *IEEE Transactions on Geoscience and Remote Sensing*, *53*(11), 6274–6285, doi:10.1109/TGRS.2015.2436431.

Taburet, G., A. Sanchez-Roman, M. Ballarotta, M.-I. Pujol, and J.-f. Legeais (2019), DUACS DT2018 : 25 years of reprocessed sea level altimetry products, *Ocean Science*, *15*, 1207–1224, doi:10.5194/os-15-1207-2019.

Talley, L. D. (2011), *Descriptive physical oceanography: an introduction*, Academic press.

Taylor, J. R., and R. Ferrari (2011), Ocean fronts trigger high latitude phytoplankton blooms, *Geophysical Research Letters*, *38*(23), doi:10.1029/2011GL049312.

Tchilibou, M. L. (2018), Dynamique méso-sousmésoéchelle et marée interne dans le Pacifique tropical: implications pour l'altimétrie et la mer des Salomon, Ph.D. thesis, Université Paul Sabatier-Toulouse III, available at `https://tel.archives-ouvertes.fr/tel-02383903/`.

Testor, P., G. Meyers, C. Pattiaratchi, R. Bachmayer, D. Hayes, T. Carval, A. Ganachaud, L. Mortier, V. Taillandier, P. Lherminier, T. Terre, M. Visbeck, J. Karstensen, G. Krahmann, M. Rixen, P.-m. Poulain, S. Osterhus, J. Tintore, B. Garau, D. Smeed, G. Griffiths, L. Merckelbach, C. Schmid, J. A. Barth, O. Schofield, S. Glenn, J. Kohut, M. J. Perry, C. Eriksen, U. Send, R. Davis, D. Rudnick, C. Jones, D. Webb, C. Lee, and B. Owens (2010), Gliders as a component of future observing systems, OceanObs' 09, available at `http://eprints.uni-kiel.de/10184/`.

Thomas, L. N., A. Tandon, and A. Mahadevan (2008), Submesoscale processes and dynamics, *Ocean modeling in an Eddying Regime*, *177*, 17–38, doi:10.1029/177GM04.

Thompson, A. F., A. Lazar, C. Buckingham, A. C. Naveira Garabato, G. M. Damerell, and K. J. Heywood (2016), Open-ocean submesoscale motions: A full seasonal cycle of mixed layer instabilities from gliders, *Journal of Physical Oceanography*, *46*(4), 1285–1307, doi:10.1175/JPO-D-15-0170.1.

Thomson, R. E., and W. J. Emery (2014), Chapter 1 - data acquisition and recording, in *Data Analysis Methods in Physical Oceanography (Third Edition)*, edited by R. E. Thomson and W. J. Emery, third edition ed., pp. 1 – 186, Elsevier, Boston, doi:10.1016/B978-0-12-387782-6.00001-6.

Tintoré, J., N. Pinardi, E. Álvarez-fanjul, E. Aguiar, D. Álvarez-berastegui, M. Bajo, R. Balbin, R. Bozzano, B. B. Nardelli, V. Cardin, B. Casas, M. Charcos-llorens, J. Chiggiato, E. Clementi, G. Coppini, F. d'Ortenzio, A. Drago, M. Drudi, G. E. Serafy, C. Ferrarin, C. Fossi, C. Frangoulis, F. Galgani, A. Novellino, D. Obaton, A. Orfila, A. Pascual, S. Speich, F. Werner, E. G. Pavia, et al. (2019), Challenges for Sustained Observing and Forecasting Systems in the Mediterranean Sea, *Frontiers in Marine Science*, *6*(September), 568, doi:10.3389/fmars.2019.00568.

Todd, R. E., F. P. Chavez, S. Clayton, S. E. Cravatte, M. P. Goes, M. I. Graco, X. Lin, J. Sprintall, N. V. Zilberman, M. Archer, et al. (2019), Global Perspectives on Observing Ocean Boundary Current Systems, *Frontiers in Marine Science*, *6*, 423, doi:10.3389/fmars.2019.00423.

Torres, H. S., P. Klein, D. Menemenlis, B. Qiu, Z. Su, J. Wang, S. Chen, and L.-L. Fu (2018), Partitioning Ocean Motions Into Balanced Motions and Internal Gravity Waves : A Modeling Study in Anticipation of Future Space Missions, *Journal of Geophysical Research: Oceans*, *123*(11), 8084–8105, doi:10.1029/2018JC014438.

Torres, H. S., P. Klein, L. Siegelman, B. Qiu, S. Chen, C. Ubelmann, J. Wang, D. Menemenlis, and L.-L. Fu (2019), Diagnosing ocean-wave-turbulence interactions from space, *Geophysical Research Letters*, *46*(15), 8933–8942, doi:10.1029/2019GL083675.

Ubelmann, C., J. Verron, J. M. Brankart, E. Cosme, and P. Brasseur (2009), Impact of data from upcoming altimetric missions on the prediction of the three-dimensional circulation in the tropical Atlantic Ocean, *Journal of Operational Oceanography*, *2*(1), 3–14, doi:10.1080/1755876X.2009.11020104.

Ubelmann, C., P. Klein, and L.-L. Fu (2015), Dynamic interpolation of sea surface height and potential applications for future high-resolution altimetry mapping, *Journal of Atmospheric and Oceanic Technology*, *32*(1), 177–184, doi:10.1175/JTECH-D-14-00152.1.

Ubelmann, C., G. Dibarboure, and P. Dubois (2018), A Cross-Spectral Approach to Measure the Error Budget of the SWOT Altimetry Mission over the Ocean, *Journal of Atmospheric and Oceanic Technology*, *35*(4), 845–857, doi:10.1175/JTECH-D-17-0061.1.

Uchida, T., R. Abernathey, and S. Smith (2017), Seasonality of eddy kinetic energy in an eddy permitting global climate model, *Ocean Modelling*, *118*(2017), 41–58, doi:10.1016/j.ocemod.2017.08.006.

Vazquez-Cuervo, J., J. Gomez-Valdes, M. Bouali, L. E. Miranda, T. Van der Stocken, W. Tang, and C. Gentemann (2019), Using saildrones to validate satellite-derived sea surface salinity and sea surface temperature along the california/baja coast, *Remote Sensing*, *11*(17), 1964, doi:10.3390/rs11171964.

Vergara, O., R. A. Morrow, M.-I. Pujol, G. Dibarboure, and C. Ubelmann (2020), Global submesoscale transition scale estimation using alongtrack satellite altimetry, *Earth and Space Science Open Archive*, p. 19, doi:10.1002/essoar.10501996.1.

Verron, J., P. Bonnefond, L. Aouf, F. Birol, S. A. Bhowmick, S. Calmant, T. Conchy, J.-f. Crétaux, G. Dibarboure, A. K. Dubey, Y. Faugère, K. Guerreiro, P. K. Gupta, M. Hamon, F. J. Id, R. Kumar, R. M. Id, A. Pascual, M.-I. Pujol, and E. Rémy (2018), The Benefits of the Ka-Band as Evidenced from the SARAL / AltiKa Altimetric Mission : Scientific Applications, *Remote Sensing*, *10*(2), 163, doi:10.3390/rs10020163.

Verron, J., P. Bonnefond, O. Andersen, F. Ardhuin, M. Bergé-Nguyen, S. Bhowmick, D. Blumstein, F. Boy, L. Brodeau, J.-F. Crétaux, M. L. Dabat, G. Dibarboure, S. Fleury, F. Garnier, L. Gourdeau, K. Marks, D. Sandwell, W. H. F. Smith, and E. Zaron (2020), The SARAL / AltiKa mission : A step forward to the future of altimetry, *Advances in Space Research*, doi:10.1016/j.asr.2020.01.030.

Viglione, G. A., A. F. Thompson, M. M. Flexas, J. Sprintall, and S. Swart (2018), Abrupt Transitions in Submesoscale Structure in Southern Drake Passage : Glider Observations and Model Results, *Journal of Physical Oceanography*, *48*(9), 2011–2027, doi:10.1175/JPO-D-17-0192.1.

Voosen, P. (2018), Saildrone fleet could help replace aging buoys, *Sciecne*, *358*(6380), 1082–1083, doi:10.1126/science.359.6380.1082.

Wan, X., S. Jin, B. Liu, S. Tian, W. Kong, and R. F. Annan (2020), Effects of interferometric radar altimeter errors on marine gravity field inversion, *Sensors*, *20*(9), 2465, doi:10.3390/s20092465.

Wang, J., L.-L. Fu, B. Qiu, D. Menemenlis, J. T. Farrar, Y. Chao, A. F. Thompson, and M. M. Flexas (2018), An Observing System Simulation Experiment for the Calibration and Validation of the Surface Water Ocean Topography Sea Surface Height Measurement Using In Situ Platforms, *Journal of Atmospheric and Oceanic Technology*, *35*(2), 281–297, doi:10.1175/JTECH-D-17-0076.1.

Wang, J., L.-L. Fu, H. S. Torres, S. Chen, B. Qiu, and D. Menemenlis (2019a), On the spatial scales to be resolved by the surface water and ocean topography Ka-band radar interferometer, *Journal of Atmospheric and Oceanic Technology*, *36*(1), 87–99, doi:10.1175/JTECH-D-18-0119.1.

Wang, S., F. Qiao, D. Dai, and X. Zhou (2019b), Anisotropy of the sea surface height wavenumber spectrum from altimeter observations, *Scientific Reports*, pp. 1–10, doi:10.1038/s41598-019-52328-w.

Xu, Y., and L.-L. Fu (2012), The Effects of Altimeter Instrument Noise on the Estimation of the Wavenumber Spectrum of Sea Surface Height, *Journal of Physical Oceanography*, *42*(12), 2229–2233, doi:10.1175/JPO-D-12-0106.1.

Yan, R., L. Shao, and Y. Liu (2013), Nonlocal hierarchical dictionary learning using wavelets for image denoising, *IEEE Transactions on Image Processing*, *22*(12), 4689–4698, doi:10.1109/TIP.2013.2277813.

Yaremchuk, M., J. d'Addezio, G. Panteleev, and G. Jacobs (2018), On the approximation of the inverse error covariances of high-resolution satellite altimetry data, *Quarterly Journal of the Royal Meteorological Society*, *144*(715), 1995–2000, doi:10.1002/qj.3336.

Yaremchuk, M., J. M. d'Addezio, and G. Jacobs (2020), Facilitating inversion of the error covariance models for the wide-swath altimeters, *Remote Sensing*, *12*(11), 1823, doi:10.3390/rs12111823.

Yu, X., A. C. Naveira Garabato, A. P. Martin, C. E. Buckingham, L. Brannigan, and Z. Su (2019), An annual cycle of submesoscale vertical flow and restratification in the upper ocean, *Journal of Physical Oceanography*, *49*(6), 1439–1461, doi:10.1175/JPO-D-18-0253.1.

Zhang, Z., and B. Qiu (2018), Evolution of Submesoscale Ageostrophic Motions Through the Life Cycle of Oceanic Mesoscale Eddies, *Geophysical Research Letters*, *45*(11), 847–855, doi:10.1029/2018GL080399.